FACULTEIT TOEGEPASTE WETENSCHAPPEN
DEPARTEMENT BURGERLIJKE BOUWKUNDE
AFDELING BOUWMECHANICA
W. DE CROYLAAN 2
B-3001 HEVERLEE

KATHOLIEKE
UNIVERSITEIT
LEUVEN

SYSTEM IDENTIFICATION AND DAMAGE DETECTION IN CIVIL ENGINEERING

Promotor:
Prof. dr. ir. G. De Roeck

Proefschrift voorgedragen tot
het behalen van het doctoraat
in de toegepaste wetenschappen

door

Bart PEETERS

December 2000

FACULTEIT TOEGEPASTE WETENSCHAPPEN
DEPARTEMENT BURGERLIJKE BOUWKUNDE
AFDELING BOUWMECHANICA
W. DE CROYLAAN 2
B-3001 HEVERLEE

KATHOLIEKE
UNIVERSITEIT
LEUVEN

SYSTEM IDENTIFICATION AND DAMAGE DETECTION IN CIVIL ENGINEERING

Jury:
Prof. dr. ir. E. Aernoudt, voorzitter
Prof. dr. ir. G. De Roeck, promotor
Prof. dr. ir. A. Cunha (University of Porto)
Prof. dr. ir. G. Degrande
Prof. dr. ir. B. De Moor
Prof. dr. ir. W. Heylen
Dr. ir. H. Van der Auweraer (LMS International)
Prof. dr. ir. G. Vermeir

Proefschrift voorgedragen tot
het behalen van het doctoraat
in de toegepaste wetenschappen

door

Bart PEETERS

UDC 534.32:624 December 2000

http://www.bwk.kuleuven.ac.be/bwm/

D/2000/7515/44

ISBN 90-5682-274-8

VOORWOORD

Met deze thesis komt het einde aan een boeiende periode van zes jaar. Het is meteen ook een mooie gelegenheid om enkele mensen te bedanken die belangrijk waren in de totstandkoming van dit werk of voor wat ze betekenen in mijn leven.

Guido De Roeck heeft zijn rol als promotor perfect vervuld. Hij overtuigde me om het doctoraat aan te vatten, zorgde voor een goede omkadering in de vorm van interessante en motiverende onderzoeksprojecten en liet me ruim de vrijheid om mijn weg te zoeken in het onderzoeksdomein, zonder evenwel het doel uit het oog te verliezen. Naast begeleider van onderzoek is hij ook een begeleider van mensen. Ik bewonder hem voor zijn inzet en inzicht om van zijn steeds veranderende afdeling een hechte groep mensen te vormen.

Ik zou graag de leden van de jury willen bedanken: Alvaro Cunha, Geert Degrande, Bart De Moor, Ward Heylen, Herman Van der Auweraer en Gerrit Vermeir. Gedurende de jaren dat ik aan dit doctoraat werkte, heb ik de gelegenheid gehad om elk van hen meermaals te ontmoeten, in Leuven of iets verder van huis. Nieuwe ideeën en een toegenomen motivatie waren steeds het resultaat van deze ontmoetingen. Ik ben vereerd dat zij in mijn jury zetelen. Ik dank ook Etienne Aernoudt voor het vervullen van de voorzitterstaak.

I would like to thank the members of the jury: Alvaro Cunha, Geert Degrande, Bart De Moor, Ward Heylen, Herman Van der Auweraer and Gerrit Vermeir. During the years that I was working on this thesis, we were able to meet at several occasions, in Leuven or elsewhere. These encounters were a great source of inspiration and motivation. I am honoured that they accepted to be a member of my jury. I am also thanking Etienne Aernoudt for being the president of the jury.

Prof. George Moustakides from the University of Patras, Greece deserves my gratitude for his hospitality and time during my two stays at his institute. I enjoyed our cooperation.

De collega's van de afdeling bouwmechanica dank ik voor alle leuke momenten op het werk, maar ook na de uren. Aan de talloze weekendjes, fietstochten, etentjes, kerstfeestjes en kaartavonden bewaar ik mooie herinneringen.

De partners die betrokken waren bij de onderzoeksprojecten wens ik te bedanken voor de prettige samenwerking.

Bart Van den Branden heeft met veel beroepsernst en enthousiasme aan MACEC gewerkt. "*It is a nice piece of software*," zoals ooit iemand terecht opmerkte na een demo. Ik heb het geluk gehad om nog met talrijke andere gemotiveerde eindwerkstudenten samen te werken. Allen bedankt!

Op het financiële vlak dank ik onze universiteit voor de kans die ze me gaf om zes jaar als assistent te werken. Het IWT, het FWO-Vlaanderen en de Europese Commissie sponsorden de onderzoeksprojecten waaraan ik meewerkte en waarvan talrijke resultaten opgenomen zijn in dit werk.

Op het einde van dit voorwoord wens ik ook nog enkele mensen in de bloemetjes te zetten die, hoewel niet rechtstreeks bij dit werk betrokken, voor mij van onschatbare waarde zijn.

Mijn ouders dank ik voor de vrijheid, de bezorgdheid, de kansen en het vertrouwen dat ik nu al bijna dertig jaar mag genieten.

Mijn schoonouders dank ik voor het opvangen van de familie tijdens congressen of nog eens het laatste weekendje werken aan mijn doctoraat.

Een zeer speciale plaats in dit voorwoord en in mijn hart reserveer ik voor Hilde en Karel. Hen te zien lachen maakt van mij de gelukkigste man op de wereld.

Bart Peeters
Leuven, december 2000

ABSTRACT

This thesis addresses two key issues of a real-life vibration-based structural health monitoring system. The first issue is the determination of an experimental model of a vibrating structure from output-only data. The use of freely available ambient excitation sources reduces significantly the cost of testing. Besides, there is no alternative in a continuous monitoring system. By applying advanced subspace methods to acceleration measurements, a high-quality experimental model can be identified. This is verified by many simulation, laboratory and real-life experiments.

The second issue is the detection of damage under varying environmental conditions. The problem is that both damage and temperature are affecting the experimental model of a structure. A statistical system identification solution is developed to separate these influences. A thorough analysis of bridge vibration test data is presented. The tests were unique in that they combined long-term monitoring with the application of realistic damage scenarios. The conclusion is that damage can successfully be detected under varying environmental conditions.

NOMENCLATURA

A, B, C, D	Discrete-time state-space model
A_c, B_c, C_c, D_c	Continuous-time state-space model
a_i, b_i	"Modal a" and "modal b" coefficient
$a(q)$	**AR** operator polynomial
B_2	Input location matrix (**FE** model)
$b(q)$	**MA** operator polynomial
C_a, C_v, C_d	Output location matrices for acceleration, velocity and displacement (**FE** model)
c	Constant offset term
d	Number of model parameters
$\hat{d}_k$	Simulation error at time instant k
e_k	White noise term at time instant k
e_k^0	White noise term of the true system at time instant k
e_k^b	White noise term of the backward model at time instant k
$f(t)$	Excitation force vector at time t (**FE** model)
f	Frequency [Hz]
f_i	Eigenfrequency [Hz]
f_s	Sampling frequency [Hz]
fl	Number of flops
G	"Next state - output" covariance matrix
G^{ref}	Reduced "next state - output" covariance matrix
$G_{c,m}$	Continuous-time stochastic modal participation matrix
G_m	Stochastic modal participation matrix
G_m^{ref}	Reduced stochastic modal participation matrix
$G(q), H(q), J(q)$	Transfer operators
$<g_{c_i}^T>$	Continuous-time stochastic modal participation vector (row of $G_{c,m}$)
H_0, J_0	Transfer operators corresponding to the true system
$H_c(j\omega)$	Frequency Response Function
$H_c(s)$	Transfer function in the Laplace-domain
H^{ref}	Output data block Hankel matrix

h_k	Discrete-time impulse response at time instant k
I	Identity matrix
i	Half the number of block rows of the output data Hankel matrix H^{ref}
j	Imaginary unit $j^2 = -1$
K	Kalman gain
k	Discrete time instant $t = k\Delta t,\ k \in \mathbb{N}$
k_i	Modal stiffness
L	Selection matrix that selects the references from the outputs
L^T	Discrete-time modal input matrix (modal participation matrix) $L^T = \Psi^{-1} B$
L_c^T	Continuous-time modal input matrix (modal participation matrix) $L_c^T = \Psi^{-1} B_c$
l	Number of outputs
$<l_{c_i}^T>$	Continuous-time modal participation vector (row of L_c^T)
M, C_2, K	Mass, damping and stiffness matrix (**FE** model)
m	Number of inputs
m_i	Modal mass
N	Number of time samples
$\mathbf{N}(\mu,\sigma)$	Gaussian distribution with mean μ and standard deviation σ
n	State-space model order $n = 2n_2$
n_2	Number of **DOF**s (**FE** model)
n_a, n_α	**AR** order
n_b	Exogenous order
n_k	Time delay between input and output
n_γ	**MA** order
O_i	Observability matrix of order i
$O_{p,m}$	Modal observability matrix of order p
P	Forward state covariance matrix
P, Q	Auxiliary matrices for the derivation of the state-space model from the **FE** model
$P_{c,m}$	Solution of the continuous-time Lyapunov equation related to the modal parameters
$P_{\hat{d}_k}$	Simulation error covariance
$P_{\hat{\theta}}$	Covariance of the model parameters
p	**ARMA** model order in case the **AR** and **MA** order are the same
$\mathcal{P}_i^{\text{ref}}$	Projection of the row space of the future outputs into the row space of the past references
Q, R, S	Process and measurement noise covariance matrices

Q, R	Factors from a QR factorization
q	Forward shift operator
$q(t), \dot{q}(t), \ddot{q}(t)$	Displacement, velocity and acceleration vector at time t (**FE** model)
$q_m(t)$	Modal displacement vector
$q_k, \dot{q}_k$	Displacement and velocity vector at discrete time instant k (**FE** model)
R_e	Covariance matrix of the innovations e_k
R_i	Output covariance matrix at time lag i
R_i	Reduced output covariance matrix at time lag i
R_u	Input covariance matrix in case of white noise inputs u_k
$R_v^0(i)$	Covariance at time lag i of the true noise sequence v_k^0
R_{xy}	Covariance between variables x and y
r	Number of references
r_{xy}	Correlation between variables x and y
$S_u(s), S_y(s)$	Input and output spectrum matrix in the Laplace domain
$S_u(z), S_y(z)$	Input and output spectrum matrix in the z-domain
$S_y^{\text{ref}}(z)$	Reduced output spectrum matrix
s	Laplace domain variable
T	Similarity transformation
$T_{1\|i}^{\text{ref}}$	Output covariances block Toeplitz matrix
t	Continuous time variable
$t_{\alpha/2,\nu}$	Variable of the Student's t-distribution
$U(s)$	Input in the Laplace-domain
U, S, V	**SVD** factors
$u(t)$	Input at time t
u_k	Input at time instant k
V	Discrete-time modal output matrix (mode shape matrix) $V = C\Psi$
V_c	Continuous-time modal output matrix (mode shape matrix) $V_c = C_c\Psi$
$\{v_{c_i}\}$	Mode shape vector
v_k	Measurement noise at time instant k
v_k^0	True system noise at time instant k, $v_k^0 = H_0 e_k^0$
w_k	Process noise vector at time instant k
$X(s)$	State in the Laplace domain
$X(z)$	State in the z-domain
$\hat{X}_i$	Kalman filter state sequence
$x(t)$	State at time t
$x_m(t)$	Modal state at time t, $x(t) = \Psi x_m(t)$
$x_m^{(i)}(t)$	i^{th} Component of the modal state

x_k	State at time instant k
$Y(s)$	Output in the Laplace domain
$Y_p^{\text{ref}}, Y_{0\|i-1}^{\text{ref}}$	Hankel matrix of past reference outputs
$Y_f, Y_{i\|2i-1}$	Hankel matrix of all future outputs
$y(t)$	Output at time t
$y_i(t)$	Contribution of mode i to the output at time t
y_k	Output at time instant k
y_k^{ref}	Reference output at time instant k
y_{i_k}	Contribution of mode i to the output at time instant k
Z	Matrix of regressor vectors φ_k
z	z-domain variable

α, β	Rayleigh damping constants $C_2 = \alpha M + \beta K$
α_i	**AR** matrix parameters
α_i^b	Reduced backward **AR** matrix parameters
Γ	Diagonal matrix having $2\xi_i\omega_i$ as elements
Γ_i^{ref}	Reduced reversed stochastic controllability matrix of order i
$\Gamma_{p,m}^{\text{ref}}$	Reduced reversed stochastic modal controllability matrix of order p
γ_i	**MA** matrix parameters
γ_i^b	Reduced backward **MA** matrix parameters
Δt	Sampling period
$\delta(t)$	Dirac delta
δ_k	Kronecker delta
$\varepsilon_k(\hat{\theta})$	Model residual
Θ	Complex eigenvector matrix of the **FE** model (non-proportional damping)
θ	Model parameter vector
θ_0	Model parameter vector corresponding to the true system
Λ	Diagonal matrix containing the eigenvalues of the **FE** model λ_i
Λ_c	Diagonal matrix containing the continuous-time eigenvalues λ_i, λ_i^*
Λ_d	Diagonal matrix containing the discrete-time eigenvalues μ_i, μ_i^*
λ	Variance of a white noise sequence
λ_0	Variance of the white noise sequence corresponding to the true system
λ_i	Continuous-time eigenvalue
μ_i	Discrete-time eigenvalue
ν	Degrees of freedom of a Student's t-distribution

Φ	Real eigenvector matrix of the **FE** model (proportional damping)
φ_i	Real eigenvector of the **FE** model (proportional damping)
φ_k	Regressor vector at time lag k
ξ_i	Modal damping ratios
Σ	State covariance matrix
σ_x	Standard deviation of variable x
Ψ	Complex eigenvector matrix of the state-space model
Ω	Diagonal matrix containing the circular eigenfrequencies ω_i [rad/s]
ω	Circular frequency [rad/s]
ω_i	Circular eigenfrequency [rad/s]

$(\bullet)^*$	Complex conjugate
$(\bullet)^\dagger$	Moore-Penrose pseudo-inverse
$(\bullet)^H$	Complex conjugate transpose
$(\bullet)^T$	Transpose
$\hat{x}$	Estimate of a stochastic variable x
$\overline{x}$	Mean value of a variable x
E[•]	Expected value
L[•]	Laplace transform
Z[•]	z-transform

ARMA	**A**uto**R**egressive **M**oving **A**verage
ARX	**A**uto**R**egressive e**X**ogenous
CMIF	**C**omplex **M**ode **I**ndication **F**unction
CVA	**C**anonical **V**ariate **A**nalysis
DFT	**D**iscrete **F**ourier **T**ransform
DOF	**D**egree **O**f **F**reedom
ERA	**E**igensystem **R**ealization **A**lgorithm
EVD	**E**igen**V**alue **D**ecomposition
FE	**F**inite **E**lement
FFT	**F**ast **F**ourier **T**ransform
FOH	**F**irst-**O**rder **H**old
FPE	**F**inal **P**rediction **E**rror
FRF	**F**requency **R**esponse **F**unction
GUI	**G**raphical **U**ser **I**nterface

ITD	**I**brahim **T**ime **D**omain
IV	**I**nstrumental **V**ariable
LS	**L**east **S**quares
LSCE	**L**east **S**quares **C**omplex **E**xponential
MAC	**M**odal **A**ssurance **C**riterion
MACEC	**M**odal **A**nalysis on **C**ivil **E**ngineering **C**onstructions
MDL	**M**inimum **D**escription **L**ength
ML	**M**aximum **L**ikelihood
PEM	**P**rediction **E**rror **M**ethod
PP	**P**eak **P**icking
PTD	**P**olyreference **T**ime **D**omain
RD	**R**andom **D**ecrement
SSI-COV	**COV**ariance-driven **S**tochastic **S**ubspace **I**dentification
SSI-DATA	**DATA**-driven **S**tochastic **S**ubspace **I**dentification
SVD	**S**ingular **V**alue **D**ecomposition
ZOH	**Z**ero-**O**rder **H**old

CONTENTS

1

INTRODUCTION

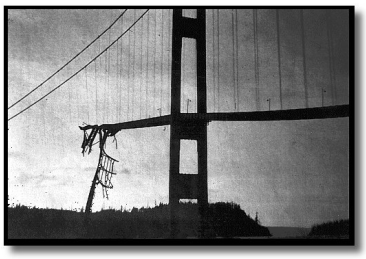

This first chapter contains the general introduction and motivation of the this thesis. The subject of this work — structural health monitoring with emphasis on vibration-based methods — is discussed in Section 1.1. In Section 1.2, our own contributions to the solution of the structural health monitoring problem are highlighted. In Section 1.3, finally, the organization of the text is outlined.

1.1 VIBRATION-BASED HEALTH MONITORING

Structural health monitoring is an active field of research, driven by the need to complement subjective visual inspection methods by objective nondestructive evaluation tools based on physical measurements and computer analyses. Health monitoring techniques may be classified as *global* or *local*. Local methods concentrate on a part of the structure and are based on acoustics, eddy currents, hardness testing, magnetic fields, radiography, X-rays, ... [HOUS97]. One of the few global monitoring methods is based on vibration measurements. Vibration-based damage detection relies upon the fact that a local stiffness change affects the global dynamic characteristics of the structure. In the "0 Hz variant", displacements are measured while a static load is applied to the structure.

The main advantage of a global method is that measurements at one location are sufficient to assess the condition of the whole structure. The measurement location may differ from the location of the damage. Vibration-based methods can be applied intermittently — implying a temporarily deployment of the sensors and the acquisition system — or continuously — implying the embedment of the sensors in the structure. In the continuous setting, a shift from a *preventive time-based* to a *predictive condition-based* maintenance strategy is achieved. This shift reduces both the risk of a serious failure of the structure and the overall maintenance costs by excluding unnecessary inspection activities.

The promising perspective of vibration-based health monitoring inspired many researchers all over the world. Doebling *et al.* surveyed and classified the literature [DOEB96]. Usually four levels of damage identification are discriminated (see for instance [RYTT93]):

- level 1 – *detection*: Is the structure damaged or not?
- level 2 – *localization*: Where is the damaged area located?
- level 3 – *quantification*: What is the extent of damage?
- level 4 – *prediction*: What is the remaining service life of the structure?

The damage detection problem (level 1) is basically equivalent to detecting a change in the dynamic characteristics, such as eigenfrequencies, of the structure. There are two approaches to extend vibration-based methods beyond level 1. In a first approach, a large number of sensors is used to allow the location of damage based on detecting a local mode shape change. The localization accuracy is typically limited to the spatial resolution of the measurement mesh. A second approach requires less sensors, but needs an analytical model of the structure. Parameters of the model that are related to damage are *updated* so that the dynamic characteristics of the model corresponds to the measurements. *Finite Element Model updating* methods fall into this category [FRIS95].

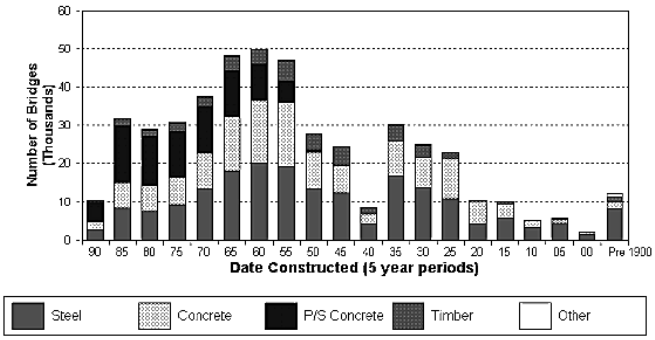

Figure 1.1: Age distribution of bridges in the USA [CHAS97]. The time axis is running from right to left.

Although vibration-based structural health monitoring is applicable to a large range of structures, bridges are considered as important applications. As indicated on Figure 1.1, the main bridge-building boom in the USA was situated in the sixties when the interstate system was constructed. The situation in Europe is similar with the construction of the highways in the same era. Most of these bridges are reaching their critical age and it is expected that the budget demands for maintenance will peak in 2010. Vibration-based monitoring is certainly a helpful tool in assessing the condition of these bridges and in making maintenance schedules.

More recent long-span cable-stayed and suspension bridges are equipped with an embedded monitoring system consisting of sensors such as: accelerometers, anemometers, displacement transducers, inclinometers, strain gauges, temperature sensors, ... Examples of instrumented bridges exist all over the world. As reported in [FARR99b], one of the best-equipped bridges is probably the Tsing Ma Bridge in Hong Kong (see Figure 1.2). The bridge was built in 1997, has a main span of 1377 m and is monitored by nearly 600 sensors.

Bridge monitoring systems are not only used to detect damage. Reported applications and objectives of existing monitoring systems include: quality control during the construction of the bridge; verifying design parameters of a newly constructed bridge; serving as a warning system for traffic closure when the bridge is subjected to excessive wind loading; and condition assessment about its serviceability and ultimate limit state. However, generally speaking, there is some vagueness in how the measurement data are currently interpreted in terms of condition assessment and apparently a lot of "engineering judgement" comes into play [HOUS97].

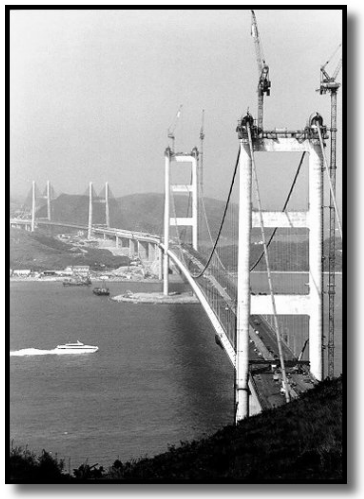

Figure 1.2: The Tsing Ma Bridge in Hong Kong is equipped with nearly 600 sensors.

In vibration-based health monitoring, lots of measurement data are generated. There is the need to compress the amount of data by estimating an *experimental model* of the structure that essentially contains the same information as the original vibration data. The process of finding a model from data is called *system identification*. General system identification is a research branch of electrical engineering. An authoritative reference is the book of Ljung [LJUN99]. Recent advances in the field are the development of *subspace* methods [VANO96] and *maximum likelihood* frequency-domain methods [SCHO91].

The application of system identification to vibrating structures yielded a new research domain in mechanical engineering, known as *experimental modal analysis*. The identified model is in this case a *modal model* consisting of eigenfrequencies, damping ratios, mode shapes and modal participation factors[1]. The first book on the subject was written by Ewins [EWIN84]. More recent overviews can be found in [HEYL95, MAIA97, ALLE99].

Usually, the identification of damage is based on changes in the modal model. An alternative approach to damage detection consists of identifying a model of the healthy structure only. Afterwards, statistical hypothesis tests are carried out to judge whether new data can still be explained by the initial model. This approach was developed at INRIA, France [MOUS86a, MOUS86b, MOUS88, BASS93a, BASS93b, MEVE00]. The main

[1]These notions will be introduced in Chapter 2.

advantage of the method is that no new model needs to be estimated as new data become available, a procedure which is sometimes difficult to automate.

1.2 FOCUS OF THE THESIS

It might be clear from previous section that a lot of work on vibration-based structural health monitoring has already been carried out. Nevertheless many of the proposed damage identification methods are still in the stage of numerical simulations or the traditional laboratory "saw-cuts".

This thesis addresses two key issues of a real-life monitoring system. The first issue is the determination of an experimental model of a vibrating structure from output-only data. By the use of freely available ambient excitation sources the cost of testing is significantly reduced, because no expensive input devices such as shakers are needed. Moreover in a continuous monitoring system it is unthinkable that the structure would be excited by a measurable artificial source. Of course, the problem of obtaining modal parameters from output-only data is basically solved since a few decades. This basic solution consists of selecting the peaks of the spectra of the output signals. However, as will be shown in Chapter 3, more advanced methods were recently developed that considerably increase the quality of the experimental model (i.e. the modal parameters).

The second issue that is treated in this thesis is the detection of damage under varying environmental conditions. The problem is that both damage and temperature affect the eigenfrequencies of a structure. A solution is proposed to separate these influences. It should be noted that only level 1 damage identification (see Subsection 1.1) is addressed in this thesis. The proposed method detects damage without locating or quantifying it. However, the development of a damage detection method that can be applied in a continuous and automatic way is considered as a critical step. It would mean that an early-warning system becomes available that is only based on a few sensors and does not need a numerical model of the structure.

More specifically, the original contributions of this work are the following:

- Finite Element models of vibrating structures excited by white noise are related to stochastic state-space models and modal models. The analysis of these models and the relations between them are indicating how they can be estimated from measurement data and subsequently used in modal and spectrum analysis. The modal parameters are considered as important features for identifying structural damage.

- Almost all state-of-the-art stochastic system identification methods are critically reviewed and synthesized. They are classified by the primary data type they require: spectra, covariances or the original time data. The methods are not only theoretically compared but also by means of a Monte-Carlo simulation study. Among other things, the theoretical comparison reveals that ─ due to historical reasons ─ essentially the same methods have received different names in literature. For instance, the well-known *polyreference time domain* method applied to covariances (instead of impulse responses) can be considered as an *instrumental variable* method and the *eigensystem realization algorithm* applied to covariances is equivalent to the *covariance-driven subspace* method. The comparative simulation study illustrates the practical use of the methods and allows to assess the quality of the identification results.

- The *data-driven stochastic subspace* method was adapted and extended to make it more suitable for modal analysis. The adaptation consists of reducing the dimensions of the matrices (and the computation time) by removing some of the redundancy that is typically present in a modal analysis experiment because usually many sensors are used. The extension consists of efficiently combining the (classical) stabilization diagram with subspace methods. The stabilization diagram is used to extract the modal parameters from the identified state-space models. Also the technique to split the total measured time response in modal responses is an original contribution. The first applications of the data-driven stochastic subspace method to output-only modal analysis are dating from 1995 [PEET95].

- A method is proposed to distinguish environmental effects from damage events. Both are influencing the measured eigenfrequencies of a structure. The method consists of identifying a dynamic environmental model from temperature-eigenfrequency data of the healthy structure. A statistical test is developed to decide whether new data still follows the original environmental model or that the structure is damaged. The originality of the method lies in the facts that subspace identification is used in an automatic way to obtain the eigenfrequencies from acceleration data and that dynamic **ARX** environmental models are used instead of static linear regression models.

- On the level of implementation, the development of a *Graphical User Interface* for output-only modal analysis was managed. Also an *automatic modal analysis* procedure is developed that is based on the automatic interpretation of stabilization diagrams. Such a procedure is crucial in a continuous monitoring system that relies upon the evolution of the modal parameters.

- On the level of applications, a fair amount of experimental work was carried out. Four reinforced concrete beams were progressively damaged and vibration experiments were performed at each intermediate damage stage. The aim of the beam tests was not only to provide experimental data to validate system identification methods but also to verify whether it is fundamentally possible to measure the damage-induced changes in the dynamics of a structure. Also vibration experiments were performed on a steel transmitter mast and some Belgian highway bridges in order to get a "feeling" for real-life testing and data.

- Finally a thorough analysis of data from the Swiss Z24-Bridge is presented. The data are unique in that they combine long-term monitoring with the application of realistic damage scenarios. It is demonstrated that damage could successfully be detected under varying environmental conditions.

1.3 ORGANIZATION OF THE TEXT

In our contribution to vibration-based health monitoring, two system identification approaches emerge. The first (and largest) part deals with *output-only system identification* and describes how important features of a structure can be extracted from vibration measurements. Hereby it is not necessary to have an exact knowledge of the excitation (the input) that causes the structural vibrations (the output). The modal parameters — which are in fact the mentioned features — contain useful information about the condition of the structure.

The second part is an application of *input-output system identification*. A remaining problem after the first part is that the modal parameters do not only change with the structural condition but also with environmental parameters. The separation of both influences is achieved by identifying an *environmental model* of the healthy structure from measured ambient information such as temperatures (the input) and extracted features such as eigenfrequencies (the output).

A more detailed chapter-by-chapter overview is given in the following (see also Figure 1.3).

Chapter 1
: introduces the thesis by situating the subject, highlighting the own contributions and clarifying the organization of the text.

Chapter 2

discusses several models of vibrating structures. Step-by-step, models that are close to physical reality are transformed to general dynamic models that are useful in system identification. This chapter connects Finite Element Models of civil engineering structures, state-space models originating from electrical engineering and modal models initially developed in mechanical engineering. A simulation example is introduced that illustrates the modelling concepts.

Chapter 3

deals with stochastic system identification methods. These methods identify some of the models of Chapter 2 from output-only data. Spectrum-driven, covariance-driven and data-driven methods are consecutively discussed. To clarify the theory and illustrate the practical use, all methods are applied to a simulation example.

Chapter 4

describes the implementation of a Graphical User Interface to stochastic system identification methods. Next to identification, also preprocessing and 3D mode shape visualization tools are incorporated in the program. Additionally, an automatic modal analysis procedure is proposed making it possible to digest a large number of data sets.

Chapter 5

treats two applications. Vibration tests on progressively damaged concrete beams revealed the damage-detection potential of the modal parameters. The tests were carried out in controlled laboratory conditions. In the second example, the modal parameters of a steel mast excited by wind are determined. This is a true real life test in which the possibilities of stochastic system identification can be explored.

Chapter 6

is again a more theoretical chapter. It presents the use of system identification to obtain an environmental model that relates temperatures to eigenfrequencies. It is also indicated how the model can be used to separate temperature effects from damage events in measured vibration data.

Chapter 7

presents system identification and damage detection results from the Z24-Bridge. All developments of this thesis can be applied to that example. Different excitation sources are compared, the evolution of the modal parameters of the bridge with increasing damage is described and an environmental model of the bridge is identified and successfully applied to detect damage.

Chapter 8

summarizes the conclusions of this work. Additionally some unsolved problems and suggestions for future research related to vibration-based health monitoring are mentioned.

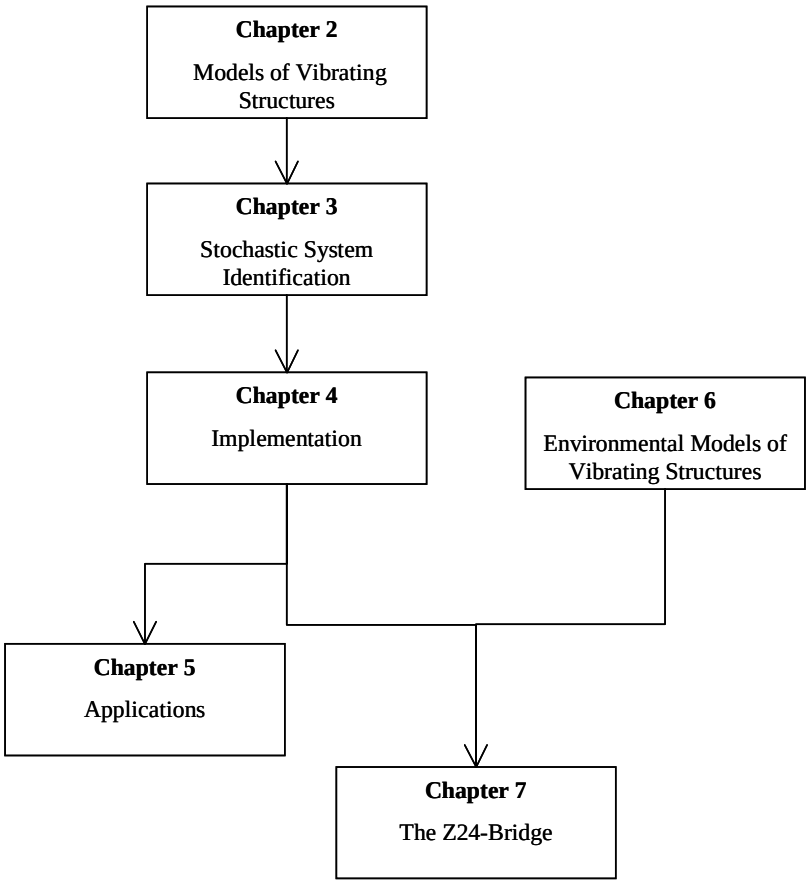

Figure 1.3: Organization of the text. The left part of the chart is concerned with the identification of a model of a vibrating structure. The right part describes how the environmental parameters are influencing this model. All theoretical developments come together in the Z24-Bridge application of Chapter 7.

2

MODELS OF VIBRATING STRUCTURES

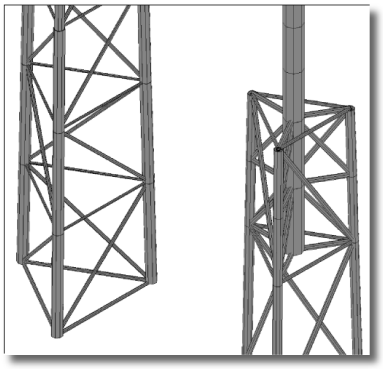

This chapter discusses models of vibrating structures. Step-by-step, Finite Element models (Section 2.2) that are close to physical reality are transformed to models that are more useful in a system identification context. Sections 2.3–2.5 are discussing different types of state-space models. Section 2.6 introduces **ARMA** models. Frequency-domain models are treated in Sections 2.7–2.8. Section 2.9, finally, concludes the chapter.

2.1 INTRODUCTION

In this chapter, several models of vibrating structures are presented. Finite Element models of civil engineering structures, state-space models originating from electrical engineering and modal models initially developed in mechanical engineering are interconnected. The main purpose of studying the relation between these models is to provide a justification for the choice of the model structures in the system identification methods of next chapter. To make it more concrete, in this chapter it is, among other things, shown that a stochastic state-space model and an **ARMA** model can truly represent a vibrating structure excited by white noise. By consequence, the identification of such models has a physical basis.

The relation between the models are also indicating how the modal parameters can be extracted once a model is identified from data. The frequency-domain models are necessary to perform a spectrum analysis.

The discussed models differ in that they describe continuous-time relations (cf. analytical models) or discrete-time relations (cf. experimental models). Some models are describing input-output relations; others — if the deterministic input is unknown — are describing output-only relations. Finally, all models are available both in time as in frequency domain.

2.2 FINITE ELEMENT MODELS

The dynamic behaviour of a discrete mechanical system consisting of n_2 masses connected through springs and dampers is described by following matrix differential equation:

$$M\ddot{q}(t) + C_2\dot{q}(t) + Kq(t) = f(t) = B_2u(t) \tag{2.1}$$

where $M, C_2, K \in \mathbb{R}^{n_2 \times n_2}$ are the mass, damping and stiffness matrices; $q(t) \in \mathbb{R}^{n_2}$ is the displacement vector at continuous time t. A dot over a time function denotes the derivative with respect to time: $\dot{q}(t)$ is the velocity vector and $\ddot{q}(t)$ the acceleration vector. The vector $f(t) \in \mathbb{R}^{n_2}$ is the excitation force. It is factorized into a matrix $B_2 \in \mathbb{R}^{n_2 \times m}$ that specifies the locations of the inputs and a vector $u(t) \in \mathbb{R}^m$ describing the m inputs in time. For systems with distributed parameters (e.g. civil engineering structures), Equation (2.1) is obtained as the **F**inite **E**lement (**FE**) approximation of the system with only n_2 **D**egrees **O**f **F**reedom (**DOF**s) left. The structure is divided in elements. From the geometry and material properties of the elements, the global mass matrix M and stiffness matrix K are generated. The presence of the damping term is partially based on physical observation and partially on mathematical convenience: by adding viscous damping the observed decaying vibrations are modelled. However due to the lack of identifiable or measurable material

constants that govern the global damping behaviour of a structure, it is generally impossible to assemble the damping matrix C_2 in the same way as M and K. Damping will be introduced in Subsection 2.2.2.

It is assumed that the **FE** model (2.1) is a good representation of a vibrating structure, although it is already an approximation of the true behaviour. Besides, the primary interest of this work lies not in obtaining the **FE** model as such. It is used as a starting point to derive other models that are more suited in an experimental modelling context. Firstly, it is not possible (and also not necessary) to measure all **DOF**s of the **FE** model. The number of **DOF**s needed for an accurate **FE** model is typically some orders of magnitude larger than the number of **DOF**s required for an accurate experimental model[1]. Secondly, this equation is in continuous-time, whereas measurements are mostly sampled at discrete time instants. And finally, there is some noise modelling needed: there may be other unknown excitation sources apart from $f(t)$ and measurement noise is always present in real life. In the following sections we will evolve to models that overcome these shortcomings of model (2.1).

2.2.1 The undamped eigenvalue problem

The computation of the eigenvalues and eigenvectors from Equation (2.1) is studied. The following material is standard and can be found in many modal analysis textbooks [EWIN84, HEYL95, MAIA97]. One of the reasons why it is still repeated here is to introduce the notation used in this thesis. The derivation starts with the most simple case where damping is assumed to be zero. The solutions of the homogeneous **FE** model differential equations without damping:

$$M\ddot{q}(t) + Kq(t) = 0 \tag{2.2}$$

will have the following form: $q(t) = \varphi_i e^{\lambda_i t}$. By inserting this form into (2.2), a generalized eigenvalue problem is obtained [GOLU89]:

$$K\varphi_i = M\varphi_i(-\lambda_i^2) \tag{2.3}$$

where $\varphi_i \in \mathbb{R}^{n_2}$ $(i = 1, ..., n_2)$ represents any of the n_2 real eigenvectors and $-\lambda_i^2$ is a real eigenvalue. In the undamped case, an eigenvalue is usually denoted as the square of an eigenfrequency ω_i^2, therefore:

---

[1]The number of **DOF**s required for an accurate experimental model depends on the envisaged use of the model. If one is interested in measuring the eigenfrequencies of the structure, one well-chosen **DOF** suffices. If the experimental model will be used to locate damage based on mode shapes changes, more **DOF**s need to be measured in order to obtain a mode shape with a fine spatial resolution.

$$\lambda_i = j\omega_i$$

where j is the imaginary unit, defined as $j^2 = -1$. All n_2 eigenvalue problems (2.3) can be reformulated in one matrix expression:

$$K\Phi = M\Phi\Omega^2 \tag{2.4}$$

where $\Phi \in \mathbb{R}^{n_2 \times n_2}$ contains the eigenvectors as columns and $\Omega = \left[\backslash \omega_{i} \backslash\right] \in \mathbb{R}^{n_2 \times n_2}$ is a diagonal matrix containing the eigenfrequencies ω_i [rad/s]. It can be proven that the following orthogonality conditions hold:

$$\Phi^T M \Phi = \left[\backslash m_{i} \backslash\right], \quad \Phi^T K \Phi = \left[\backslash k_{i} \backslash\right] \tag{2.5}$$

where m_i are the *modal masses* and k_i the *modal stiffnesses*. The superindex 'T' denotes transpose. Introducing Equation (2.5) in (2.4) yields:

$$\omega_i^2 = \frac{k_i}{m_i}$$

Eigenvectors are determined up to a scaling factor. In many cases they are mass-normalized and Equation (2.5) becomes:

$$\Phi^T M \Phi = I_{n_2}, \quad \Phi^T K \Phi = \Omega^2$$

where I_{n_2} denotes an identity matrix of dimension $n_2 \times n_2$. In the following, we will drop the subindex of the identity matrix if its dimension is clear from the context. Eigenvectors are also called *modal vectors* and in a structural vibration context also *mode shapes*, because they have a nice visual interpretation as the deformation shape of a structure. Note that in the undamped case the eigenvectors are real. One speaks also of *normal modal vectors*.

2.2.2 Proportional damping

By pre-multiplying by Φ^T and introducing the coordinate transformation $q(t) = \Phi q_m(t)$, the second order **FE** model Equation (2.1) is transformed into:

$$\Phi^T M \Phi \ddot{q}_m(t) + \Phi^T C_2 \Phi \dot{q}_m(t) + \Phi^T K \Phi q_m(t) = \Phi^T B_2 u(t) \tag{2.6}$$

The vector $q_m(t) \in \mathbb{R}^{n_2}$ contains the so-called modal displacements. The orthogonality properties (2.5) can be introduced to simplify the first and third term of the left hand side. Up to now the damping matrix C_2 was undefined. Here the special case of proportional damping is imposed: the eigenvectors are also diagonalizing C_2:

$$\Phi^T C_2 \Phi = \left[\backslash c_i \backslash\right] = \left[\backslash 2\xi_i \omega_i m_i \backslash\right] = \Gamma \left[\backslash m_i \backslash\right] \tag{2.7}$$

The second equality follows by the definition of the modal damping ratios $\xi_i = c_i / 2m_i\omega_i$; the third defines $\Gamma = \left[\backslash 2\xi_i \omega_i \backslash\right]$. By introducing Equations (2.5) and (2.7) into (2.6), this last equation is decoupled (all left hand side matrices are diagonal):

$$I\ddot{q}_m(t) + \Gamma \dot{q}_m(t) + \Omega^2 q_m(t) = \left[\backslash \frac{1}{m_i} \backslash\right] \Phi^T B_2 u(t) \tag{2.8}$$

Again, the solutions of the homogeneous **FE** model differential equations with proportional damping will have the form $q(t) = \varphi_i e^{\lambda_i t}$. It is straightforward to prove that the eigenvectors are the same as in the undamped case. From Equation (2.8) it is found that the eigenvalues λ_i satisfy:

$$\lambda_i^2 + 2\xi_i \omega_i \lambda_i + \omega_i^2 = 0$$

yielding the following solutions:

$$\lambda_i,\ \lambda_i^* = -\xi_i \omega_i \pm j\sqrt{1-\xi_i^2}\,\omega_i$$

where superindex '*' denotes complex conjugate. If a damping description is required in a **FE** analysis, one often specifies a number of modal damping ratios ξ_i corresponding to the number of modes of interest. These ratios are, for instance, experimentally determined by applying system identification techniques to vibration data (see Chapter 3). Eventually a full damping matrix can be synthesized from Equation (2.7):

$$C_2 = \Phi^{-T} \left[\backslash 2\xi_i \omega_i m_i \backslash\right] \Phi^{-1} = M\Phi \left[\backslash \frac{1}{m_i} \backslash\right] \left[\backslash 2\xi_i \omega_i \backslash\right] \Phi^T M \tag{2.9}$$

The second equality follows by introducing Equation (2.5).

A special case of proportional damping is the so-called Rayleigh damping: the damping matrix is a linear combination of the mass and stiffness matrix:

$$C_2 = \alpha M + \beta K \tag{2.10}$$

where α and β are two scalar constants. At first sight this seems to be a strange constraint on the damping behaviour of a structure. However, Equation (2.10) only means that the damping is distributed over the structure in the same way as the mass and the stiffness are; which is a quite natural assumption. As already said, it is very difficult to quantify the true structural damping mechanisms. Therefore one is often satisfied with the mathematically simple proportional damping assumption in a **FE** analysis.

2.2.3 General viscous damping

If the assumption of proportional damping is not valid, e.g. in the case of a localized damper, another approach has to be followed to find the eigenvalues. Also the experimental determination of damping most often relies upon general viscous damping models. In case of non proportional damping, the eigenvectors Φ of the undamped system (2.2) are not the same as the eigenvectors of the damped system. In order to find the eigenvalues of a structure with general viscous damping the second order equation of motion (2.1) has to be reformulated as a first order equation. By adding the identity $M\dot{q}(t) = M\dot{q}(t)$ and defining:

$$x(t) = \begin{pmatrix} q(t) \\ \dot{q}(t) \end{pmatrix}, \quad P = \begin{pmatrix} C_2 & M \\ M & 0 \end{pmatrix}, \quad Q = \begin{pmatrix} K & 0 \\ 0 & -M \end{pmatrix} \tag{2.11}$$

following first order equation is derived from (2.1):

$$P\dot{x}(t) + Qx(t) = \begin{pmatrix} B_2 \\ 0 \end{pmatrix} u(t) \tag{2.12}$$

where $x(t) \in \mathbb{R}^n$ is called the *state vector* (see also Section 2.3). The related eigenvalue problem is:

$$P\Psi\Lambda_c + Q\Psi = 0 \tag{2.13}$$

where $\Psi \in \mathbb{C}^{n \times n}$ contains the $n = 2n_2$ complex eigenvectors as columns and $\Lambda_c = \left[\backslash \lambda_i \backslash \right] \in \mathbb{C}^{n \times n}$ is a diagonal matrix containing the n complex eigenvalues λ_i [rad/s]. It can be shown that Λ_c and Ψ have the following structure:

$$\Lambda_c = \begin{pmatrix} \Lambda & 0 \\ 0 & \Lambda^* \end{pmatrix}, \quad \Psi = \begin{pmatrix} \Theta & \Theta^* \\ \Theta\Lambda & \Theta^*\Lambda^* \end{pmatrix} \tag{2.14}$$

where $\Lambda, \Theta \in \mathbb{C}^{n_2 \times n_2}$ are the eigenvalues and eigenvectors of the original second order system. It is easy to show from Equation (2.13) that they satisfy:

$$M\Theta\Lambda^2 + C_2\Theta\Lambda + K\Theta = 0 \tag{2.15}$$

Note that the symbol Θ is used here instead of the symbol Φ as in the case of proportional damping (2.6) because they are indeed different vectors. Unlike Φ, the matrix Θ is generally not diagonalizing any of the matrices M, C_2, K. Analogous to the proportional damping case, the complex eigenvalues λ_i are written as:

$$\lambda_i, \lambda_i^* = -\xi_i\omega_i \pm j\sqrt{1-\xi_i^2}\,\omega_i \tag{2.16}$$

It can be proven that following orthogonality conditions hold:

$$\Psi^T P \Psi = \left[\backslash a_{i\backslash}\right], \quad \Psi^T Q \Psi = \left[\backslash b_{i\backslash}\right] \tag{2.17}$$

where $\left[\backslash a_{i\backslash}\right]$, $\left[\backslash b_{i\backslash}\right]$ are called the *modal a matrix* and *modal b matrix* respectively. Introducing Equation (2.17) in (2.13) yields:

$$\Lambda_c = \left[\backslash \lambda_{i\backslash}\right] = -\left[\backslash \frac{1}{a_{i\backslash}}\right]\left[\backslash b_{i\backslash}\right] \tag{2.18}$$

Example

At this stage, an example is introduced to illustrate the concepts of this chapter. An **FE** model of a structure is built that will be converted to the other models to be presented in this chapter. Afterwards a vibration experiment is simulated. The simulated data are then used to illustrate and compare the system identification methods of next chapter. We have chosen to discuss the different aspects of the simulation study in close connection to the theory, instead of the whole example after the theory. Therefore the example is spread over two chapters.

The considered structure is a mast structure consisting of two segments and with an equilateral triangular section. The structure is represented in Figure 2.1. Nodes 1, 2 and 3 are clamped; the others have 3 **DOF**s: two translations in the *xy*-plane and one rotation around the *z*-axis. The other **DOF**s are put equal to zero. So, the **FE** model has $n_2 = 18$ **DOF**s. The geometry and material properties of the columns differ from each other to break the symmetry. However, the differences are small, resulting in 2 pairs of closely-spaced bending modes (see further). Tower-like structures often have closely-spaced modes. The Structural Dynamics Toolbox [BALM97] for use with MATLAB [MATL96] is used to build the **FE** model.

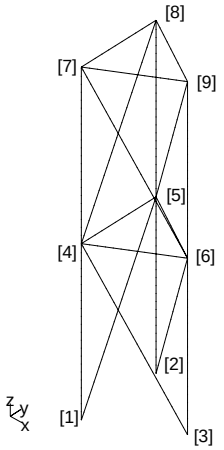

Figure 2.1: FE model of a mast structure.

The eigenfrequencies $f_i = \omega_i / 2\pi$ [Hz] and the mode shapes are obtained from the mass and stiffness matrices, *M* and *K*, by solving the generalized eigenvalue problem (2.4). The first six eigenfrequencies of the structure are represented in Table 2.1. The first six mode shapes are shown in Figure 2.2. Damping, finally, is modelled as the special case of proportional damping (Subsection 2.2.2). Therefore the mode shapes remain the same as in the undamped case. Moreover, for ease of verification of the system identification results, all modal damping ratios are put equal to 1% (which is a realistic number for a vibrating structure).

Table 2.1: First six modal parameters of the **FE** model of the mast structure. A torsion mode is denoted by 'T', a bending mode by 'BX' or 'BY', where 'X' or 'Y' specify the bending direction. The frequencies of mode 2 and 3 and also mode 5 and 6 are close to each other. Damping is modelled as proportional damping. The modal damping ratios are equal for all modes.

#	Mode type	Eigenfrequency f_i [Hz]	Damping ratio ξ_i [%]
1	T1	1.221	1
2	BX1	2.375	1
3	BY1	2.403	1
4	T2	4.083	1
5	BX2	6.936	1
6	BY2	7.015	1

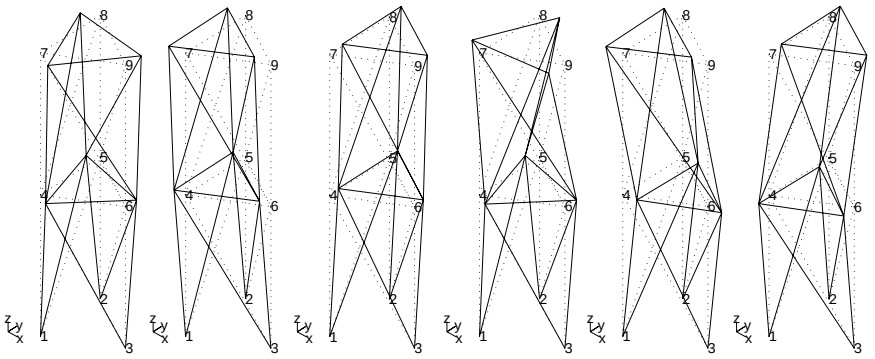

Figure 2.2: First six mode shapes: 1st torsion mode (T1), 1st bending mode in *x*-direction (BX1), 1st bending mode in *y*-direction (BY1), 2nd torsion mode (T2), 2nd bending mode in *x*-direction (BX2), 2nd bending mode in *y*-direction (BY2).

2.3 CONTINUOUS-TIME STATE-SPACE MODELS

2.3.1 A state-space model of a vibrating structure

The state equation

By casting the second order equation of motion (2.1) in first order form (2.12), an equation similar to the *state equation* from control theory is obtained. This equation usually has a normalized term in $\dot{x}(t)$. The normalization is obtained by pre-multiplying (2.12) by P^{-1}:

$$P^{-1} = \begin{pmatrix} 0 & M^{-1} \\ M^{-1} & -M^{-1}C_2M^{-1} \end{pmatrix}$$

to yield the state equation:

$$\dot{x}(t) = A_c x(t) + B_c u(t) \tag{2.19}$$

where $A_c \in \mathbb{R}^{n\times n}$ and $B_c \in \mathbb{R}^{n\times m}$ are defined as:

$$A_c = -P^{-1}Q = \begin{pmatrix} 0 & I \\ -M^{-1}K & -M^{-1}C_2 \end{pmatrix}, \quad B_c = P^{-1}\begin{pmatrix} B_2 \\ 0 \end{pmatrix} = \begin{pmatrix} 0 \\ M^{-1}B_2 \end{pmatrix} \tag{2.20}$$

The subindex '*c*' denotes continuous time. In Section 2.4, the discrete-time equivalents of these matrices will be introduced. Using the modal decomposition of *P* and *Q* (2.17) and property (2.18), A_c is rewritten as:

$$\begin{aligned} A_c &= -P^{-1}Q = -\Psi \begin{bmatrix} \ddots & & \\ & \frac{1}{a_i} & \\ & & \ddots \end{bmatrix} \Psi^T \quad \Psi^{-T} \begin{bmatrix} \ddots & & \\ & b_i & \\ & & \ddots \end{bmatrix} \Psi^{-1} \\ &= \Psi \, \Lambda_c \, \Psi^{-1} \end{aligned} \tag{2.21}$$

which is in fact a standard eigenvalue problem ($A_c\Psi = \Psi\Lambda_c$). This shows that Λ_c contains the eigenvalues and Ψ the eigenvectors of A_c. The difference of using *P* and *Q* (2.12) instead of A_c (2.19) is that *P* and *Q* can be reduced to diagonal forms by using the eigenvector matrix and its transpose whereas A_c requires the inverse of Ψ to make it diagonal.

The observation equation

In a practical vibration experiment, not all n_2 **DOF**s of the structure are measured, but only a subset. If it is assumed that measurements are taken at *l* locations and that the sensors can be either accelerometers, velocity or displacements transducers (to keep it general) the observation equation is:

$$y(t) = C_a\ddot{q}(t) + C_v\dot{q}(t) + C_d q(t) \tag{2.22}$$

where $y(t) \in \mathbb{R}^l$ are the outputs; $C_a, C_v, C_d \in \mathbb{R}^{l \times n_2}$ are the output location matrices for acceleration, velocity and displacement respectively. These matrices consist of a lot of zeros and a few ones and are in fact just selecting the measured **DOF**s out of the **FE** model **DOF**s to store them as the elements of the output vector $y(t)$. In reality it can happen that, for instance, both accelerations and velocities are simultaneously measured. Using Equation (2.1) to eliminate $\ddot{q}(t)$ and with the definition of the state vector (2.11), Equation (2.22) can be transformed into:

$$y(t) = C_c x(t) + D_c u(t) \tag{2.23}$$

where $C_c \in \mathbb{R}^{l \times n}$ is the output matrix and $D_c \in \mathbb{R}^{l \times m}$ is the direct transmission matrix. They are related to the **FE** model matrices as:

$$C_c = \begin{pmatrix} C_d - C_a M^{-1} K & C_v - C_a M^{-1} C_2 \end{pmatrix}, \quad D_c = C_a M^{-1} B_2 \tag{2.24}$$

In many publications this direct transmission matrix D_c is omitted for some reason. However the modelling of a vibration experiment where accelerometers are used (and these are the most widely used sensors) requires a direct transmission term. If $C_a = 0$ (i.e. displacements and/or velocities are measured), there is no direct transmission.

The state-space model

The classical continuous-time state-space model is found by combining Equations (2.19) and (2.23):

$$\begin{aligned} \dot{x}(t) &= A_c x(t) + B_c u(t) \\ y(t) &= C_c x(t) + D_c u(t) \end{aligned} \tag{2.25}$$

The order of the state-space model n is defined as the dimension of the state vector. The equations of motion are now written in state-space form and can be used to compute the response $y(t)$ of the structure to a given input $u(t)$. The state vector $x(t)$ contains the displacements and the velocities of all **DOF**s; see Equation (2.11).

A new state vector can be defined such that:

$$x(t) = Tz(t) \tag{2.26}$$

where $T \in \mathbb{C}^{n \times n}$ is a non-singular complex square matrix. This is called a *similarity transformation*. Substitution of this coordinate transformation into Equation (2.25) yields:

$$\begin{aligned} \dot{z}(t) &= T^{-1}A_c T z(t) + T^{-1}B_c u(t) \\ y(t) &= C_c T z(t) + D_c u(t) \end{aligned} \tag{2.27}$$

It is important to see that the transformed matrices $(T^{-1}A_c T,\ T^{-1}B_c,\ C_c T,\ D_c)$ describe the same input-output relationship as the original matrices. However, unlike $x(t)$ the new state vector $z(t)$ has not the meaning of physical displacements and velocities.

2.3.2 Modal parameters and model reduction

Relation to classical modal analysis

A special similarity transformation is the transformation to (complex) modal states $x_m(t) \in \mathbb{C}^n$:

$$x(t) = \Psi x_m(t)$$

The *modal state-space model* is obtained by substituting T by Ψ in Equation (2.27) and inserting the modal decomposition of A_c (2.21):

$$\begin{aligned} \dot{x}_m(t) &= \Lambda_c x_m(t) + L_c^T u(t) \\ y(t) &= V_c x_m(t) + D_c u(t) \end{aligned} \tag{2.28}$$

where the following definitions have been introduced:

$$\begin{aligned} L_c^T &= \Psi^{-1} B_c \\ V_c &= C_c \Psi \end{aligned} \tag{2.29}$$

As stated before, the eigenvalue matrix has the following structure (2.14), (2.16):

$$\Lambda_c = \begin{pmatrix} \Lambda & 0 \\ 0 & \Lambda^* \end{pmatrix}, \quad \Lambda = \left[-\xi_i \omega_i + j\sqrt{1-\xi_i^2}\,\omega_i \right]$$

and the eigenvector matrix can be written as (2.14):

$$\Psi = \begin{pmatrix} \Theta & \Theta^* \\ \Theta\Lambda & \Theta^*\Lambda^* \end{pmatrix} \tag{2.30}$$

The relations to notions from classical modal analysis are clear by taking a closer look at the modal input and output matrices $L_c^T,\ V_c$. By introducing the orthogonality condition

for P (2.17) and the definitions of P, B_c and Ψ (2.11), (2.20), (2.30), the modal input matrix can be written as:

$$L_c^T = \Psi^{-1} B_c = \begin{bmatrix} \ddots & & \\ & \frac{1}{a_i} & \\ & & \ddots \end{bmatrix} \Psi^T P B_c = \begin{bmatrix} \ddots & & \\ & \frac{1}{a_i} & \\ & & \ddots \end{bmatrix} \Psi^T \begin{pmatrix} B_2 \\ 0 \end{pmatrix} = \begin{bmatrix} \ddots & & \\ & \frac{1}{a_i} & \\ & & \ddots \end{bmatrix} \begin{pmatrix} \Theta^T \\ \Theta^H \end{pmatrix} B_2 \qquad (2.31)$$

By its definition (2.1), matrix B_2 selects the components of the mode shapes corresponding to an input location. Classically, the last expression of Equation (2.31) is called *modal participation matrix* and its rows are the *modal participation factors*. The superindex '*H*' denotes complex conjugate transpose.

Similarly, by introducing the definition of C_c (2.24) and Ψ (2.30), the modal output matrix can be rewritten:

$$V_c = C_c \Psi = \begin{pmatrix} C_d - C_a M^{-1} K & C_v - C_a M^{-1} C_2 \end{pmatrix} \begin{pmatrix} \Theta & \Theta^* \\ \Theta\Lambda & \Theta^* \Lambda^* \end{pmatrix} \qquad (2.32)$$

This expression can be simplified by considering only one quantity at a time. Displacements-only measurements yield:

$$V_c = C_d \begin{pmatrix} \Theta & \Theta^* \end{pmatrix} \qquad (2.33)$$

If velocities are measured, the modal output matrix becomes:

$$V_c = C_v \begin{pmatrix} \Theta\Lambda & \Theta^* \Lambda^* \end{pmatrix}$$

Specializing the expression to accelerations only yields, after introducing Equation (2.15) into (2.32):

$$V_c = C_a \begin{pmatrix} \Theta\Lambda^2 & \Theta^* \Lambda^{*2} \end{pmatrix} \qquad (2.34)$$

By their definition (2.22), the matrices C_d, C_v and C_a are selecting the components of the mode shapes corresponding to an output location. The post-multiplication by Λ or Λ^*, being diagonal matrices, scales the mode shapes by their eigenvalues. So whatever quantity is measured, V_c denotes the part of the mode shapes that can be observed from the data.

The triplet (Λ_c, L_c^T, V_c) are the *modal parameters*[2] of the structure. It is easy to verify that the modal parameters are insensitive to a change of basis of the state-space model. Applying a similarity transformation (2.26) will not affect the modal parameters.

Modal decomposition in continuous time

Interesting about the modal state-space model (2.28) is that, owing to the diagonal structure of Λ_c, the contributions of the different modes to the total response $y(t)$ of the structure can be decoupled. The contributions of mode i are described by λ_i, the i^{th} diagonal element of Λ_c; the i^{th} row of L_c^T, denoted as $<l_{c_i}^T>$; and the i^{th} column of V_c, denoted as $\{v_{c_i}\}$. It is less obvious to distinguish the different modes in matrix D_c. The *modal decomposition* of the direct transmission term is developed in the following. In case of displacement or velocity measurements, there is no direct transmission term. Therefore the derivation is restricted to the acceleration-only case. It is straightforward to show that, if $C_d = 0, D_c$ can be written in terms of the state matrices:

$$C_c A_c^{-1} B_c = C_a M^{-1} B_2 = D_c \tag{2.35}$$

The first equality is found by inserting the definitions of the state-space matrices, see Equations (2.20) and (2.24); the second equality is simply the definition of D_c (2.24). The modal decomposition is achieved by inserting the eigenvalue decomposition of A_c (2.21) and the definitions (2.29) into Equation (2.35):

$$D_c = V_c \Lambda_c^{-1} L_c^T = \sum_{i=1}^{n} \frac{1}{\lambda_i} \{v_{c_i}\} <l_{c_i}^T> \tag{2.36}$$

Matrix D_c decomposes as a sum of n rank-one matrices. We will call this *modal decomposition*.

The total output vector can be split in n modal contributions $y_i(t)$:

$$y(t) = \sum_{i=1}^{n} y_i(t)$$

where each vector $y_i(t)$ is the output of following order-one state-space model:

---

[2] More often, instead of the complex eigenvalues λ_i (the elements of Λ_c), the eigenfrequencies ω_i or f_i and the modal damping ratios ξ_i are specified. Their equivalence is clear from Equation (2.16).

$$\dot{x}_m^{(i)}(t) = \lambda_i\, x_m^{(i)}(t) + \langle l_{c_i}^T \rangle\, u(t)$$
$$y_i(t) = \{v_{c_i}\} x_m^{(i)}(t) + \frac{1}{\lambda_i}\{v_{c_i}\}\langle l_{c_i}^T \rangle\, u(t)$$

The complex scalar $x_m^{(i)}(t)$ denotes the i^{th} component of the modal state vector.

Model reduction in continuous time

The modal state-space model offers a nice interpretation of model reduction as the elimination of certain modes. The following model reduction procedure is proposed. The modal state-space model (2.28) is rearranged to have the r to-be-retained modes first:

$$\begin{matrix} r \\ n-r \end{matrix} \begin{matrix} \updownarrow \\ \updownarrow \end{matrix} \begin{pmatrix} \dot{x}_r(t) \\ \dot{x}_e(t) \end{pmatrix} = \begin{pmatrix} \Lambda_{c_r} & 0 \\ 0 & \Lambda_{c_e} \end{pmatrix} \begin{pmatrix} x_r(t) \\ x_e(t) \end{pmatrix} + \begin{pmatrix} L_{c_r}^T \\ L_{c_e}^T \end{pmatrix} u(t)$$
$$y(t) = \begin{pmatrix} V_{c_r} & V_{c_e} \end{pmatrix} \begin{pmatrix} x_r(t) \\ x_e(t) \end{pmatrix} + D_c u(t)$$

where $x_r(t) \in \mathbb{C}^r$ is the state vector of the reduced system and $x_e(t) \in \mathbb{C}^{n-r}$ are the states that will be eliminated. Typically, model reduction is obtained by setting the derivative of $x_e(t)$ to zero in the state equation. The resulting expression for $x_e(t)$ is introduced in the observation equation. Doing so, the reduced state-space model reads:

$$\begin{aligned} \dot{x}_r(t) &= \Lambda_{c_r} x_r(t) + L_{c_r}^T u(t) \\ y(t) &= V_{c_r} x_r(t) + D_{c_r} u(t) \end{aligned} \tag{2.37}$$

where the reduced matrix D_{c_r} equals:

$$D_{c_r} = D_c - V_{c_e} \Lambda_{c_e}^{-1} L_{c_e}^T = V_{c_r} \Lambda_{c_r}^{-1} L_{c_r}^T$$

The first equality follows from the elimination of $x_e(t)$ from the observation equation; the second equality is obtained by introducing the modal decomposition of D_c (2.36).

The reduced model (2.37) is again a step closer to the experimental world. A vibration experiment is always *band-limited*. This means that the data contains information over a certain frequency bandwidth. Only modes that have frequencies in (or close to) this bandwidth will show up in the data. This experimental fact corresponds very well to the

idea of the reduced model that only contains a limited number of modes, whereas the order of the original state-space model is typically a very large number (a few thousands for a complex structure) because it was derived from a **FE** model[3].

2.3.3 The special case of proportional damping

Proportional damping was introduced to simplify the mathematics related to the modelling of vibrating structures. Because viscous damping (which includes proportional damping as a special case) is more general and realistic, this subsection will not take a step closer to the experimental world. The interest of this subsection lies in performing simulations, where often the proportional damping assumption is preferred. Also some system identification methods explicitly assume a proportionally damped model.

Proportional damping is just a special case of viscous damping and the expressions derived in previous subsections could still be used, eventually taking into account the special structure of the eigenvector matrix (2.14):

$$\Psi = \begin{pmatrix} \Theta & \Theta^* \\ \Theta\Lambda & \Theta^*\Lambda^* \end{pmatrix} = \begin{pmatrix} \Phi & \Phi \\ \Phi\Lambda & \Phi\Lambda^* \end{pmatrix} \tag{2.39}$$

where the general complex modes Θ have been replaced by the normal modes Φ, see Equation (2.4). These modes are real or have at least a constant phase angle and can always be scaled to real ones. In case of proportional damping, the *modal a matrix* can be rewritten, by combining Equations (2.17), (2.11), (2.5), (2.7) and (2.16), as:

$$\begin{aligned} \left[a_i\right] &= \Psi^T P \Psi \\ &= \begin{pmatrix} \left[m_i 2j\sqrt{1-\xi_i^2}\ \omega_i\right] & 0 \\ 0 & \left[-m_i 2j\sqrt{1-\xi_i^2}\ \omega_i\right] \end{pmatrix} \\ &= \begin{pmatrix} \left[m_i\right](\Lambda - \Lambda^*) & 0 \\ 0 & \left[m_i\right](\Lambda^* - \Lambda) \end{pmatrix} \end{aligned}$$

[3]In fact an **FE** model can on its turn be considered as a reduced model of a real structure. Indeed, a real structure with distributed parameters has an infinite amount of modes, whereas the number of modes of the **FE** model equals the number of **DOF**s.

In case of normal modes the state-space model is often written in a different form. This *normal mode state-space model* is obtained by applying following similarity transformation to the original state-space model that is expressed in terms of the **FE** model matrices M, C_2, K (2.25):

$$x(t) = T_n z(t) \ , \quad T_n = \begin{pmatrix} \Phi & 0 \\ 0 & \Phi \end{pmatrix} \tag{2.40}$$

where the subindex 'n' denotes the normal-mode case. Obviously, with Equations (2.40) and (2.11), the new state vector $z(t)$ combines the modal displacements and velocities (2.6):

$$z(t) = \begin{pmatrix} q_m(t) \\ \dot{q}_m(t) \end{pmatrix}$$

The *normal-mode state-space model* is written as:

$$\begin{aligned} \dot{z}(t) &= A_n z(t) + B_n u(t) \\ y(t) &= C_n z(t) + D_n u(t) \end{aligned} \tag{2.41}$$

where the state-space matrices are obtained, by introducing (2.40), (2.20), (2.24), (2.5) and (2.7), as:

$$\begin{aligned} A_n &= T_n^{-1} A_c T_n &&= \begin{pmatrix} 0 & I \\ -\Omega^2 & -\Gamma \end{pmatrix} \\ B_n &= T_n^{-1} B_c &&= \begin{pmatrix} 0 \\ \left[\backslash 1/m_i \backslash\right] \Phi^T B_2 \end{pmatrix} \\ C_n &= C_c T_n &&= \begin{pmatrix} C_d \Phi - C_a \Phi \Omega^2 & C_v \Phi - C_a \Phi \Gamma \end{pmatrix} \\ D_n &= D_c &&= C_a \Phi \left[\backslash 1/m_i \backslash\right] \Phi^T B_2 \end{aligned} \tag{2.42}$$

It is straightforward to apply model reduction to this normal-mode state-space model. Only the relevant modes can be selected from the modal parameter matrices Ω, Γ, $\left[\backslash 1/m_i \backslash\right]$, Φ.

Finally, the normal-mode state-space model (2.41) can also be related to the (complex) modal state-space model (2.28). In case of proportional damping, following relation exist between both state vectors:

$$z(t) = T_c x_m(t) \ , \quad T_c = \begin{pmatrix} I & I \\ \Lambda & \Lambda^* \end{pmatrix}$$

and the inverse relation is:

$$x_m(t) = T_c^{-1} z(t) \;, \quad T_c^{-1} = \begin{pmatrix} -(\Lambda - \Lambda^*)^{-1}\Lambda^* & (\Lambda - \Lambda^*)^{-1} \\ (\Lambda - \Lambda^*)^{-1}\Lambda & -(\Lambda - \Lambda^*)^{-1} \end{pmatrix}$$

2.4 DISCRETE-TIME STATE-SPACE MODELS

2.4.1 About sampling

Up to now all equations were expressed in continuous time, whereas in reality measurements are taken at discrete time instants. In order to fit models to measurements (i.e. system identification), these models need to be converted to discrete time. Another reason for looking at discrete models is that they are needed for performing simulations. If it would be possible to find an analytical solution for the response of a structure to a given input, this analytical expression could be evaluated at any time instant *t*, without the need to convert the model to discrete time. However in most cases there is no analytical solution and one has to rely upon a numerical solution method to simulate the response of a structure. For instance, time integration schemes with a possible adaptive time step could be used. The approach that is useful for this thesis starts by choosing a certain fixed sampling period Δt [s]. The continuous-time equations are discretized and solved at all discrete time instants k [-], where $t = k\Delta t,\ k \in \mathbb{N}$. Typical for the sampling of a continuous-time equation is that a certain behaviour of the time-dependent variables between two samples has to be assumed. A **Z**ero-**O**rder **H**old (**ZOH**) assumption for instance, means that the input is piecewise constant over the sampling period. Under this assumption, the continuous-time state-space model (2.25) is converted to the *discrete-time state-space model*:

$$\begin{aligned} x_{k+1} &= Ax_k + Bu_k \\ y_k &= Cx_k + Du_k \end{aligned} \tag{2.43}$$

where $x_k = x(k\Delta t) = (q_k^T \;\; \dot{q}_k^T)^T$ is the discrete-time state vector containing the sampled displacements and velocities; u_k, y_k are the sampled input and output; A is the discrete state matrix; B is the discrete input matrix; C is the discrete output matrix; D is the direct transmission matrix. They are related to their continuous-time counterparts (2.20) as:

$$\begin{aligned} &A = \mathrm{e}^{A_c \Delta t} \;, \quad B = \int_0^{\Delta t} \mathrm{e}^{A_c \tau}\, \delta\tau \; B_c = (A - I) A_c^{-1} B_c \\ &C = C_c \quad , \; D = D_c \end{aligned} \tag{2.44}$$

These relations are classical and are, for instance, derived in [JUAN94]. The second equality for B is only valid if A_c is invertible. The matrices C_c and D_c are not influenced by **ZOH**-sampling.

If one assumes that the inputs are piecewise linear over the sampling period, one speaks of **F**irst-**O**rder **H**old (**FOH**). In this case more complex relations exist between the continuous-time and discrete-time state-space matrices (see for instance [FRAN97]). The matrix D will differ from D_c. Also the discrete state vector is not the sampled displacement-velocity vector anymore.

2.4.2 Modal parameters and model reduction

The eigenvalue decomposition of the discrete state matrix A is found by inserting the eigenvalue decomposition of the continuous state matrix A_c into Equation (2.44):

$$A = e^{A_c \Delta t} = e^{\Psi \Lambda_c \Psi^{-1} \Delta t} = \Psi e^{\Lambda_c \Delta t} \Psi^{-1} = \Psi \Lambda_d \Psi^{-1} = \Psi \left[\backslash \mu_i \backslash \right] \Psi^{-1} \tag{2.45}$$

The third equality can be proven by the series expansion of the exponential function[4]; the two last equalities define the notation of the discrete eigenvalue matrix. So, the discrete eigenvectors are equal to the continuous ones and the discrete eigenvalues, denoted as μ_i, are related to the continuous eigenvalues as:

$$\mu_i = e^{\lambda_i \Delta t} \quad \Leftrightarrow \quad \lambda_i = \frac{\ln(\mu_i)}{\Delta t}$$

Similar to definition (2.29), the discrete modal participation matrix and the observed mode shapes are written as:

$$\begin{aligned} L^T &= \Psi^{-1} B \\ V &= C \Psi \end{aligned} \tag{2.46}$$

The discrete modal participation factors are different from the continuous ones due to the different B-matrix. The observed mode shapes, on the contrary, are the same in discrete as in continuous time. In the acceleration-only case, the modal decomposition of D is found as follows:

---

[4]The McLaurin series expansion of the exponential function is: $e^M = \sum_{k=0}^{\infty} \frac{1}{k!} M^k$.

$$D = D_c = V_c \Lambda_c^{-1} L_c^T = V (\Lambda_d - I)^{-1} L^T = \sum_{i=1}^{n} \frac{1}{\mu_i - 1} \{v_i\} < l_i^T >$$

The derivation makes use of Equations (2.44), (2.36), (2.29), (2.46) and (2.45). The notation for the columns and rows of a matrix has been introduced before.

The discrete-time model reduction is similar to the continuous one. This reduction can be formally proven by putting the next states (that have to eliminated) equal to the current states. This is the discrete-time equivalent of setting the derivative of the continuous states to zero.

2.4.3 Impulse responses

Impulse responses play an important role in system identification. A discrete-time impulse is defined as a unit input at $k = 0$ and otherwise zero. The impulse responses are the outputs of the system when excited by an impulse applied at any of the m input locations. These m response vectors are usually combined in a $l \times m$ impulse response matrix. Under zero initial conditions $x_0 = 0$, it is straightforward to prove from (2.43), that the impulse response matrices $h_k \in \mathbb{R}^{l \times m}$ can be computed from the system matrices as:

$$\begin{aligned} h_0 &= D \\ h_k &= CA^{k-1}B \quad (k > 0) \end{aligned} \tag{2.47}$$

The relation between impulse responses and state-space matrices (2.47) originates from the famous paper by Ho and Kalman [HOKA66]. Many identification methods (the so-called realization methods) are based on this property. The impulse responses can also be written as a function of the modal parameters:

$$\begin{aligned} h_0 &= V(\Lambda_d - I)^{-1} L^T \\ h_k &= V \Lambda_d^{k-1} L^T \qquad (k > 0) \end{aligned} \tag{2.48}$$

Example

The **FE** model of the mast structure (Figure 2.1) is converted to state-space form. It is assumed that the structure is excited at all nodes in both x and y-direction independently. Therefore, the input matrix $B_2 \in \mathbb{R}^{n_2 \times m}$ (2.1) is a 18×12 matrix consisting of zeros and ones at the appropriate positions. By assuming that the triangles at each floor are undeformable, it suffices to measure 3 **DOF**s per floor to characterise the complete deformation of the structure. The sensors and measurement directions are shown in Figure 2.3. As in reality, the

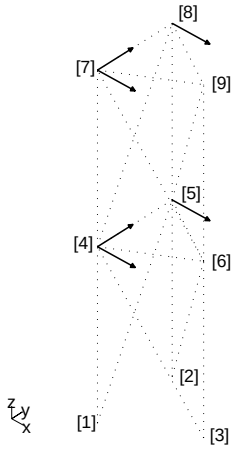

Figure 2.3: Sensors and measurement directions.

measurements are accelerations. The output matrix $C_a \in \mathbb{R}^{l \times n_2}$ (2.22) is a 6×18 matrix consisting of zeros and ones.

The approach of Subsection 2.3.3 is followed to obtain a state space model. The reduced modal parameter matrices are used to build a normal-mode state-space model (A_n, B_n, C_n, D_n), see Equations (2.41) and (2.42). The reduction consists of selecting only the first six modes:

$$\Omega_r = \left[\backslash \omega_i^2 \backslash\right], \quad \Gamma_r = \left[\backslash 2\xi_i\omega_i \backslash\right], \quad \left[\backslash 1/m_i \backslash\right], \quad \Phi_r = \left(\ldots\{\varphi_i\}\ldots\right) \quad (i = 1,2,\ldots,6)$$

The dimensions of the state-space model are: the model order $n = 2n_2 = 12$, the number of inputs $m = 12$ and the number of outputs $l = 6$.

Assuming a **ZOH** on the inputs, and a sampling period $\Delta t = 0.01\,\mathrm{s}$, a discrete-time state-space model (A, B, C, D) is obtained, see Equations (2.43) and (2.44). Note that the sampling frequency $f_s = 1/\Delta t$ is chosen such that the Nyquist frequency $f_N = f_s/2$ is well above the largest eigenfrequency: $f_6 = 7.015\,\mathrm{Hz}$ (see also Table 2.1). As input u_k, random numbers from a normal distribution are taken. The inputs are white, both in space and in time, and the covariance matrix is the identity matrix:

$$\mathbf{E}[u_p u_q^T] = R_u \delta_{pq} = I_m \delta_{pq}$$

where **E** is the expected value operator; δ_{pq} is the Kronecker delta (if $p = q$ then $\delta_{pq} = 1$, otherwise $\delta_{pq} = 0$); p, q are two arbitrary time instants.

The first input signal is shown in Figure 2.4 and the first output signal is shown in Figure 2.5. A typical impulse response function, computed from the discrete state-space model according to Equation (2.47), is shown in Figure 2.6.

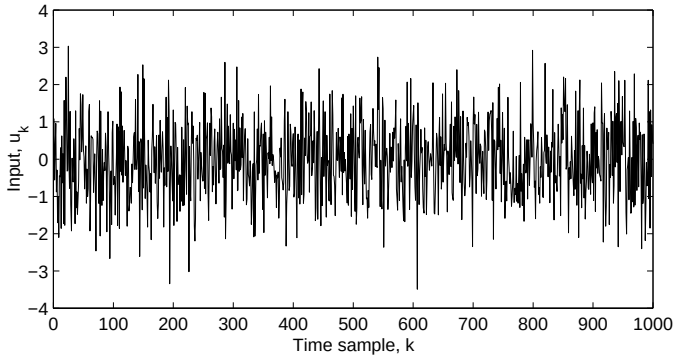

Figure 2.4: Part of the first white noise input signal. This signal is applied to node 4 in the *x*-direction. There are 12 independent input signals.

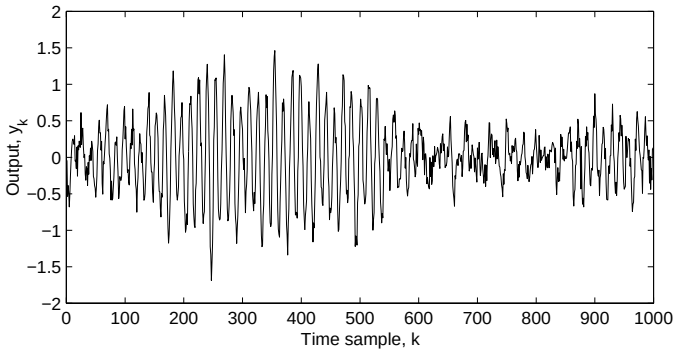

Figure 2.5: Part of the first output signal. This signal is the simulation of the accelerations of node 4 in the *x*-direction. There are 6 output signals.

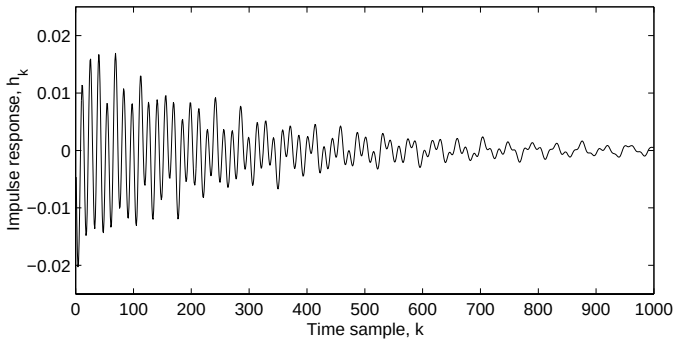

Figure 2.6: Part of element (1,1) of the impulse response function matrix h_k. Only the time lags $k>0$ are shown. The represented impulse response function is the acceleration response of the structure at node 4 in the *x*-direction of an impulse applied at the same **DOF**.

2.5 STOCHASTIC STATE-SPACE MODELS

2.5.1 The stochastic components

This section describes the final step towards the experimental world: noise is added. Up to now it was assumed that the system was only driven by a deterministic input u_k. However, the deterministic models are not able to exactly describe real measurement data. Stochastic components have to be included in the models and following *discrete-time combined deterministic-stochastic state-space model* is obtained:

$$\begin{aligned} x_{k+1} &= Ax_k + Bu_k + w_k \\ y_k &= Cx_k + Du_k + v_k \end{aligned} \tag{2.49}$$

where $w_k \in \mathbb{R}^n$ is the process noise due to disturbances and modelling inaccuracies; $v_k \in \mathbb{R}^l$ is the measurement noise due to sensor inaccuracy. They are both unmeasurable vector signals assumed to be zero mean, white and with covariance matrices:

$$\mathbf{E}\left[\begin{pmatrix} w_p \\ v_p \end{pmatrix} \begin{pmatrix} w_q^T & v_q^T \end{pmatrix}\right] = \begin{pmatrix} Q & S \\ S^T & R \end{pmatrix} \delta_{pq} \tag{2.50}$$

where **E** is the expected value operator; δ_{pq} is the Kronecker delta (if $p = q$ then $\delta_{pq} = 1$, otherwise $\delta_{pq} = 0$); p, q are two arbitrary time instants.

However, as explained in Section 1.2 the primary case of interest for this thesis is a purely stochastic system. In a civil engineering context, the only vibration information that is available are the responses of a structure excited by some unmeasurable inputs. Due to the lack of input information it is not possible (from a system identification point of view) to distinguish between the terms in u_k and the noise terms w_k, v_k in Equation (2.49). The *discrete-time stochastic state-space model* reads:

$$\begin{aligned} x_{k+1} &= Ax_k + w_k \\ y_k &= Cx_k + v_k \end{aligned} \tag{2.51}$$

The input is now implicitly modelled by the noise terms. However the white noise assumptions of these terms cannot be omitted: it is necessary for the proofs of the system identification methods of next chapter. The consequence is that if this white noise assumption is violated, for instance if the input contains additional to white noise also some dominant frequency components, these frequency components cannot be separated from the eigenfrequencies of the system and they will appear as (spurious) poles of the state matrix A.

2.5.2 Properties of stochastic systems

Some important properties of stochastic systems are briefly resumed. They are well-known and can, for instance, be found in [VANO96]. As already stated, the noise terms have zero mean and their covariance matrices are given by Equation (2.50). There are some further assumptions. The stochastic process is assumed to be stationary with zero mean:

$$\mathbf{E}[x_k x_k^T] = \Sigma \ , \quad \mathbf{E}[x_k] = 0 \tag{2.52}$$

where the state covariance matrix Σ is independent of the time k. Since w_k, v_k have zero mean and are independent of the actual state, we have:

$$\mathbf{E}[x_k w_k^T] = 0 \ , \quad \mathbf{E}[x_k v_k^T] = 0$$

The output covariance matrices $R_i \in \mathbb{R}^{l \times l}$ are defined as:

$$R_i = \mathbf{E}[y_{k+i} y_k^T] \tag{2.53}$$

where i is an arbitrary time lag. The *"next state - output" covariance matrix* $G \in \mathbb{R}^{n \times l}$ is defined as:

$$G = \mathbf{E}[x_{k+1} y_k^T] \tag{2.54}$$

From stationarity, the noise properties and previous definitions following properties are easily deduced:

$$\begin{aligned} \Sigma &= A\Sigma A^T + Q \\ R_0 &= C\Sigma C^T + R \\ G &= A\Sigma C^T + S \end{aligned} \tag{2.55}$$

And for $i = 1, 2, \ldots$:

$$\begin{aligned} R_i &= CA^{i-1}G \\ R_{-i} &= G^T (A^{i-1})^T C^T \end{aligned} \tag{2.56}$$

This last property is very important. This equation alone nearly constitutes the solution to the identification problem: the output covariance sequence can be estimated from the measurement data; so if we would be able to decompose the estimated output covariance sequence according to (2.56), the state-space matrices are found. This idea will be elaborated in Chapter 3. The factorization of output covariance matrices into state-space matrices is similar to the factorization property of impulse responses (2.47). For stochastic systems, the matrices (A, G, C, R_0) play the role of the deterministic system matrices (A, B, C, D). Thanks to this equivalence, input-output impulse-response-driven identification methods are easily translated into output-only covariance-driven methods.

This *stochastic realization problem* (see also Chapter 3) was first solved by Akaike [AKAI74b].

By introducing the modal parameters, Equation (2.56) can be written as:

$$\begin{aligned} R_i &= C \quad A^{i-1} \quad G \\ &= C\Psi\Lambda_d^{i-1}\Psi^{-1}G \qquad (i>0) \\ &= V\ \Lambda_d^{i-1}\ G_m \end{aligned} \tag{2.57}$$

where $G_m \in \mathbb{C}^{n\times l}$ is the "next modal state - output" covariance matrix or *stochastic modal participation matrix*. Apparently, this matrix G_m plays the role in output-only modal analysis of the modal participation matrix L^T in input-output modal analysis: compare Equation (2.57) with (2.48). In modal analysis, this observation is also used to feed classical modal parameter estimation methods that normally work with impulse responses, with output covariances instead. A paper that is often referred to in this context was written by James *et al.* [JAME95]. This paper contributed to the introduction in the mechanical engineering community of the idea that it is possible to extract modal parameters of systems that are excited by natural, unmeasurable excitation.

2.5.3 The forward innovation model

An alternative model for stochastic systems that is more suitable for some applications is the so-called *forward innovation model*. It is obtained by applying the *steady-state Kalman filter*[5] to the stochastic state-space model (2.51):

$$\begin{aligned} z_{k+1} &= Az_k + Ke_k \\ y_k &= Cz_k + e_k \end{aligned} \tag{2.58}$$

The elements of the sequence e_k are called innovations, hence the name of the model. It is a white noise vector sequence, with covariance matrix:

$$\mathbf{E}[e_p e_q^T] = R_e\delta_{pq}$$

The computation of the forward innovation model (A,K,C,R_e) from the stochastic state-space model (A,G,C,R_0) starts by finding the positive definite solution P of the *discrete Riccati equation*[6]:

---

[5]The Kalman filter is standard in control theory. Some more information is provided in Subsection 3.5.1. The reason to introduce forward innovation models at this occasion is that the **ARMA** models of next section can be obtained from these innovation models.

[6]An implementation to find the solution of this equation can, for instance, be found in [CONT97].

$$P = APA^T + (G - APC^T)(R_0 - CPC^T)^{-1}(G - APC^T)^T$$

The matrix $P \in \mathbb{R}^{n \times n}$ is the forward state covariance matrix $P = \mathbf{E}[z_k z_k^T]$. The Kalman gain is then computed as:

$$K = (G - APC^T)(R_0 - CPC^T)^{-1}$$

And the covariance matrix of the innovations equals:

$$R_e = R_0 - CPC^T$$

Example

The mast structure of Figure 2.1 is excited by white noise inputs. If these input "measurements" are not passed to the system identification methods of next chapter, the input terms of the state-space model can be considered as the stochastic components:

$$w_k = Bu_k$$
$$v_k = Du_k$$

Since $R_u = I$, their covariances can be written as:

$$\begin{pmatrix} Q & S \\ S^T & R \end{pmatrix} = \begin{pmatrix} BR_uB^T & BR_uD^T \\ DR_uB^T & DR_uD^T \end{pmatrix} = \begin{pmatrix} BB^T & BD^T \\ DB^T & DD^T \end{pmatrix}$$

From these covariances, the matrices G and R_0 can be computed according to Equation (2.55). A typical output covariance sequence, computed from the stochastic state-space matrices (A, G, C, R_0) according to Equation (2.56), is shown in Figure 2.7.

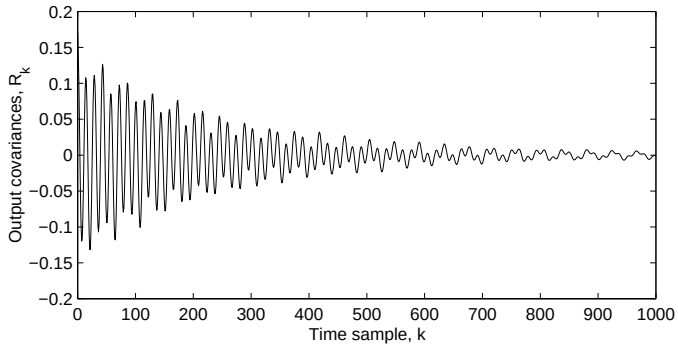

Figure 2.7: Part of element (1,1) of the output covariance sequence R_k. Only the time lags $k \geq 0$ are shown. The represented covariance is the auto-covariance of the acceleration response of the structure at node 4 in the *x*-direction.

2.6 ARMA MODELS

The more classical system identification methods [LJUN99] identify models that do not contain the state. In this section the state vector is eliminated from the forward innovation state-space model (2.58) to yield the so-called **ARMA** model.

2.6.1 Obtaining the ARMA model

An **ARMA** model is written as:

$$y_k + \alpha_1 y_{k-1} + \ldots + \alpha_{n_\alpha} y_{k-n_\alpha} = e_k + \gamma_1 e_{k-1} + \ldots + \gamma_{n_\gamma} e_{k-n_\gamma} \tag{2.59}$$

where, as before, y_k is the output vector and e_k a white noise vector sequence The left-hand side is called the **A**uto-**R**egressive (**AR**) part and the right-hand side the **M**oving **A**verage (**MA**) part, hence the name of the model. The matrices $\alpha_i \in \mathbb{R}^{l \times l}$ are the **AR** matrix parameters; matrices $\gamma_i \in \mathbb{R}^{l \times l}$ are the **MA** matrix parameters. Sometimes, in case of multiple outputs, one speaks of **ARMAV** models as to stress their multi-Variable character. It will become clear that an **ARMA** model that is deduced from a state-space model has the same **AR** order n_α as **MA** order n_γ. This is denoted as:

$$n_\alpha = n_\gamma = p$$

The **AR**matrix parameters are obtained by solving the following linear system of equations for α_i [AKAI74a]:

$$\sum_{i=1}^{p} \alpha_i C A^{p-i} = -CA^p$$

or in matrix form:

$$(\alpha_p \;\; \alpha_{p-1} \;\; \ldots \;\; \alpha_1)\, O_p = -CA^p \tag{2.60}$$

where $O_p \in \mathbb{R}^{pl \times n}$ is the so-called observability matrix defined as:

$$O_p = \begin{pmatrix} C \\ CA \\ \ldots \\ CA^{p-1} \end{pmatrix} \tag{2.61}$$

There are pl^2 unknowns and nl equations in (2.60). It is assumed for a moment that the original model order n is an integer multiple of the number of output channels l. In this case, the **ARMA** model order can be computed as:

$$p = \frac{n}{l}$$

Moreover, if the system is observable, i.e. $\text{rank}(O_p) = n$, the system of Equations (2.60) is a determined system. On the contrary, if $p > n/l$ or the system is not observable, the system of Equations (2.60) is under-determined and the **AR** matrix parameters are obtained by applying least-squares.

The determination of the **MA** parameters starts by following set of equations that is built from the forward innovation state-space model (2.58):

$$\begin{pmatrix} y_{k-p} \\ y_{k-p+1} \\ \dots \\ y_k \end{pmatrix} = \begin{pmatrix} C \\ CA \\ \dots \\ CA^p \end{pmatrix} x_{k-p} + \begin{pmatrix} I & 0 & \dots & 0 \\ CK & I & \dots & 0 \\ \dots & \dots & \dots & \dots \\ CA^{p-1}K & CA^{p-2}K & \dots & 0 \end{pmatrix} \begin{pmatrix} e_{k-p} \\ e_{k-p+1} \\ \dots \\ e_k \end{pmatrix} \tag{2.62}$$

This is denoted in short as:

$$Y_{k-p} = O_{p+1} x_{k-p} + HE_{k-p} \tag{2.63}$$

where the notation is explained by comparing Equation (2.63) with (2.62). This equation is pre-multiplied by $(\alpha_p \ \alpha_{p-1} \ \dots \ \alpha_1 \ I)$ to yield:

$$(\alpha_p \ \alpha_{p-1} \ \dots \ \alpha_1 \ I) \, Y_{k-p} = (\alpha_p \ \alpha_{p-1} \ \dots \ \alpha_1 \ I) \, HE_{k-p} \tag{2.64}$$

The term in x_{k-p} disappeared because of Equation (2.60). The left-hand side of (2.64) is just another way of writing the **AR** part of (2.59). Therefore, the right-hand side of (2.64) equals the **MA** part:

$$(\gamma_p \ \gamma_{p-1} \ \dots \ \gamma_1 \ I) = (\alpha_p \ \alpha_{p-1} \ \dots \ \alpha_1 \ I) \, H$$

2.6.2 Modal parameters of an ARMA model

This subsection discusses the determination of eigenvalues and eigenvectors of an **ARMA** model. They are obtained as the homogeneous solutions of the **ARMA** equations. In continuous time, such solutions have the form: $y(t) = v_i e^{\lambda_i t}$. The discrete-time equivalent is:

$$y_k = v_i \mu_i^k \tag{2.65}$$

where $v_i \in \mathbb{C}^l$ $(i = 1, ..., pl)$ represents any of the pl eigenvectors and $\mu_i = e^{\lambda_i \Delta t}$ is a discrete eigenvalue. By inserting (2.65) into the homogeneous **ARMA** equations, following expression is obtained:

$$v_i \mu_i^k + \alpha_1 v_i \mu_i^{k-1} + \ldots + \alpha_p v_i \mu_i^{k-p} = 0 \tag{2.66}$$

By using the symbols v_i and λ_i it is already suggested that the **ARMA** eigenvectors and eigenvalues will be the same as the state-space eigenvectors and poles. This is formally demonstrated in the following.

Remember that the eigenvalue decomposition of the state matrix A can be written as (2.45):

$$A = \Psi \Lambda_d \Psi^{-1}$$

Introducing this decomposition into Equation (2.60) and post-multiplying by Ψ yields:

$$C\Psi \Lambda_d^p + \sum_{i=1}^{p} \alpha_i C\Psi \Lambda_d^{p-i} = 0 \tag{2.67}$$

where the following property of the eigenvalue decomposition has been used:

$$A^i = \Psi \Lambda_d^i \Psi^{-1}$$

Since $V = C\Psi$ (2.46) and $\Lambda_d = \left[\backslash \mu_{i\backslash}\right]$ (2.45), it is easy to see from Equation (2.67) that the observed eigenvectors of the state-space model and their associated eigenvalues satisfy the modal **ARMA** Equation (2.66). So in case of observability of the system and $p = n/l$, the **ARMA** modes are equivalent to the state-space modes. On the contrary, if $p > n/l$ or the system is not observable, the **ARMA** model will contain, next to the state-space modes, some additional numerical modes.

The question remains how to compute the poles and eigenvectors from an **ARMA** model directly without having the initial state-space model. This is important for identification methods that identify an **ARMA** model from the data. Equation (2.66) is written in matrix form:

$$V\Lambda_d^k + \alpha_1 V \Lambda_d^{k-1} + \ldots + \alpha_p V \Lambda_d^{k-p} = 0 \tag{2.68}$$

This p^{th} order eigenvalue problem can be reduced to a standard first order problem through the companion matrix of the matrix polynomial (2.68):

$$\begin{pmatrix} 0 & I & \dots & 0 \\ 0 & 0 & \dots & 0 \\ \dots & \dots & \dots & \dots \\ 0 & 0 & \dots & I \\ -\alpha_p & -\alpha_{p-1} & \dots & -\alpha_1 \end{pmatrix} \begin{pmatrix} V \\ V\Lambda_d \\ \dots \\ V\Lambda_d^{p-2} \\ V\Lambda_d^{p-1} \end{pmatrix} = \begin{pmatrix} V \\ V\Lambda_d \\ \dots \\ V\Lambda_d^{p-2} \\ V\Lambda_d^{p-1} \end{pmatrix} \Lambda_d \tag{2.69}$$

In a more compact form, the last equation is written as:

$$\mathrm{A}_p^{\mathrm{comp}} \, O_{p,m} = O_{p,m} \Lambda_d$$

where $\mathrm{A}_p^{\mathrm{comp}} \in \mathbb{R}^{pl \times pl}$ is the companion matrix containing the p **AR** parameters α_i; the matrix $O_{p,m} \in \mathbb{C}^{pl \times pl}$ is the *modal observability matrix*, defined as:

$$O_{p,m} = O_p \Psi$$

From the definition of the observability matrix (2.61) and the modal decomposition of A, it is found that the modal observability matrix indeed corresponds to the matrices in Equation (2.69).

To conclude, the discrete eigenvalues are obtained by computing the eigenvalue decomposition of the companion matrix of the **AR** matrix parameters. The observed eigenvectors are the first l rows of the eigenvectors of the companion matrix, in MATLAB notation:

$$V = O_{p,m}(1{:}l, :)$$

In this section it was shown that a p^{th} order **ARMA** model is a good representation of a vibrating structure with pl modes. Note that a p^{th} order **AR** model is not an equivalent representation of such a structure. The **MA** part should be taken into account too. It can however be shown that an **AR** model with infinite order is theoretically equivalent to a finite-order **ARMA** model. This motivated the use of **AR** models in system identification of vibrating structures. Unfortunately the theoretical assumption of infinite order, practically means that many numerical poles need to be introduced to obtain a reasonable data fit in the identification. The difficulty is to separate these numerical poles from the true system poles. This matter will also be discussed in the system identification chapter.

2.7 CONTINUOUS-TIME FREQUENCY-DOMAIN MODELS

Although measurement data are usually available as samples of the input and output time signals, it is very useful to look at the frequency-domain representation of these signals. Many interesting signal's features are revealed in frequency domain. For instance, the eigenfrequencies of a lightly damped structure emerge immediately as the peaks in a frequency-domain plot of a measurement signal. The mathematical tool to convert a time signal to the frequency domain is the Fourier transform. Next to the fact that it provides useful insights, another reason for the popularity of frequency-domain representations is that, since a few decades, a very efficient algorithm exists that implements the Fourier transform, known as the **F**ast **F**ourier **T**ransform (**FFT**) algorithm [COOL65].

As the paradoxical title of this section indicates, models are going to be studied that are the frequency-domain equivalents of the continuous-time models of Section 2.3. The main reason to look at these models is that many identification methods exist that identify a continuous-time frequency-domain model from samples of the Fourier transforms of the signals. A special class of these methods assumes a model that is parametrized in terms of the modal parameters of the structure instead of the rather abstract state-space matrices.

We will first introduce the Laplace transform. When applied to time-domain models, the Laplace transform leads to the concept of transfer function. Finally the spectrum is introduced which is more relevant in case of output-only data (and where the input data is assumed to be white noise).

2.7.1 The Laplace transform

The Laplace transform converts linear time-variant differential equations to algebraic equations. The one-sided Laplace transform of a time function $x(t)$ is defined as:

$$X(s) = \mathbf{L}[x(t)] = \int_0^\infty x(t) e^{-st} dt$$

where $s \in \mathbb{C}$ is a scalar complex variable. It is assumed that $x(t) = 0$ prior to $t = 0$. An important property of the Laplace transform is:

$$\mathbf{L}[\dot{x}(t)] = sX(s) - x(0)$$

If the initial condition is zero $x(0) = 0$, a derivative in time domain is equivalent to a multiplication by s in the Laplace domain. For obvious reasons the Laplace transform is also called the s-transform

2.7.2 The transfer function

Under zero initial conditions, the application of the *s*-transform to the continuous-time state-space model (2.25) yields:

$$\begin{aligned} sX(s) &= A_c X(s) + B_c U(s) \\ Y(s) &= C_c X(s) + D_c U(s) \end{aligned}$$

By eliminating the states $X(s)$, following input-output relation is obtained:

$$Y(s) = H_c(s)U(s) \tag{2.70}$$

The matrix $H_c(s)$ is called transfer function and equals:

$$H_c(s) = C_c(sI - A_c)^{-1}B_c + D_c$$

Similar as in time domain, modal decomposition can be applied to this expression. By inserting the eigenvalue decomposition of A_c (2.21) and the definitions of the participation factors L_c^T and the observed mode shapes V_c (2.29), we obtain:

$$H_c(s) = V_c(sI - \Lambda_c)^{-1}L_c^T + D_c \tag{2.71}$$

This modal state-space transfer function can be written in more familiar forms known from classical modal analysis. The transfer function is then expressed in terms of the modal parameters of the original **FE** model. This is elaborated in Appendix A.1.

The Frequency Response Function

From a practical point of view, the **F**requency **R**esponse **F**unction (**FRF**) is more important. It is defined as the transfer function in which the complex Laplace variable is restricted to purely imaginary values $s = j\omega$ where ω [rad/s] can be any frequency of interest. The **FRF** is denoted as:

$$H_c(j\omega) = C_c(sI - A_c)^{-1}B_c + D_c \Big|_{s=j\omega} \tag{2.72}$$

or equivalently as one of its modally decomposed forms (see Apendix A.1). The practical relevance of the **FRF** lies in the fact that it is easily identified from the measured time data by applying so-called non-parametric methods. These methods are mainly based on the application of the **FFT**. The second identification step consist then of identifying parametric models like (2.72) from the estimated **FRF** (see Chapter 3).

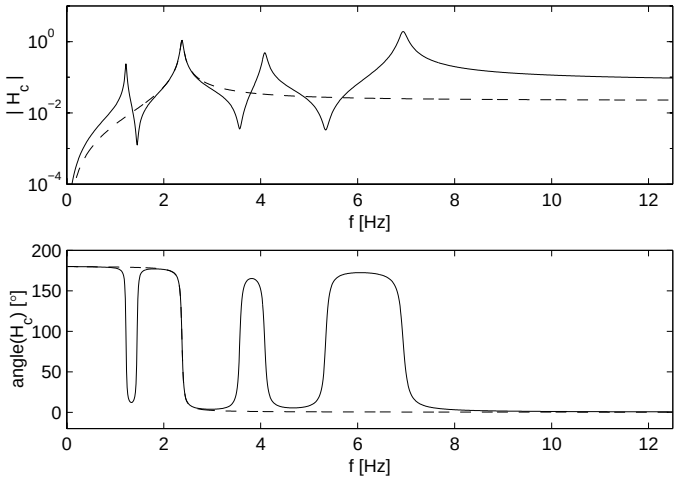

Figure 2.8: Part of element (1,1) of the **FRF** matrix $H_c(j\omega)$. It represents the **FRF** from the input at node 4 (*x*-direction) to the output at the same **DOF**. The top figure is the absolute value of the **FRF**; the bottom figure shows the phase angle. The full line is the full **FRF**. The bending modes in the *y*-direction are not visible. The dashed line represents the contribution of the second mode to the **FRF**.

Example

The **FRF** matrix of the mast structure (Figure 2.1) is computed by evaluating expression (2.72) at frequencies *f*, ranging from 0 to 12.5 Hz ($s = j\omega$, $\omega = 2\pi f$). A typical element of the **FRF** is shown in Figure 2.8.

2.7.3 The spectrum

In this section we will examine the case where the input signal $u(t)$ is not a deterministic signal. Stochastic signals are characterized by their statistical properties. The discussion is restricted to the case of a zero mean $\mathbf{E}[u(t)] = 0$, white noise input sequence. The covariance function $R_u(\tau)$ of such a sequence can be written as:

$$R_u(\tau) = \mathbf{E}[u(t+\tau)\,u^T(t)] = R_u\delta(\tau)$$

where $R_u \in \mathbb{R}^{m\times m}$ is a constant matrix and $\delta(\tau)$ is the Dirac delta function ($\delta(\tau) = \infty$ at $\tau = 0$ and $\delta(\tau) = 0$ elsewhere). The Dirac delta function has the following property:

$$\int_{-\infty}^{\infty} f(t)\,\delta(t-a)\,dt = f(a) \tag{2.73}$$

for any function $f(t)$ which is continuous at time a. These definitions of white noise are the continuous-time counterparts of the discrete white noise definitions given in Section 2.5.1.

The spectrum $S_x(s)$ of a stationary stochastic process $x(t)$ is defined as the double-sided s-transform[7] of its covariance function $R_x(t)$:

$$S_x(s) = \int_{-\infty}^{\infty} R_x(t) e^{-st} dt$$

So in case of white noise, the spectrum is a constant matrix because of property (2.73):

$$S_u(s) = \int_{-\infty}^{\infty} R_u(t) e^{-st} dt = R_u$$

This is also called a "flat" spectrum. The diagonal elements of the spectrum matrix are called *power spectra* and the other elements *cross spectra*.

If two processes $u(t), y(t)$ are related by the transfer function $H_c(s)$ as in Equation (2.70), it can be proven [LJUN99] that their spectra are related by:

$$S_y(s) = H_c(s) S_u(s) H_c^T(s^*)$$

or, more specifically in case of a white noise input:

$$S_y(s) = H_c(s) R_u H_c^T(s^*) \tag{2.74}$$

By inserting the modal decomposition of the transfer function (2.71), following expression is obtained for the spectrum:

$$S_y(s) = (V_c(sI - \Lambda_c)^{-1} L_c^T + D_c)\ R_u\ (D_c^T + L_c(s^* I - \Lambda_c)^{-1} V_c^T) \tag{2.75}$$

Some identification methods of Chapter 3 need an expression for the spectrum that is written as a sum of modal contributions instead of a product. The application of the partial fraction expansion to Equation (2.75) require the solution of a continuous-time Lyapunov equation. This is elaborated in detail in Appendix A.2.

---

[7] For purely imaginary values of s, the double-sided s-transform equals the Fourier transform: $S_x(j\omega) = \int_{-\infty}^{\infty} R_x(t) e^{-j\omega t} dt$.

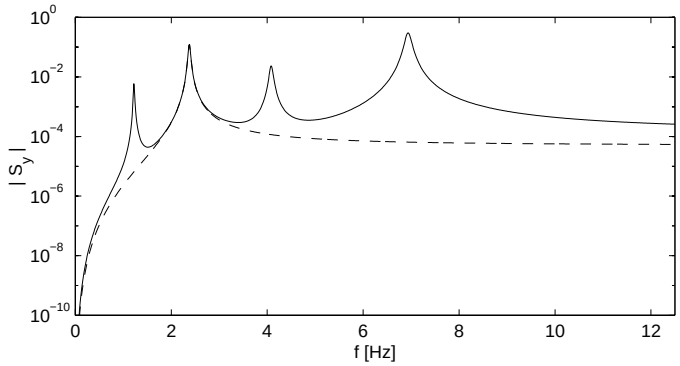

Figure 2.9: Part of element (1,1) of the spectrum matrix $S_y(j\omega)$. It represents the power spectrum of the acceleration response of the structure at node 4 (*x*-direction). The full line is the full **FRF**. The bending modes in the *y*-direction are not visible. The dashed line represents the contribution of the second mode to the spectrum.

Example

The spectrum matrix of the mast structure (Figure 2.1) is computed by evaluating expression (2.74) at frequencies *f*, ranging from 0 to 12.5 Hz ($s = j\omega$, $\omega = 2\pi f$). A typical element of the spectrum matrix is shown in Figure 2.9.

2.8 DISCRETE-TIME FREQUENCY-DOMAIN MODELS

Unlike in time domain, frequency-domain identification does not require discrete-time models. It is, for instance, possible to identify a continuous-time frequency-domain model from samples of the Fourier transforms of the signals. The reason why this section on frequency-domain equivalents to the discrete-time models is added is that there do exist identification methods that assume such models. Another reason is that these models provide a tool to assess the quality of a time-domain identification method. The identified time-domain model can be analytically converted to frequency domain and can be compared to a non-parametric estimate of the frequency data (obtained by applying the **FFT** to the data).

2.8.1 The *z*-transform

The *z*-transform is the discrete-time analogy of the *s*-transform. It is defined as:

$$X(z) = \mathbf{Z}[x_k] = \sum_{k=0}^{\infty} x_k z^{-k}$$

where $z \in \mathbb{C}$ is a scalar complex variable. An important property of the *z*-transform is:

$$\mathbf{Z}[x_{k+1}] = z(X(z) - x_0)$$

If the initial condition is zero $x_0 = 0$, a forward time shift in time domain corresponds to a multiplication by *z* in the *z*-domain.

By taking the *s*-transform of a continuous-time signal that equals a given discrete-time signal at the discrete samples and is zero elsewhere, it can be shown that the *z*-transform coincides with the *s*-transform by setting $z = e^{s\Delta t}$ [JUAN94]. Therefore, a restriction to purely imaginary values of the *s*-variable in continuous-time corresponds to a restriction to values on the unit circle in discrete-time:

$$z = e^{j\omega\Delta t} \tag{2.76}$$

2.8.2 The spectrum of a stochastic state-space model

In discrete-time, the spectrum of a stationary stochastic process is defined as the double-sided *z*-transform of its covariance sequence. Therefore the discrete-time output spectrum equals:

$$S_y(z) = \sum_{k=-\infty}^{\infty} R_k z^{-k} \tag{2.77}$$

where R_k is the output covariance at time lag *k*, defined in Equation (2.53). By substituting *z* according to Equation (2.76), the Fourier transform in discrete-time is obtained:

$$S_y(e^{j\omega\Delta t}) = \sum_{k=-\infty}^{\infty} R_k e^{-j\omega k\Delta t} \tag{2.78}$$

In case of a stationary process, the following property holds:

$$R_{-k} = R_k^T$$

and the spectrum (2.77) can be written as:

$$S_y(z) = S_y^+(z) + (S_y^+(z^{-1}))^T$$

where $S_y^+(z)$ is defined as:

$$S_y^+(z) = \frac{R_0}{2} + \sum_{k=1}^{\infty} R_k z^{-k} \tag{2.79}$$

The important factorization property of the output covariances was given in Equation (2.56):

$$R_k = CA^{k-1}G$$

If A is a stable matrix, we have the following series expansion:

$$(zI - A)^{-1} = \sum_{k=1}^{\infty} A^k z^{-k}$$

This series is found after inserting the factorization property (2.56) into (2.79). Consequently, following closed-form expression is found for the spectrum (2.77):

$$S_y(e^{j\omega\Delta t}) = C(zI - A)^{-1}G + R_0 + G^T(z^{-1}I - A^T)^{-1}C^T \Big|_{z = e^{j\omega\Delta t}} \tag{2.80}$$

2.8.3 The spectrum of a forward innovation model

An alternative expression for the spectrum of a stochastic system is found from the forward innovation model that was defined as (2.58):

$$\begin{aligned} z_{k+1} &= Az_k + Ke_k \\ y_k &= Cz_k + e_k \end{aligned}$$

where the innovation sequence is a zero mean white noise sequence with covariance R_e. The forward state covariance matrix is denoted as $P = \mathbf{E}[z_k z_k^T]$.

By introducing the forward shift operator q ($qz_k = z_{k+1}$), the state vector can be eliminated from the model to yield:

$$y_k = H(q)e_k \tag{2.81}$$

where $H(q)$ is the *transfer operator* that can be computed as:

$$H(q) = C(qI_n - A)^{-1}K + I_l$$

Since a forward time shift in time domain corresponds to a multiplication by z in the z-domain, we can simply substitute q by z to yield the transfer function. If z is restricted to

values on the unit circle $z = e^{j\omega\Delta t}$ (2.76), the discrete-time Frequency Response Function is obtained.

The interpretation of Equation (2.81) is that y_k is a stationary stochastic process obtained by filtering white noise through the filter $H(q)$. By consequence the spectrum of y_k can be written as [LJUN99]:

$$S_y(e^{j\omega\Delta t}) = H(z) R_e H^T(z^{-1}) \Big|_{z = e^{j\omega\Delta t}}$$

or, after introducing the expression for the transfer function:

$$S_y(e^{j\omega\Delta t}) = (C(zI_n - A)^{-1}K + I_l)\, R_e\, (I_l + K^T(z^{-1}I_n - A^T)^{-1}C^T) \Big|_{z = e^{j\omega\Delta t}} \quad (2.82)$$

Of course, this forward-innovation spectrum is equivalent to the covariance spectrum (2.80). The latter can be considered as the partial fraction expansion of the forward-innovation spectrum (2.82). Similar to the continuous-time case (see Appendix A.2), the matrices of the partial fraction expansion are obtained by solving a Lyapunov equation. The forward state covariance matrix *P* is found as the solution of:

$$P = APA^T + KR_eK^T$$

which is a so-called discrete-time Lyapunov equation. The matrices *G* and R_0 are recovered as:

$$G = APC^T + KR_e$$
$$R_0 = CPC^T + R_e$$

Example

The discrete-time spectrum matrix of the mast structure (Figure 2.1) is computed by evaluating expression (2.80) at frequencies *f*, ranging from 0 to 12.5 Hz ($z = e^{j\omega\Delta t}$, $\omega = 2\pi f$). A typical cross spectrum is shown in Figure 2.10. The discrete-time spectrum is compared to the continuous-time spectrum. Due to the high sampling rate ($f_s = 100\,\text{Hz}$), there is not much difference.

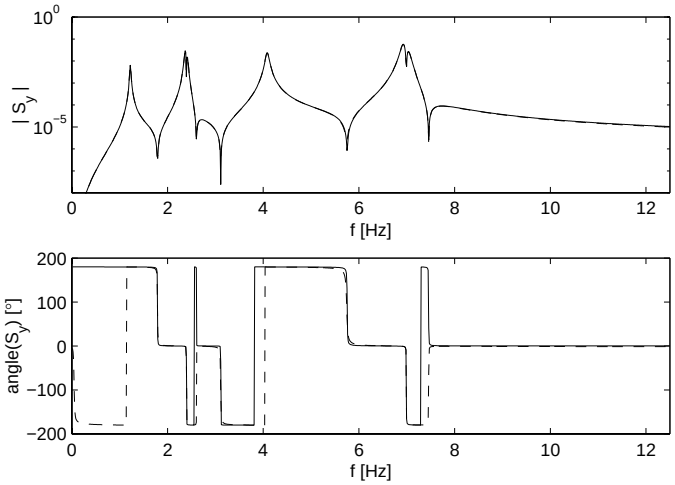

Figure 2.10: Part of element (5,4) of the spectrum matrix $S_y(j\omega)$. It represents the cross spectrum between the acceleration in the *y*-direction at node 8 and the acceleration in the *x*-direction at node 7. The top figure is the absolute value of the spectrum; the bottom figure shows the phase angle. The full line is the continuous-time spectrum and the dashed line represents the discrete-time spectrum. The two pairs of closely-spaced modes are visible on this cross spectrum plot.

2.9 CONCLUSIONS

This chapter presented several models of vibrating structures. They differed in that they are in continuous-time or discrete-time; that they are input-output or output-only models and that they are in time domain or in frequency domain. The chapter started by **FE** models. The evolution from the analytical to the experimental world consisted of following steps: the **FE** model is reduced, sampled and a noise model is added. A simulation example illustrated the modelling concepts.

Next chapter relies heavily upon the results obtained in this chapter. It will be shown how the stochastic state-space model, the **ARMA** model and the continuous-time frequency-domain models can be identified from measurements.

3

STOCHASTIC SYSTEM IDENTIFICATION

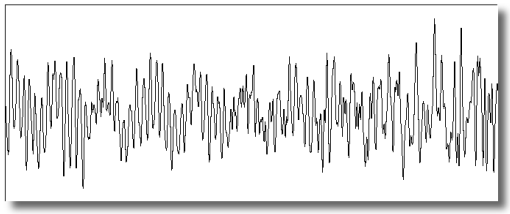

In this chapter stochastic system identification methods are discussed and compared. Section 3.2 introduces the primary data types that are required by the identification methods: time data, covariance sequences or spectra. In Section 3.3, spectrum-driven methods are discussed. Section 3.4 deals with covariance-driven methods and Section 3.5 treats data-driven methods. Covariance- and data-driven subspace methods are compared in Section 3.6. Useful postprocessing tools are presented in Section 3.7. In Section 3.8, all methods are experimentally compared. Section 3.9, finally, concludes the chapter.

3.1 INTRODUCTION

This chapter deals with *stochastic system identification* methods. In a civil engineering context, structures such as bridges and towers are the *systems*; the estimation of the modal parameters is the particular type of *identification* and *stochastic* means that the structure is excited by an unmeasurable input force and that only output measurements (e.g. accelerations) are available. In these methods the deterministic knowledge of the input is replaced by the assumption that the input is a realization of a stochastic process (white noise).

System identification starts by adopting a certain model that is believed to represent the system. Next, values are assigned to the parameters of the model as to match the measurements. In previous chapter, several equivalent models for a vibrating structure were studied. From that chapter, the type of models to work with are clear, only the model order remains to be chosen. In this chapter an overview is given of system identification methods that estimate the parameters of the stochastic models of previous chapter. These methods can be divided according to the type of data that they require: raw time data, covariances or spectra. The overview of the methods is given in the reverse order as compared to the overview of the models of chapter 2: we start with frequency-domain spectrum-driven methods to end with time-domain data-driven methods. This presentation order corresponds to the historical application of stochastic system identification methods: from picking the peaks of spectral densities to subspace methods that make extensively use of concepts from numerical linear algebra.

3.2 DATA TYPES

In principle (output) data y_k is available as discrete samples of the time signal. This section deals with the transformation of time data to covariances or spectra. Also some notations are introduced.

3.2.1 Time data

Measurements for modal analysis applications typically contain some redundancy. Since the spatial resolution of the experimental mode shapes is determined by the position and the number of the sensors, usually many sensors (mostly accelerometers) are used in a modal analysis experiment. Theoretically, if none of the sensors is placed at a node of a mode, all signals carry the same information on eigenfrequencies and damping ratios. To decrease this redundancy, some signals are *partially* omitted in the identification process, leading to algorithms that are faster and require less computer memory without losing a lot of accuracy. In the end, the omitted sensors are again included to yield the "full" mode

shapes[1]. Assume that the l outputs are split in a subset of r well-chosen reference sensors and a subset of $l-r$ other sensors, and that they are arranged so as to have the references first:

$$y_k = \begin{pmatrix} y_k^{\text{ref}} \\ y_k^{\sim\text{ref}} \end{pmatrix}, \quad y_k^{\text{ref}} = L\, y_k, \quad L = (I_r \;\; 0) \tag{3.1}$$

where $y_k^{\text{ref}} \in \mathbb{R}^r$ are the reference outputs and $y_k^{\sim\text{ref}} \in \mathbb{R}^{l-r}$ are the others; $L \in \mathbb{R}^{r \times l}$ is the selection matrix that selects the references. The choice of the reference sensors in output-only modal analysis corresponds to the choice of the input locations in traditional input-output modal analysis [EWIN84, HEYL95].

It is useful in the development of some of the identification methods to gather the output measurements in a block Hankel[2] matrix with $2i$ block rows and N columns. The first i blocks have r rows, the last i have l rows. For the statistical proves of the methods, it is assumed that $N \to \infty$. The Hankel matrix $H^{\text{ref}} \in \mathbb{R}^{(r+l)i \times N}$ can be divided into a past reference and a future part:

$$H^{\text{ref}} = \frac{1}{\sqrt{N}} \left(\begin{array}{cccc} y_0^{\text{ref}} & y_1^{\text{ref}} & \cdots & y_{N-1}^{\text{ref}} \\ y_1^{\text{ref}} & y_2^{\text{ref}} & \cdots & y_N^{\text{ref}} \\ \cdots & \cdots & \cdots & \cdots \\ y_{i-1}^{\text{ref}} & y_i^{\text{ref}} & \cdots & y_{i+N-2}^{\text{ref}} \\ \hline y_i & y_{i+1} & \cdots & y_{i+N-1} \\ y_{i+1} & y_{i+2} & \cdots & y_{i+N} \\ \cdots & \cdots & \cdots & \cdots \\ y_{2i-1} & y_{2i} & \cdots & y_{2i+N-2} \end{array} \right) = \left(\begin{array}{c} Y_{0|i-1}^{\text{ref}} \\ \hline Y_{i|2i-1} \end{array} \right) = \left(\begin{array}{c} Y_p^{\text{ref}} \\ \hline Y_f \end{array} \right) \begin{array}{l} \updownarrow ri \\ \updownarrow li \end{array} \quad \begin{array}{c} \text{"past"} \\ \text{"future"} \end{array} \tag{3.2}$$

Note that the output data is scaled by a factor $1/\sqrt{N}$. The subscripts of $Y_{i|2i-1} \in \mathbb{R}^{li \times N}$ are the subscripts of the first and last element in the first column of the block Hankel matrix. The subscripts p and f stand for past and future. The matrices Y_p^{ref} and Y_f are defined by splitting H^{ref} in two parts of i block rows. Another division is obtained by adding one block row to the past references and omitting the first block row of the future outputs. Because the references are only a subset of the outputs, $l-r$ rows are left over in this new division. These rows are denoted by $Y_{i|i}^{\sim\text{ref}} \in \mathbb{R}^{(l-r) \times N}$:

---

[1] This rather abstract explanation will become more clear when the identification methods are developed.

[2] A Hankel matrix is a matrix that is constant along its anti-diagonal.

$$H^{\text{ref}} = \begin{pmatrix} Y_{0|i}^{\text{ref}} \\ \hline Y_{i|i}^{\sim\text{ref}} \\ \hline Y_{i+1|2i-1} \end{pmatrix} = \begin{pmatrix} Y_p^{\text{ref}+} \\ \hline Y_{i|i}^{\sim\text{ref}} \\ \hline Y_f^- \end{pmatrix} \begin{matrix} \updownarrow r(i+1) \\ \updownarrow l-r \\ \updownarrow l(i-1) \end{matrix} \tag{3.3}$$

3.2.2 Covariance estimates

Output covariances are defined in Equation (2.53) as:

$$R_i = \mathbf{E}[y_{k+i} y_k^T] = \lim_{N\to\infty} \frac{1}{N} \sum_{k=0}^{N-1} y_{k+i} y_k^T$$

The second equality follows from the ergodicity[3] assumption. The reduced covariances between all outputs and the references are defined as the first r columns of the full covariance matrices:

$$R_i^{\text{ref}} = \mathbf{E}[y_{k+i} (y_k^{\text{ref}})^T] = R_i L^T \in \mathbb{R}^{l\times r} \tag{3.4}$$

Similarly, the *reduced "next state - output" covariance matrix* G^{ref} is defined as:

$$G^{\text{ref}} = \mathbf{E}[x_{k+1} (y_k^{\text{ref}})^T] = G L^T \in \mathbb{R}^{n\times r} \tag{3.5}$$

And for $i = 1, 2, \ldots$:

$$\begin{aligned} R_i^{\text{ref}} &= R_i L^T = C A^{i-1} G^{\text{ref}} \\ (R_i^{\text{ref}})^T &= L R_{-i} = (G^{\text{ref}})^T (A^{i-1})^T C^T \end{aligned} \tag{3.6}$$

These equations are equivalent to the factorization properties of the full covariance matrices (2.56).

The output covariances are gathered in a block Toeplitz[4] matrix $T_{1|i}^{\text{ref}} \in \mathbb{R}^{li\times ri}$ that can be computed from the data block Hankel matrix. Indeed, for $N\to\infty$ and assuming ergodicity, we have:

---

[3] Ergodicity means that the expected value of a time sample of a stationary stochastic process (i.e. the average over an infinite number of processes) can be replaced by the average over one infinitely long record of the process.

[4] A Toeplitz matrix is a matrix that is constant along its diagonal.

$$T_{1|i}^{\text{ref}} = Y_f\,(Y_p^{\text{ref}})^T = \begin{pmatrix} R_i^{\text{ref}} & R_{i-1}^{\text{ref}} & \dots & R_1^{\text{ref}} \\ R_{i+1}^{\text{ref}} & R_i^{\text{ref}} & \dots & R_2^{\text{ref}} \\ \dots & \dots & \dots & \dots \\ R_{2i-1}^{\text{ref}} & R_{2i-2}^{\text{ref}} & \dots & R_i^{\text{ref}} \end{pmatrix} \tag{3.7}$$

Of course, in reality a finite number N of data is available and a covariance estimate $\hat{R}_i$ is simply obtained by dropping the limit:

$$\hat{R}_i = \frac{1}{N}\sum_{k=0}^{N-1} y_{k+i}y_k^T \tag{3.8}$$

Instead of computing the covariance estimate by multiplication and summation of time samples, a high-speed implementation of the convolution in Equation (3.8) is possible by applying the **FFT** to the time signals, cross-multiplying the Fourier transforms and applying the inverse **FFT** to the cross-products. The inverse **FFT** results in a periodic covariance function estimate. The bias error due to this *circular convolution* is avoided by zero-padding the original signals [BEND93]. A disadvantage of using covariances as primary data in identification is that it squares up the data. This may affect the numerical accuracy [GOLU89].

3.2.3 Spectrum estimates

Another useful data format is the spectrum $S_y \in \mathbb{C}^{l\times l}$, defined in Equation (2.78) as the discrete-time Fourier transform of the covariance sequence:

$$S_y(e^{j\omega\Delta t}) = \sum_{k=-\infty}^{\infty} R_k e^{-j\omega k\Delta t}$$

Introducing the reference sensors (3.1) yields a $l\times r$ complex spectrum matrix $S_y^{\text{ref}} = S_y L^T$ that consists of the first r columns of the full spectrum matrix.

Again, only a finite number of data is available: the covariances are estimated as in (3.8) and cannot be computed up to infinite time lag. There is a whole literature on estimating spectra from data [MARP87, BEND93, STOI97]. Two popular non-parametric spectrum estimates are the *weighted averaged periodogram* (also known as *modified Welch's periodogram*) and the *weighted correlogram*. Weighting means that the signal is weighted by one of the classical windows (Bartlett, Hamming, Hanning, ...) to reduce leakage.

Welch's method starts with computing the **D**iscrete **F**ourier **T**ransform (**DFT**) of the weighted output signal:

$$Y(e^{j\omega\Delta t}) = \sum_{k=0}^{N-1} w_k \, y_k e^{-j\omega k\Delta t} \tag{3.9}$$

where w_k denotes the window function in this context. If N is a power of 2, the **DFT** can be efficiently computed at the discrete frequencies

$$\omega = \frac{l}{N} \frac{2\pi}{\Delta t}, \quad l = 0,\ldots,N-1$$

by using the **FFT**. An unbiased estimate of the spectrum is the weighted periodogram, i.e. the **DFT** of (3.9) times its complex conjugate transpose and scaled by the squared norm of the window:

$$\hat{S}_y(e^{j\omega\Delta t}) = \frac{1}{\sum_{k=0}^{N-1} |w_k|^2} Y(e^{j\omega\Delta t}) Y^T(e^{-j\omega\Delta t}) \tag{3.10}$$

The variance of the estimate is reduced by splitting the signal in segments, computing the weighted periodograms of all segments and taking the average. The spectrum estimate in (3.10) yields a rank-one matrix (a column vector multiplied by a row vector). Segment averaging increases the rank of the estimate because several rank-one estimates are added.

The weighted correlogram method starts by computing the covariance estimates as in (3.8). The weighted correlogram is defined as the **DFT** of the weighted covariance estimates:

$$\hat{S}_y(e^{j\omega\Delta t}) = \sum_{k=-L}^{L} w_k \, \hat{R}_k e^{-j\omega k\Delta t} \tag{3.11}$$

where L is the maximum number of time lags.

By using measurement hardware such as frequency analysers which deliver spectra instead of the original time data, the user could forget that these spectra are in fact computed as in (3.10) or (3.11). Consequently, they have to be considered as estimates and not as true spectra. Limitations and drawbacks of the **DFT** related to modal analysis are discussed in [MITC86] and [PAND91a]. Advantages of frequency-domain identification are discussed in [SCHO91] and also recapitulated in [McKE95] and [LJUN99]. Evidently, the frequency-domain advantages related to the use of a periodic input signal are not carrying over to the output-only case.

Example

The mast example of previous chapter (Figure 2.1) is used again in this chapter to illustrate and compare the system identification methods. As explained previously (see Page 29), the structure is excited by white noise inputs and 6 acceleration outputs are simulated, sampled at 100 Hz. The output data are filtered with an eight-order Chebyshev type I lowpass filter with a cutoff frequency of 10 Hz. Afterwards the data is resampled[5] at a lower rate: $f_s = 25\,\text{Hz}$. This preprocessing corresponds to practice where the measurements are filtered with an (analog) lowpass filter before sampling to prevent aliasing. The filtering introduces additional poles in the data. Finally, white measurement noise is added to the outputs, with a noise-to-signal ratio $\text{N/S} = 10\%$. The N/S ratio is the ratio of the standard deviations of the noise sequence and the output signal. After resampling 16384 data points per output channel are left. The first (preprocessed) output signal is partly shown in Figure 3.1. A typical estimated covariance sequence $\hat{R}_i(1,1)$ (3.8) is shown in Figure 3.2. It is compared with the true covariance sequence, computed from the stochastic state-space matrices (A, G, C, R_0) according to Equation (2.56).

An estimated power spectrum $\hat{S}_y(1,1)$, using Welch's method, is shown and compared with the true spectrum (2.80) in Figure 3.3. The cutoff frequency (10 Hz) of the lowpass filter is clearly visible. One of the consequences of adding measurement noise, is that the spectrum does not go to zero for $f \to 0\,\text{Hz}$, as would be expected in the case of acceleration measurements (and indicated by the true spectrum). Finally, two non-parametric spectrum estimates are compared in Figure 3.4: the weighted averaged periodogram (3.10) and the weighted correlogram (3.11).

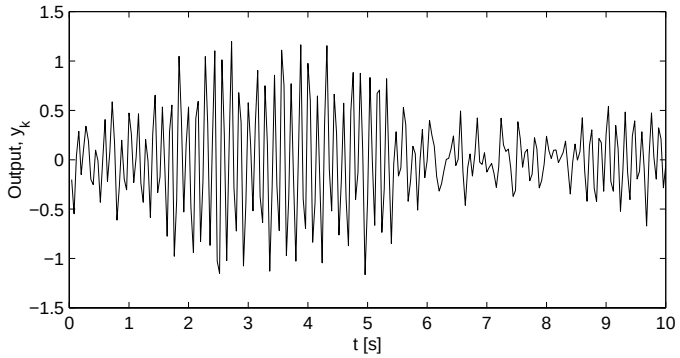

Figure 3.1: Part of the first output signal. By comparing this preprocessed signal with the original signal (Figure 2.5), the lower sampling rate is obvious.

[5]The described filtering and resampling procedure corresponds to the application of the `decimate` command of MATLAB's Signal Processing Toolbox [SIGN97].

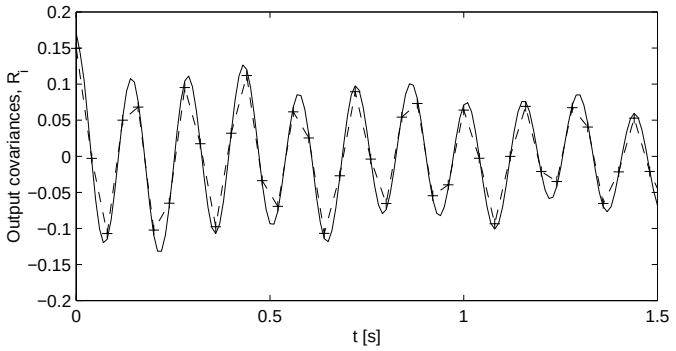

Figure 3.2: The full line represents the true output covariance sequence. The dashed line with the '+' markers is the estimated output covariance sequence. The sampling frequency of the true covariance sequence is 4 times higher, but otherwise both sequences correspond very well.

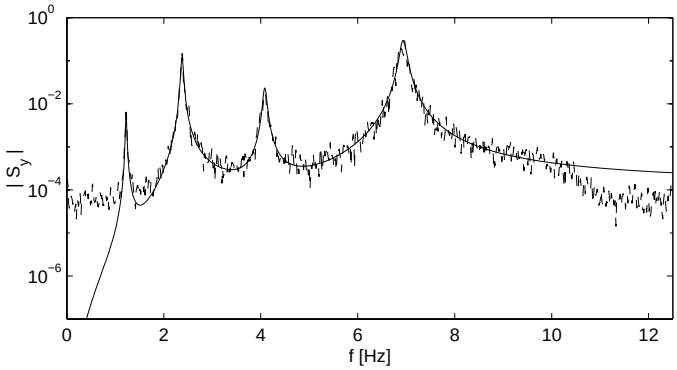

Figure 3.3: The full line represents the true spectrum and the dashed line the estimated spectrum using Welch's averaged periodogram method: the 16384 data samples are divided in 8 segments of 2048 points; after multiplication with a Hanning window, an **FFT** was applied to every segment; finally the 8 **FFT**s are averaged to yield the spectrum estimate. The influence of the lowpass filter at 10 Hz and the added measurement noise are clearly visible.

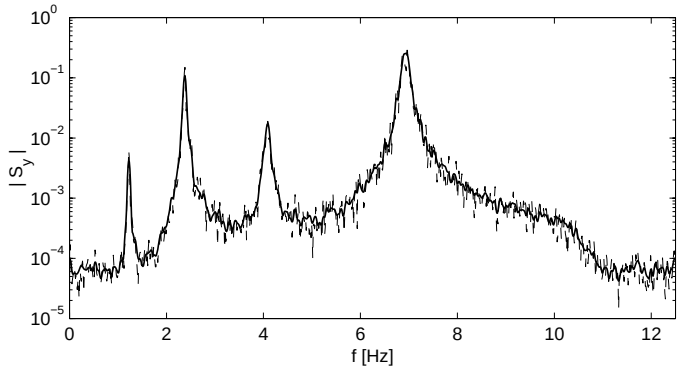

Figure 3.4: Comparison of non-parametric spectrum estimates. The full line represents the weighted correlogram (3.11) with the number of time lags $L = 512$. The estimated covariances are multiplied with a Hanning window before the **FFT**. The dashed line represents the weighted averaged periodogram (3.10), see also Figure 3.3. The correlogram looks smoother.

3.3 FREQUENCY-DOMAIN SPECTRUM-DRIVEN METHODS

A spectrum-driven identification method estimates the parameters of a spectrum model from "measured" samples of the spectrum matrix. As explained in previous section, these samples are obtained by applying a non-parametric identification method to the time-domain measurements. The spectrum can be parametrized in terms of the modal parameters[6] as in (A.6) or (A.8) or in terms of rather abstract matrices as in (2.80) or (2.82), from which the modal parameters can be extracted in a second stage. The overview starts with the *peak-picking* method which seems to be very relevant for the civil engineering practice. In more than 90% of the cases, a peak-picking variant is used to estimate the modal parameters of a structure excited by an ambient load. Next, a *singular-value-decomposition* extension to peak picking is discussed that overcomes some of the drawbacks. A final section reviews some recent, more advanced methods that solve the spectrum-driven identification problem.

3.3.1 Peak picking (PP)

The method

The most simple approach to estimate the modal parameters of a structure subjected to ambient loading is the so-called **P**eak-**P**icking (**PP**) method. The method is named after the

[6]This particular parametrization is also called *pole-residue form.*

key step of the method: the identification of the eigenfrequencies as the peaks of a spectrum plot. Probably because of its simplicity it is the most widely used method in civil engineering. The method is for instance discussed in [BEND93]. We will give a theoretical justification of the method in view of the results of previous chapter.

In case of acceleration measurements, the following expression for the modally decomposed spectrum was obtained (A.7):

$$S_y(s) = \left(\sum_{i=1}^{n} \frac{s^2}{\lambda_i^2 (s-\lambda_i)} \{v_{c_i}\} < l_{c_i}^T > \right) R_u \left(\sum_{i=1}^{n} \frac{(s^*)^2}{\lambda_i^2 (s^*-\lambda_i)} \{l_{c_i}\} < v_{c_i}^T > \right) \quad (3.12)$$

This expression is the product of two summations wherein each term represents the contribution of a certain mode. A term of the left factor is proportional to $(s-\lambda_i)^{-1}$ and reaches a maximum if s approaches $\lambda_i = -\xi_i \omega_i + j(1-\xi_i^2)^{1/2} \omega_i$ (2.16). For low damping ratios, this is achieved around $s = j\omega_i$. If additionally the assumption is made that the modes have well-separated frequencies, the spectrum at any eigenfrequency ω_i is dominated by a single mode and can be approximated by:

$$S_y(j\omega_i) \approx \frac{\{v_{c_i}\} < l_{c_i}^T > R_u \{l_{c_i}^*\} < v_{c_i}^H >}{(\xi_i \omega_i)^2}$$

By defining the complex scalar α_i as:

$$\alpha_i = \frac{1}{(\xi_i \omega_i)^2} < l_{c_i}^T > R_u \{l_{c_i}^*\}$$

the approximated spectrum at resonance can be rewritten as:

$$S_y(j\omega_i) \approx \alpha_i \{v_{c_i}\} < v_{c_i}^H > \quad (3.13)$$

The interpretation of this equation is that at resonance, each column (or equivalently each row) of the spectrum matrix can be considered as an estimate of the observed mode shape $\{v_{c_i}\}$ up to some scaling factor. Of course, if the column (or row) corresponds to a **DOF** of the structure that is situated at a node of a certain mode, this mode cannot be identified.

The damping ratios remain to be determined. In [BEND93] it is suggested to use the half-power bandwidth method to estimate the damping. Assume that ω_1 and ω_2 are the two frequencies left and right from, and as close as possible to the eigenfrequency ω_i, where the magnitude of a certain element of the spectrum matrix is half the resonance magnitude. A damping estimate is then obtained as:

$$\xi_i = \frac{\omega_2 - \omega_1}{2\omega_i}$$

It is however believed (and confirmed by our numerical example; see Figure 3.19) that this estimate is not very accurate.

Refinements and practical issues

Some refinements of the **PP** method exist. The coherence function between two channels tend to go to one at the resonance frequencies because of the high signal-to-noise ratio at these frequencies [BEND93]. Consequently inspecting the coherence function can assist in selecting the eigenfrequencies. Also the phase angles of the cross spectra are helpful: if real modes are expected, the phase angles should be either 0° or 180° at the resonance frequencies.

A practical implementation of the **PP** method was realized by Felber [FELB93]. In order to get a global picture of the eigenfrequencies, he suggested to compute an averaged normalized power spectrum from the diagonal elements of the spectrum matrix. By adding and subtracting signals from symmetric points of the structure the "nature" of a mode (e.g. torsion versus bending) may be highlighted.

If a good reference sensor (3.1) is chosen only the spectra between all sensors and the single reference sensor need to be estimated from the time data and not the full spectrum matrix. This reduces the work in (3.10) or (3.11). The reason is that, theoretically one column (or one row) of the spectrum matrix suffices to obtain the mode shape estimates (3.13).

Discussion

The method assumes that the damping is low and that the modes are well-separated. A Violation of these assumptions leads to erroneous results. In fact the method identifies *operational deflection shapes*[7] instead of mode shapes and for closely-spaced modes such an operational deflection shape will be the superposition of multiple modes. Other disadvantages are that the selection of the eigenfrequencies can become a subjective task if the spectrum peaks are not very clear and that the eigenfrequencies have to be a subset

[7] An operational deflection shape is here defined as the deformation of the structure when it is excited by a pure harmonic. Theoretically it is a combination of all mode shapes, but in practice only the modes having an eigenfrequency close to the excitation frequency contribute significantly.

of the discrete frequency values of the **DFT** (This is of course no problem if the frequency resolution is fine enough).

Despite these drawbacks many civil engineering cases exist where the method is successfully applied; see for instance [FELB96] and [CUNH99]. The popularity of the method is due to its implementation simplicity and its speed, because it basically relies upon the **FFT**. For tower-like structures the peak-picking method may become problematic since the bending modes along any of the 2 principal axes and/or any of the torsion modes are likely to have closely-spaced frequencies. For bridge-like structures this seems to be less the case.

Example

The **PP** method is applied to the simulated data from the mast structure (Figure 2.1). The spectrum matrix is estimated by Welch's method (3.10) according to the processing parameters explained in Figure 3.3. The frequency resolution is $\Delta f = 1/T = 0.0122\,\text{Hz}$, where T is the measurement time of one segment $T = N\Delta t = 2048\times 0.04\,\text{s}$ (N is the number of data points per segment). The trace[8] of the spectrum matrix is shown in Figure 3.5. This kind of plot is typically used in the **PP** method to identify the eigenfrequencies by picking the peaks. The true eigenfrequencies are also shown as vertical lines. It is impossible to identify the two closely-spaced modes around 2.4 Hz. The spectrum trace has only one peak at this frequency. Eventually, the two close modes around 7 Hz could be identified (see zoom of Figure 3.5). It is however more likely that the two peaks of the spectrum trace are due to the typical erratic behaviour of the non-parametric spectrum estimates.

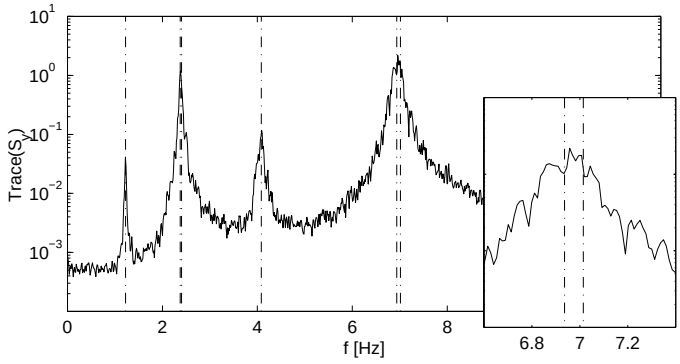

Figure 3.5: The trace of the spectrum matrix as a function of the frequency. The true eigenfrequencies are shown as dash-dotted vertical lines. The overlayed plot is a zoom of the trace around 7 Hz.

[8]The trace of a matrix is the sum of its main diagonal elements. By consequence the trace of the spectrum matrix is the sum of the power spectra.

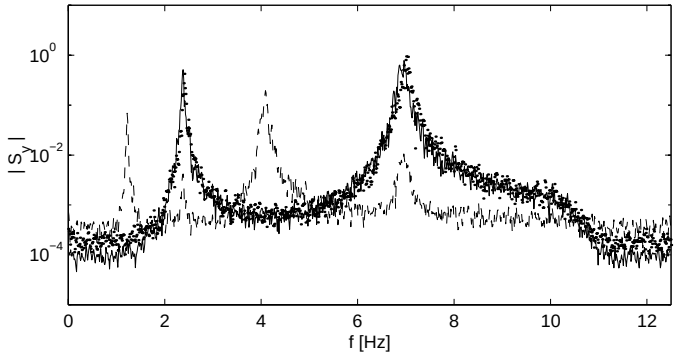

Figure 3.6: The transformed spectra. The full line is the spectrum of the *x*-bending signals; the dotted line represents *y*-bending and the dashed line represents torsion.

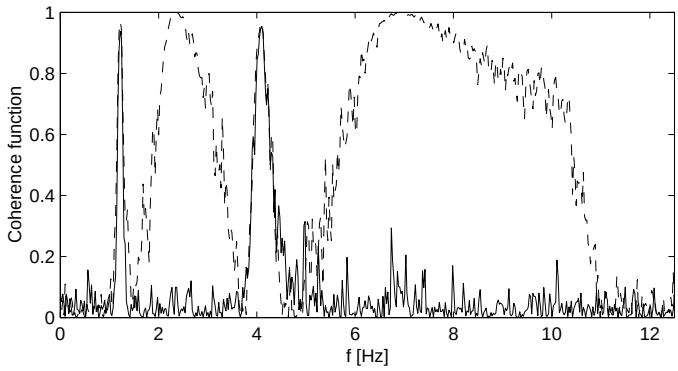

Figure 3.7: Two coherence functions. The full line is the coherence function between channels 4 and 5 (i.e. one channel in *x*-direction, the other in *y*-direction); the dashed line is the coherence between channels 4 and 6 (i.e. two channels in *x*-direction).

More information can be obtained by further processing the signals. By applying a suitable transformation to the spectrum matrix, the "nature" of the modes can be highlighted. The transformation is based on the geometry of the structure and the location of the sensors. The transformed spectra are shown in Figure 3.6. The *x*-bending, the *y*-bending and torsion components of the modes have been separated. Even from this plot, the close modes are not easily identifiable. Both the *x*-bending and *y*-bending graph have a peak around 2.4 and 7 Hz, but this can also signify that these modes are a combination of *x*- and *y*-bending.

Plots of coherence functions are most useful to improve the results of the **PP** method. In Figure 3.7 the coherence functions between channels 4 and 5 (full line) and channels 4 and 6 (dashed line) are shown. The torsion modes are clear in both coherence functions, but the bending modes do not show up in the coherence function between a signal in *x*-direction (channel 4) and a signal in *y*-direction (channel 5). This means that the *x* and *y*-bending modes are different modes, although they have very close frequencies.

By transforming the spectrum matrix and inspecting coherence functions, it was possible to identify the close modes with the **PP** method. It may however be clear that the success of these proposed enhancements heavily depends on the geometry of the structure and the skill of the analyst. The identified modal parameters are presented at the end of this chapter, together with the results of the other identification methods.

3.3.2 Complex mode indication function (CMIF)

The method

A more advanced method consists of computing the eigenvalue decomposition or **S**ingular **V**alue **D**ecomposition (**SVD**) of the spectrum matrix[9]. This "method based upon the diagonalization of the spectral density matrix" (as it was called) was already used in the beginning of the eighties to obtain the modes of a vibrating system subjected to natural excitation [PREV82]. Some years later, the method was also applied to **FRF**s and became known as the **C**omplex **M**ode **I**ndication **F**unction (**CMIF**). As suggested by the name, the **CMIF** was originally intended as a tool to count the number of modes that is present in measurement data. As a useful by-product the **CMIF** also identifies the modal parameters from **FRF**s [SHIH88]. Recently the spectrum-driven method received again attention as an alternative for the **PP** method in civil engineering applications [BRIN00][10].

The method is based on the fact that the transfer function or spectrum matrix evaluated at a certain frequency is only determined by a few modes. The number of significantly contributing modes determines the rank of the spectrum matrix. The **SVD** is typically used for estimating the rank of a matrix: the number of non-zero singular values equals the rank [GOLU89]. The spectrum matrix is related to the transfer function matrix H_c and the input covariance matrix R_u as (2.74):

$$S_y(s) = H_c(s) R_u H_c^T(s^*)$$

Let us assume that R_u is of full rank. Since the rank of a product of matrices equals the lowest rank of any of its factors, it suffices to discuss the rank of the transfer function H_c, which, in case of acceleration measurements, is modally decomposed as (A.3):

[9] Since the spectrum matrix is a Hermitian matrix, its eigenvalue decomposition coincides with its **SVD**.

[10] Although in this paper, the method is called "frequency domain decomposition method", we will stick to the best-known name (**CMIF**) in this thesis.

$$H_c(s) = \sum_{i=1}^{n} \frac{s^2}{\lambda_i^2 (s - \lambda_i)} \{v_{c_i}\} < l_{c_i}^T >$$

As already indicated in previous section, at a certain frequency only a few modes are determining the response. At resonance the transfer function reaches a local maximum and in case of well-separated modes only one mode is important. This means that the rank of H_c is approximately one at resonance. If two or more modes have about the same eigenfrequencies, the rank will be two or more at that frequency.

As said the rank of H_c carries over to the rank of the spectrum matrix S_y. The **SVD** of this matrix can be written as:

$$S_y(s) = U(s)\Sigma(s)U^H(s) = \sum_{v=1}^{l} \sigma_v(s)\{u_v(s)\} < u_v^H(s) > \tag{3.14}$$

where $U(s)$, $V(s)$ are complex unitary matrices. The diagonal matrix $\Sigma(s)$ contains on its diagonal the real positive singular values in descending order. At resonance, the number of singular values that reach a local maximum equal the number of closely-spaced modes. The function $\Sigma(s)$ is the actual **CMIF**.

If only one mode is important at a certain resonance frequency ω_i, the spectrum approximates a rank-one matrix and can be decomposed as (3.14):

$$S_y(j\omega_i) \approx \sigma_1^2(j\omega_i) \{u_1(j\omega_i)\} < u_1^H(j\omega_i) > \tag{3.15}$$

By comparing this expression to (3.13) it is concluded that the first singular vector at resonance is an estimate of the mode shape at that frequency. In case of mode multiplicity at a resonance frequency, every singular vector corresponding to a non-zero singular value yields a mode shape estimate, if the mode shapes are orthogonal to each other. This last condition is only approximately true.

Discussion

The **CMIF** method can be considered as an **SVD** extension to the **PP** method. The **SVD** is able to resolve mode multiplicity. The method can also be applied to the reduced spectrum matrix $S_y^{\text{ref}} = S_y L^T \in \mathbb{C}^{l \times r}$. In this case, the maximum number of detectable multiple poles cannot exceed *r*, the smallest dimension of S_y^{ref}. Another limit on the maximum pole multiplicity is the number of rank-one averages that constitutes the spectrum estimate (3.10).

Extensions of the **CMIF** method are possible that do estimate eigenfrequencies and damping ratios differently as in the **PP** method. After applying the **SVD** to the spectrum matrix, this matrix is in fact decomposed in single-**DOF** systems. To such a system, single-**DOF** modal parameter estimation methods could be applied [EWIN84, HEYL95, MAIA97, ALLE99].

Example

The **SVD** is applied to the estimated spectrum matrix of the mast structure (Figure 2.1). The obtained singular values as a function of the frequency are plotted in Figure 3.8. Since the full spectrum matrix is used, there are six singular values. Around 2.4 and 7 Hz, there are two significant singular values, indicating that there are two close modes at these frequencies. In the neighbourhood of these frequencies, the first singular vector is an estimate of the "strongest" mode, whereas the second singular vector is an estimate of the other mode. Since the maximum mode multiplicity is two, it would have been sufficient to apply the **SVD** to the reduced spectrum matrix that only consists of the spectra between all sensors and two reference sensors. The detailed modal parameter estimation results are presented at the end of this chapter.

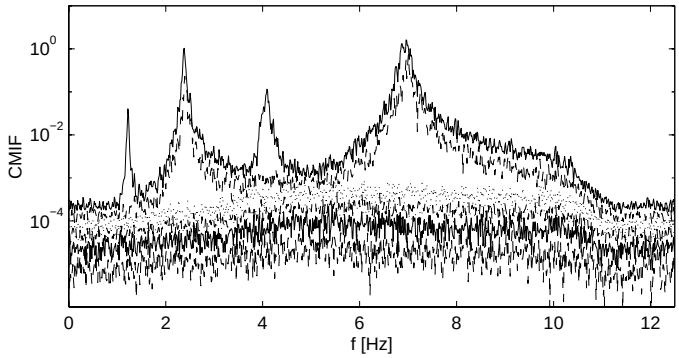

Figure 3.8: The Complex mode indication function (**CMIF**). The singular values of the spectrum matrix are plotted as a function of the frequency. Around 2.4 Hz and 7 Hz, two singular values are significant, indicating that there are two close modes.

3.3.3 Other spectrum-driven methods

In this section some other more advanced spectrum-driven methods are briefly reviewed. Contrary to the **PP** method or the **CMIF** that consider only one mode at a time, these methods estimate the parametrized spectrum matrix as a whole.

Frequency-domain maximum likelihood identification

Maximum **L**ikelihood (**ML**) identification is an optimization based method that estimates the parameters of a model by minimizing an error norm. A discussion on the use of the **ML** estimator to identify parametric frequency-domain models can be found in [SCHO91, PINT94]. The **ML** method results in equations that are non-linear in the unknown parameters. This requires an iterative procedure with related problems such as: convergence not being guaranteed, local minima, sensitivity to initial values and a high computational load. However, it seems that these drawbacks have been overcome and it has been shown that **ML** identification is a robust method to find the modal parameters of a structure from a large and noisy data set [GUIL98]. Originally intended for application to **FRF**s, the method was extended to use spectra as primary data, so that it also could be used in output-only cases [HERM98, GUIL99].

Spectrum-driven stochastic subspace identification

Subspace identification will be explained in detail in the sections on covariance-driven and data-driven identification methods. The major advantage of subspace identification is the absence of non-linear parametric optimization problems. In [VANO97] a "typical" subspace algorithm was developed to identify a state-space model (2.51) by fitting the expression for a discrete-time spectrum (2.80) to measured samples of the spectrum matrix. The algorithm is perhaps not a pure spectrum-driven method because the first step consists of transforming the spectrum samples back to time domain by applying the inverse **DFT**. The algorithm is certainly useful in these cases where, for some reason, only spectrum measurements are available. For lightly damped systems and for a small number of frequency samples, the inverse **DFT** of the measured spectrum is not a very good estimate of the output covariance function. This fact is taken into account in [VANO97], based on results from [McKE95] where an explicit formula is derived for the inverse **DFT** of a finite sequence of **FRF** samples, which differ from the impulse response expression.

3.4 TIME-DOMAIN COVARIANCE-DRIVEN METHODS

In this section some covariance-driven methods are reviewed. An important feature of a covariance matrix is that it can be factorized into the system matrices, as pointed out in Equation (2.56). A first method belongs to the class of so-called *instrumental variable* methods. Although its algorithm is formulated in terms of the covariances, it does not use the factorization property. The second method, on the contrary, is completely based on the factorization property. It is a so-called subspace method.

3.4.1 The instrumental variable (IV) method

Although the **I**nstrumental **V**ariable (**IV**) method is far from new, it is extensively discussed in this thesis in order to highlight the correspondence to the so-called **P**olyreference **T**ime **D**omain (**PTD**) method after substituting impulse responses by output covariances. The **PTD** method is probably the most widely-used traditional[11] modal parameter estimation method.

Instrumental-variable theory

In Chapter 2, it was found that an **ARMA** model of suitable order can represent a vibrating structure. Unfortunately, the application of a classical *prediction error method* [LJUN99] to an **ARMA** model results in a highly non-linear parameter estimation problem; see also Subsection 3.4.3 and 3.5.2. The non-linearity is caused by the **MA** parameters. The advantage of the **IV** method is that it identifies only the **AR** parameters (and that this is achieved in a linear way), while the underlying model structure still is an **ARMA** model. In Subsection 2.6.2, it was shown that for the extraction of the modal parameters there is no need to identify the **MA** part, since they only rely upon the **AR** part. The **ARMA** representation of a vibrating structure was given by Equation (2.59):

$$y_k + \alpha_1 y_{k-1} + \ldots + \alpha_p y_{k-p} = e_k + \gamma_1 e_{k-1} + \ldots + \gamma_p e_{k-p}$$

If the **ARMA** order p times the number of outputs l is equal to or larger than the system order n ($pl \geq n$), the system poles are included in the model.

The idea of system identification is to "fit" such a model to measured data y_k. A good parameter estimation method should extract the maximum information from the data, leaving residuals e_k that are uncorrelated with past data. This is formally written as:

[11] Traditional means here that it is an input-output based method.

$$\forall i>0 \,:\, \mathbf{E}[e_k y_{k-i}^T] \;=\; \mathbf{E}[e_k]\mathbf{E}[y_{k-i}^T] \;=\; 0 \tag{3.16}$$

where the first equality says that e_k and y_{k-i} are uncorrelated; and the second equality follows from the zero-mean property of the noise sequence. If on the other hand, the residuals are correlated with past data, they still contain useful but unmodeled information and the model is not ideal. The derivation of the **IV** method starts by imposing conditions like (3.16) to the **ARMA** model in order to get rid of the right hand side (the **MA** part). The "oldest" noise term is e_{k-p}; so by post-multiplying the **ARMA** model by y_{k-p-i}^T (for $i>0$) and by taking the expectation we obtain:

$$\forall i>0 \,:\, \mathbf{E}[y_k y_{k-p-i}^T] \;+\; \alpha_1 \mathbf{E}[y_{k-1} y_{k-p-i}^T] \;+\; \ldots \;+\; \alpha_p \mathbf{E}[y_{k-p} y_{k-p-i}^T] \;=\; 0$$

Because of stationarity we have: $\mathbf{E}[y_k y_{k-i}^T] = \mathbf{E}[y_{k+i} y_k^T] = R_i$, and the basic **IV** equation can be written in terms of the output covariances R_i:

$$\forall i>0 \,:\, R_{p+i} \;+\; \alpha_1 R_{p+i-1} \;+\; \ldots \;+\; \alpha_p R_i \;=\; 0 \tag{3.17}$$

By replacing the output covariances by their estimates $\hat{R}_i$ (3.8) and writing down the equation for all available time lags *i*, the **AR** parameters $\alpha_1,\ldots,\alpha_p$ can be estimated by solving the resulting over-determined set of equations in a least squares sense. Finally, the eigenvalues and the observed mode shapes are obtained from the eigenvalue decomposition of the companion matrix of the **AR** coefficients as described in Section 2.6.2.

A more general discussion and some more references on **IV** methods can be found in [LJUN99]. Interesting to note (and very relevant for civil engineering practice) is that the **IV** method is robust against non-stationary inputs (e.g. a white noise sequence with time-varying covariance). The proofs are more involved in this case [BENV85].

Introducing the reference sensors

A formulation in terms of the covariances between all sensors and the subset of reference sensors (3.4) is now be derived. We start with a reversed-time (or backward) **ARMA** model that only uses the reference outputs:

$$y_k^{\text{ref}} \;+\; \alpha_1^b \, y_{k+1}^{\text{ref}} \;+\; \ldots \;+\; \alpha_p^b \, y_{k+p}^{\text{ref}} \;=\; e_k^b \;+\; \gamma_1^b e_{k+1}^b \;+\; \ldots \;+\; \gamma_p^b e_{k+p}^b$$

The model is running backward in time: the current output $y_k^{\text{ref}} \in \mathbb{R}^r$ is written in terms of future outputs. Since only reference outputs are used, the backward matrix coefficients and

the residuals have reduced dimensions: $\alpha_i^b \in \mathbb{R}^{r\times r}$, $\gamma_i^b \in \mathbb{R}^{r\times r}$ and $e_k^b \in \mathbb{R}^r$. The order p of the reduced model is now related to the system order as: $p \geq n/r$.

A good (backward) model yields residuals that are uncorrelated with future outputs:

$$\forall i>0 \,:\, \mathbf{E}[e_k^b y_{k+i}^T] = 0$$

Note that this is, theoretically, a stricter condition as (3.16): the residuals e_k^b of a model that only uses the reference outputs are uncorrelated with all future outputs. However, due to the redundancy in the data, there is practically not much difference between this condition and (3.16). Using (3.4), the basic **IV** Equation (3.17) is now written as:

$$\forall i>0 \,:\, LR_{-p-i} + \alpha_1^b\, LR_{-p-i+1} + \ldots + \alpha_p^b\, LR_{-i} = 0 \tag{3.18}$$

From the definition of the covariances and because of stationarity, it holds that: $R_{-i}^T = R_i$. By taking the transpose of previous equation and writing it down for q available time lags i, following set of equations is obtained that can be solved for the backward **AR** coefficients in a least squares sense:

$$\begin{pmatrix} R_p^{\text{ref}} & R_{p-1}^{\text{ref}} & \ldots & R_1^{\text{ref}} \\ R_{p+1}^{\text{ref}} & R_p^{\text{ref}} & \ldots & R_2^{\text{ref}} \\ \ldots & \ldots & \ldots & \ldots \\ R_{p+q-1}^{\text{ref}} & R_{p+q-2}^{\text{ref}} & \ldots & R_q^{\text{ref}} \end{pmatrix} \begin{pmatrix} (\alpha_1^b)^T \\ (\alpha_2^b)^T \\ \ldots \\ (\alpha_p^b)^T \end{pmatrix} = - \begin{pmatrix} R_{p+1}^{\text{ref}} \\ R_{p+2}^{\text{ref}} \\ \ldots \\ R_{p+q}^{\text{ref}} \end{pmatrix} \tag{3.19}$$

The integer q is related to the overdetermination of this system of equations: there are qlr equations for pr^2 unknowns.

Computing the modal parameters

Similarly to the derivations in Section 2.6, it can be shown that the backward **ARMA** model is equivalent to a so-called *backward-innovation state-space model* and that the backward **AR** matrices are related to the state-space matrices as:

$$(G^{\text{ref}})^T (A^T)^p + \sum_{i=1}^{p} \alpha_i^b (G^{\text{ref}})^T (A^T)^{p-i} = 0 \tag{3.20}$$

where $G^{\text{ref}} \in \mathbb{R}^{n\times r}$ has been defined in Equation (3.5). By introducing the eigenvalue decomposition of A, post-multiplying by Ψ^{-T} and defining:

$$G_m^{\text{ref}} = \Psi^{-1} G^{\text{ref}}$$

Equation (3.20) can be rewritten as:

$$(G_m^{\text{ref}})^T \Lambda_d^p + \alpha_1^b (G_m^{\text{ref}})^T \Lambda_d^{p-1} + \ldots + \alpha_p^b (G_m^{\text{ref}})^T = 0 \tag{3.21}$$

This equation reveals that the eigenvalues Λ_d and the *reduced stochastic modal participation matrix* G_m^{ref} can be computed from the eigenvalue decomposition of the companion matrix of the backward **AR** coefficients (see also Section 2.6.2).

The observed mode shapes need to be determined in a second step. The factorization property of the output covariances (3.6) is useful for this purpose:

$$\begin{aligned} R_i^{\text{ref}} &= C \quad A^{i-1} \quad G^{\text{ref}} \\ &= C \Psi \Lambda_d^{i-1} \Psi^{-1} G^{\text{ref}} \\ &= V \ \Lambda_d^{i-1} \ G_m^{\text{ref}} \end{aligned}$$

By writing down this equation for p time lags i, following set of equations is obtained in V:

$$V \Gamma_{p,m}^{\text{ref}} = (R_p^{\text{ref}} \quad R_{p-1}^{\text{ref}} \quad \ldots \quad R_1^{\text{ref}}) \tag{3.22}$$

where $\Gamma_{p,m}^{\text{ref}} \in \mathbb{C}^{n \times pr}$ is the so-called *reversed extended modal stochastic controllability matrix*, defined as:

$$\Gamma_{p,m}^{\text{ref}} = (\Lambda_d^{p-1} G_m^{\text{ref}} \quad \Lambda_d^{p-2} G_m^{\text{ref}} \quad \ldots \quad \Lambda_d G_m^{\text{ref}} \quad G_m^{\text{ref}})$$

This matrix can be constructed from the results of the first step of the method. The right hand side of Equation (3.22) was already estimated from the data in the first step of the method: it is the first row of the Toeplitz matrix in Equation (3.20).

Implementation and stabilization

A typical problem of estimating a parametric model from data is the determination of the model order. A p^{th} order **ARMA** model based on r reference outputs contains pr poles. Consequently, an indication of the model order is given by the "expected" number of poles covered by the data. This expected number can be based on physical insight or counted as

twice[12] the number of peaks in the frequency-plot of a non-parametric spectrum estimate (see also the **PP** method, Subsection 3.3.1). A more accurate model order estimate is provided by the **CMIF**, a frequency-plot of the singular values of a non-parametric spectrum estimate (Subsection 3.3.2).

More formal procedures estimate models of different order and compare these models according to a quality criterion such as Akaike's **F**inal **P**rediction **E**rror (**FPE**) or Rissanen's **M**inimum **D**escription **L**ength (**MDL**) criterion [LJUN99]. These criteria include a penalty for model complexity, avoiding an overfit.

However, in modal analysis one is usually not interested in a good model as such, but rather in the modal parameters extracted from that model. Practical experience with parametric models in modal analysis applications learnt that it is better to over-specify the model order and to eliminate spurious numerical poles afterwards. The famous stabilization diagram (see for instance [HEYL95, ALLE99]) is a great tool to achieve this goal. The poles corresponding to a certain model order are compared to the poles of a one-order-lower model. If the eigenfrequency, the damping ratio and the related mode shape (or modal participation factor) differences are within preset limits, the pole is labelled as a stable one. If we choose, for instance, the following limits: 1% for eigenfrequencies, 5% for damping ratios and 2% for the modal vectors, the stability requirements are:

$$\begin{aligned} 100\% \ \frac{f^{(p)} - f^{(p+1)}}{f^{(p)}} &< 1\% \\ 100\% \ \frac{\xi^{(p)} - \xi^{(p+1)}}{\xi^{(p)}} &< 5\% \\ 100\% \ (1 - \mathbf{MAC}(p, p+1)) &< 2\% \end{aligned} \tag{3.23}$$

where 'p' denotes the model order at which f, ξ and the mode shapes $\{v\}$ are identified[13]. The **M**odal **A**ssurance **C**riterion (**MAC**) is nothing else than the (squared) correlation between two modal vectors:

$$\mathbf{MAC}(p, p+1)) \ = \ \frac{\left| v^{(p)H} v^{(p+1)} \right|^2}{(v^{(p)H} v^{(p)}) \ (v^{(p+1)H} v^{(p+1)})} \tag{3.24}$$

[12] Every spectrum peak corresponds to a pair of complex conjugated poles. Therefore the model order is twice the number of resonance frequencies.

[13] The mode shapes $\{v\}$ are sometimes replaced by (the transpose of) the modal participation factors $\{g\}$.

By definition the **MAC** is a number between 0 and 1. It is often used in modal analysis applications because it is able to characterize the correspondence between mode shapes in one number.

The spurious numerical poles will not stabilize at all during this process and can be sorted out of the modal parameter data set more easily. For an efficient construction of the stabilization diagram, it is important to avoid repetitive computations of common steps when estimating models of different order. For the **IV** method this is trivially achieved by estimating the covariance Toeplitz matrix (3.7) only once. First the maximum number of poles $n_{\max}$ is specified. Depending on the quality of the data $n_{\max}$ should significantly exceed the number of expected poles: a high model order is required to identify poles that are buried in noise. The maximum **ARMA** model order $p_{\max}$ is the nearest integer towards infinity to $n_{\max}/r$. Including the right hand side of (3.19), the **IV** method requires a covariance Toeplitz matrix of maximum $p_{\max}+1$ block columns and q block rows. Comparing the two expressions for the Toeplitz matrix, (3.7) and (3.19), i can be determined as $i = p_{\max}+1$ and q can be chosen equal to $q = i$. By this choice, the overdetermination of (3.19) is ensured. The lower order models (for $p < p_{\max}$) are simply obtained by selecting the last p block columns of the initially constructed covariance Toeplitz matrix and solving (3.19) for the **AR** coefficients.

Relation to other methods

It is known for some time that there exist similar mathematical expressions for impulse responses and output covariances (of a system excited by white noise), see for instance [AKAI74b, BEND93] and Subsection 2.5.2. In modal analysis, this observation is used to feed classical modal parameter estimation methods, that normally work with impulse responses, with output covariances instead. Although derived in a different way, the final equations of the **IV** method correspond to the **P**olyreference **T**ime **D**omain (**PTD**) method after substituting impulse responses by output covariances. The **PTD** method is probably the most widely-used traditional modal parameter estimation method. It contains the (**L**east **S**quares) **C**omplex **E**xponential (**LSCE**) and the **I**brahim **T**ime **D**omain (**ITD**) methods as special cases. For an overview, relations between these traditional (input-output) methods and the original references, see [LEUR84, ALLE94, HEYL95, ALLE99].

The backward reference model (3.18) is the most useful in practice: in a first stage (3.21) the poles Λ_d and the stochastic participation matrix G_m^{ref} are obtained in an efficient way. In a full model (i.e. all outputs are considered as references) the involved matrices are larger. This has a negative effect on the computational efficiency. Also the stabilization diagram makes less sense in case of a full model: every time the model order p is increased by one, there are l additional poles (against only r in case of a reference model). This means that already in a few steps a model is obtained that includes a large number of poles

and that there is not much stability information. In a second stage the full mode shapes are obtained according to Equation (3.22). Note that a forward reference model (similar to (3.17)) isn't too useful: a first stage would yield the mode shapes at the reference locations only $LV \in \mathbb{C}^{r \times n}$ and a second stage the full participation matrix $G_m \in \mathbb{C}^{l \times n}$, whereas one is obviously more interested in the full mode shapes.

Instead of estimating the mode shapes according to Equation (3.22) that re-uses the output covariances, it is common practice to use a frequency-domain fitting procedure [HERM99]. In this case the spectrum matrix is estimated from the data by a non-parametric identification method (see Subsection 3.2.3). Afterwards parametric spectrum models, like (A.6) or (A.8), are fitted to the nonparametric spectrum estimate. Because the poles and covariance matrices G_m^{ref} are known from the first **IV** step, the models (A.6)(A.8) are linear in the mode shapes *V*, and linear least squares can be applied.

Example

The **IV** method is applied to the simulated data of the mast structure (Figure 2.1). Sensor 5 in the *y*-direction and sensor 6 in the *x*-direction are considered as reference sensors. The output covariances $\hat{R}_k^{\text{ref}}$ are estimated for lags $k = 1, 2, ..., 2i-1$ with $i = 40$ (This is a user's choice). They are gathered in a $li \times ri$ $(= 240 \times 80)$ Toeplitz matrix (3.7). A stabilization diagram is constructed by identifying **ARMA** models for orders $p = 1, 2, ..., 30$. Since $r = 2$, these models have $2, 4, ..., 60$ poles. Note that the maximum **ARMA**-model order would be $p_{\max} = i - 1 = 39$. In a first stage, the discrete-time eigenvalues μ_i (diagonal elements of Λ_d) and the output-only modal participation factors $< g_i^{\text{ref}\,T} > \in \mathbb{C}^2$ (rows of G_m^{ref}) are computed from the **AR** coefficients (3.21). The eigenfrequencies and damping ratios are related to the discrete-time eigenvalues as (see Equations (2.16) and (2.45)):

$$\mu_i, \mu_i^* = \exp\left(\left(-\xi_i \omega_i \pm j\sqrt{1-\xi_i^2}\,\omega_i \right) \Delta t \right)$$

The stabilization diagram is shown in Figure 3.9. The two zooms reveal that it is possible to distinguish the two pairs of close modes. Although the trace of the spectrum matrix is not directly related to the **IV** method, it is plotted over the stabilization diagram as a visual aid to select the stable poles.

By selecting one stable pole at each vertical frequency line where stable poles are present, the analyst obtains a set of eigenfrequencies f_i, damping ratios ξ_i and output-only modal participation factors $< g_i^{\text{ref}\,T} >$. From this stable set the full mode shapes can be obtained in a second stage as formulated in (3.22). The detailed modal parameter estimation results are presented at the end of this chapter.

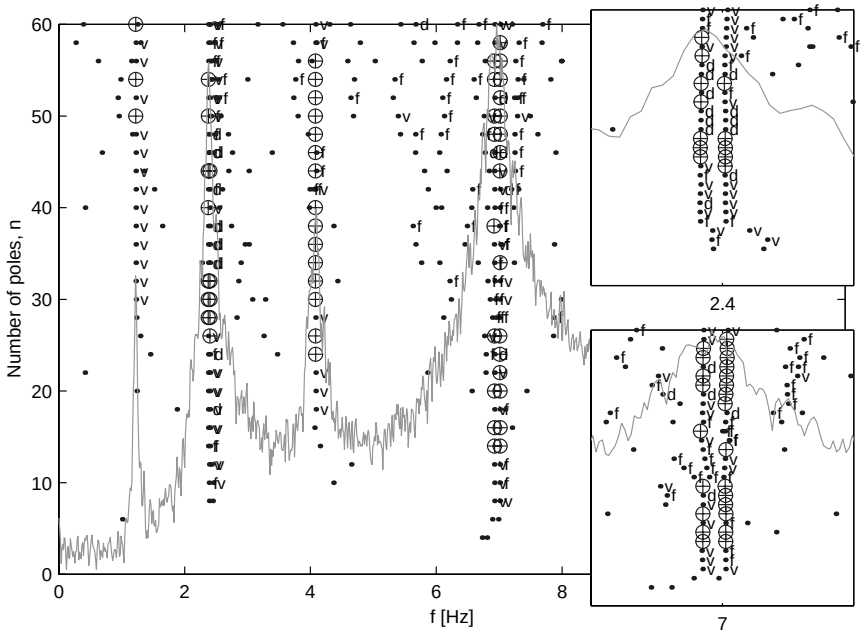

Figure 3.9: Stabilization diagram obtained with the **IV** method. The criteria are 1% for frequencies, 2% for damping ratios and 1% for the participation vector correlations (3.23). The used symbols are: '⊕' for a stable pole; '**.**v' for a pole with stable frequency and vector; '**.**d' for a pole with stable frequency and damping; '**.**f' for a pole with stable frequency and '**.**' for a new pole. The model orders are ranging from 1 to 30. Since the number of references is 2, the number of poles is twice the model order. Two zooms are added that concentrate on the close modes around 2.4 and 7 Hz.

3.4.2 Covariance-driven stochastic subspace identification (SSI-COV)

Like the **CMIF** method can be considered as an **SVD**-enhanced **PP** method, covariance-driven subspace can — somewhat disrespectful — be considered as an **SVD**-enhanced instrumental-variable method. While in the **IV** method, the factorization property of the output covariances (2.56), (3.6) was only used in a second stage to obtain the mode shapes, it is really the basis of the subspace method. The **COV**ariance-driven **S**tochastic **S**ubspace **I**dentification method (**SSI-COV**) is addressing the so-called *stochastic realization problem*, i.e. the problem of identifying a stochastic state-space model from output-only data.

Stochastic realization is closely related to deterministic (input-output) realization, that goes back to Ho and Kalman [HOKA66] and was extended with the **SVD** to treat noisy data in [ZEIG74] and [KUNG78]. The so-called **E**igensystem **R**ealization **A**lgorithm (**ERA**), developed by Juang [JUAN85, JUAN94], is a modal analysis application of these

deterministic realization algorithms. The stochastic (output-only) realization problem is solved in [AKAI74b, AOKI87, ARUN90]. Application of stochastic realization to modal parameter estimation was reported by Benveniste and Fuchs [BENV85]. They also proved that their algorithm is robust against non-stationary inputs (e.g. a white noise sequence with time-varying covariance).

The **SSI-COV** method identifies a stochastic state-space model from output-only data. The stochastic state-space model, introduced in Subsection 2.5.1, has the following form:

$$\begin{aligned} x_{k+1} &= Ax_k + w_k \\ y_k &= Cx_k + v_k \end{aligned} \tag{3.25}$$

where w_k and v_k are vector signals assumed to be zero mean, white and with covariance matrices:

$$\mathbf{E}\left[\begin{pmatrix} w_p \\ v_p \end{pmatrix} \begin{pmatrix} w_q^T & v_q^T \end{pmatrix}\right] = \begin{pmatrix} Q & S \\ S^T & R \end{pmatrix} \delta_{pq} \tag{3.26}$$

Stochastic realization theory

In this section a modified version of the classical covariance-driven stochastic realization algorithm is presented. The modification consists of reformulating the algorithm so that it only needs the covariances between the outputs and a limited set of reference outputs instead of the covariances between all outputs. This corresponds to classical modal analysis, where the impulse response matrices h_k are rectangular matrices having l rows (i.e. the number of outputs) and m columns (i.e. the number of inputs). In output-only cases, the impulse responses are substituted by output covariances and the inputs by the reference outputs (see also [JAME95, HERM99]). As in the **IV** method, the output covariances are gathered in a block Toeplitz matrix $T_{1|i}^{\text{ref}}$ (3.7). Applying the factorization property (3.6) to $T_{1|i}^{\text{ref}}$ yields:

$$T_{1|i}^{\text{ref}} = \begin{pmatrix} R_i^{\text{ref}} & R_{i-1}^{\text{ref}} & \dots & R_1^{\text{ref}} \\ R_{i+1}^{\text{ref}} & R_i^{\text{ref}} & \dots & R_2^{\text{ref}} \\ \dots & \dots & \dots & \dots \\ R_{2i-1}^{\text{ref}} & R_{2i-2}^{\text{ref}} & \dots & R_i^{\text{ref}} \end{pmatrix} = \begin{pmatrix} C \\ CA \\ \dots \\ CA^{i-1} \end{pmatrix} \underbrace{\begin{pmatrix} A^{i-1}G^{\text{ref}} & \dots & AG^{\text{ref}} & G^{\text{ref}} \end{pmatrix}}_{n} = O_i \, \Gamma_i^{\text{ref}} \tag{3.27}$$

where the definitions of the *extended observability matrix* $O_i \in \mathbb{R}^{li \times n}$ and the *reversed extended stochastic controllability matrix* $\Gamma_i^{\text{ref}} \in \mathbb{R}^{n \times ri}$ are obvious from (3.27). For $ri \geq n$, and if the system is observable and controllable, the rank of the $li \times ri$ Toeplitz matrix equals n, since it is the product of a matrix with n columns and a matrix with n rows. The **SVD** is a numerically reliable tool to estimate the rank of a matrix. The application of the **SVD** to the block Toeplitz matrix yields:

$$T_{1|i}^{\text{ref}} = USV^T = \begin{pmatrix} U_1 & U_2 \end{pmatrix} \begin{pmatrix} S_1 & 0 \\ 0 & 0 \end{pmatrix} \begin{pmatrix} V_1^T \\ V_2^T \end{pmatrix} = U_1 S_1 V_1^T \tag{3.28}$$

where $U \in \mathbb{R}^{li \times li}$ and $V \in \mathbb{R}^{ri \times ri}$ are orthonormal matrices ($U^T U = UU^T = I_{li}$ and $V^T V = VV^T = I_{ri}$) and $S \in (\mathbb{R}^+)^{li \times ri}$ is a diagonal matrix containing the positive singular values in descending order. The rank of a matrix is found as the number of non-zero singular values. In the last equality of (3.28), the zero singular values and corresponding singular vectors are omitted: $U_1 \in \mathbb{R}^{li \times n}$, $S_1 \in (\mathbb{R}_0^+)^{n \times n}$, $V_1 \in \mathbb{R}^{ri \times n}$. By comparing (3.27) to (3.28), the matrices O_i and Γ_i^{ref} can be computed by splitting the **SVD** in two parts:

$$\begin{aligned} O_i &= U_1 S_1^{1/2} T \\ \Gamma_i^{\text{ref}} &= T^{-1} S_1^{1/2} V_1^T \end{aligned} \tag{3.29}$$

where $T \in \mathbb{C}^{n \times n}$ is a non-singular matrix. It is easy to see that this matrix T can be considered as a similarity transformation that is applied to the identified state-space model; see also Equation (2.26). In other words, whatever the choice of T may be, similarity-equivalent state-space models will result and we can simply set: $T = I$. The solution of the identification problem is now straightforward. From the definitions of the extended

observability matrix O_i and the reversed extended stochastic controllability matrix Γ_i^{ref} (3.27), we know that C equals the first l rows of O_i and G^{ref} equals the last r columns of Γ_i^{ref}; or written in MATLAB notation:

$$\begin{aligned} C &= O_i(1{:}l,:) \\ G^{\text{ref}} &= \Gamma_i^{\text{ref}}(:, r(i-1)+1{:}ri) \end{aligned} \tag{3.30}$$

A first possible way [ZEIG74] to compute the state transition matrix A follows from the decomposition property of a shifted block Toeplitz matrix:

$$T_{2|i+1}^{\text{ref}} = O_i \; A \; \Gamma_i^{\text{ref}} \tag{3.31}$$

where the shifted matrix $T_{2|i+1}^{\text{ref}}$ has a similar structure as $T_{1|i}^{\text{ref}}$ (3.7), but is composed of covariances R_k^{ref} from lag 2 to $2i$. Matrix A is found by introducing (3.29) in (3.31) and solving for A:

$$A = O_i^{\dagger} \; T_{2|i+1}^{\text{ref}} \; (\Gamma_i^{\text{ref}})^{\dagger} = S_1^{-1/2} \; U_1^T \; T_{2|i+1}^{\text{ref}} \; V_1 \; S_1^{-1/2} \tag{3.32}$$

where $(\bullet)^{\dagger}$ denotes the Moore-Penrose pseudo-inverse of a matrix.

Alternatively [KUNG78], matrix A could also be computed by exploiting the shift structure of the extended observability matrix O_i:

$$A = O_i(1{:}l(i-1),:)^{\dagger} \; O_i(l+1{:}li,:) \tag{3.33}$$

An equivalent least-squares expression could be derived that makes use of the reversed extended stochastic controllability matrix instead. However, since $r < l$, there is less over-determination in this case.

At this point the identification problem is theoretically solved: the system order n is found as the number of non-zero singular values in (3.28) and the system matrices $A, G^{\text{ref}}, C, R_0^{\text{ref}}$ can be computed as in Equations (3.30) and (3.32) or (3.33). The fourth system matrix R_0^{ref} (see discussion in Subsection 2.5.2) is simply the zero-lag output covariance matrix. The two matrices A, C are sufficient to compute the modal parameters. As discussed in Subsection 2.4.2, the discrete poles Λ_d and the observed mode shapes V are computed as (see also (2.45), (2.46)):

$$\begin{aligned} A &= \Psi \Lambda_d \Psi^{-1} \\ V &= C\Psi \end{aligned} \tag{3.34}$$

Implementation and stabilization

In reality the number of measurements is not infinite and the output covariances have to be estimated $\hat{R}_i^{\text{ref}}$ (3.8). Since these output covariances form the basis of the realization method (3.27), it is evident that the identified system matrices also have to be considered as estimates: $\hat{A}, \hat{G}^{\text{ref}}, \hat{C}, \hat{R}_0^{\text{ref}}$.

Another remark is that in theory the system order *n* can be determined by inspecting the number of non-zero singular values of $T_{1|i}^{\text{ref}}$ (3.28). In practice however, the estimated covariance Toeplitz matrix $\hat{T}_{1|i}^{\text{ref}}$ is affected by "noise" leading to singular values that are all different from zero. As typical noise sources we have:

- Modelling inaccuracies. It is possible that the true system that generated the data cannot be modelled exactly as a stochastic state-space model. An attempt to model this system by a state-space model introduces an error in these cases.

- Measurement noise: introduced by the sensors and the electronics of the measurement hardware.

- Computational noise due to the finite precision of any computer.

- The finite number of data. The covariances have to be estimated, so that the factorization property (3.6) does not hold exactly. As a consequence the rank of the covariance Toeplitz matrix will not be exactly *n*; see Equation (3.27).

In practice, the order can be determined by looking at a "gap" between two successive singular values. The singular value where the maximal gap occurs yields the model order. This criterion should however not be applied too dogmatically. For large, real structures there is generally no clear gap.

To obtain a good model for modal analysis applications, it is probably a better idea to construct a stabilization diagram, by identifying a whole set of models with different order. The stabilization diagram was already introduced in Subsection 3.4.1 and Equation (3.23). In case of the **SSI-COV** method, an efficient construction of the stabilization diagram is achieved by computing the **SVD** of the covariance Toeplitz matrix (3.28) only once. The number of block rows and columns *i* of $T_{1|i}^{\text{ref}}$ should be such that $ri \geq n_{\max}$, the maximum model order (see also the discussion on page 70, Subsection 3.4.1). Models of different order are then obtained by including a different number of singular values and vectors in the computation of O_i and Γ_i^{ref} (3.29), from which the system matrices and the modal parameters are deduced as described in previous subsection.

Example

The **SSI-COV** method is applied to the simulated data of the mast structure (Figure 2.1). The same 240×80 covariance Toeplitz matrix as in the **IV** example is formed (see Page 72). The key step of **SSI-COV** is the **SVD** of this Toeplitz matrix (3.28). The singular values are plotted on a log scale in Figure 3.10.

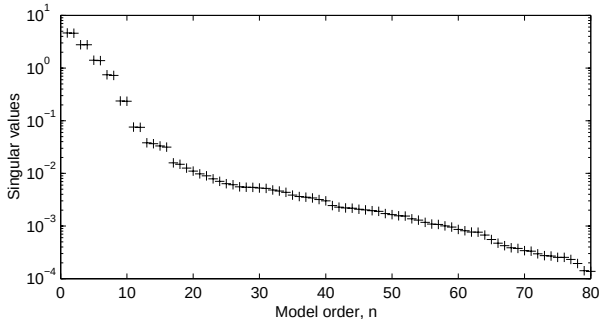

Figure 3.10: Singular values of the covariance Toeplitz matrix. The true model order is 12, but it seems that 16 singular values are significant. By lowpass filtering the data (see Page 55), additional poles were introduced.

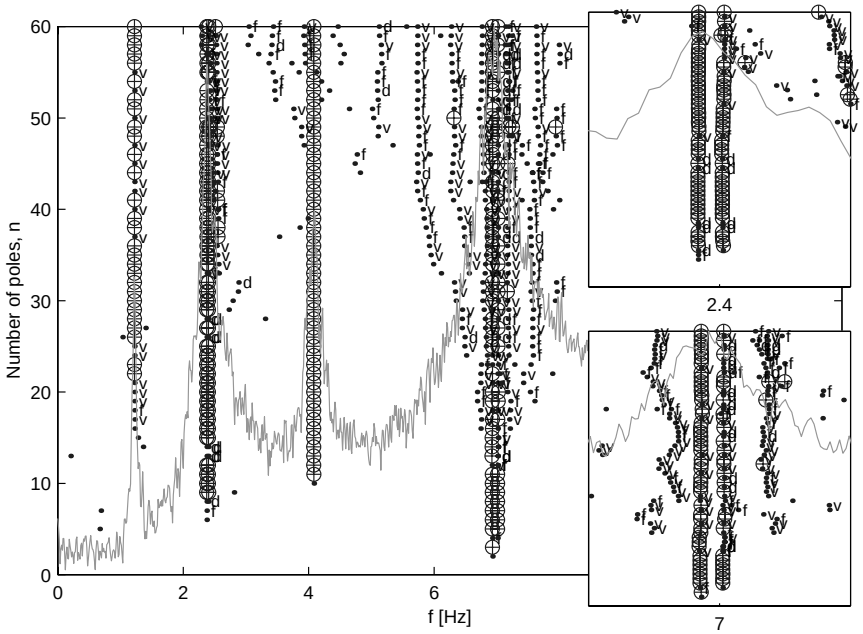

Figure 3.11: Stabilization diagram obtained with the **SSI-COV** method. The criteria are 1% for frequencies, 2% for damping ratios and 1% for the mode shape correlations (3.23). The used symbols are: '⊕' for a stable pole; '**.**v' for a pole with stable frequency and vector; '**.**d' for a pole with stable frequency and damping; '**.**f' for a pole with stable frequency and '**.**' for a new pole. The model orders are ranging from 2 to 60. Two zooms are added that concentrate on the close modes around 2.4 and 7 Hz.

A stabilization diagram is constructed by identifying state-space models for orders $n = 2, 3, ..., 60$. The modal parameters are computed from the identified model matrices A and C, according to Equation (3.34). The stabilization diagram is shown in Figure 3.11. The two zooms reveal that it is possible to distinguish the two pairs of close modes. Although the trace of the spectrum matrix is not directly related to the **SSI-COV** method, it is plotted over the stabilization diagram as a visual aid to select the stable poles. The detailed modal parameter estimation results are presented at the end of this chapter.

3.4.3 Other covariance-driven methods

The random decrement technique

The **R**andom **D**ecrement technique (**RD**) was introduced by Cole [COLE68] and evolved to an output-only modal analysis technique [IBRA77, ASMU97, IBRA98]. The **RD** technique converts random responses due to unknown or unmeasured stationary random input to free decays. In [ASMU97] it is shown that so-called **RD** functions are closely related to output covariance functions. That is the reason to classify the **RD** technique as a covariance-driven method in this thesis (although **RD** functions are not exactly the same as covariances). It must be added that the **RD** technique is not a "new" system identification method, but since the **RD** functions can be considered as free decays and are related to covariances, all covariance-driven methods can be applied to **RD** functions as well.

Recent developments

Recently, it is shown how the problem of **MA** parameter estimation from covariances can be formulated as a semidefinite program [STOI00]. The proposed algorithm is computationally fast, statistically accurate, and reliable. In [MARI00], these ideas are extended and combined with subspace-based techniques to solve multivariate **ARMA** parameter estimation problems. Their solution method does not suffer from stability and positive realness problems that other subspace methods may experience when applied to specially designed simulated data [DAHL98]. It is beyond the scope of this thesis to go into further detail; the interested reader is referred to the cited references.

3.5 TIME-DOMAIN DATA-DRIVEN METHODS

The main advantage of data-driven algorithms is that they do not require any further preprocessing in order to obtain spectra or covariances. These methods identify models directly from the time signals. A first method is the data-driven subspace method, that is closely related to the covariance-driven subspace method of Subsection 3.4.2. Afterwards the classical *prediction error method* that identifies **AR**(**MA**) models from time data is briefly reviewed.

3.5.1 Data-driven stochastic subspace identification (SSI-DATA)

Recently a lot of research effort in the system identification community was spent to subspace identification as evidenced by the book of Van Overschee and De Moor [VANO96] and the second edition of Ljung's book [LJUN99]. Subspace methods identify state-space models from (input and) output data by applying robust numerical techniques such as *QR* factorization, **SVD** and least squares. As opposed to **SSI-COV**, the **DATA**-driven **S**tochastic **S**ubspace **I**dentification method (**SSI-DATA**) avoid the computation of covariances between the outputs. It is replaced by projecting the row space of future outputs into the row space of past outputs. In fact, the notions covariances and projections are closely related. They both are aimed to cancel out the (uncorrelated) noise. The first **SSI-DATA** algorithms can be found in [VANO91, VANO93]. A general overview of data-driven subspace identification (both deterministic and stochastic) is provided in the book of Van Overschee and De Moor [VANO96]. Although somewhat more involved as compared to previous methods, it is also possible with **SSI-DATA** to reduce the dimensions of the matrices by introducing the idea of the reference sensors. This is demonstrated in [PEET99f, PEET99d] and also in this subsection.

The derivation of **SSI-DATA** is given for the reference-sensor case. The original algorithm is simply recovered by considering all sensors as references. First, the Kalman filter states will be introduced because of their importance in subspace identification. Next, the principles of **SSI-DATA** are explained. And finally, the implementation of the projection in terms of the *QR* factorization is discussed.

As the **SSI-COV** method, the **SSI-DATA** method identifies a stochastic state-space model (3.25), (3.26) from output-only data.

Kalman filter states

The Kalman filter plays an important role in **SSI-DATA**. In Subsection 2.5.3, it was indicated how the forward innovation model (2.58) can be obtained by applying the steady-

state Kalman filter to the stochastic state-space model (2.51). In this section, the *non-steady-state Kalman filter* is introduced. The Kalman filter is described in many books. A nice derivation can be found in Appendix B of [JUAN94]. The aim of the Kalman filter is to produce an optimal prediction for the state vector x_k by making use of observations of the outputs up to time $k-1$ and the available system matrices together with the known noise covariances. These optimal predictions are denoted by a hat: $\hat{x}_{k+1}$. When the initial state estimate $\hat{x}_0 = 0$, the initial covariance of the state estimate $P_0 = \mathbf{E}[\hat{x}_0 \hat{x}_0^T] = 0$ and the output measurements $y_0, ..., y_{k-1}$ are given, the non-steady-state Kalman filter state estimates $\hat{x}_k$ are obtained by the following recursive formulas:

$$\begin{aligned} \hat{x}_k &= A\hat{x}_{k-1} + K_{k-1}(y_{k-1} - C\hat{x}_{k-1}) \\ K_{k-1} &= (G - AP_{k-1}C^T)(R_0 - CP_{k-1}C^T)^{-1} \\ P_k &= AP_{k-1}A^T + (G - AP_{k-1}C^T)(R_0 - CP_{k-1}C^T)^{-1}(G - AP_{k-1}C^T)^T \end{aligned} \tag{3.35}$$

expressing the Kalman state estimate, the Kalman filter gain matrix and the Kalman state covariance matrix. The Kalman filter state sequence $\hat{X}_i \in \mathbb{R}^{n \times N}$ is defined as:

$$\hat{X}_i = (\hat{x}_i \;\; \hat{x}_{i+1} \;\; \dots \;\; \hat{x}_{i+N-1}) \tag{3.36}$$

The correct interpretation of the $(q+1)^{\text{th}}$ column of this matrix is that this state $\hat{x}_{i+q}$ is estimated according to Equation (3.35) by using only *i* previous outputs: $y_q, ..., y_{i+q-1}$. By consequence, two consecutive elements of $\hat{X}_i$ cannot be considered as consecutive iterations of (3.35). More details can be found in [VANO96]. Important to note is that a closed-form expression exists for this Kalman filter state sequence and that it is this sequence that will be recovered by the **SSI-DATA** algorithm (see further).

Data-driven stochastic subspace identification theory

The **SSI-DATA** algorithm starts by projecting the row space of the future outputs into the row space of the past reference sensors. The idea behind this projection is that it retains all the information in the past that is useful to predict the future. The notation and definition of this projection is:

$$\mathcal{P}_i^{\text{ref}} = Y_f \,/\, Y_p^{\text{ref}} = Y_f (Y_p^{\text{ref}})^T \, (Y_p^{\text{ref}} (Y_p^{\text{ref}})^T)^{\dagger} \, Y_p^{\text{ref}} \tag{3.37}$$

The matrices $Y_f \in \mathbb{R}^{li \times N}$ and $Y_p^{\text{ref}} \in \mathbb{R}^{ri \times N}$ are partitions of the data Hankel matrix $H^{\text{ref}} \in \mathbb{R}^{(r+l)i \times N}$, as indicated in Equation (3.2). From the definition (3.37), it is clear that projections and covariances are closely related. Indeed the matrix products $Y_f (Y_p^{\text{ref}})^T$ and $Y_p^{\text{ref}} (Y_p^{\text{ref}})^T$ are in fact block Toeplitz matrices containing covariances between (reference) outputs; see also Equation (3.7). Note that expression (3.37) is only the definition of $\mathcal{P}_i^{\text{ref}}$; it does not

indicate how the projection is computed. As we will see further, it is computed by the numerically robust *QR* factorization.

The main theorem of stochastic subspace identification [VANO96] states that the projection $\mathcal{P}_i^{\text{ref}}$ can be factorized as the product of the extended observability matrix O_i (3.27) and the Kalman filter state sequence $\hat{X}_i$ (3.36):

$$\mathcal{P}_i^{\text{ref}} = O_i \hat{X}_i = \begin{pmatrix} C \\ CA \\ \dots \\ CA^{i-1} \end{pmatrix} (\hat{x}_i \;\; \hat{x}_{i+1} \;\; \dots \;\; \hat{x}_{i+N-1}) \;\; \updownarrow \;\; n \qquad (3.38)$$

$$\leftrightarrow$$

$$n$$

The prove of this theorem for the case where all outputs are considered as references ($Y_p^{\text{ref}} \rightarrow Y_p$) can be found in [VANO96]. In the present case, where only the past reference outputs have been used, the proof is almost the same, except for the significance of the obtained Kalman filter state sequence $\hat{X}_i$. The non-steady-state Kalman filter is applied to a reduced state-space model that includes only the reference outputs. Following substitutions have to be made in Equation (3.35):

$$\begin{aligned} y_k &\rightarrow y_k^{\text{ref}} = L y_k \\ G &\rightarrow G L^T \\ C &\rightarrow L C \\ R_0 &\rightarrow L R_0 L^T \end{aligned}$$

At first sight, the choice of the reference sensors seems to be unimportant: for all choices the factorization (3.38) is found. Indeed, theoretically the internal state of a system does not depend on the choice and number of observed outputs. However in identification problems where the states are estimated based on observations, the choice and number of outputs does matter: different reference outputs will lead to different Kalman filter state estimates $\hat{X}_i$.

Since the projection matrix is the product of a matrix with *n* columns and a matrix with *n* rows (3.38), its rank equals *n* (if $li \geq n$). The **SVD** is a numerically reliable tool to estimate the rank of a matrix. After omitting the zero singular values and corresponding singular vectors, the application of the **SVD** to the projection matrix yields:

$$\mathcal{P}_i^{\text{ref}} = U_1 S_1 V_1^T \qquad (3.39)$$

where $U_1 \in \mathbb{R}^{li \times n}$, $S_1 \in (\mathbb{R}_0^+)^{n \times n}$ and $V_1 \in \mathbb{R}^{N \times n}$. The extended observability matrix and the Kalman filter state sequence are obtained by splitting the **SVD** in two parts:

$$\begin{aligned} O_i &= U_1 S_1^{1/2} T \\ \hat{X}_i &= O_i^{\dagger} \mathcal{P}_i^{\text{ref}} \end{aligned} \tag{3.40}$$

In the following, we will set the similarity transformation matrix $T = I$; see also the discussion after Equation (3.29).

Up to now we found the order of the system *n* (as the number of non-zero singular values in Equation (3.39)), the observability matrix O_i and the state sequence $\hat{X}_i$. However, the identification problem is to recover the system matrices A, G, C, R_0. If the separation between past reference and future outputs in the Hankel matrix is shifted one block row down, as indicated in Equation (3.3), another projection can be defined:

$$\mathcal{P}_{i-1}^{\text{ref}} = Y_f^- \Big/ Y_p^{\text{ref}\,+} = O_{i-1} \hat{X}_{i+1}$$

where the proof of the second equality is similar to proof of the main subspace theorem (3.38). The extended observability matrix O_{i-1} is simply obtained after deleting the last *l* rows of O_i:

$$O_{i-1} = O_i(1{:}l(i-1), :)$$

The state sequence $\hat{X}_{i+1}$ can now be computed as:

$$\hat{X}_{i+1} = O_{i-1}^{\dagger} \mathcal{P}_{i-1}^{\text{ref}}$$

At this moment the Kalman state sequences $\hat{X}_i$, $\hat{X}_{i+1}$ are calculated using only the output data. The system matrices can now be recovered from following overdetermined set of linear equations, obtained by stacking the state-space models for time instants *i* to $i + N - 1$:

$$\begin{pmatrix} \hat{X}_{i+1} \\ Y_{i|i} \end{pmatrix} = \begin{pmatrix} A \\ C \end{pmatrix} \hat{X}_i + \begin{pmatrix} W_i \\ V_i \end{pmatrix}$$

where $Y_{i|i} \in \mathbb{R}^{l \times N}$ is a Hankel matrix with only one block row (3.2) and $W_i \in \mathbb{R}^{n \times N}$, $V_i \in \mathbb{R}^{l \times N}$ are the residuals. Since the Kalman state sequences and the outputs are known and the residuals are uncorrelated with $\hat{X}_i$, the set of equations can be solved for *A*, *C* in a least square sense:

$$\begin{pmatrix} A \\ C \end{pmatrix} = \begin{pmatrix} \hat{X}_{i+1} \\ Y_{i|i} \end{pmatrix} \hat{X}_i^{\dagger} \tag{3.41}$$

The noise covariances Q, R and S are recovered as the covariances of the least-squares residuals:

$$\begin{pmatrix} Q & S \\ S^T & R \end{pmatrix} = \begin{pmatrix} W_i \\ V_i \end{pmatrix} (W_i^T \quad V_i^T) \tag{3.42}$$

From the properties of stochastic systems (Subsection 2.5.2), it is easy to see how the matrices A, C, Q, R, S can be transformed to A, G, C, R_0. First the Lyapunov equation is solved for Σ:

$$\Sigma = A\Sigma A^T + Q$$

after which G and R_0 can be computed as:

$$\begin{aligned} R_0 &= C\Sigma C^T + R \\ G &= A\Sigma C^T + S \end{aligned} \tag{3.43}$$

At this point the identification problem is theoretically solved: based on the outputs, the system order n and the system matrices A, G, C, R_0 are found.

The matrices A, C are sufficient to compute the modal parameters. As discussed in Subsection 2.4.2, the discrete poles Λ_d and the observed mode shapes V are computed as (see also (2.45), (2.46)):

$$\begin{aligned} A &= \Psi \Lambda_d \Psi^{-1} \\ V &= C\Psi \end{aligned}$$

Positive realness

The computation of Q, R, S according to (3.42) only leads to asymptotically[14] unbiased estimates if the number of block rows in the Hankel matrices goes to infinity: $i \to \infty$. So in practice, since $i \neq \infty$, a bias will be introduced on Q, R, S (and thus also on G, R_0)[15].

---

[14] Asymptotic means that the number of data (theoretically) goes to infinity: $N \to \infty$.

[15] The modal parameters are only determined from A, C and are by consequence not suffering from this bias on G, R_0.

Other algorithms exist that compute asymptotically unbiased estimates. Unfortunately these algorithms do not guarantee the positive realness of the identified covariance sequence. More details on positive realness can be found in [VANO96]. Important for the following of this thesis is that only positive real sequences have a corresponding spectrum matrix that is positive definite for all frequencies ω. If a matrix is positive definite, then all its diagonal entries are positive [GOLU89]. In Subsection 3.7.1, we will encounter an example of an identified power spectrum that becomes negative at certain frequencies (which has of course no physical meaning). A power spectrum is a diagonal entry of the spectrum matrix and therefore this matrix cannot be positive definite. The model was indeed identified with the **SSI-COV** method, a method that does not guarantee the positive-realness of the identified covariance sequence.

Also important is that only positive real sequences can be converted to a forward innovation state-space model. Such a model is sometimes useful, as we will see further. The conversion starts by solving the Riccati equation for P (see also Subsection 2.5.3):

$$P = APA^T + (G - APC^T)(R_0 - CPC^T)^{-1}(G - APC^T)^T$$

The covariance matrix of the innovations is computed as:

$$R_e = R_0 - CPC^T$$

And finally the Kalman gain is obtained as:

$$K = (G - APC^T)R_e^{-1}$$

Although, we never encountered practical positive realness problems when applying the **SSI-DATA** method to our numerous examples, it is shown in [DAHL98] that the problem is theoretically not solved by the outlined **SSI-DATA** algorithm. More discussions on the topic can be found in [MARI00]; see also Subsection 3.4.3.

Implementation

Really crucial in the successful implementation of data-driven subspace algorithms in general is the *RQ* factorization of data Hankel matrices. Such a factorisation applied to the output Hankel matrix of Equation (3.2), (3.3) reads:

$$H^{\text{ref}} = \begin{pmatrix} Y_p^{\text{ref}} \\ \hline Y_f \end{pmatrix} = \begin{pmatrix} Y_p^{\text{ref}+} \\ \hline Y_{i|i}^{\sim\text{ref}} \\ \hline Y_f^- \end{pmatrix} = RQ^T \tag{3.44}$$

where $Q \in \mathbb{R}^{N \times N}$ is an orthonormal matrix: $Q^T Q = Q Q^T = I_N$ and $R \in \mathbb{R}^{(r+l)i \times N}$ is a lower triangular matrix. Since $(r+l)i < N$, it is possible to omit the zeros in R and the corresponding rows in Q^T:

$$H^{\text{ref}} = \begin{array}{c} \\ ri \\ r \\ l-r \\ l(i-1) \end{array} \begin{array}{c} \begin{array}{cccc} ri & r & l-r & l(i-1) \end{array} \\ \begin{pmatrix} R_{11} & 0 & 0 & 0 \\ R_{21} & R_{22} & 0 & 0 \\ R_{31} & R_{32} & R_{33} & 0 \\ R_{41} & R_{42} & R_{43} & R_{44} \end{pmatrix} \end{array} \begin{array}{c} N \to \infty \\ \begin{pmatrix} Q_1^T \\ Q_2^T \\ Q_3^T \\ Q_4^T \end{pmatrix} \end{array} \begin{array}{l} \\ ri \\ r \\ l-r \\ l(i-1) \end{array}$$

The division in block rows and columns is made such that the submatrices in (3.44) can all be expressed in terms of the R and Q submatrices. It is easy to show that the RQ factorization yields following very simple expressions for the projections of future row spaces into past row spaces:

$$\mathcal{P}_i^{\text{ref}} = \begin{pmatrix} R_{21} \\ R_{31} \\ R_{41} \end{pmatrix} Q_1^T, \quad \mathcal{P}_{i-1}^{\text{ref}} = \begin{pmatrix} R_{41} & R_{42} \end{pmatrix} \begin{pmatrix} Q_1^T \\ Q_2^T \end{pmatrix}$$

Also $Y_{i|i} \in \mathbb{R}^{l \times N}$, the output sequence that is present in the least-squares equations in A, C (3.41) is easily written in terms of the RQ factors:

$$Y_{i|i} = \begin{pmatrix} R_{21} & R_{22} & 0 \\ R_{31} & R_{32} & R_{33} \end{pmatrix} \begin{pmatrix} Q_1^T \\ Q_2^T \\ Q_3^T \end{pmatrix}$$

Since $\hat{X}_i = O_i^{\dagger} \mathcal{P}_i^{\text{ref}}$ and $\hat{X}_{i+1} = O_{i-1}^{\dagger} \mathcal{P}_{i-1}^{\text{ref}}$, all right-hand-side quantities of the least-squares Equation (3.41) can be expressed in terms of the RQ factors. Because of their orthonormality, the Q factors cancel out in this equation. So in this first step (3.44) the Q matrix should not be calculated. The MATLAB function `qr` [MATL96], for instance, allows for the computation of the R factor only. Since typically $(r+l)i \ll j$, an important data reduction is obtained by replacing the $(r+l)i \times N$ data Hankel matrix H^{ref} by its R factor of dimension $(r+l)i \times (r+l)i$.

The computation of this *R* factor is the most demanding step of the **SSI-DATA** algorithm. The number of flops *fl* is proportional to the number of columns and to the square of the number of rows of the data Hankel matrix:

$$fl = ((r+l)i)^2 N$$

Assuming the same number of block rows *i* and the same number of data points *N*, the gain in computational efficiency by introducing the reference sensors (subindex 'ref') as opposed to using all sensors as references (subindex 'all') can be expressed as:

$$\frac{fl_{\text{all}}}{fl_{\text{ref}}} = \left(\frac{2l}{r+l} \right)^2 \tag{3.45}$$

which is significant in modal analysis where often many sensors *l* are used and only few of them need to be considered as references *r*.

Evidently, due to the finite data length, the identified state-space model is only an estimate of the true underlying state-space model that generated the data. This is denoted as $\hat{A}, \hat{G}, \hat{C}, \hat{R}_0$ for a covariance model and as $\hat{A}, \hat{K}, \hat{C}, \hat{R}_e$ for a forward innovation model. The matrices $\hat{A}, \hat{C}$ are asymptotically unbiased estimates, but as stated before, a small bias was introduced on the estimates of the other matrices.

The same remark as in the **SSI-COV** method concerning the determination of the model order *n* applies here. Due to noise (modelling inaccuracies, measurement noise and computational noise) none of the singular values in Equation (3.39) are exactly zero and the order can only be determined by looking at a "gap" between two successive singular values. The singular value where the maximal gap occurs yields the model order. However in many practical cases, no gap is visible. As previously, the problem of order determination is better solved by constructing a stabilization diagram (3.23). The number of block rows *i* of H^{ref} should be such that $ri \geq n_{\max}$, the maximum model order. Models of different order are then obtained by including a different number of singular values and vectors in the computation of O_i and $\hat{X}_i$ (3.40), from which the system matrices and the modal parameters are deduced as described previously.

Example

The **SSI-DATA** method is applied to the simulated data of the mast structure (Figure 2.1). The first step of **SSI-DATA** is the computation of the *R*-factor of a $(r+l)i \times N$ ($=320 \times 16305$) data Hankel matrix (3.44). Next the **SVD** of this *R*-factor is computed (3.39). Several variants of stochastic subspace identification exist (Section 3.6). They differ in the weighting of the *R*-factor before application of the **SVD**. One of these variants is so-called **C**anonical **V**ariate **A**nalysis (**CVA**), in which the singular values can be interpreted as the cosines of the principal angles between two subspaces: the row space of the future outputs Y_f and the row space of the past (reference) outputs Y_p^{ref}. These principal angles are plotted in Figure 3.13.

A stabilization diagram is constructed by identifying state-space models for orders $n = 2, 3, ..., 60$. The modal parameters are computed from the identified model matrices *A* and *C*, according to Equation (3.34). The stabilization diagram is shown in Figure 3.12. The two zooms reveal that it is possible to distinguish the two pairs of close modes. Although the trace of the spectrum matrix is not directly related to the **SSI-DATA** method, it is plotted over the stabilization diagram as a visual aid to select the stable poles. The detailed modal parameter estimation results are presented at the end of this chapter.

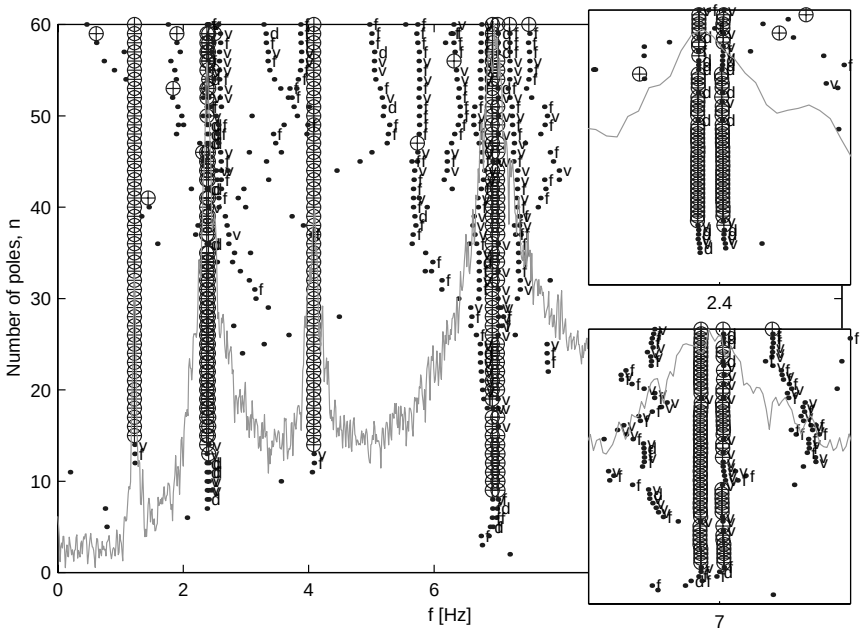

Figure 3.12: Stabilization diagram obtained with the **CVA** variant of the **SSI-DATA** method. The criteria are 1% for frequencies, 2% for damping ratios and 1% for the mode shape correlations (3.23). The used symbols are: '⊕' for a stable pole; '**.**v' for a pole with stable frequency and vector; '**.**d' for a pole with stable frequency and damping; '**.**f' for a pole with stable frequency and '**.**' for a new pole. The model orders are ranging from 2 to 60. Two zooms are added that concentrate on the close modes around 2.4 and 7 Hz.

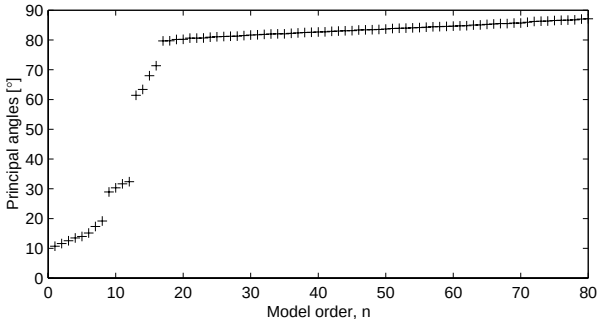

Figure 3.13: Principal angles between the row space of future outputs and the row space of past reference outputs. The true model order is 12, but it seems that 16 principal angles are significantly different from 90°. By lowpass filtering the data (see Page 55), additional poles were introduced.

3.5.2 Other data-driven methods

The prediction error method applied to an **ARMA** *model*

Prediction **E**rror **M**ethods (**PEM**) can be considered as a general system identification framework [LJUN99]. These methods identify the parameters of a model by minimizing the so-called prediction errors[16]. The straightforward application of **PEM** to estimate an **ARMA** model (2.59) from data results in a highly nonlinear optimization problem with related problems as: convergence not being guaranteed, local minima, sensitivity to initial values and a high computational load. Despite these drawbacks, the **PEM** has been applied to identify the modal parameters of civil engineering structures, see for instance [PIOM93, ANDE97]. However, in contrast to nonlinear frequency-domain methods (see Subsection 3.3.3), nonlinear time-domain methods (such as **PEM** applied to an **ARMA** model) never reached an acceptable level of robustness for civil engineering modal analysis applications [PEET99a]. Apparently the **PEM** works on simulated examples or single-output cases, but suffers from divergence or an unreasonable computation time in case of a large number (10 or more) of sometimes noisy outputs.

The prediction error method applied to an **AR** *model*

The non-linearity of the **PEM** is caused by the **MA** part of the **ARMA** model. By omitting the moving-average part, an auto-regressive model is obtained:

[16] Prediction errors are the part of the output data that cannot be predicted from past data.

$$y_k + \alpha_1 y_{k-1} + \ldots + \alpha_p y_{k-p} = e_k$$

and the **PEM** reduces to a linear least squares problem, which is easily solved. Unfortunately, a p^{th}-order **AR** model is not an equivalent representation of a vibrating structure with *pl* modes. However, the use of an **AR** model as a substitution of an **ARMA** model can be justified if the **AR** model order goes to infinity: $p \to \infty$. In practice this means that many spurious poles will be introduced that need to be separated from the true system poles. The use of **AR** models for modal parameter estimation is, for instance, demonstrated in [PAND91a, DERO95].

3.6 COVARIANCE-DRIVEN VS. DATA-DRIVEN SUBSPACE

This section points out some of the similarities and differences between the **SSI-COV** (Subsection 3.4.2) and the **SSI-DATA** method (Subsection 3.5.1). First the similarities. Both methods start with a data reduction step. In the **SSI-COV** algorithm the raw time histories y_k, consisting of *l* channels of *N* data points, are converted to the covariances of the Toeplitz matrix $T_{1|i}^{\text{ref}} = Y_f Y_p^{\text{ref}\,T}$ (3.7). The number of elements is reduced from $l \times N$ to $li \times ri$; with *r* the number of references and $N \to \infty$. In the **SSI-DATA** algorithm a similar reduction is obtained by projecting the row space of the future outputs into the row space of the past reference outputs $\mathcal{P}_i^{\text{ref}} = Y_f \,/\, Y_p^{\text{ref}}$ (3.37). This projection is computed from the *QR* factorization of the data Hankel matrix (3.2). A significant data reduction is obtained because only a part of the *R* factor is needed in the sequel of the algorithm. Both methods then proceed with an **SVD**. The decomposition of $T_{1|i}^{\text{ref}}$ reveals the order of the system, the column space of O_i and the row space of Γ_i^{ref} (3.29). Similarly the decomposition of $\mathcal{P}_i^{\text{ref}}$ reveals the order of the system, the column space of O_i and the row space of $\hat{X}_i$ (3.40).

Several variants of stochastic subspace identification exist. They differ in the weighting of the data matrices ($T_{1|i}^{\text{ref}}$ for **SSI-COV** and $\mathcal{P}_i^{\text{ref}}$ for **SSI-DATA**) before the application of the **SVD**. The weighting determines the state-space basis in which the identified model will be identified. More details can be found in [ARUN90] and [VANO96]. One of these variants is so-called **C**anonical **V**ariate **A**nalysis (**CVA**), in which the singular values can be interpreted as the cosines of the principal angles between two subspaces: the row space of the future outputs Y_f and the row space of the past (reference) outputs Y_p^{ref}. In the **SSI-COV** implementation of **CVA**, the weighting of the covariance Toeplitz matrix before the application of the **SVD** goes as follows [AKAI74b, ARUN90]:

$$(Y_f Y_f^T)^{-1/2} \; T_{1|i}^{\text{ref}} \; (Y_p^{\text{ref}} Y_p^{\text{ref}\,T})^{-1/2}$$

In the **SSI-DATA** implementation of **CVA**, the weighting of the projection matrix before the application of the **SVD** goes as follows [VANO96]:

$$(Y_f Y_f^T)^{-1/2} \cdot \mathcal{P}_i^{\text{ref}}$$

Also the other subspace variants have equivalent implementations for both **SSI-COV** and **SSI-DATA**.

There are also differences between the covariance-driven and data-driven approaches. As indicated in Subsection 3.2.2, the covariance Toeplitz matrix can be computed in a very fast way by using the **FFT** algorithm. The corresponding step in **SSI-DATA** algorithm is the relatively slow *QR* factorization. Therefore **SSI-COV** is much faster than **SSI-DATA**. In favour of the data-driven method is that it is implemented as a numerically robust square root algorithm: the output data is not squared up as in the covariance-driven algorithm. More advantages of the data-driven method become clear in next section, where some postprocessing tools for the identified state-space model are presented: an analytical expression for the spectrum matrix and the separation of the total response in modal contributions.

3.7 POSTPROCESSING

This section deals with some useful postprocessing tools. In the present context, postprocessing means everything that comes after the identification of a parametric model. Once such a model is available, it can be analytically converted to other presentation forms. *Modal analysis*, a first type of postprocessing, was in fact already discussed in connection with the various identification methods. For instance, the modal parameters can be extracted from the **AR** parameters identified with the **IV** method; see Equations (3.21), (3.22). Similarly, the state-space matrices identified with **SSI-COV** or **SSI-DATA** allow us to compute the modal parameters, as formulated in (3.34). Other postprocessing tools such as *spectrum analysis* and *modal responses* are subsequently treated.

3.7.1 Spectrum analysis

The covariance-driven and data-driven system identification methods use *time-domain* data to identify a model. It is however interesting to assess the *frequency-domain* performance of these methods. Hereto, the identified models are converted to a spectrum model and compared with a non-parametric spectrum estimate, such as the periodogram (3.10) or correlogram (3.11). These estimates are directly obtained by applying the **FFT** to the time

data without any modelling involved. In Chapter 2, a closed-form expression for the spectrum of a discrete-time stochastic state-space model was derived, see Equation (2.80):

$$S_y(e^{j\omega\Delta t}) = C(zI - A)^{-1}G + R_0 + G^T(z^{-1}I - A^T)^{-1}C^T\Big|_{z = e^{j\omega\Delta t}} \tag{3.46}$$

By introducing the eigenvalue decomposition of A ($A = \Psi\Lambda_d\Psi^{-1}$), following "modal" spectrum is obtained:

$$S_y(e^{j\omega\Delta t}) = V(zI - \Lambda_d)^{-1}G_m + R_0 + G_m^T(z^{-1}I - \Lambda_d)^{-1}V^T\Big|_{z = e^{j\omega\Delta t}} \tag{3.47}$$

The **IV** *method*

The **IV** method yields the modal matrices $\Lambda_d \in \mathbb{C}^{n\times n}$, $G_m^{\text{ref}} \in \mathbb{C}^{n\times r}$ and $V \in \mathbb{C}^{l\times n}$, see (3.21) and (3.22). The matrix $R_0^{\text{ref}} \in \mathbb{R}^{l\times r}$ is directly estimated from the data. So only in case all sensors were considered as references, the complete spectrum matrix can be computed according to Equation (3.47). Otherwise only the power and cross spectra between the reference channels can be computed: $LS_yL^T \in \mathbb{C}^{r\times r}$.

The **SSI-COV** *method*

The **SSI-COV** method yields the state-space matrices $A \in \mathbb{R}^{n\times n}$, $G^{\text{ref}} \in \mathbb{R}^{n\times r}$ and $C \in \mathbb{R}^{l\times n}$, see (3.30) and (3.32). The matrix $R_0^{\text{ref}} \in \mathbb{R}^{l\times r}$ is directly estimated from the data. So only in case all sensors were considered as references, the complete spectrum matrix can be computed according to Equation (3.46). Otherwise only the power and cross spectra between the reference channels can be computed: $LS_yL^T \in \mathbb{C}^{r\times r}$.

The **SSI-DATA** *method*

The **SSI-DATA** method yields the full state-space matrices $A \in \mathbb{R}^{n\times n}$, $G \in \mathbb{R}^{n\times l}$, $C \in \mathbb{R}^{l\times n}$ and $R_0 \in \mathbb{R}^{l\times l}$, see (3.41) and (3.43). So, whatever the number of references is, it is theoretically possible to compute the complete spectrum matrix $S_y \in \mathbb{C}^{n\times n}$ according to Equation (3.46).

Example

The simulated data of the mast structure (Figure 2.1) is used to compare the parametric spectrum estimates (3.46), (3.47) with a non-parametric estimate. For all three methods (**IV**, **SSI-COV** and **SSI-DATA**) a model is identified that contains 20 poles. The analytical expression for the spectrum is evaluated for frequencies ranging from 0 to 12.5 Hz. The comparison is made in Figure 3.14. A 20-pole model is satisfactory for the subspace methods, but for the **IV** method a higher order model should be used. The spectrum matrix obtained with the **SSI-DATA** method is theoretically the full spectrum matrix, regardless the number of reference sensors used. However, from a plot of the power spectrum of a non-

reference channel (Figure 3.15), it is clear that spectra involving a non-reference channel are not as accurately estimated as reference spectra.

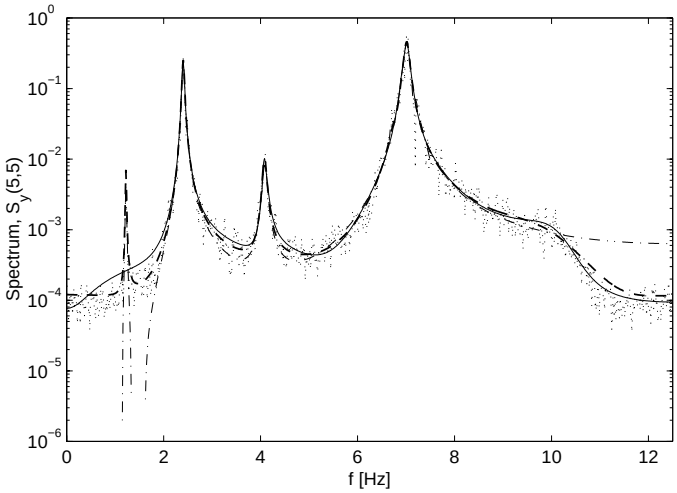

Figure 3.14: Comparison of power spectra of the 5th output channel. The rather erratic dotted line is the non-parametric estimate (Welch's method). The full line is the **IV** spectrum; the dash-dotted line is the **SSI-COV** spectrum and the thick dashed line represents the **SSI-DATA** spectrum. The 20-pole model resulting from the **IV** method failed to identify the first pole. This was also observed in the stabilization diagram (Figure 3.9), where the first pole was not yet stable at n = 20. The 20-pole models from the subspace methods caught all true poles. However the **SSI-COV** power spectrum becomes negative at certain frequencies, which is due to the unsatisfied positive realness (Page 84) condition. Although it is not the case in this example, also the **IV** spectrum can become negative. As discussed on Page 84, the **SSI-DATA** method overcomes this problem.

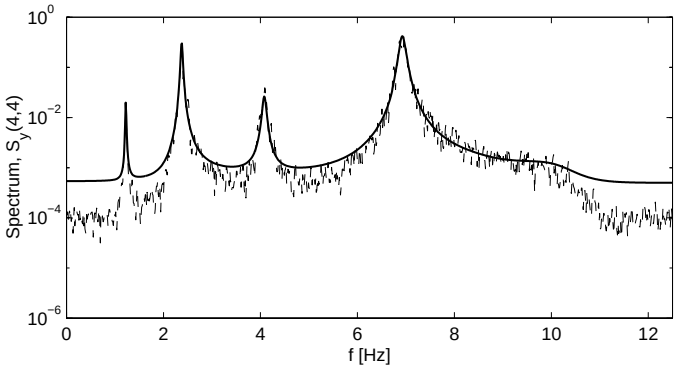

Figure 3.15: Comparison of power spectra of the 4th output channel (This is a non-reference channel). The rather erratic dashed line is the non-parametric estimate (Welch's method). The thick full line represents the **SSI-DATA** spectrum. The correspondence at the peaks is very good, but between the peaks the **SSI-DATA** spectrum of a non-reference channel is not as accurate.

3.7.2 Modal response and prediction errors

This subsection presents a technique to split the total measured response in *modal responses*. A modal response is defined as the response of a single **DOF** system, having the same eigenfrequency and damping ratio as the considered mode, to the same force as applied to the full system. The technique assumes that the identified model is written in forward innovation form (2.58):

$$\begin{aligned} z_{k+1} &= Az_k + Ke_k \\ y_k &= Cz_k + e_k \end{aligned}$$

where $K \in \mathbb{R}^{n \times l}$ is the Kalman gain and $e_k \in \mathbb{R}^l$ is the white noise innovation sequence with covariance matrix $\mathbf{E}[e_p e_q^T] = R_e \delta_{pq}$. This model can be written in the modal basis:

$$\begin{aligned} z_{m,k+1} &= \Lambda_d\, z_{m,k} + K_m e_k \\ y_k &= V\, z_{m,k} + e_k \end{aligned}$$

where $\Psi^{-1} z_k = z_{m,k}$ and $\Psi^{-1} K = K_m$. Because Λ_d is a diagonal matrix, each element of the modal state vector $z_{m,k}$ represents the contribution of a single mode. By eliminating the innovations in the first equation and re-arranging the second, following state-space model is obtained:

$$\begin{aligned} z_{m,k+1} &= (\Lambda_d - K_m V)\, z_{m,k} + K_m\, y_k \\ e_k &= -V\, z_{m,k} + y_k \end{aligned} \tag{3.48}$$

The idea is now to use this state-space model $(\Lambda_d - K_m V,\ K_m,\ -V,\ I)$ in a simulation. All state-space matrices are known from the identification and the measured output y_k serves as input in the simulation. The results from the simulation are the modal state sequence $z_{m,k}$ and the innovation sequence e_k. The innovations can be interpreted as one-step-ahead prediction errors [LJUN99]. The one-step-ahead predicted output is defined as:

$$\hat{y}_k = V\, z_{m,k}$$

The prediction errors are the differences between the true output and the predicted output: $e_k = y_k - \hat{y}_k$. Because each element $z_{m,k}^{(i)}$ of the modal state vector $z_{m,k}$ represents the contribution of a single mode, the predicted output can be split in modal responses as:

$$\hat{y}_k = \sum_{i=1}^{n} \hat{y}_{i_k} = \sum_{i=1}^{n} \{v_i\}\, z_{m,k}^{(i)} \tag{3.49}$$

where $\hat{y}_{i_k} \in \mathbb{C}^l$ is the (complex) response of the i^{th} mode. By combining the responses of a complex conjugated pair, a real output is obtained.

The approach of this section can only be applied to models that are identified with the **SSI-DATA** method. In order to obtain the forward innovation model, the full G matrix is needed and not only G^{ref} as obtained with the **SSI-COV** method (see also Subsection 3.5.1). Another more important problem, that could not be overcome by considering all sensors as references, is that the implementation of **SSI-COV** does not guarantee the positive realness of the identified covariance sequence. One of the consequences is that it is not always possible to obtain a forward innovation model [VANO96].

Example

The separation of the total response in modal responses is illustrated with the simulated data of the mast structure (Figure 2.1). A 20-pole model is identified with the **SSI-DATA** method. Afterwards, the modal state sequence is simulated according to Equation (3.48) and the modal responses are computed as in (3.49). The modal responses of channels 5 and 6 are shown in Figure 3.16 and 3.17, respectively.

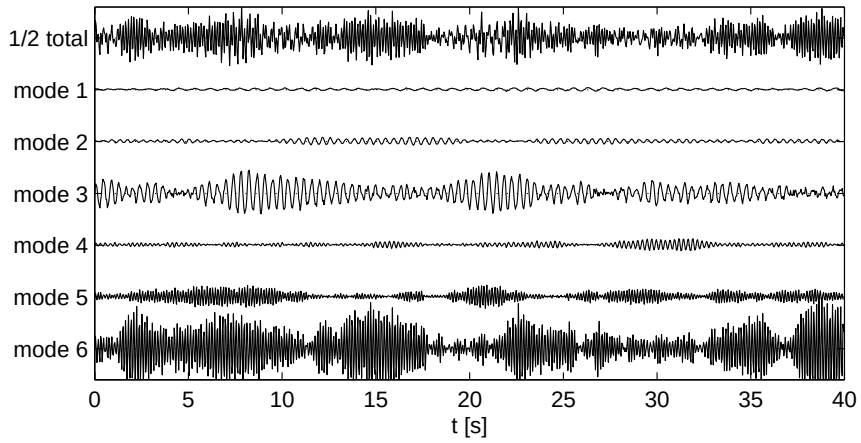

Figure 3.16: Modal responses of channel 5. The measured total response is shown in the top chart. The amplitudes of this signal have been multiplied by 0.5 for scaling purposes. The contributions of the 6 modes are subsequently presented. The sum of these 6 signals plus the prediction errors equals the measured response. Channel 5 measures a signal in y-direction, with important contributions from the 3rd and 6th mode, which are bending modes in the y-direction.

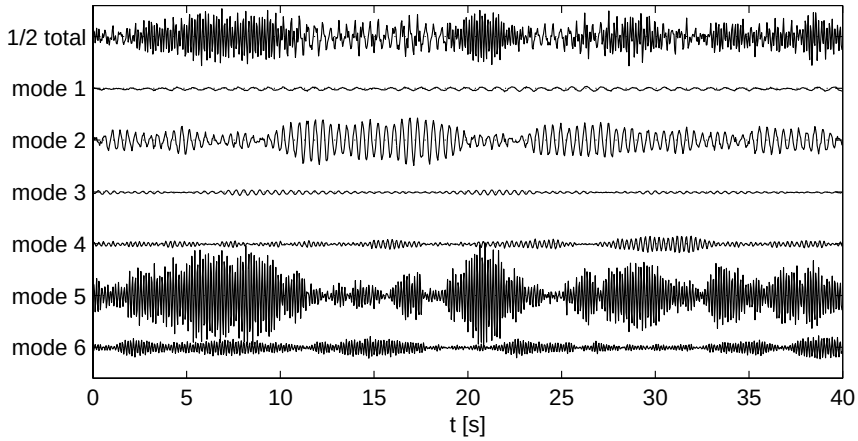

Figure 3.17: Modal responses of channel 6. The measured total response is shown in the top chart. The amplitudes of this signal have been multiplied by 0.5 for scaling purposes. The contributions of the 6 modes are subsequently presented. The sum of these 6 signals plus the prediction errors equals the measured response. Channel 6 measures a signal in *x*-direction, with important contributions from the 2nd and 5th mode, which are bending modes in the *x*-direction.

3.8 EXPERIMENTAL COMPARISON OF SYSTEM IDENTIFICATION METHODS

This section brings together the modal parameter estimation results of the discussed identification methods. The lay-out of the other parts concerning the simulated example is used.

Example

The practical application of a certain identification method was already illustrated in close connection with its theoretical development. A systematic comparison of the identification results in terms of the modal parameters, however, was postponed until this section. There exist other validation tools for system identification (see for instance [LJUN99]), but we are most interested in the modal parameter estimation performance of a method. The reason is that we consider modal parameters as essential information to base damage detection methods on. The comparison is made by a so-called Monte-Carlo analysis.

One Monte-Carlo simulation consists of the following steps. A white-noise input sequence is generated and applied to the mast structure (Figure 2.1). The simulated outputs are corrupted by 10% white measurement noise, see Page 55. These "noisy" outputs are then fed to the system identification methods: peak picking (**PP**), complex mode indication function (**CMIF**), instrumental variable (**IV**), covariance-driven stochastic subspace identification (**SSI-COV**) and data-driven stochastic subspace identification (**SSI-DATA**). From the six

outputs, channels 5 and 6 are considered as references. This has the following consequences for the primary data passed to the identification methods: the "past" part of the data Hankel matrix (3.2) consists only of these channels; only the covariances between all channels and these references are computed (3.8) and only the spectra between all channels and the references are computed (3.10). Every method yields a set of modal parameter estimates. This procedure is repeated for 100 different realizations of the input sequence and the measurement noise. Some effort was spent in automating the parameter estimation procedure to exclude any user interaction during the 100 simulations.

However, some foreknowledge in favour of the **PP** method could not be avoided. Although only 4 peaks are visible in the trace of the spectrum matrix (Figure 3.5), we selected 6 frequencies at the peaks of the transformed spectra (Figure 3.6). The *x*-bending modes are determined from the 6^{th} column of the spectrum matrix, corresponding to a signal in *x*-direction. Similarly, the *y*-bending modes are determined from the 5^{th} column, corresponding to a signal in *y*-direction. Failing to do so would result in completely erroneous mode shape estimates. Also in estimating the damping ratios with the half-power bandwidth method (that complements the **PP** method), the same foreknowledge was present. The other methods could be applied in an objective way. The parametric methods (**IV**, **SSI-COV**, **SSI-DATA**) are complemented with a stabilization diagram for pole selection. To construct such a diagram, models containing 2 to 60 poles were identified. The selection of the poles relies upon an automatic interpretation of the stabilization diagrams (See Section 4.2). As apparent from Figures 3.9, 3.11 and 3.12, the subspace methods require a lower model order to find stable poles. This observation is valid in general, although the figures only represent one Monte-Carlo run.

The results are represented in three Figures and synthesized in one Table. In our discussion of the **CMIF** method (see Subsection 3.3.2), we did not include an alternative frequency or damping estimation procedures as compared to the **PP** method. The only difference is that the **CMIF** can detect closely-spaced modes and finds the eigenfrequencies in a more objective way. Therefore the **CMIF** frequencies and damping ratios are not presented in the Figures and Table to follow. The results of **SSI-COV** and **SSI-DATA** are so close to each other, that only **SSI-DATA** is presented.

Figure 3.18 shows the eigenfrequency estimation results for 100 Monte-Carlo simulations. The bias and variance of the estimates are tabulated in Table 3.1. All methods yield (almost) unbiased eigenfrequency estimates. Although still small, the standard deviation of the **PP** estimates is three times higher than for the other methods.

Figure 3.19 and also Table 3.1 represent the damping estimation results. Notwithstanding the foreknowledge in favour of the **PP** method, the very high bias of the damping estimates (for modes 1, 4, 5 and 6) is striking. It was our experience that this bias can be shifted to other modes by changing the options of the non-parametric spectrum estimate: frequency resolution, applied window, number of averages and number of overlapping samples. It seems however impossible to decrease the bias on all modes or to predict the biased modes. This example confirms the "common sense" that the half-power bandwidth method is not a reliable method to estimate damping.

Figure 3.20 and Table 3.1 represent the mode shape results in terms of the **MAC** (3.24). This time also the **CMIF** results are represented. The mentioned foreknowledge is the reason why the **PP** method performed reasonably well. The quality of a **CMIF** mode estimate varied considerably with the selected singular vectors around a peak in the decomposed spectrum. Moreover it was generally not the singular vector corresponding to a peak that gave the best estimate. The **IV** method had some problems in estimating the torsion modes (mode 1 and 4), that have a relatively small contribution in the total response. This smaller contribution is obvious in time domain (Figures 3.16, 3.17) and frequency domain (Figure 3.14). Concerning mode shape estimation, the advantage of using subspace methods emerges: they clearly outperform the others.

By taking a close look at the values in Table 3.1, some (small) differences between the covariance-driven and the data-driven subspace method can be observed. It seems however that these differences originate from the weighting of the data matrices that was not equivalent (see Section 3.6). The **CVA** weighting was applied in case of **SSI-DATA**, whereas the covariance Toeplitz matrix of **SSI-COV** was not weighted. Afterwards we performed an additional simulation exercise with a **CVA**-weighted Toeplitz matrix and this yielded almost exactly the same results as the **CVA SSI-DATA** method.

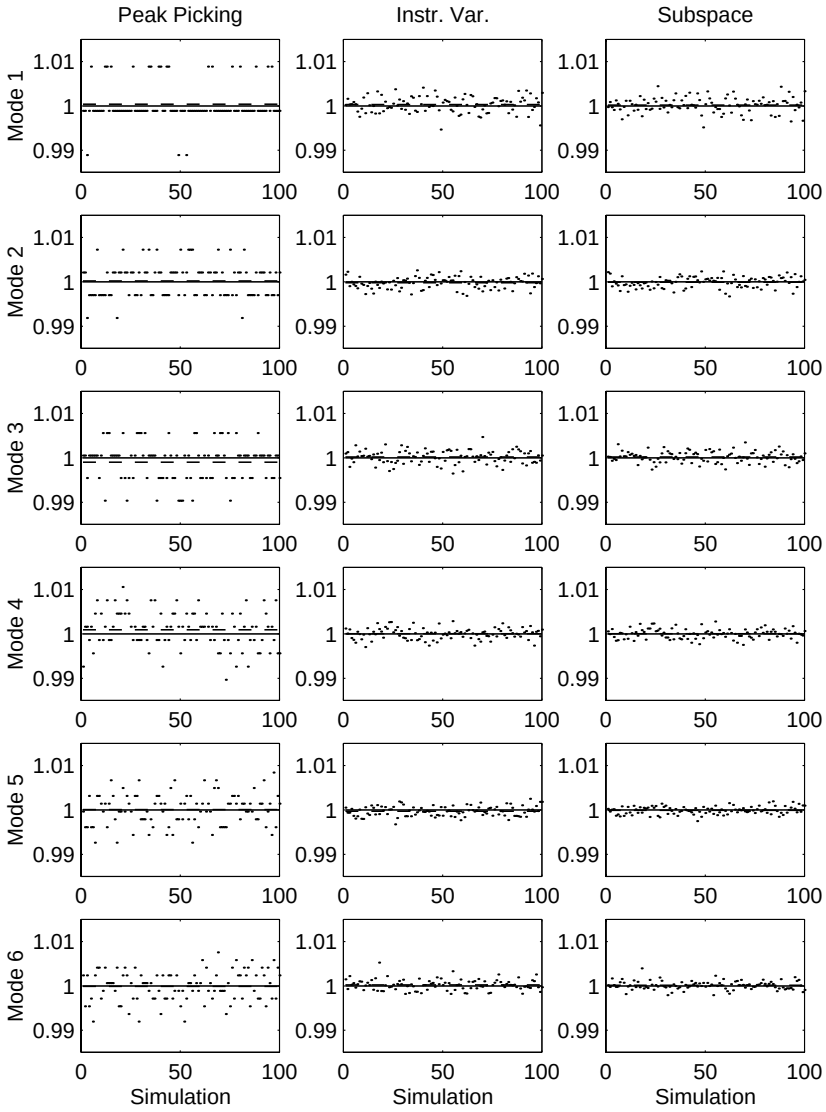

Figure 3.18: Eigenfrequency estimation results from 100 Monte-Carlo simulations. The estimates are divided by the true values (a value of 1 on the graphs indicates a perfect estimate). These relative frequencies are shown as dots. The scatter of this quantity gives an idea about the variance of the estimate. The average estimate is also shown (as a dashed line). The deviation of this quantity from 1 (full line) corresponds to the bias of the estimate. The rows show the 6 modes; the columns represent the results of 3 identification methods: **PP**, **IV** and **SSI-DATA**. The eigenfrequency estimates of the **PP** method can only take the discrete values determined by the frequency resolution of the spectrum. All methods yield unbiased eigenfrequency estimates. Although still small, the standard deviation of the **PP** estimates is three times higher than for the other methods. See also Table 3.1.

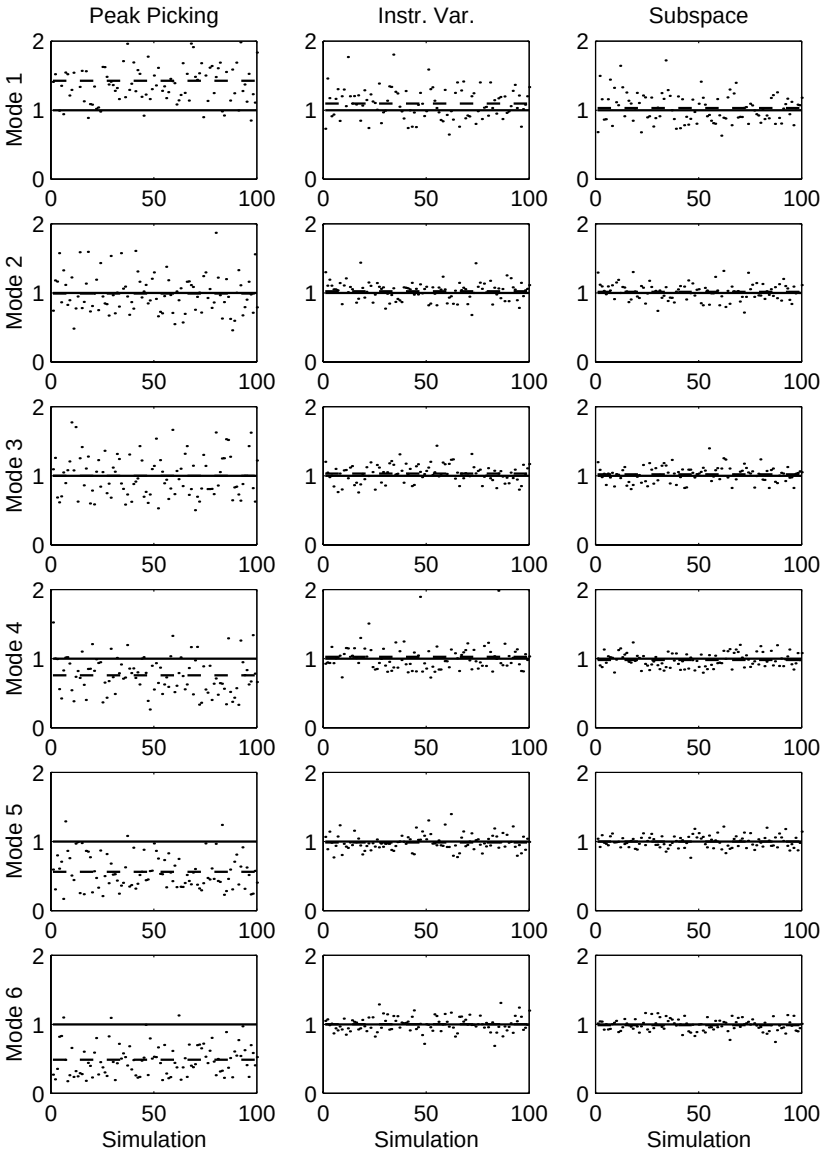

Figure 3.19: Damping ratio estimation results from 100 Monte-Carlo simulations. The estimates are divided by the true values (a value of 1 on the graphs indicates a perfect estimate). These relative damping ratios are shown as dots. The scatter of this quantity gives an idea about the variance of the estimate. The average estimate is also shown (as a dashed line). The deviation of this quantity from 1 (full line) corresponds to the bias of the estimate. The rows show the 6 modes; the columns represent the results of 3 identification methods: **PP**, **IV** and **SSI-DATA**. Especially the very high bias of the **PP** damping estimates is striking. It is rather a coincidence that mode 2 and 3 have unbiased damping estimates. See also Table 3.1.

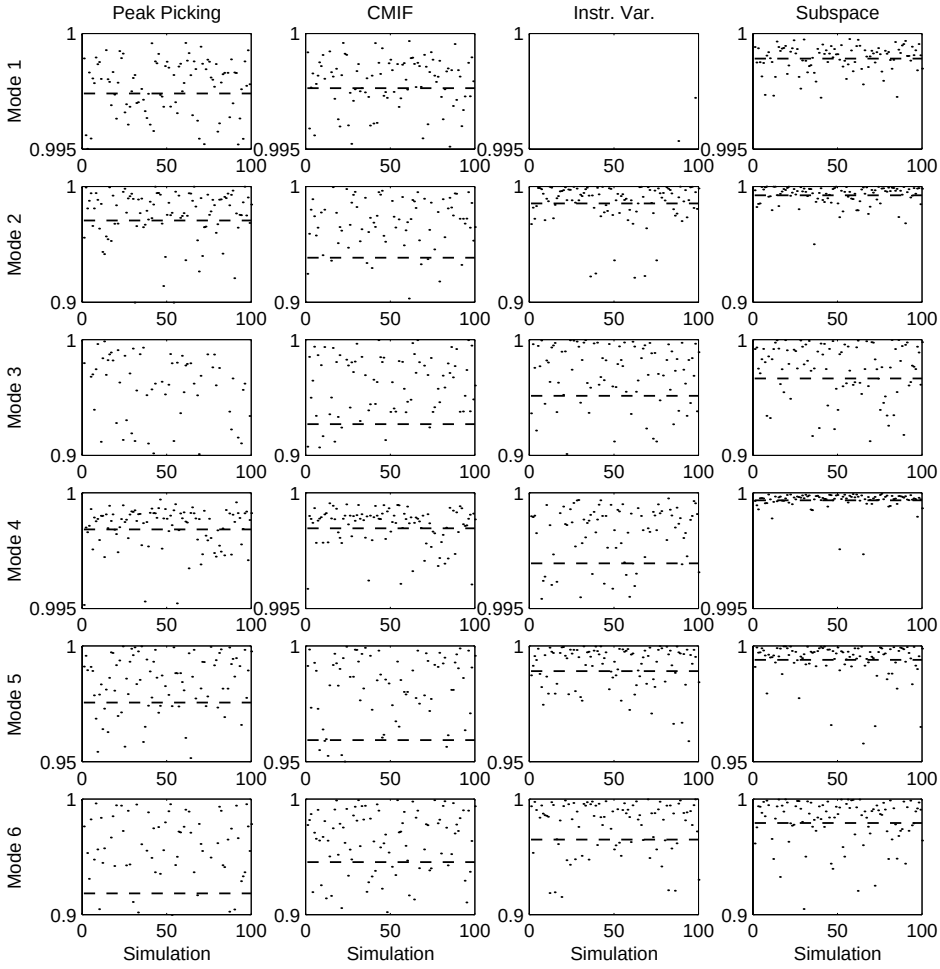

Figure 3.20: Mode shape estimation results from 100 Monte-Carlo simulations. The **MAC** values (3.24) between the estimated and the true mode shapes are shown (as dots). The average **MAC** is also shown (as a dashed line). The rows show the 6 modes; the columns represent the results of 4 identification methods: **PP**, **CMIF**, **IV** and **SSI-DATA**. The scaling of the *y*-axis varies in vertical direction (to accommodate to the changing estimation quality of the different modes), but not in horizontal direction, allowing an easy comparison of the methods. The **IV** estimates for the first mode are too bad to fit into the scales. Also the average correlation of the **PP** estimates of the third mode could not be represented. The subspace methods clearly outperform the others. See also Table 3.1.

Table 3.1: Modal parameter estimation results from 100 Monte-Carlo simulations. The relative bias and relative standard deviation are given. The frequency and damping estimation procedure is the same in **CMIF** as in **PP**. Therefore these results are only given once. The usual definitions of bias and standard deviation are not valid in the case of the mode shape correlations. However, they are computed in the same way. A graphical representation of these results can be found in Figures 3.18–3.20.

	PP		**CMIF**		**IV**		**SSI-COV**		**SSI-DATA**	
	Bias [%]	*Std [%]*	Bias [%]	*Std [%]*	Bias [%]	*Std [%]*	Bias [%]	*Std [%]*	Bias [%]	*Std [%]*
Eigenfrequencies	0.037	*0.43*			0.029	*0.18*	0.05	*0.18*	0.018	*0.18*
	0.022	*0.38*			0.021	*0.13*	0.011	*0.13*	0.01	*0.12*
	0.095	*0.43*			0.019	*0.15*	0.019	*0.13*	0.022	*0.12*
	0.092	*0.42*			0.003	*0.13*	0.001	*0.12*	0.002	*0.11*
	0.009	*0.36*			0.028	*0.11*	0.016	*0.1*	0.009	*0.09*
	0.011	*0.35*			0.023	*0.12*	0.011	*0.1*	0.012	*0.1*
Damping ratios	42.7	*25*			9.6	*20*	9.4	*23*	3	*20*
	0.7	*28*			2.4	*13*	2.2	*12*	1.5	*12*
	0	*30*			3.3	*12*	3.4	*11*	2.1	*11*
	24.1	*35*			2.6	*23*	0.7	*12*	1.9	*10*
	43.9	*43*			1.2	*12*	0.9	*13*	0.1	*9*
	51.3	*47*			0.2	*11*	0.6	*9*	1.3	*8*
Mode shape correlations (**MAC**)	0.26	*0.16*	0.24	*0.14*	5.01	*5.1*	0.18	*0.14*	0.11	*0.03*
	2.93	*3.66*	6.14	*7.77*	1.46	*1.78*	0.94	*1.08*	0.76	*0.82*
	11.4	*14.6*	7.3	*9.36*	4.85	*6.06*	3.79	*4.52*	3.35	*4.02*
	0.16	*0.11*	0.15	*0.11*	0.3	*0.41*	0.03	*0.02*	0.03	*0.04*
	2.44	*2.82*	4.07	*5.51*	1.09	*1.34*	0.85	*1.1*	0.6	*0.78*
	8.16	*8.23*	5.45	*7*	3.5	*4.86*	2.68	*2.7*	2.07	*2.31*

3.9 CONCLUSIONS

This chapter presented 5 stochastic system identification methods in detail, and briefly reviewed some others. The main focus of this thesis is on time-domain methods, although some simple frequency-domain methods were included for comparison and because of their historical value. Next to the theoretical development of a method, its practical application was illustrated with a Monte-Carlo simulation study.

The main conclusions are synthesized in Table 3.2.

The basic peak-picking method (**PP**) finds the eigenfrequencies as the peaks of non-parametric spectrum estimates. This frequency selection procedure becomes a subjective task in case of noisy civil-engineering data, weakly-excited modes and relatively close eigenfrequencies. The related half-power bandwidth damping estimation method is unreliable; and operational deflection shapes are identified instead of mode shapes. The advantage of this **FFT**-based method is its processing speed ('++' in Table 3.2), although the total analysis time can increase considerably by the amount of user interaction needed to improve the results ('−' in Table 3.2): inspection of spectra form added and subtracted signals, interpretation of coherence functions, trial of different reference sensors to get reasonable mode shapes, ...

The complex mode indication function (**CMIF**) is an **SVD**-extension of the **PP** method, allowing for an objective selection of the eigenfrequencies and the identification of closely-spaced modes. It seems however that the mode shape estimation quality depends on the selected singular vector around resonance (and that it is not always the vector at resonance that gives the best estimates). The modal responses can be more or less computed in the **CMIF** method by transforming the frequency lines around resonance in the decomposed spectrum back to time domain ('+ / −' in Table 3.2).

The parametric methods (**IV**, **SSI-COV**, **SSI-DATA**) share the advantage that stabilization diagrams can be constructed by identifying parametric models of increasing order. These diagrams are very valuable in separating the true system poles from the spurious numerical poles.

The instrumental-variable method (**IV**) does not involve an **SVD** and consequently suffers from the lack of a noise-truncating mechanism. This is reflected in the fact that the mode shape estimates are less accurate than in the subspace methods and that higher order models are required to obtain good modal parameter estimates. A lot of additional poles are necessary for fitting the noise ('−' for the stabilization criterion in Table 3.2).

Both covariance- (**SSI-COV**) and data-driven subspace methods (**SSI-DATA**) seem to perform equally well concerning modal parameter estimation performance, although theoretically the numerical behaviour of **SSI-DATA** should be better than that of **SSI-COV** since it avoids to square up the data. The **SSI-COV** method is considerably faster than the

SSI-DATA method since its data-reduction step can be implemented with the **FFT**, whereas **SSI-DATA** requires a slower *QR* factorization step. Evidently, because it only uses linear numerical algorithms, the **SSI-DATA** method is still much faster than nonlinear prediction error methods that are sometimes proposed to estimate the modal parameters of civil-engineering structures (see Subsection 3.5.2). When it comes to postprocessing tools such as spectrum analysis and the computation of modal responses, the implementation of **SSI-DATA** is preferred (see Section 3.7).

Table 3.2: Comparison of stochastic system identification methods. '**LS**' stands for **L**east **S**quares; '**EVD**' stands for **E**igen**V**alue **D**ecomposition. A '+' ('–') means that the methods performs well (badly) for the row entry criterion. The abbreviation 'n.r.' stands for 'not relevant'. In the **PP** and **CMIF** method no complete model is identified, therefore parametric spectrum analysis is not possible. Since the **IV** and the **SSI-COV** method yield models that can generally not be converted to forward innovation form, they obtain a '–' for the modal responses criterion. The slowest method concerning pure computation time (**SSI-DATA**) receives a '+ / –' for this criterion because it still is much faster than prediction error methods.

	PP	**CMIF**	**IV**	**SSI-COV**	**SSI-DATA**
Primary data	Spec.	Spec.	Cov.	Cov.	Data
Numerical tools	**FFT**	**FFT** **SVD**	**FFT** **LS** **EVD**	**FFT** **SVD** **LS** **EVD**	*QR* **SVD** **LS** **EVD**
Computation time	+ +	+	+	+	+ / –
User interaction time	–	+ / –	+	+	+
Modal parameters:					
Stabilization	n.r.	n.r.	–	+	+
Eigenfrequencies	+ / –	+ / –	+	+	+
Damping ratios	–	–	+	+	+
Mode shapes	–	+ / –	+ / –	+	+
Postprocessing:					
Spectrum analysis	n.r.	n.r.	+	+	+ +
Modal responses	–	+ / –	–	–	+

4

IMPLEMENTATION

This chapter describes the implementation of stochastic system identification methods to estimate the modal parameters of structures excited by an unknown force. In Section 4.1, the development of a Graphical User Interface for MATLAB is described. By pushing buttons the user is guided through the whole process of output-only modal analysis: converting measurements to engineering units, preprocessing the data, system identification, extracting modal parameters from a stabilization diagram, “gluing” mode shape parts together and animating mode shapes. Section 4.2 describes a “batch” approach to modal analysis. The large amount of data collected in the course of this thesis forced us to develop an automatic modal analysis procedure that excludes any user interaction.

4.1 MACEC, A GRAPHICAL USER INTERFACE FOR OUTPUT-ONLY MODAL ANALYSIS

4.1.1 Introduction

There exist several modal analysis software packages. Originally developed in mechanical engineering for identification based on input-output data (**FRF**s or impulse responses), today some of these packages also have modules for output-only modal analysis; e.g. recent revision of the LMS CADA-X system [CADA98]. However most commercial dedicated software packages have some drawbacks in a research environment: it is impossible to review the implementation of an algorithm and it is often not straightforward to add own developments to these packages. MATLAB [MATL96] on the other hand is an open environment that offers computation, visualization and programming tools. The basic package consists of general-purpose functions that can be used to make more application-specific toolboxes. Most of the functions are accessible ASCII-files which are compiled at their first call in a session; so the user can learn from their implementation or even modify it. Some existing toolboxes in the field of system identification and modal analysis will be briefly reviewed.

Both the System Identification Toolbox [LJUN95] and the Frequency Domain System Identification Toolbox [KOLL95] offer data preprocessing, identification and model validation tools. The first identifies time domain models from the data whereas the latter operates in the frequency domain. These toolboxes have been written by people with an electrical engineering background, but since they can identify any linear dynamic system from measurements, they can also be used in mechanical and civil engineering (a bridge is assumed to be a linear dynamic system). In the end both toolboxes offer a mathematical model that matches the data. However, from previous chapters it might be clear that some postprocessing is essential for our purposes: the extraction of modal parameters from the model, the construction of stabilization diagrams and the visualization of the structure's geometry and mode shapes.

Next to official toolboxes supported and distributed by The MathWorks, there exist also many toolboxes in a connection program for MATLAB-related third party products. One of these products is the Structural Dynamics Toolbox [BALM97], that offers possibilities in experimental modal analysis, **FE** analysis and updating. The toolbox has geometry and mode shape visualization possibilities. Unfortunately, the identification is based on **FRF**s and therefore not suitable for output-only modal analysis.

From this overview of existing software packages, it is clear that the need arose to develop an own program for output-only modal analysis. The name of the program is **MACEC**, standing for **M**odal **A**nalysis on **C**ivil **E**ngineering **C**onstructions [LAQU98, PEET99b, PEET99c, VAND99].

4.1.2 Development of MACEC

In a first stage, the system identification methods described in Chapter 3 are implemented as MATLAB command-line functions. These functions are executed by typing their name together with the input and output variables. For instance:

```
» [invar] = ssi_data(y,i,'cva',ref);
```

applies the **CVA**-variant of data-driven stochastic subspace identification (see Subsection 3.5.1) to the data matrix `y`. Half the number of block rows in the data Hankel matrix (3.2) is specified by variable `i`. The reference sensors are specified as column numbers of `y` in variable `ref`. The output variable `invar` contains intermediate results after the application of the *QR* factorization and the **SVD**. A stochastic state-space model in forward innovation form `[A,K,C,Re]` is then identified in a second run of the same command:

```
» [A,K,C,Re] = ssi_data(invar,n,'model');
```

where `n` is the desired model order.

The difficulty with all these functions is that one has to know the syntax and keep track of the variables. Therefore a MSc project was set up in order to build a **G**raphical **U**ser **I**nterface (**GUI**) incorporating most of the existing functions for data conversion, system identification and adding functions for mode shape animation [LAQU98]. Instead of typing in commands, the user just has to click buttons (Figure 4.1):

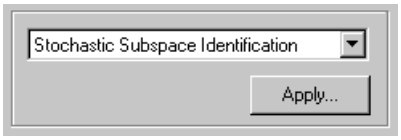

Figure 4.1: The **GUI** approach.

There might exist more flexible environments to create a **GUI**, but probably none of these have the same matrix computation and 2D and 3D visualization possibilities as MATLAB. Also algorithm development is very easy in MATLAB, because of the interaction between the function under development and the workspace: the programmer can always control the state of the variables.

Inspiration for the design and implementation of a MATLAB **GUI** was found in [MARC96, GUI97]. Two questions are very important when designing a **GUI**:

- Do the users always know where they are?
- Do they always know where to go next?

In order to get positive answers to these questions **MACEC** is constructed around one main window (Figure 4.2), that is divided into three main tasks: preprocessing - system identification - visualization. To perform each of these tasks a new window is opened and after the user has gone through all desired features of the task, the window is closed and the user returns to the main window.

4.1.3 Functions of MACEC

The main functions of **MACEC** are reviewed. They can be divided into three categories: preprocessing – system identification – visualization.

Preprocessing

The measured time data can be imported into the program in ASCII-format or a more efficient binary format. Upon loading into the program, the data is scaled to engineering units and information about the sensor location is added to the channels. If the original data was stored in Volts [V], it is scaled to obtain accelerations [m/sec^2]. Scaling the data is straightforward, once the user has created an ASCII-file containing the sensitivities of all his sensors (Figure 4.3). For the interpretation of the channels it is essential to incorporate the physical locations of the measurement points and axis (node number and **DOF**) into

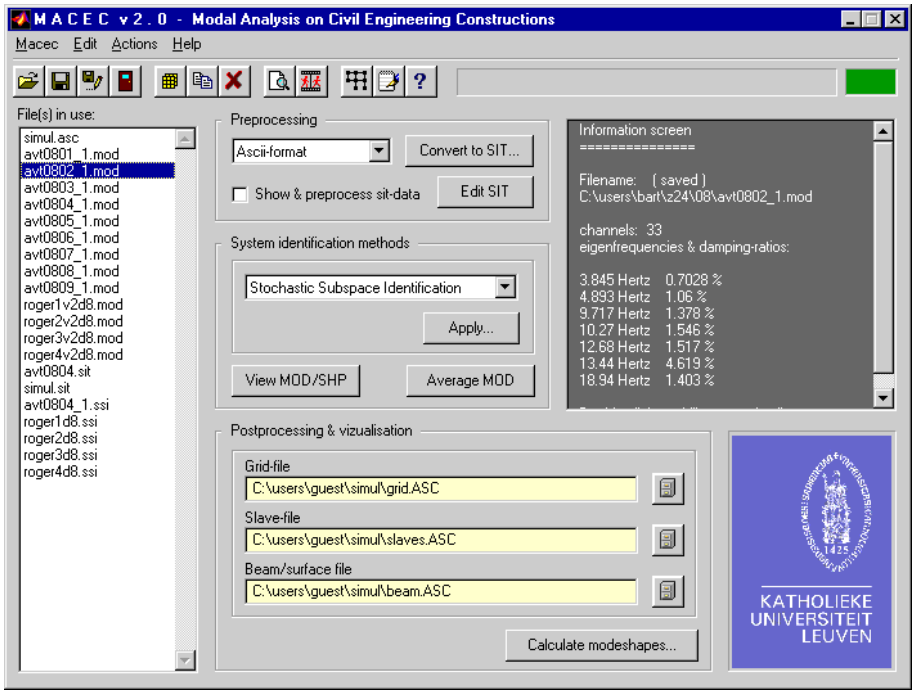

Figure 4.2: MACEC main window.

the internal data format. In case a sensitivity axis of a sensor does not coincide with one of the global axis, it can be defined with two angles: $\alpha \in]-180°, 180°]$, the angle in the XY-plane; and $\beta \in [-90°, 90°]$, the angle perpendicular to the XY-plane (Figure 4.4).

Next the true preprocessing can begin. Preprocessing is the data treatment before system identification and it highly influences the identification result. Following possibilities are implemented:

- *Decimate:* the data is low-pass filtered and resampled at a lower rate. The identification can concentrate on a limited frequency band.

- *Detrend:* the best straight line fit is removed from the data. This removes the DC-component that can badly influence the identification results.

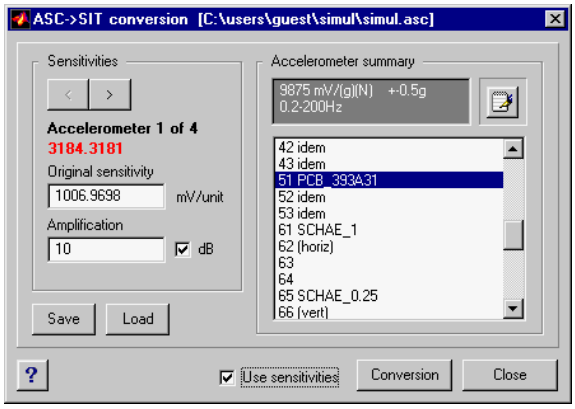

Figure 4.3: Scaling raw measurements from Volts to accelerations [m/sec^2] by selecting the used sensor and the amplification factor.

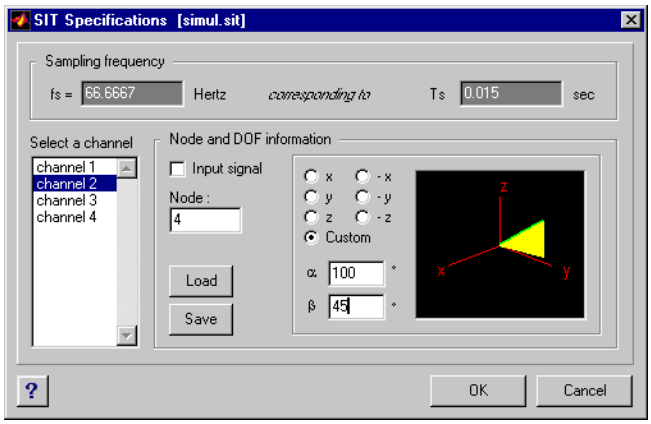

Figure 4.4: Specifying the location and sensitivity axis of the channels.

- *No Elec:* removal of spurious frequencies (e.g. at 50 Hz due to AC power supply). This operation is not the same as stopband filtering, but it really removes only the component at a certain frequency.

- *Delete channel:* removal of a complete channel. For instance a very noisy channel can be better removed to improve the identification results.

- *Time window:* a certain high-quality time segment can be selected for further analysis.

The effect of a preprocessing procedure can be seen immediately, both in time and frequency domain (Figure 4.5). There is also an "undo" possibility.

System identification

Currently two complementary methods are implemented: The **P**eak-**P**icking (**PP**) method and the data-driven stochastic subspace identification (**SSI-DATA**) method. If the user selects the **PP** method (Subsection 3.3.1), a window with the average of the power spectra is opened, the mouse pointer changes into a cross-hair and the user can pick the peaks (Figure 4.6). Operational deflection shapes are determined at the selected frequencies.

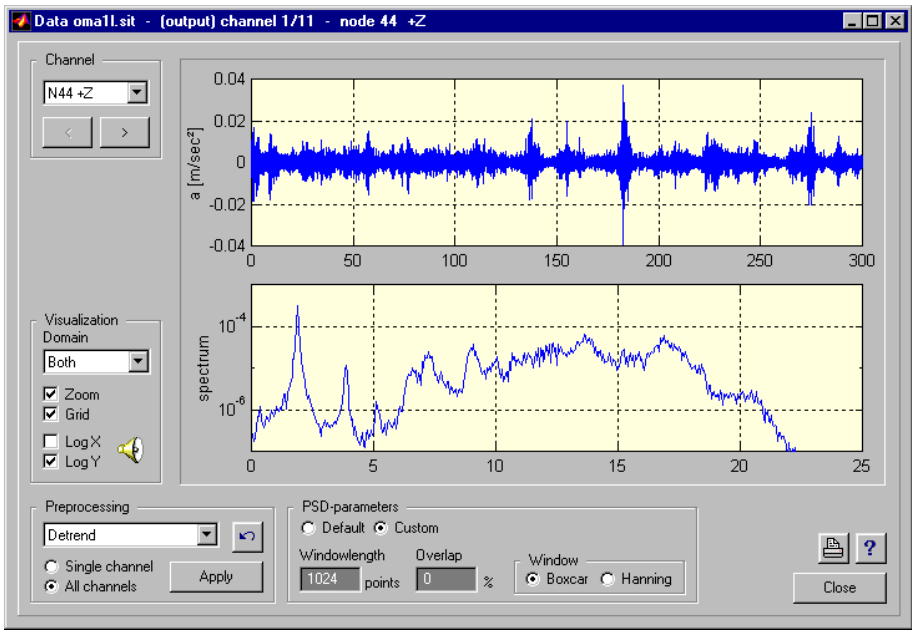

Figure 4.5: MACEC's preprocessing window with time and frequency domain representation of the signals.

The second method is **SSI-DATA** method (Subsection 3.5.1). First the user has to specify some input-parameters of the algorithm: the selection of reference channels, the maximum model order and the model order range. After some computations (*QR* factorization and **SVD**), a stabilization diagram is constructed (Figure 4.7). The user can change the stabilization criteria (defaults are 1% for eigenfrequencies, 5% for damping ratios and 1% for mode shape correlations). The better the quality of the data, the stricter these tolerances can be set. The diagram is represented together with the average of the power spectra for visual reference. The stable poles are graphically selected.

Visualization

The identified mode shapes are graphically represented as deformations of the structure. The **DOF**s were already attributed to the channels in the preprocessing step (Figure 4.4). Before visualization, a *grid* of nodes and the connections between the nodes in terms of *beams* or *surfaces* need to be defined. This is realized by loading two ASCII-files into the program: a grid file and a beam or surface file. The grid file contains 4 columns: node number and X, Y, Z coordinates. The beam file contain 2 columns: a MATLAB Line object is defined by 2 nodes; whereas the surface file has 4 columns: 4 nodes define a MATLAB Patch object. These files can easily be generated within **MACEC** with the "beam/surface-generator", see [VAND99]. Visualization of **DOF**s that were not measured can be done in a "slaving" procedure: the unmeasured slave **DOF**s are related to measured master **DOF**s.

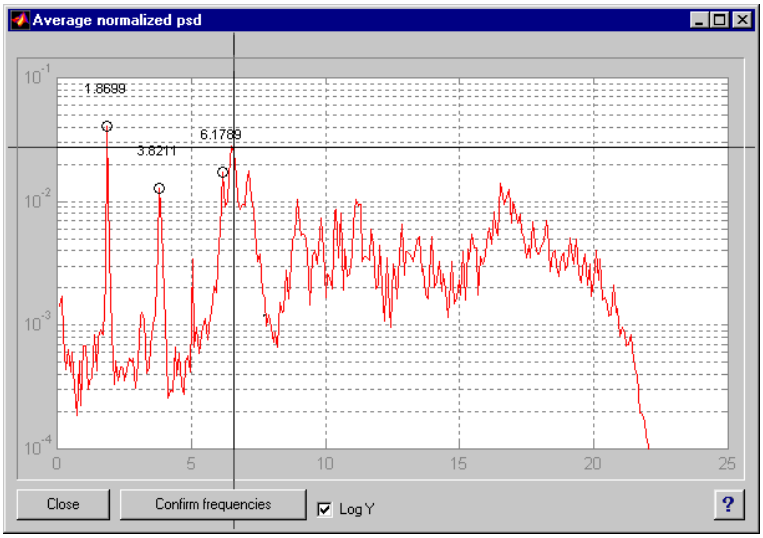

Figure 4.6: Illustration of the peak-picking procedure.

Every setup of simultaneously measured channels yields after identification a part of the global mode shape. These parts are glued together with the aid of reference sensors, common to all setups. These common sensors are automatically detected by **MACEC**. As illustrated in Figure 4.8, least squares approximation is used to determine the scaling factor of a certain mode between two setups. The scaling factor is different from one if the (unknown) excitation changes from one setup to another, which is generally the case.

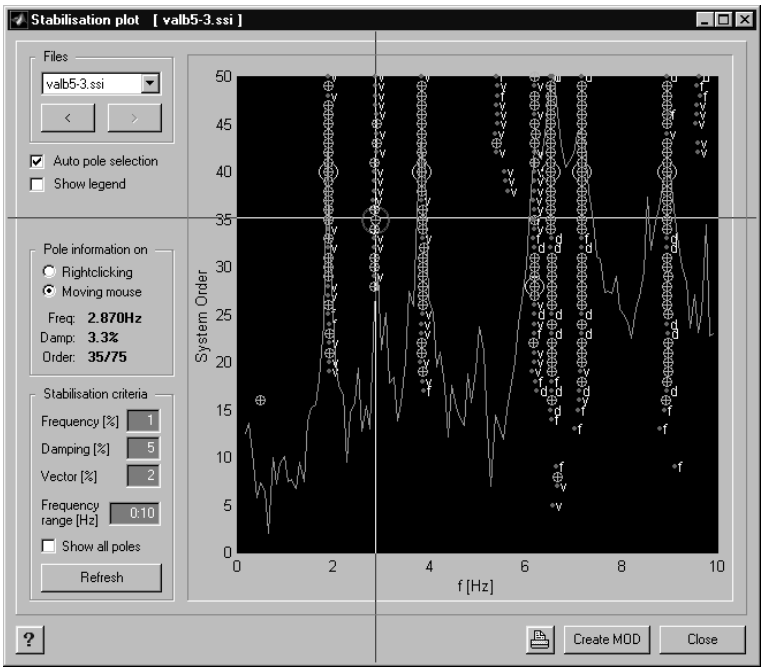

Figure 4.7: Stabilization diagram for pole selection in the **SSI-DATA** method.

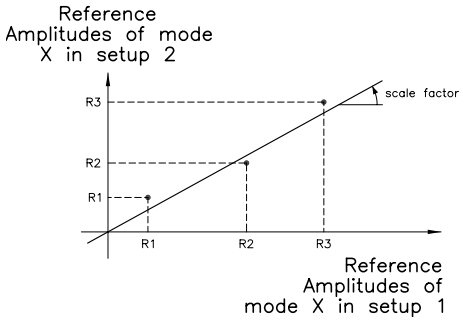

Figure 4.8: Use of reference sensors to glue mode shape parts.

Now we are ready to visualize the mode shapes. The visualization window (Figure 4.9) offers a lot of possibilities: scrolling through all modes, representation of undeformed structure and node numbers, 3D-view with possibility to change the viewpoint, animation of mode shapes, ...

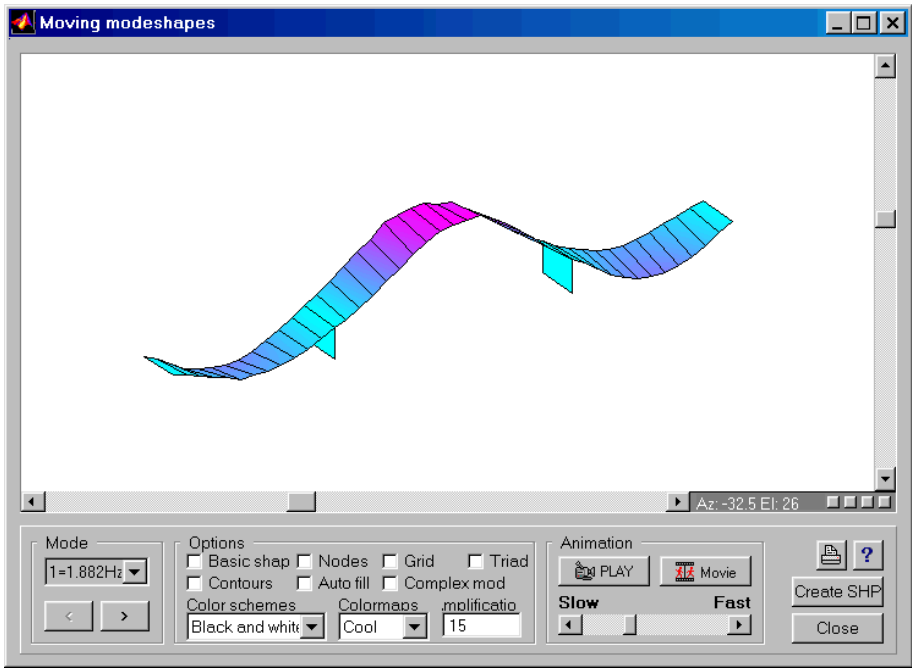

Figure 4.9: The mode -shape visualization window of **MACEC**.

4.2 AUTOMATIC MODAL ANALYSIS

There are cases that user interaction is not desired. A first example was already encountered in Chapter 3, where 100 Monte-Carlo simulations were performed to study the statistical properties of stochastic system identification methods. In each simulation run, the stabilization diagrams of the **IV**, **SSI-COV** and **SSI-DATA** method needed to be interpreted to find the stable poles. A second, more practical example is *continuous* monitoring of structures. In this case, the vibration monitoring system yields massive amounts of data. Modal parameters have to be extracted from these data, since our approach to damage detection requires the modal parameters as damage indices. Such a continuous-monitoring case will be treated in Chapter 7.

From this, it is clear that a realistic monitoring system should incorporate an *automatic modal analysis* procedure that excludes any user interaction. Nevertheless the idea of the stabilization diagram should not be abandoned since it proved to be essential in distinguishing true system poles from numerical poles. To reconcile these requirements, a procedure was developed that relies upon the automatic interpretation of stabilization diagrams. It consists of following three steps:

1. One single representative data set is used to perform a classical identification (with user interaction!). Such an analysis gives an idea about the quality of the data and the choices of the stabilization criteria for eigenfrequencies, damping ratios and mode shapes.

2. The automatic procedure takes off. The stabilization diagram is scanned and columns of stable poles are identified. The elements of such a column have close frequencies and high mode shape correlations. To exclude accidentally stable poles, a column should contain a minimum number of stable poles, otherwise it is rejected. As representative for a column, the pole having its eigenfrequency closest to the average of the column is selected. This procedure is repeated for every data set.

3. There is no guarantee that every data set yields the same stable poles. For instance, the input may change from one data set to another. Sometimes a pole is missing (not well excited) or an additional pole is identified (at an harmonic of the input). Therefore the stabilization approach is followed again in this step to pair the poles between two data sets. Sometimes the stabilisation requirements for frequencies have to be reduced. This will be the case in Chapter 7, where varying frequencies are normal due to varying environmental conditions.

The proposed automatic modal analysis procedure was tested on data sets of varying quality: the numerical simulations of Chapter 2 and 3, the reinforced concrete beam data and the steel mast data of Chapter 5 and the prestressed concrete bridge data of Chapter 7. The results are presented in the respective chapters. In all these cases it turned out to be a robust method.

4.3 CONCLUSIONS

In this chapter the development of a **GUI** for MATLAB was described. The goal was a complete and user-friendly package for output-only modal analysis (with civil engineering applications in mind). MATLAB was selected as development environment because of its extensive computation and visualization tools. Another reason was that it is a very open programming environment with access to most of the code, allowing the programmer to easily modify implementations or add new features. The toolbox has preprocessing, system identification and visualization possibilities that allow both a fast quality check of the data on site (**PP** method) and a more accurate analysis afterwards (**SSI-DATA** method).

Additionally an automatic modal analysis procedure was proposed that is able to treat a large number of data sets without any user interaction. This automatization is a key issue of a continuous monitoring system that is based on modal parameters.

5

APPLICATIONS

The simulation example of Chapter 2 and 3 proved to be very useful to compare system identification methods. Although the simulation study was carefully designed to be in close agreement with reality, a system identification method should also be assessed using real vibration data. In Section 5.1, data from vibration tests on reinforced concrete beams are used. A laboratory test under well-controlled experimental conditions in terms of boundary conditions and excitation sources, is a logical second step after performing numerical simulations. Particularly interesting about the tests on the beams is that they were artificially damaged in order to verify the damage-detection potential of the dynamic characteristics. In Section 5.2, data from a steel mast excited by wind load is used. This is a true real-life test. An application concerning the vibration monitoring of a rigid prestressed concrete bridge, is deferred to Chapter 7.

5.1 REINFORCED CONCRETE BEAMS

5.1.1 Introduction

As a part of the experimental work of this thesis, 4 reinforced concrete beams were extensively tested. The aim of the beam tests was not only to provide experimental data for the system identification methods, but also to verify whether it is fundamentally possible to measure the damage-induced changes in the dynamics of a structure. Therefore the beams were subjected to progressive artificial damage. At each intermediate damage state, a vibration experiment was set up. The 4 beams differed in the induced damage pattern. Results from the 2nd and 3rd beam are presented in this thesis. Results on the 4 beams can be found in [PEET96, PEET97, MAEC98a, DEVI99, PEET99a, MAEC00a].

The usefulness of the beam tests is confirmed by the fact that they were selected as "benchmark" tests by working group 2 of COST[1] action F3 on Structural Dynamics. Published results on this benchmark case can be found in [PASC99b, PASC99a].

First the static and dynamic test procedures are described and some typical measurement data represented. Next the application of stochastic subspace identification to the vibration data is illustrated. And finally, the evolution of the modal parameters throughout the damage stages is tracked.

5.1.2 Data acquisition

The beams

All 4 test beams have the same dimensions. Four objectives were envisaged when designing the test beams:

- The first eigenfrequency should have the same order of magnitude as the lowest eigenfrequencies encountered in typical civil engineering structures like bridges, i.e. 2-10 Hz. An advantage of a low fundamental eigenfrequency is that within a measurable frequency interval, e.g. 0-1000 Hz, a lot of modes will be present. This is important because there is some belief that the higher modes are influenced more by cracking than the lower ones. The eigenfrequencies are

[1]COST stands for European **Co**-operation in the Field of **S**cientific and **T**echnical Research [http://www.belspo.be/cost/], [http://www.ulg.ac.be/ltas-vis/costf3/costf3.html].

proportional to h/L^2. With the height $h = 0.2$ m and the length $L = 6$ m, a first eigenfrequency of about 20 Hz was obtained.

- Earlier test programs in other institutions [DIET80, ROHR91] have revealed the difficulty of obtaining simple supports for dynamic tests: ambient vibration interferes with the artificial force input, finite rigidity of the supports can influence mode shapes and eigenfrequencies, and radiation will add extra damping to the inherent damping of the concrete beam. Therefore, a completely free test setup is adopted which means that the beam is supported by a number of very flexible springs resulting in rigid body eigenfrequencies of about 1 Hz, which is much lower than the eigenfrequency of the first bending mode, $f_1 \approx 20$ Hz. A consequence is that the static test configuration will be different from the dynamic one. Also in [BRIN95] a free-free dynamic test setup is adopted. Due to the limited length of the concrete test beam, the eigenfrequencies were quite high. The first eigenfrequency was $f_1 = 278.8$ Hz.

- To avoid any coupling effect between horizontal and vertical bending modes, the width $w = 0.25$ m of the beam is chosen to be different from the height.

- The reinforcement ratio should be within a realistic range. By a proper choice of the steel quality, the interval between onset of cracking and beam failure can be made large enough to allow modal analysis at well separated levels of cracking.

These four objectives result in a 6 m long beam of rectangular cross section $A = 200 \times 250\ \text{mm}^2$. There are 6 reinforcement bars of diameter $\varphi = 16$ mm, equally distributed over tension and compression side, corresponding to a reinforcement ratio of

Figure 5.1: Steel reinforcement for the concrete beams.

about 1.4%. Shear reinforcement consists of vertical stirrups of diameter 8 mm, every 200 mm. The reinforcement is shown in Figure 5.1. A total beam mass of $m = 750$ kg results in a density of the reinforced concrete of $\rho = 2500$ kg/m^3.

Static tests

As stated in the introduction, we concentrate on beams 2 and 3 in this thesis. **Beam 2** is simply supported with a span of 3.6 m and two cantilevers of 1.2 m to minimize the influence of the own weight. A static load is applied at the centre of the beam, resulting in a maximum bending moment at the position where the load is applied. The bending moments decrease linearly to reach zero at the supports. The static test setup for **beam 2** is illustrated in Figure 5.2. The loading sequence is represented in Table 5.1.

Beam 3 is also simply supported, but now the full length of the beam is used. Two static loads are applied at 2 m from both sides of the beam. This is a so-called four-point bending test. The bending moments are constant between the loads and vary linearly between a load and a support. The static test setup for **beam 3** is illustrated in Figure 5.3. The loading sequence is represented in Table 5.2.

Table 5.1: Loading sequence of **beam 2**.

Load step	0	1	2	3	4
Total load [kN]	0	8	15	24	32

Table 5.2: Loading sequence of **beam 3**.

Load step	0	1	2	3	4	5	6
Total load [kN]	0	2×4	2×6	2×12	2×18	2×24	2×25.3

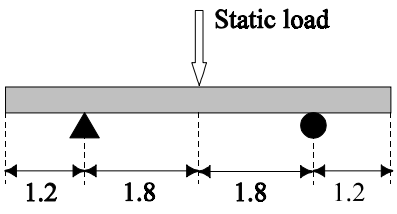

Figure 5.2: Static test setup for **beam 2**. A triangle represents a hinge; a circle represents a roller. The unit of distance is 1 m.

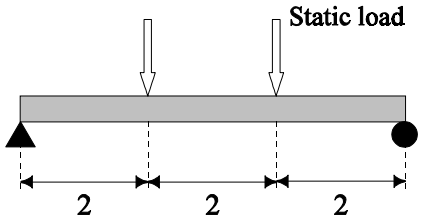

Figure 5.3: Static test setup for **beam 3**. A triangle represents a hinge; a circle represents a roller. The unit of distance is 1 m.

During the application of the static load, the deflection of the beams at several locations is measured (Figures 5.4 and 5.5). At the maximum load of each step, also crack widths and strains are measured. The progressive cracking of the beams is represented in Figures 5.6 and 5.7. Figure 5.8 gives an idea about the deflection of **beam 3** during one of the final load steps.

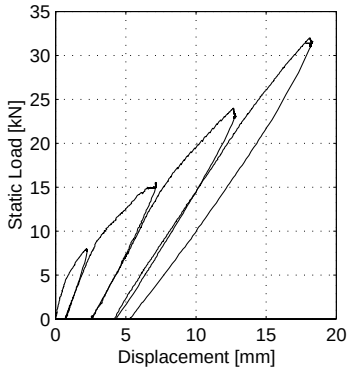

Figure 5.4: Force-Displacement diagram (**Beam 2**). The displacements at mid-section are shown.

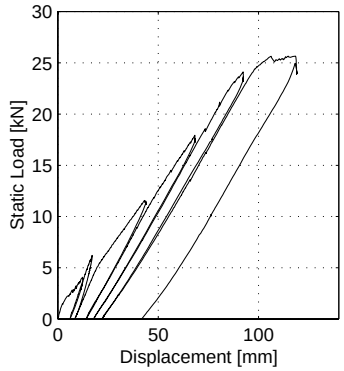

Figure 5.5: Force-Displacement diagram (**Beam 3**). The displacements at mid-section are shown.

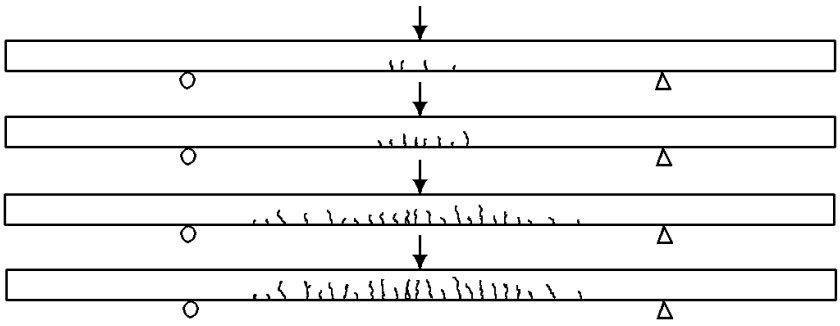

Figure 5.6: Progressive cracking (**Beam 2**). The visually observed cracks at the maximum load of the 4 load steps are shown from top to bottom.

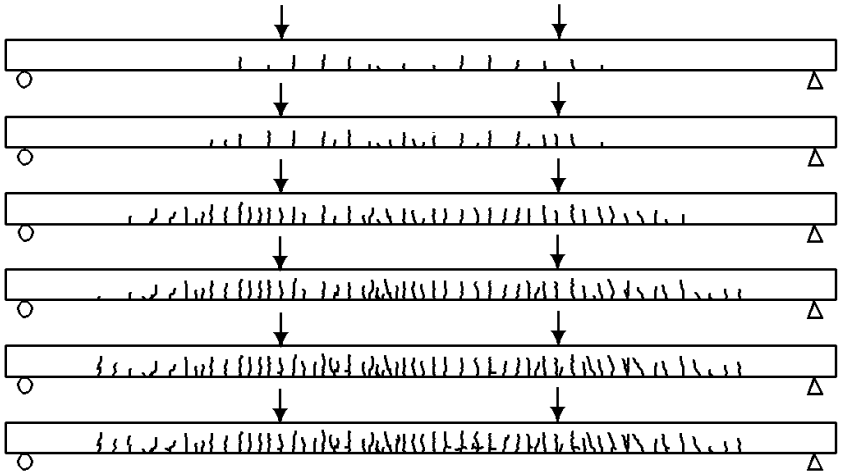

Figure 5.7: Progressive cracking (**Beam 3**). The visually observed cracks at the maximum load of the 6 load steps are shown from top to bottom.

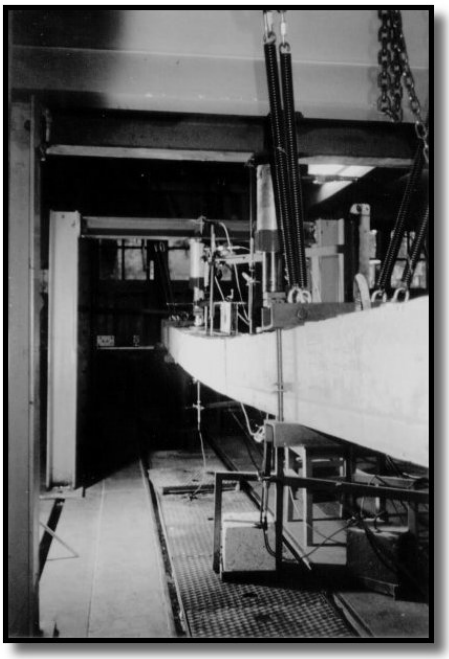

Figure 5.8: Deflection of **beam 3** during one of the final load steps.

Dynamic tests

After each load step, the beams are unloaded, flexible springs are connected to the beams and the supports are removed. The springs are connected at the theoretical nodal points of the first bending mode, located at a distance from a side of $0.224L = 1.344$ m. Figure 5.9 gives an impression of the dynamic test setup. Due to the low-pass filtering characteristics of a free-free setup, there were no ambient sources to excite the beam. Therefore artificial excitation was applied. An impulse hammer and an electromagnetic shaker were subsequently applied. The dynamic force is applied in vertical direction at an outer point of an end section. This ensures the excitation of both vertical bending and torsion modes. Every 20 cm, accelerations are measured at both sides of the beam. A pseudo-random (also called multi-sine) signal was chosen to drive the shaker. Typical impact test data is shown in Figure 5.10.

5.1.3 System identification

The data-driven stochastic subspace identification (**SSI-DATA**) method is applied to the impact response data. It may seem strange to use an impact excitation to validate a stochastic system identification method. Indeed, strictly speaking one of the assumptions of a stochastic system is violated, namely the white noise assumption of the input. However the use of an impact instead of white noise does not introduce additional poles in the data (which would be identified erroneously as system poles by output-only system identification methods). The system identification results of **beam 2** in its undamaged state are presented in this Subsection.

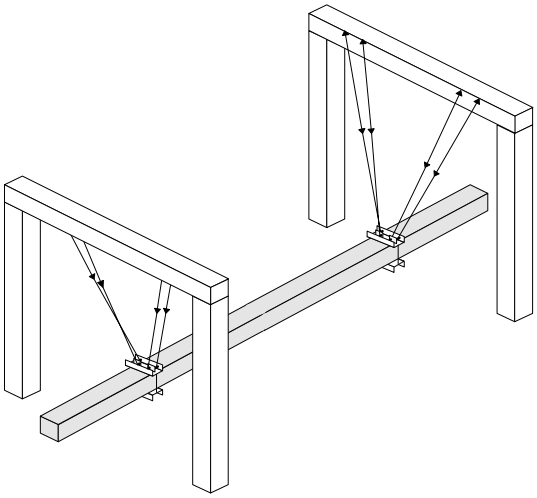

Figure 5.9: Dynamic test setup for both beams.

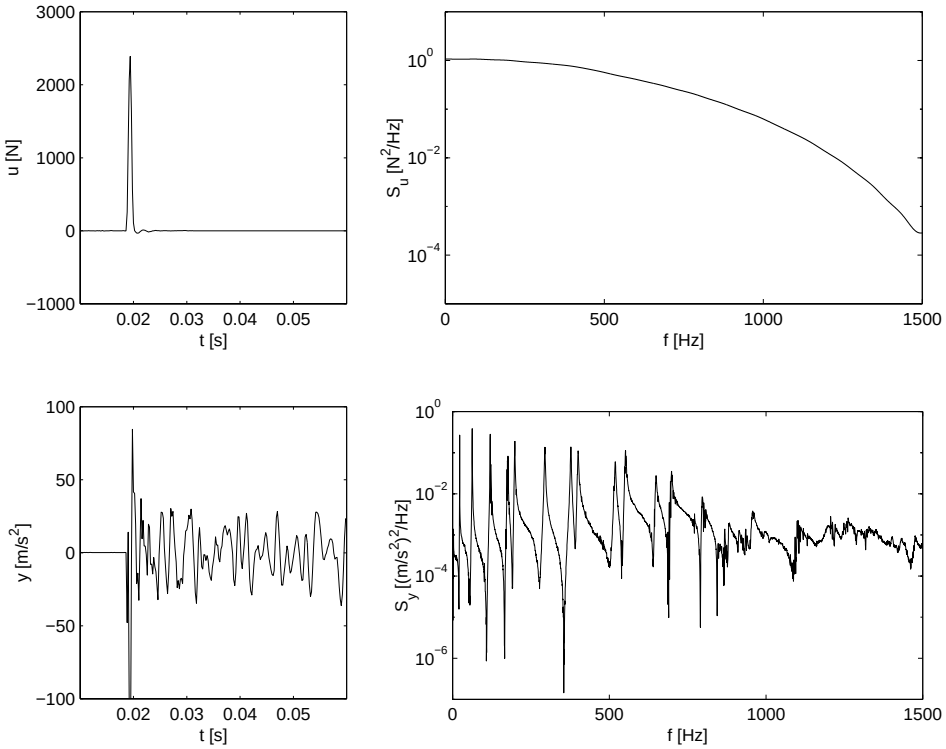

Figure 5.10: Typical impact data. The top row represents the impact force; the bottom row represents an acceleration response. The left column contain time histories; the corresponding spectra are shown in the right column. The sampling frequency is 5000 Hz. The impact hammer was able to generate a reasonable response in a frequency range from 0 to 700 Hz.

Modal parameters

The whole surface of the beam was scanned with accelerometers in 6 setups. The 2 accelerometers at one of the sides of the beam are the reference sensors which remained on their position during the 6 setups. They are necessary to merge the relative modal amplitudes of different setups in an output-only modal analysis. Every impact test was repeated 4 times. By consequence 24 independent samples are available to estimate the eigenfrequencies and damping ratios. A typical stabilisation diagram is shown in Figure 5.11. Table 5.3 represents the mean values $\bar{f}, \bar{\xi}$ and estimated standard deviations $\hat{\sigma}_f$, $\hat{\sigma}_\xi$ of the 12 modes that could be identified in the range $0 \rightarrow 700$ Hz. The corresponding mode shapes are shown in Figure 5.12. The represented hammer results are in good agreement with the shaker results where a pseudo-random input signal was used. A pseudo-random signal consists of discrete sines, all with the same amplitude but with a random phase angle. A comparison between hammer and shaker results can be found in [PEET97].

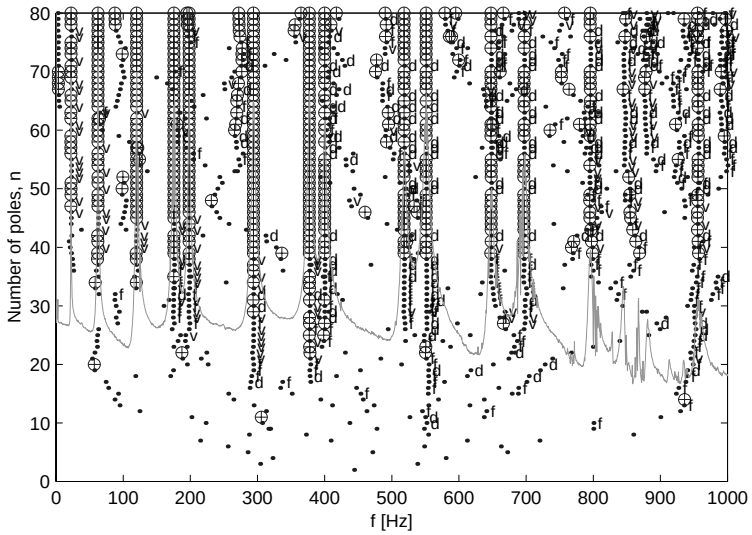

Figure 5.11: Stabilization diagram obtained by applying the **SSI-DATA** method to impact data. The criteria are 1% for frequencies, 5% for damping ratios and 2% for the mode shape correlations. The used symbols are: '⊕' for a stable pole; '**.**v' for a pole with stable frequency and vector; '**.**d' for a pole with stable frequency and damping; '**.**f' for a pole with stable frequency and '**.**' for a new pole.

Table 5.3: Estimated eigenfrequencies and damping ratios of **beam 2** in its undamaged state. The mean values and estimated standard deviations are based on 24 samples (6 setups × 4 impacts). The first 12 bending and torsion modes are given. The mode type has to be interpreted as follows: 'B' stands for bending; 'T' for torsion; then a counter is given and finally it is specified whether it is a symmetric mode (s) or an anti-symmetric one (a).

Mode type	B1 (s)	B2 (a)	B3 (s)	T1 (a)	B4 (a)	B5 (s)
$\overline{f}$ [Hz]	22.35	62.43	119.9	175.5	198.1	293.9
$\hat{\sigma}_f$ [Hz]	0.02	0.03	0.08	0.08	0.08	0.1
$\overline{\xi}$ [%]	0.5	0.38	0.5	0.64	0.44	0.45
$\hat{\sigma}_\xi$ [%]	0.1	0.01	0.1	0.06	0.01	0.02
Mode type	T2 (s)	B6 (a)	B7 (s)	T3 (a)	B8 (a)	T4 (s)
$\overline{f}$ [Hz]	377	400	518.1	551	647.5	695
$\hat{\sigma}_f$ [Hz]	0.1	0.1	0.2	0.1	0.2	2
$\overline{\xi}$ [%]	0.37	0.45	0.45	0.41	0.45	0.5
$\hat{\sigma}_\xi$ [%]	0.03	0.02	0.03	0.02	0.02	0.1

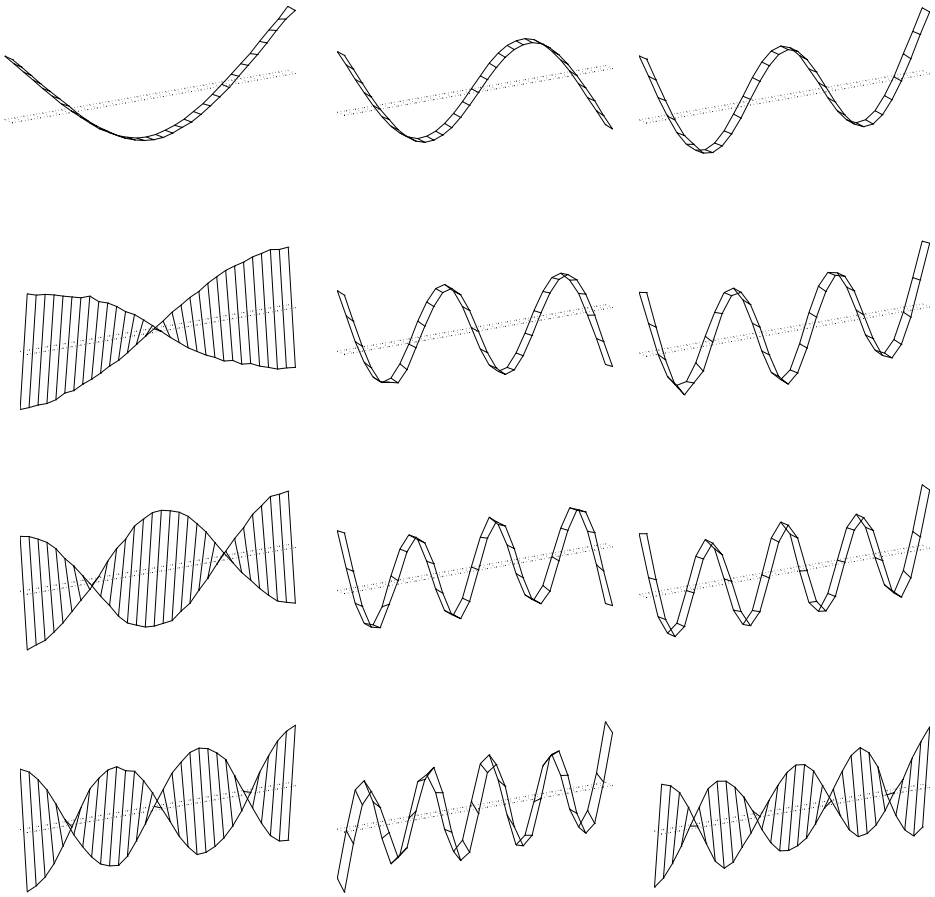

Figure 5.12: First 12 identified mode shapes, ordered from left to right from top to bottom. These mode shapes are obtained by applying the **SSI-DATA** method to impact data.

Postprocessing

Some postprocessing tools are applied to impact data from the first set-up of **beam 2** in its undamaged state. Each setup consists of 12 output channels. The data were sampled at a rate of 5000 Hz and 12288 data points were measured. Before identification the data was low-pass filtered and resampled at a rate of 1250 Hz. The **SSI-DATA** method is used to identify a 70-pole state-space model. Channels 1, 2 and 7 are chosen as reference channels in the identification. As explained in Subsection 3.7.1, the identified stochastic state-space model can be considered as a parametric spectrum estimate. Figures 5.13 and 5.14 compare some elements of this spectrum matrix with a non-parametric spectrum estimates (using

Welch's method, see Subsection 3.2.3). There is a remarkable agreement, indicating that the **SSI-DATA** method is able to identify successfully a high-order system.

Experience learnt that, when applying subspace methods to impact data, it is important to include enough zeros in the data before the impact takes place. Otherwise the amplitudes of the estimated spectrum will be a few orders of magnitude lower than Welch's periodogram. It was observed that the number of zeros before the impact should be at least the number of block rows in the data Hankel matrix (3.2). Without sufficient zeros, the last rows of this Hankel matrix would contain response data that only starts after the impact and would have a much lower energy content.

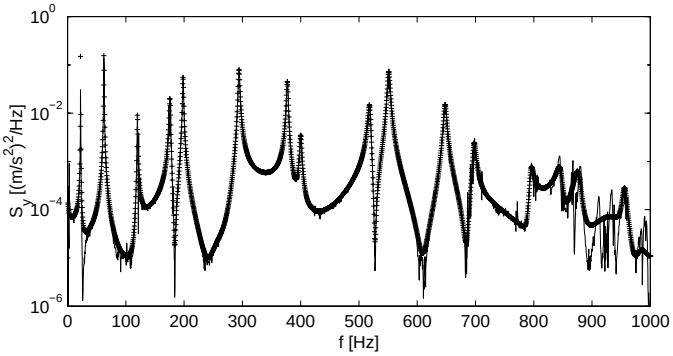

Figure 5.13: Comparison of power spectra of channel 12. The full line is Welch's periodogram; the crosses represent the **SSI-DATA** parametric estimate. Although the represented channel is not a reference channel, the agreement is excellent.

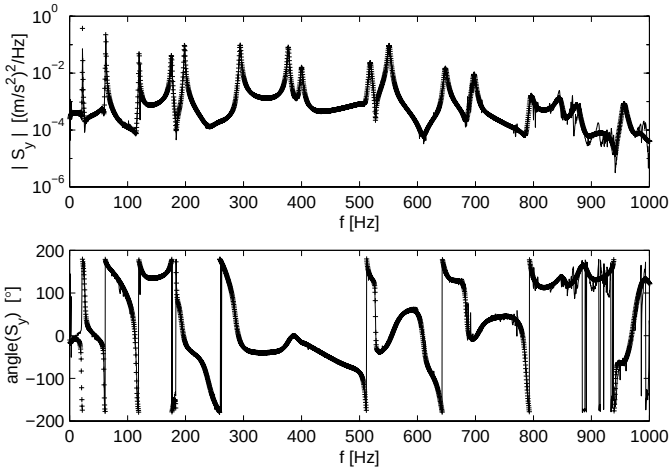

Figure 5.14: Comparison of cross spectra between channel 1 and channel 12. The full line is Welch's periodogram; the crosses represent the **SSI-DATA** parametric estimate. The top figure shows the absolute value of the spectrum; the bottom figure shows the phase angle. Again the agreement is excellent.

In a next stage the frequency content is further reduced by low-pass filtering. We concentrate on the first 5 modes to study the modal responses and the prediction errors (Subsection 3.7.2). The modal responses of the first output signal are shown in Figure 5.15. The prediction error sequence e_k of the same signal is shown in Figure 5.16. Classically, the prediction errors are white noise, but in this case, the prediction error sequence looks more like a low-pass filtered impulse. This is in fact no surprise, since the prediction errors not only depend on the modelling inaccuracies and the measurement noise but also on the "unknown" input. Notice that the input was measured in this case, but it is unknown in the sense that it was not used in the system identification method. From the covariance matrix of the prediction errors $R_e = \mathbf{E}[e_k e_k^T]$, shown in Figure 5.17, it is even possible to locate the unknown input.

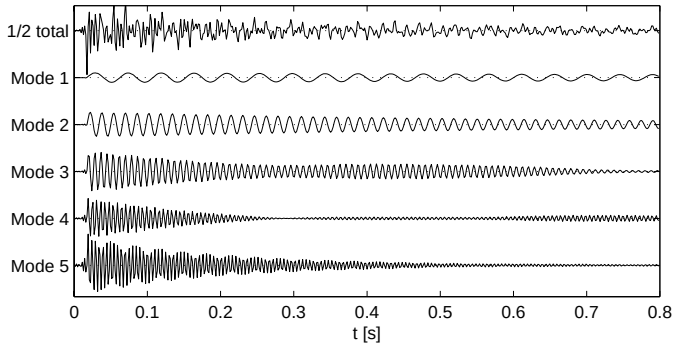

Figure 5.15: Modal responses of the first channel. The measured total response is shown in the top chart. The amplitudes of this signal have been multiplied by 0.5 for scaling purposes. The contributions of the 5 modes are subsequently presented.

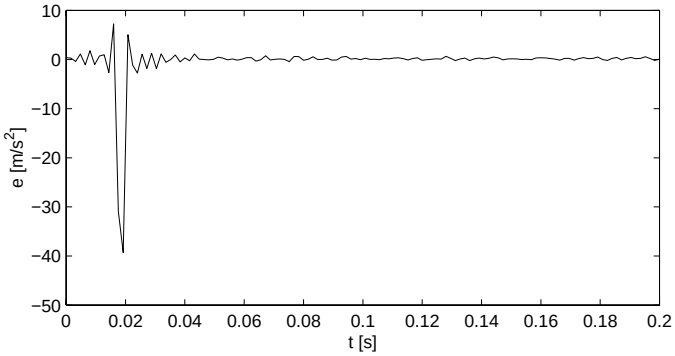

Figure 5.16: Prediction error of the first channel. It is not a white noise sequence, but rather a low-pass filtered impulse, where the offline filter was applied in both forward and backward direction. This filtering procedure corresponds to the `decimate` command of [SIGN97] that was indeed applied to the data.

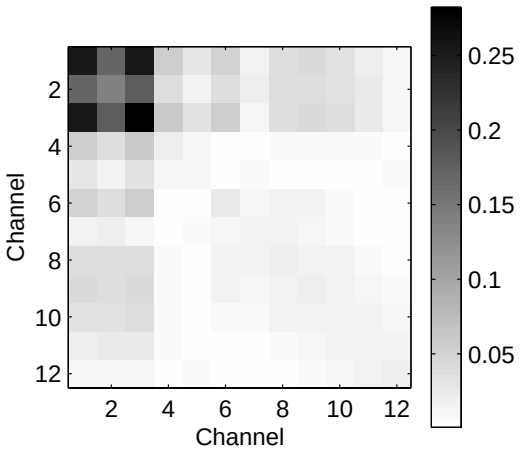

Figure 5.17: Covariance matrix R_e of the prediction errors. The largest values indicate the location of the input. The true excitation was indeed applied between accelerometer 1 and 3. The location of the sensors and the force is represented in Figure 5.18.

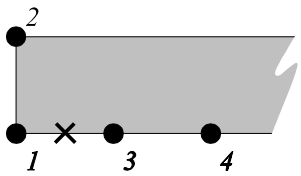

Figure 5.18: Top view of a part of the beam. The location of the sensors is represented by large dots. The hammer impact location is situated at the cross.

5.1.4 Evolution of the modal parameters

The **SSI-DATA** method is used to estimate the modal parameters of the beams at each intermediate load step. The evolution of eigenfrequencies and damping ratios of the beams throughout the damage stages is represented in Figures 5.19–5.22. Due to damage the eigenfrequencies are decreasing by 25% or less and the damping ratios are increasing by a factor 2 to 5. Contrary to an obstinate belief, it is not the case that the higher modes are more sensitive to damage.

It is important to judge of these changes with respect to the uncertainties of the estimates. The statistical analysis that was presented in Table 5.3 for **beam 2** in its undamaged state

is repeated for every state and for both beams. From the mean value $\bar{x}$ and estimated standard deviation $\hat{\sigma}_x$ of a stochastic variable x, the $100(1-\alpha)\%$ confidence interval on the true value of x is given by:

$$\left[\bar{x} - t_{\frac{\alpha}{2},\nu} \hat{\sigma}_x , \quad \bar{x} + t_{\frac{\alpha}{2},\nu} \hat{\sigma}_x \right]$$

where $t_{\alpha/2,\nu}$ is found from a statistical table of Student's t-distribution. The symbol ν is the number of **DOF**s, which is one less than the number of samples N in this case, $\nu = N - 1 = 23$. In order to compute the 95% confidence interval, for instance, we have $\alpha = 0.05$ and $t_{\alpha/2,\nu} = 2.07$. Figures 5.23–5.26 show the evolution of eigenfrequencies and damping ratios for modes 2, 3 and 4 together with the 95% confidence intervals. The decrease of eigenfrequencies is statistically relevant. Concerning damping, the situation is rather unclear. In general the damping seems to increase, but the uncertainty on the estimates is quite high.

As shown in [PEET96], the mode shapes are also changing due to damage. The changes remained small however. The mode shape curvatures are much more sensitive parameters than the mode shapes themselves. They are also a better indicator for local defects. Unfortunately it is numerically not evident to compute the curvatures of an estimated mode shape. Ideas related to the computation of modal curvatures and their use for damage localization can be found in [PAND91b, MAEC99, MAEC00a].

As a general conclusion of the laboratory beam tests, we can state that vibration-based damage detection is very promising. We should however not forget that the experimental conditions were more advantageous than in a real situation. Therefore Chapter 7 of this thesis will deal with a real case from civil engineering practice: an existing bridge was subjected to realistic damage scenarios and the dynamic tests were performed under varying environmental conditions that are possibly eroding the damage-detection potential of vibration-based monitoring.

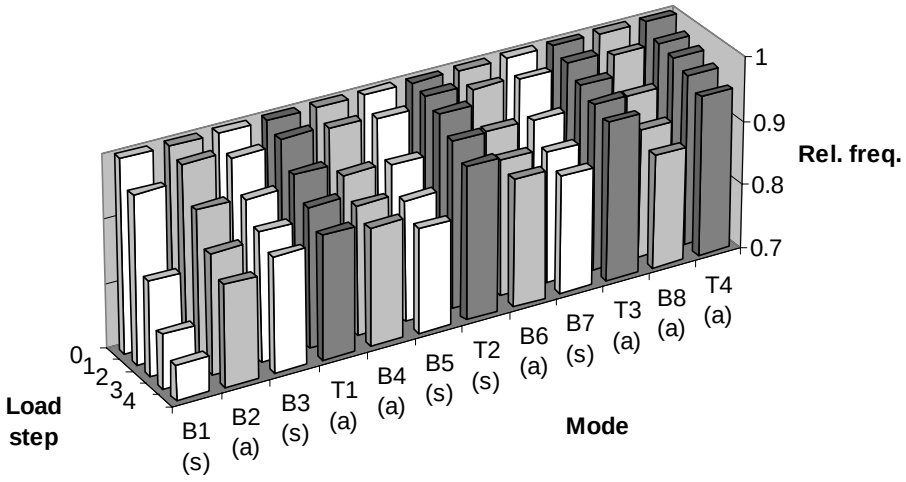

Figure 5.19: Relative changes due to damage of the first 12 eigenfrequencies of **beam 2**. The symmetric bending modes have white bars; the anti-symmetric have light gray bars and the torsion modes are represented by dark gray bars. The undamaged state is represented by load step 0, see Table 5.1. The first eigenfrequency decreases with 25% and the others with 14% or less.

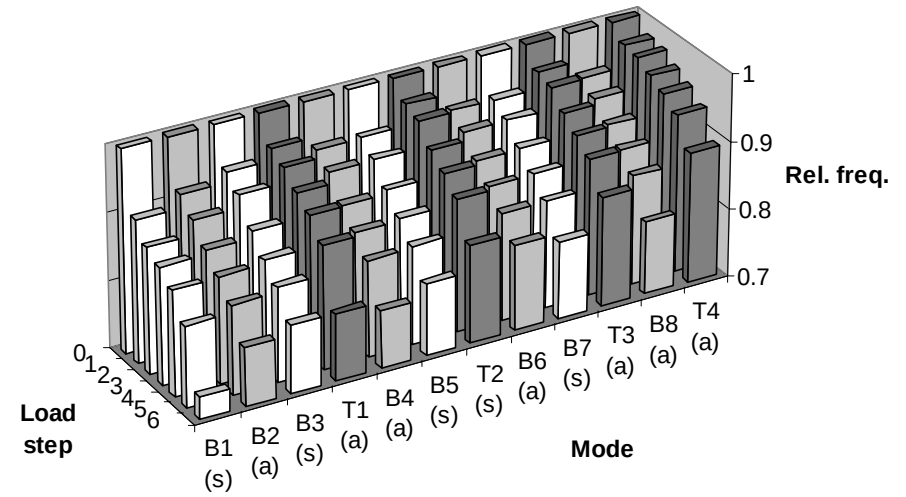

Figure 5.20: Relative changes due to damage of the first 12 eigenfrequencies of **beam 3**. The symmetric bending modes have white bars; the anti-symmetric have light gray bars and the torsion modes are represented by dark gray bars. The undamaged state is represented by load step 0, see Table 5.2. The first eigenfrequency decreases with 25% and the others with 22% or less.

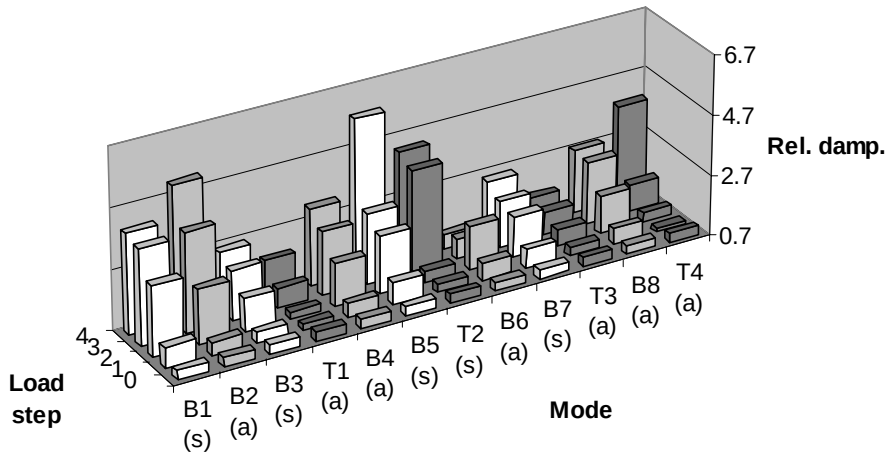

Figure 5.21: Relative changes due to damage of the first 12 modal damping ratios of **beam 2**. The order of the load steps is reversed as compared to Figure 5.19 to improve visibility. The damping ratios are increasing with a factor 2 to 5 due to damage.

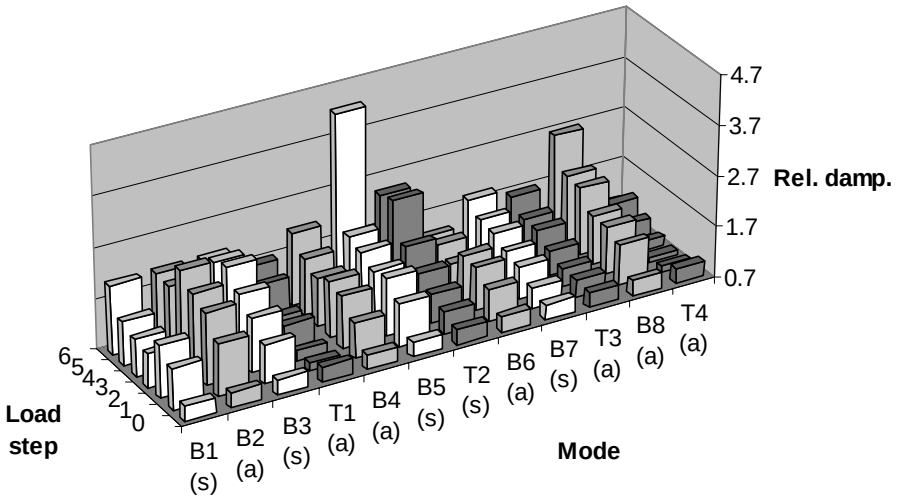

Figure 5.22: Relative changes due to damage of the first 12 modal damping ratios of **beam 3**. The order of the load steps is reversed as compared to Figure 5.20 to improve visibility. With an exception of mode 'B5 (s)', the damping ratios are increasing with a factor 2 due to damage.

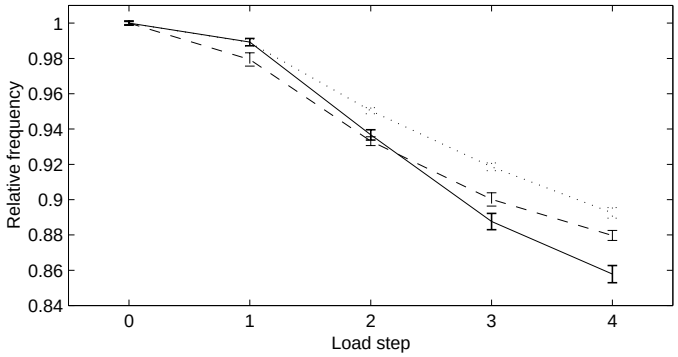

Figure 5.23: Relative eigenfrequency changes for mode 2, 3 and 4 (**beam 2**). The 95% confidence intervals are also given. The full line represents mode 2; the dashed line is mode 3 and the dotted line is mode 4. The decrease of the eigenfrequencies due to damage is statistically relevant. The results for the other modes are similar.

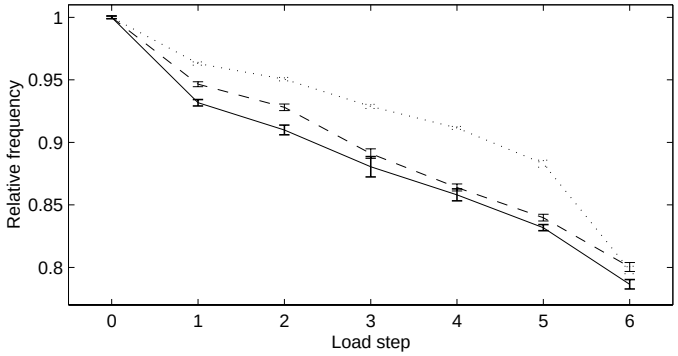

Figure 5.24: Relative eigenfrequency changes for mode 2, 3 and 4 (**beam 3**). The 95% confidence intervals are also given. The full line represents mode 2; the dashed line is mode 3 and the dotted line is mode 4. The decrease of the eigenfrequencies due to damage is statistically relevant. The results for the other modes are similar.

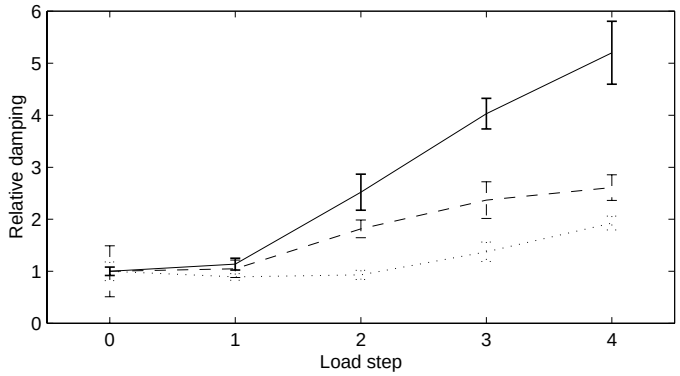

Figure 5.25: Relative damping ratio changes for mode 2, 3 and 4 (**beam 2**). The 95% confidence intervals are also given. The full line represents mode 2; the dashed line is mode 3 and the dotted line is mode 4. Damping seems to increase with damage, but the uncertainty on the damping estimates is quite high. The results for the other modes are similar.

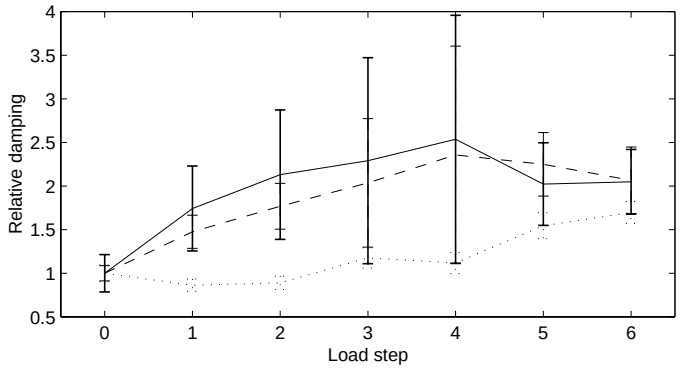

Figure 5.26: Relative damping ratio changes for mode 2, 3 and 4 (**beam 3**). The 95% confidence intervals are also given. The full line represents mode 2; the dashed line is mode 3 and the dotted line is mode 4. Damping seems to increase with damage, but the uncertainty on the damping estimates is quite high. The results for the other modes are similar.

5.2 STEEL MAST

5.2.1 Introduction

In the design process of a steel transmitter mast, the damping ratios of the lower modes are important factors. The wind turbulence spectrum (Figure 5.27) has a peak value at a very low frequency around 0.04 Hz [BALE93]. All eigenfrequencies of the considered structure are situated at the descending part of the turbulence power spectrum, and thus in fact only the few lower modes of vibration are important for determining the structure's response to dynamic wind load. The structure under consideration is a steel frame structure with antennae attached to the top. In order to prevent malfunctioning of the antennae, the rotation at the top has to be limited to 1°. Only once in 10 years, this value may be exceeded. The dynamic response (and thus the rotation angle) of a structure reaches its maximum at resonance, where the amplitude is inversely proportional to the damping ratio. So the damping is directly related to the maximum rotation angle. A high damping ratio means that the amount of steel needed to meet the specification of limited rotation can be reduced.

The only way to determine the true damping ratios is by performing a vibration test on the structure. Such a test does not only yield the damping ratios, but also the eigenfrequencies and the mode shapes at the sensor locations. This allows to validate and eventually update a finite element model of the structure. The most practical way to excite the mast is using the wind. Since it is very difficult, if not impossible, to measure the dynamic wind load, only responses were recorded and the mast tests constitutes an excellent real-life example to validate stochastic system identification methods.

The mast was tested twice with an interval of more than one year. The reason for the second test was that the dynamic behaviour of the mast changed because of the installation

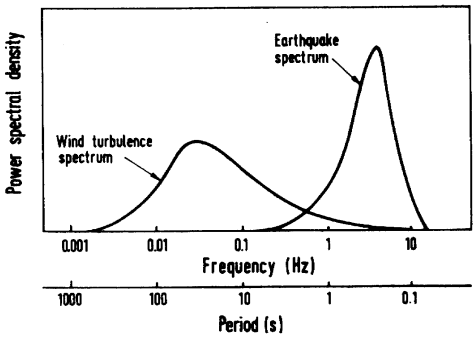

Figure 5.27: Typical wind turbulence spectrum compared with an earthquake spectrum [BALE93].

of eccentric antennae at the top (see further). Both tests are summarized in this thesis. More extensive results can be found in [PEET98a, PEET99f, PEET99e]. First the mast structure and the data acquisition is presented. Next the application of stochastic subspace identification to the vibration data is illustrated.

5.2.2 Data acquisition

The tested mast structure is a part of a cellular phone network. The mast is situated in the port of Antwerp. Figure 5.28 shows the mast on 24 February 1997, the date of the first test. Figure 5.29 is a photograph that was taken on 26 March 1998, the date of the second test. The difference is that the second time the sectorial antennae were installed. They are expected to have an important influence on the dynamics of the structure, since their added mass is considerable (+10%) and they are located close to the top, a position where large displacements occur. A typical cross section is given in Figure 5.30. The mast has a triangular cross section consisting of 3 circular hollow section profiles of which the section and the thickness decrease from bottom to top. The 3 main tubes are connected with smaller tubes forming the diagonal and horizontal members of the truss structure. The structure is composed of 5 segments of 6 m, reaching a height of 30 m. At the top in the centroid of the section an additional tube rises above the truss structure resulting in a total

Figure 5.28: Steel mast structure on 24 February 1997, before the installation of the antennae.

Figure 5.29: Steel mast structure on 26 March 1998, after the installation of the antennae.

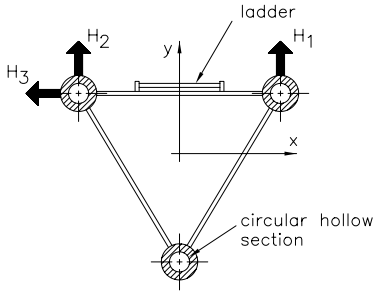

Figure 5.30: Cross section of the mast. The accelerometer positions are indicated with H1, H2 and H3.

height of 38 m. The antennae are connected to this tube at a height of 33 m. A ladder is attached to one side of the triangle. Together with the diagonals, this ladder is disturbing somewhat the symmetry of the structure. The mast is founded on a thick concrete slab supported by three piles.

The measured **DOF**s are the following: every 6 m, from 0 to 30 m, 3 horizontal accelerations were measured. Their measurement direction are indicated in Figure 5.30 as H1, H2 and H3. Assuming that the triangular cross section remains undeformed during the test, the 3 measured accelerations are sufficient to describe the complete horizontal movement of the considered section. At ground level (0 m) also 3 vertical accelerations were measured in order to have a complete description of all displacement components of the foundation. During the second test 2 supplementary perpendicular sensors were installed on the central tube at 33 m. These 2 sensors, also measuring in horizontal direction, allow a better characterization of the mode shapes. Due to the limited number of acquisition channels and high sensitivity accelerometers, the described measurement grid of 23 sensor positions was split in 4 setups. In output-only modal analysis where the input force remains unknown and may vary between the setups, the different measurement series can only be linked if there are some sensors in common. The three sensors at 30 m are suited as references since it is not expected that these are situated at a node of any mode shape.

The cut-off frequency of the analog anti-aliasing filter was set at 20 Hz. The data were sampled at a rate of 100 Hz during 5 minutes for each setup. Figure 5.31 compares the power spectra of the signals measured at the same location in both tests. It is clear that the dynamic behaviour of the mast changed quite drastically due to the added eccentric mass of the antennae.

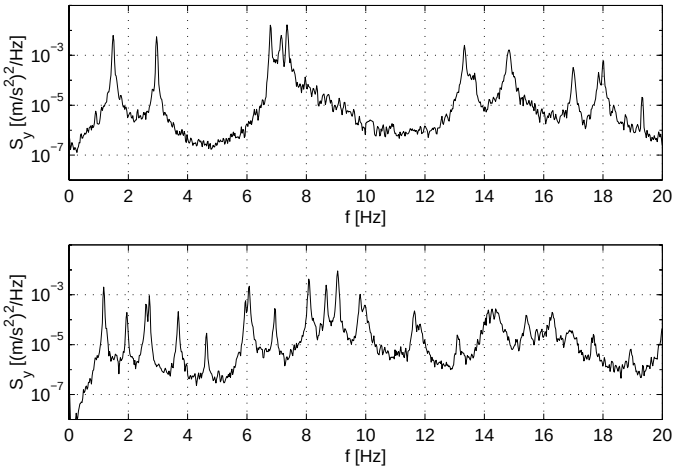

Figure 5.31: Comparison of power spectra of the signals measured at 30 m in Y-direction (Figure 5.30). The top spectrum represents the first test (24 February 1997); the bottom spectrum originates from the second test (26 March 1998). The differences are due to the installation of the antennae.

From the relative heights of the peaks in the *acceleration* spectra, one can definitely not conclude that only the lower modes are important for determining the structure's response to dynamic wind load. However, as stated in the introduction, the most important design criterion for this kind of structures is a maximum rotation angle. Therefore *displacements* are the quantities to look at. Roughly speaking, the peaks in Figure 5.31 have to be divided by ω^2 to obtain displacements and, indeed, the lower modes are becoming more important.

5.2.3 System identification

The data-driven stochastic subspace identification (**SSI-DATA**) method is applied to the mast response data. We emphasize the differences between the two tests and examine the influence of the choice and number of reference sensors on the identification results.

Modal parameters

Before identification the data was decimated with factor 8: it was filtered through a digital low-pass filter with a cut-off frequency of 5 Hz and resampled at 12.5 Hz. This operation reduces the number of data points and makes the identification more accurate in the considered frequency range $0 \rightarrow 5$ Hz. The higher modes, situated in the range $5 \rightarrow 20$ Hz, are identified in a separate analysis without low-pass filtering and using only a limited time frame. As usual, the modal parameters are selected from a stabilization diagram (Figure 5.32). Table 5.4 presents the mean values $\overline{f}, \overline{\xi}$ and estimated standard deviations $\hat{\sigma}_f$, $\hat{\sigma}_\xi$

of the first 7 modes for both tests. We may have high confidence in the identified frequencies, since their standard deviations are extremely low. Due to the increased mass, the eigenfrequencies of the second test are lower. As usual the damping ratio estimates are more uncertain. The very low damping values indicate that there are not much damping mechanisms present in such a steel structure. It seems that fixing the antennae had some positive influence on the damping ratios, in the sense that they are higher for the lower modes. Nevertheless, they are still lower than the values that can be found in design codes, which is a rather unsafe situation. Some representative mode shapes identified from the second test are shown in Figure 5.33. The mode shape results from the first test and a comparison with an **FE** analysis can be found in [PEET98a].

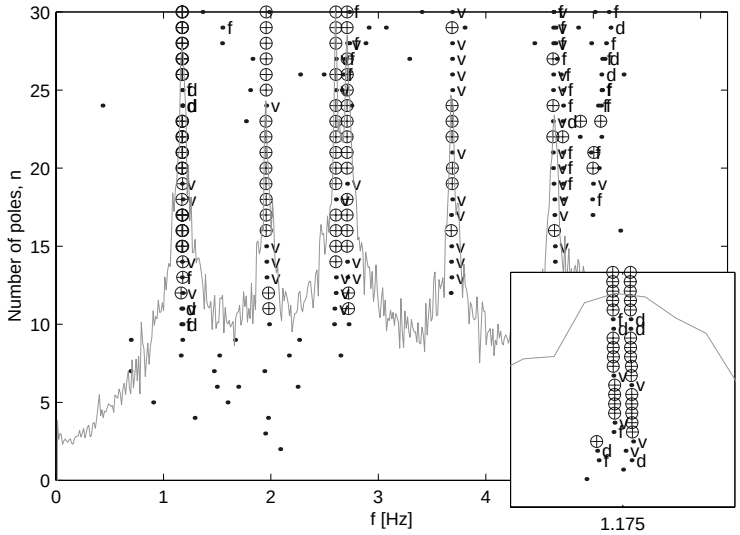

Figure 5.32: Stabilization diagram obtained by applying the **SSI-DATA** method to low-pass filtered mast data (second test). The criteria are 1% for frequencies, 5% for damping ratios and 2% for the mode shape correlations. The used symbols are: '⊕' for a stable pole; '.v' for a pole with stable frequency and vector; '.d' for a pole with stable frequency and damping; '.f' for a pole with stable frequency and '.' for a new pole. A zoom is added that concentrate on the close modes around 1.175 Hz.

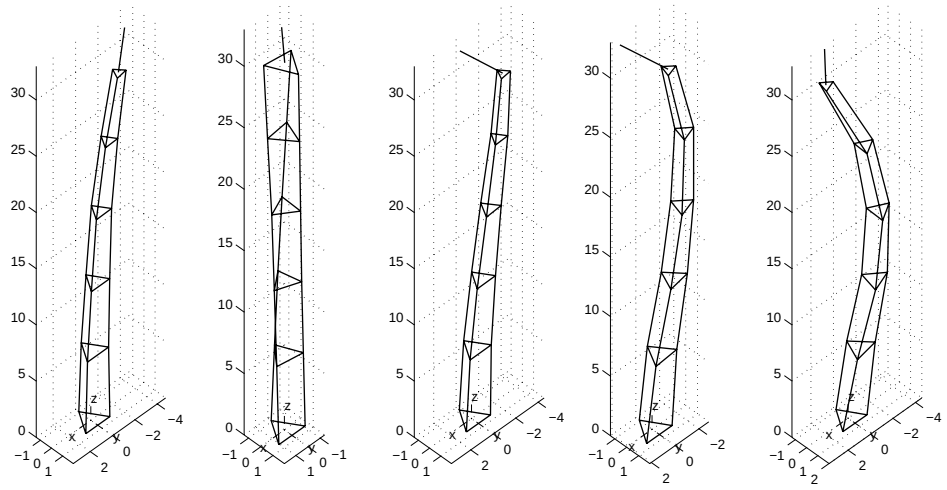

1. f = 1.17 Hz. **3**. f = 1.95 Hz. **5**. f = 2.71 Hz. **7**. f = 4.63 Hz. **9**. f = 6.08 Hz.

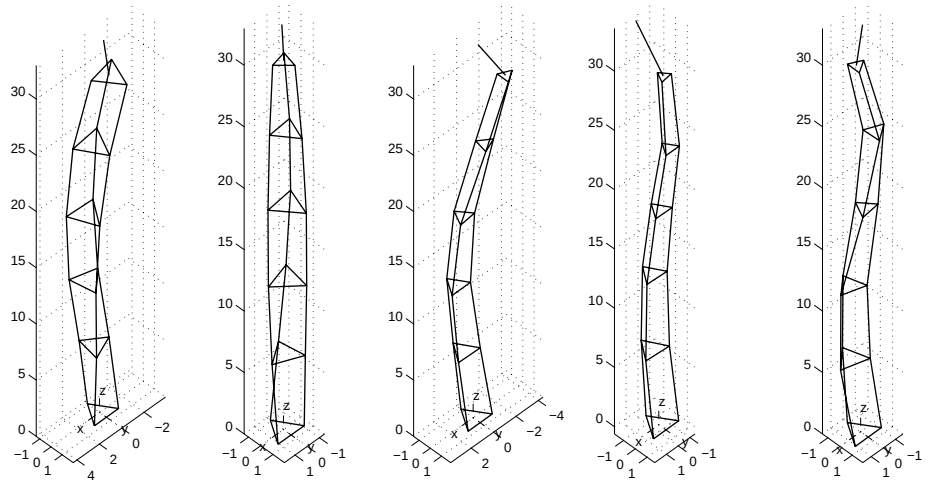

10. f = 6.95 Hz. **11**. f = 8.09 Hz. **13**. f = 9.06 Hz. **17**. f = 11.8 Hz. **18**. f = 13.1 Hz.

Figure 5.33: Some representative mode shapes (second test), identified with the **SSI-DATA** method. The mode numbers are indicated in bold. Also the corresponding eigenfrequencies are given. The Z-axis represents the height with a unit of 1 m. The other axes represent relative modal amplitudes.

Table 5.4: Estimated eigenfrequencies and damping ratios of both tests of the mast structure (in '97 without and in '98 with antennae). The mean values and estimated standard deviations are based on 8 samples (4 setups, each setup measured twice). The first 7 modes are given.

Mode number		1	2	3	4	5	6	7
'97 Test	$\overline{f}$ [Hz]	1.487	1.492	2.953	2.976	6.793	7.155	7.343
	$\hat{\sigma}_f$ [Hz]	0	0	0	0	0	0	0
	$\overline{\xi}$ [%]	0.5	0.4	0.2	0.18	0.14	0.32	0.29
	$\hat{\sigma}_\xi$ [%]	0.2	0.3	0.1	0.07	0.03	0.07	0.08
'98 Test	$\overline{f}$ [Hz]	1.17	1.179	1.953	2.61	2.711	3.687	4.628
	$\hat{\sigma}_f$ [Hz]	0	0	0	0	0	0	0
	$\overline{\xi}$ [%]	0.5	0.7	0.7	0.3	0.17	0.2	0.2
	$\hat{\sigma}_\xi$ [%]	0.2	0.2	0.1	0.1	0.05	0.1	0.1

Influence of reference sensors

The low-pass filtered data of the second test is used to examine the influence of the choice and number of references on the identification results. Two types of analyses are performed. In a first analysis, all outputs $l = 9$ are considered as references $r = 9$. This case will be called "full analysis". Next, only the outputs located at a height of 30 m are considered as references $r = 3$ and the others are partially omitted in the identification process, as explained in Subsection 3.5.1. This case is called "reduced analysis". The number of data points *N* and half the number of block rows *i* in the data Hankel matrix (3.2) are the same in both cases, so that the reduced analysis only required 44% of the computational time as compared to the full analysis; see equation (3.45). We have chosen $i = 10$, so that the maximum model order equals $ri = 30$ in the reduced analysis and $li = 90$ in the full analysis. This is reflected in Figure 5.34, where the principal angles (Section 3.6) obtained in both cases are shown. The graph suggests that the reduced analysis required a lower-order model to fit the data. We can think of two possible explanations: the reduced analysis is not able to extract all features from the data or it gets faster rid of the noise because the reference outputs are chosen so as to have the best signal-to-noise ratios. The detailed analysis in [PEET99f] revealed that the estimated modal parameters are almost exactly identical in both analyses. So if the first explanation would be true, it seems to have no consequences on the quality of the modal parameters.

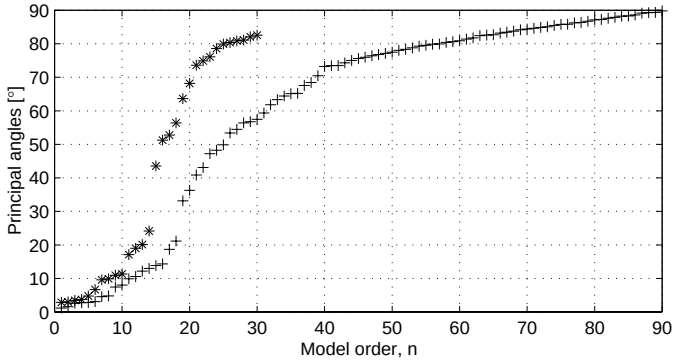

Figure 5.34: Principal angles between the row space of future outputs and the row space of past outputs. The used symbols are: '*' for the reduced analysis and '+' for the full analysis. The true model order is found from the gap between the principal angles. The gap for the reduced analysis is situated at $n = 14$ and for the full analysis at $n = 18$.

However, there are some objective differences between the full and reduced analysis. In Figure 5.35, the power spectra from a reference signal are compared. The full and reduced analyses perform equally well. Figure 5.36 shows the spectra of a non-reference signal. In this case the reduced analysis had some problems in modelling the frequency ranges between resonance peaks.

It is also interesting to take a look at the prediction errors (Subsection 3.7.2). The prediction errors cumulate modelling inaccuracies, measurement noise and the unknown input. In order to obtain one number, the total prediction error $\varepsilon^{(i)}$ for channel *i* is defined as:

$$\varepsilon^{(i)} = \sqrt{\frac{\sum_{k=1}^{N} (y_k^{(i)} - \hat{y}_k^{(i)})^2}{\sum_{k=1}^{N} (y_k^{(i)})^2}} \times 100\%$$

where $y_k^{(i)}$ is the i^{th} output channel. In Table 5.5, the prediction errors for two different reduced analyses and the full analysis are presented. It is confirmed that the non-reference channels are not so well modelled as the reference channels.

From the comparison between the reduced and full analysis, we can conclude that the reduced analysis is considerably faster, while it yields identical results in terms of the identified modal parameters. The analysis of spectra and prediction errors made clear that the non-reference channels are more affected by modelling errors. These errors are mainly situated between the resonance peaks and not at the resonances.

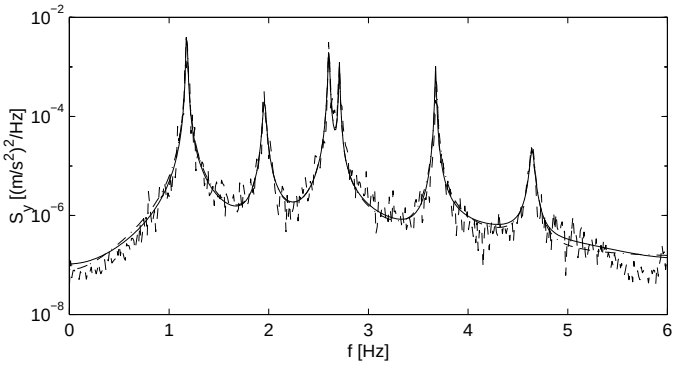

Figure 5.35: Comparison of power spectra of a reference signal. The dashed line is Welch's periodogram; the full line represents the full analysis and the dash-dotted line is the spectrum from the reduced analysis. All spectra are well in line.

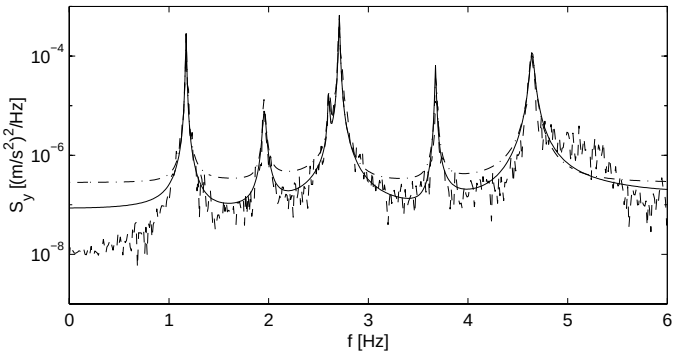

Figure 5.36: Comparison of power spectra of a non-reference signal. The dashed line is Welch's periodogram; the full line represents the full analysis and the dash-dotted line is the spectrum from the reduced analysis. The frequency ranges between resonance peaks is not well tracked by the reduced analysis.

Table 5.5: Total prediction errors $\varepsilon^{(i)}$ [%] for all 9 output channels. Two reduced analyses (one with channels 1, 2, 3 as references, the other with channels 2, 3, 8 as references) and the full analysis are presented. In the reduced analyses, the prediction errors are lower for the reference channels and comparable with the full analysis. The prediction errors for non-reference channels are considerably higher.

Channel	1	2	3	4	5	6	7	8	9
References: 1, 2, 3	**15**	**14**	**14**	17	17	24	23	23	25
References: 2, 3, 8	17	**13**	**14**	18	13	24	22	**14**	27
Full analysis	13	13	14	13	13	18	13	14	14

5.3 CONCLUSIONS

To complement the simulation example of Chapter 2 and 3, two real vibration experiments were discussed in this chapter. They confirmed the identification quality of stochastic subspace identification methods.

The beam tests proved that it is fundamentally possible to measure the damage-induced changes in the dynamics of a structure. The main purpose of the mast test was to measure the damping ratios. The data was also used to study the influence of the choice and number of reference sensors on the identification results.

6

ENVIRONMENTAL MODELS OF VIBRATING STRUCTURES

In this chapter, a method is proposed to distinguish temperature effects from damage events. The chapter is organized as follows. Section 6.1 motivates the chapter: from literature and our own experience it is clear that there is an influence of temperature on the eigenfrequencies of a construction. A system identification approach is proposed to quantify this influence. Section 6.2 discusses how an accurate environmental model can be obtained from temperature - frequency data. The use of the environmental model for simulations is outlined in Section 6.3. The idea is that, if the bridge has changed, the simulated frequencies will significantly deviate from the measured frequencies. All elements of the proposed damage detection method are synthesized in Section 6.4. Section 6.5, finally, concludes the chapter.

6.1 INTRODUCTION

6.1.1 Motivation

In almost all studies on vibration-based damage detection, the varying environmental conditions are disregarded. Indeed, in numerical simulations and laboratory tests they do not play any role, but when it comes to a real-life situation as the monitoring of a bridge, it can be suspected that temperature differences of about 50°C during the year will have an influence on the dynamic characteristics. It is for instance known that the Young's modulus of concrete decreases with increasing temperature and that also boundary conditions may be temperature-dependent. Both parameters have their influence on the eigenfrequencies. Damage (a loss of stiffness), on the other hand, decreases the eigenfrequencies (Take a look at Figures 5.19 and 5.20!). The problem is that damage-induced frequency changes can be completely masked by changes due to normal varying environmental parameters. Figure 6.1 synthesizes the motivation of this chapter. It is a preview of the results obtained on the Z24-Bridge that will be treated in full detail in Chapter 7.

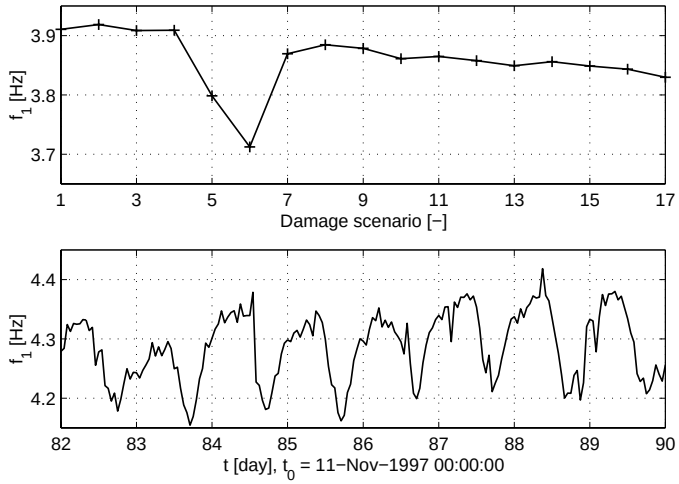

Figure 6.1: Damage events *vs.* temperature effects on the first eigenfrequency of the Z24-Bridge. The top figure represents the evolution of the frequency as a function of the applied damage scenarios. Scenarios 3 to 7 are reversible (see Chapter 7 for details). The bottom figure represents these temperature effects on the first eigenfrequency during a cold period in the beginning of February 1998. The results of this chapter were already used to filter out the temperature effects in the top figure. The scaling of the *y*-axis is the same in both figures. The normal frequency changes are as large as the changes due to damage!

Other experimental evidence of the relation between temperature and eigenfrequencies can be found in literature. Alampalli [ALAM98] reports that the relative eigenfrequency differences δf of a bridge due to freezing of the supports ($\delta f = 40 - 50\%$) were an order of magnitude larger than changes due to damage ($\delta f = 3 - 8\%$), which was in this case an artificial saw cut across the bottom flanges of both girders. It must be mentioned that the studied bridge was relatively small, with a span of 6.76 m and a width of 5.26 m and it was tested using an impact hammer. Roberts and Pearson [ROBE98] are describing a monitoring program on a 9-span bridge with a total length of 840 m. They found that normal environmental changes could account for changes in eigenfrequencies of as much as $3 - 4\%$ during the year. Farrar *et al.* [FARR97] found that the first eigenfrequency of the Alamosa Canyon Bridge varies approximately 5% during a 24 h time period. In a paper by Sohn *et al.* [SOHN99], the same bridge data is used to build a regression model that describes the variation of eigenfrequencies due to varying temperatures. The model is used to establish confidence intervals of the frequencies for a new temperature profile. Rücker *et al.* [RUCK95] showed that the temperature effects on the dynamics of a 7-span highway bridge in Berlin can also not be neglected. Rohrmann *et al.* [ROHR00] are examining the physical phenomena that are possibly causing the frequency changes of 10% during the year observed at that bridge. Finally, Askegaard and Mossing [ASKE88] found that a 3-span reinforced concrete footbridge exhibits normal frequency variations of 10% during the year.

Mode-shape-based damage identification methods may still work in the presence of temperature variations. Most of above observations are the result of a continuous-monitoring program that only consists of a few accelerometers (in order to reduce the costs). Theoretically, one well-placed sensor suffices to retrieve the eigenfrequency information. Owing to the limited number of sensors, experimental evidence of the influence of temperature on the mode shapes is lacking. It is however generally assumed that an eventual influence will be much smaller than the local change in the mode shape (or its curvature) that would occur at the location of damage. These local changes are typically the basis for mode-shape-based damage localization methods.

6.1.2 A system identification approach

From literature and our own experience it is clear that, especially in continuous monitoring systems, the need arises to separate abnormal frequency changes from normal changes. The idea is to find an *environmental model* that quantifies the relation between environmental parameters and eigenfrequencies. Having a model at hand, it would be possible to predict the frequencies of the structure from measured temperatures. If the prediction of a frequency does not correspond (within certain confidence intervals) to the measured frequency, something "abnormal" is going on and the structure is possibly damaged.

A first approach to establish an environmental model could be a detailed analysis of the physics that drive the eigenfrequency changes. From material research it should be able to find a relation between temperature and the *dynamic* Young's modulus *E* of concrete and asphalt. The eigenfrequencies of a homogeneous specimen are proportional to the square root of Young's modulus: $f \sim \sqrt{E}$. Another physical fact is that freezing of the soil changes the boundary conditions of a structure [ALAM98] and this affect again the structural stiffness and thus the eigenfrequencies. One could try to quantify this (nonlinear) relation. The full story is even more complex. A single structure may consist of steel, concrete and asphalt parts that all play their role in the stiffness. In the process of heating up and cooling down, the thermal inertia of these materials are also important and temperature differentials will exist. Most references cited in previous subsection are giving physical explanations for the frequency changes, however they do not explicitly quantify it. In Rohrmann *et al.* [ROHR00] the physical phenomena are examined in more detail by building a combined thermal-structural **FE** model that uses meteorological data of the Berlin area to compute eigenfrequencies of the studied bridge.

From all this, it may be clear that finding a "physical" environmental model is almost impossible. In these situations, one typically relies upon a *system identification approach*. Mathematical methods are used to derive a black-box model that is entirely based on measurements.

In Chapter 3, the inputs are unmeasurable ambient forces and *output-only* system identification methods are used to estimate a model from measured output data (accelerations). In a second step eigenfrequencies are obtained from the modal decomposition of the model. In this chapter, the inputs are measurable ambient parameters (temperatures) and the outputs are the estimated eigenfrequencies. Hence classical *input-output* system identification can be used to estimate a model. In a second step the model will be used for simulation. A whole chapter (Chapter 2) was devoted to justify the choice of a model structure that was assumed in the identification. The chosen models could all represent a vibrating structure. Here, such a justification is not given and a (simple) model structure is proposed that is not necessarily able to represent the "true" system of temperature-driven frequency changes. However, model validation tools are applied to ensure that the model accurately describes the input-output behaviour so that it can be used with confidence for simulations. Except for the derivation of the simulation error and its statistics, this chapter was inspired by [LJUN99].

6.2 IDENTIFYING THE MODEL

6.2.1 ARX models

A straightforward approach to obtain an environmental model is to apply (multiple) linear regression: a relation between a frequency and some of the environmental parameters measured at the same time instant is derived by applying linear least squares to the data (see for instance [MONT91]). These "static" linear regression models, that only relate simultaneously measured data, are not very flexible in the sense that they are not able to model the dynamics of the heating up/cooling down process of the structure. Therefore we are looking at "dynamic" models instead.

Probably the most simple dynamic model described in the system identification literature (see for instance [LJUN99]) is the **ARX** model that consists of an **A**uto-**R**egressive output and an e**X**ogeneous input part:

$$y_k + a_1 y_{k-1} + \ldots + a_{n_a} y_{k-n_a} = b_1 u_{k-n_k} + b_2 u_{k-n_k-1} + \ldots + b_{n_b} u_{k-n_k-n_b+1} + e_k \tag{6.1}$$

where y_k is the output — in this case an eigenfrequency — at time instant k; u_k is the input — in this case a temperature — and e_k is the equation error term modelling the disturbances that act on the input-output process. Typical sources for the disturbances are unmodelled inputs and measurement noise. This term is not known, but it is assumed that it is white noise, with zero mean $\mathbf{E}[e_k] = 0$ and covariance

$$\mathbf{E}[e_{k+i} e_k] = \lambda \delta_i \tag{6.2}$$

For establishing confidence intervals on the model, we additionally assume that e_k has a Gaussian distribution. The **ARX** model is characterized by 3 numbers: the auto-regressive order n_a, the exogeneous order n_b and the pure time delay between input and output n_k. The orders n_a and n_b are determining the number of model parameters, gathered in the column vector θ:

$$\theta^T = [\, a_i \ (i=1,\ldots,n_a) \quad b_j \ (j=1,\ldots,n_b) \,] \tag{6.3}$$

By introducing the shift operator, $q^{-1} y_k = y_{k-1}$, and defining the operator polynomials:

$$\begin{aligned} a(q) &= 1 + a_1 q^{-1} + \ldots + a_{n_a} q^{-n_a} \\ b(q) &= b_1 q^{-n_k} + b_2 q^{-n_k-1} + \ldots + b_{n_b} q^{-n_k-n_b+1} \end{aligned} \tag{6.4}$$

the **ARX** model can also be written as:

$$a(q)y_k = b(q)u_k + e_k \tag{6.5}$$

The "static" regression model corresponds to the **ARX** model with a special choice of the model orders and time delay. More specifically, it is an ARX010 model (with $[n_a, n_b, n_k] = [0,1,0]$):

$$y_k = b_1 u_k + e_k \tag{6.6}$$

If more than 1 input variable is included, Equations (6.1) and (6.6) are still valid but u_k is a column vector and the b coefficients are row vectors. The advantage of general **ARX** models over static regression models is that they are dynamic models: the current output and input are related to outputs and inputs at previous time instants.

In system identification the data is often normalized: the means are removed (otherwise there would be an offset term in Equations (6.1) and (6.6)) and the result is divided by the sample standard deviation. The mean value $\bar{x}$ and sample standard deviation $\hat{\sigma}_x$ of variable x are defined as:

$$\bar{x} = \frac{1}{N}\sum_{k=1}^{N} x_k \ , \quad \hat{\sigma}_x = \sqrt{\frac{1}{N-1}\sum_{k=1}^{N}(x_k - \bar{x})^2} \tag{6.7}$$

Where x_k denotes a sample of variable x. The notation $\hat{\sigma}_x$ is explained by the fact that it is an unbiased estimate of the true standard deviation σ_x, in case x is a stochastic variable. The normalized input and output data u_k, y_k are then computed from the **m**easured data $u_k^{\mathrm{m}}, y_k^{\mathrm{m}}$ as:

$$u_k = \frac{u_k^{\mathrm{m}} - \bar{u}}{\hat{\sigma}_u} \ , \quad y_k = \frac{y_k^{\mathrm{m}} - \bar{y}}{\hat{\sigma}_y} \tag{6.8}$$

It can be instrumental to transform an identified **ARX** model back to the engineering units of the original data. This is achieved by introducing Equation (6.8) in the "normalized" **ARX** model (6.5):

$$a(q)y_k^{\mathrm{m}} = b(q)\frac{\hat{\sigma}_y}{\hat{\sigma}_u}u_k^{\mathrm{m}} + \hat{\sigma}_y e_k + c \tag{6.9}$$

where the offset c is computed as:

$$c = a(1)\bar{y} - b(1)\frac{\hat{\sigma}_y}{\hat{\sigma}_u}\bar{u} \tag{6.10}$$

6.2.2 ARX models and least squares (LS)

The popularity of **ARX** models is based on the fact that an estimate of the parameter vector θ is easily obtained by applying linear **L**east **S**quares (**LS**). To show this, the **ARX** equation (6.1) is reformulated as:

$$y_k = \varphi_k^T \theta + e_k$$

with:

$$\varphi_k^T = [\ -y_{k-1} \ \ldots \ -y_{k-n_a} \ u_{k-n_k} \ \ldots \ u_{k-n_k-n_b+1}]$$

Assuming that the number of available input-output samples is such that this equation can be written down *N* times, following matrix equation is obtained:

$$Y = Z\,\theta + E$$

in which following definitions have been used:

$$Y = \begin{pmatrix} y_1 \\ y_2 \\ \ldots \\ y_N \end{pmatrix} \in \mathbb{R}^N \ , \quad Z = \begin{pmatrix} \varphi_1^T \\ \varphi_2^T \\ \ldots \\ \varphi_N^T \end{pmatrix} \in \mathbb{R}^{N\times(n_a+n_b)} \ , \quad E = \begin{pmatrix} e_1 \\ e_2 \\ \ldots \\ e_N \end{pmatrix} \in \mathbb{R}^N$$

This over-determined set of equations is solved in a **LS** sense to yield an estimate of θ:

$$\hat{\theta} = (Z^T Z)^{-1} Z^T Y$$

In order to examine the statistical properties of the estimate, it is assumed that the "true" system can be described by:

$$y_k = \varphi_k^T \theta_0 + e_k^0 \ , \quad \mathbf{E}[(e_k^0)^2] = \lambda_0 \tag{6.11}$$

We also assume, for the moment, that φ_k is a deterministic sequence. This corresponds to the usual **LS** assumption that the regressor variable is deterministic (i.e. it can be measured without an error) whereas the dependent variable is stochastic. Under these assumptions it can be proven that [LJUN99]:

- $\hat{\theta}$ is a consistent estimate of θ_0, i.e. $\hat{\theta} \to \theta_0$ as $N \to \infty$.
- The **LS** estimate is unbiased, i.e.

$$\mathbf{E}[\hat{\theta}] = (Z^T Z)^{-1} Z^T \mathbf{E}[Y] = (Z^T Z)^{-1} Z^T Z \, \theta_0 = \theta_0$$

  The derivation uses the fact that φ_k is a deterministic sequence and that the noise has zero mean.

- The covariance of the **LS** estimate is given by:

$$P_{\hat{\theta}} = \mathbf{E}[(\hat{\theta} - \theta_0)(\hat{\theta} - \theta_0)^T] = \lambda_0 (Z^T Z)^{-1}$$

  The true noise covariance λ_0 is of course unknown, but an unbiased estimate is provided by (see [LJUN99], Page 554):

$$\hat{\lambda} = \frac{1}{N-d} \sum_{k=1}^{N} \varepsilon_k^2(\hat{\theta}) = \frac{1}{N-d} \sum_{k=1}^{N} (y_k - \varphi_k^T \hat{\theta})^2 = \frac{1}{N-d} |Y - Z\hat{\theta}|^2$$

  in which the number of estimated parameters is denoted as $d = \dim(\theta)$ and the residuals are defined as $\varepsilon_k(\hat{\theta}) = y_k - \varphi_k^T \hat{\theta}$. By consequence, an *estimate* of the covariance of the *estimate* can be computed as:

$$\hat{P}_{\hat{\theta}} = \hat{\lambda} (Z^T Z)^{-1} \in \mathbb{R}^{d \times d} \tag{6.12}$$

Notice that it was necessary to assume that φ_k is a deterministic sequence. On the other hand y_k is a stochastic variable as indicated by Equation (6.11). Since φ_k contains past outputs, both assumptions are contradictory and, strictly speaking, the derivations of the statistical properties are not valid. In [LJUN99], two chapters are spent examining the statistical properties of general input-output models. Evidently, the proves are more involved, but when applying the results to the **ARX** case, the same expressions as above are found. The difference is that the covariance matrix $P_{\hat{\theta}}$ has to be considered as the asymptotic (i.e. for $N \to \infty$) covariance matrix.

6.2.3 Quality assessment

Having a lot of input candidates (e.g. the temperature has been measured at several locations) and the possible choices for the model orders and the time delay n_a, n_b, n_k there are many different **ARX** models that can be identified from the data. By consequence, criteria are needed that assess and compare the quality of models. We will consider a few of them. A more general discussion on the issue can be found in [LJUN99].

The Least Squares method minimizes the sum of squares of the equation errors e_k. A first quality criterion is thus the value of the loss function:

$$V = \frac{1}{N} \sum_{k=1}^{N} \varepsilon_k^2(\hat{\theta}) \tag{6.13}$$

The problem of using the loss function as a quality criterion is that it continuously decreases as the model order increases. Other criteria include penalties for model complexity like Akaike's **F**inal **P**rediction **E**rror (**FPE**) criterion or Rissanen's **M**inimum **D**escription **L**ength (**MDL**) criterion [LJUN99].

The square roots of the diagonal elements of the estimated covariance matrix $\hat{P}_{\hat{\theta}}$ (6.12) are estimates of the standard deviations $\hat{\sigma}_{\hat{\theta}_i}$ of the model parameter estimates $\hat{\theta}_i$ ($i = 1,...,d$). These standard deviations are a measure of the accuracy of the estimate. If some parameters have a large relative standard deviation, too many parameters have been included in the model and the model order should be reduced.

One of the basic assumptions is that e_k^0 is a white noise sequence. This means that the noise covariance function equals, see Equation (6.2):

$$R_e^0(i) = \mathbf{E}[e_{k+i}^0 e_k^0] = \lambda_0 \delta_i$$

A quality check consists of verifying whether the estimated model yields residuals that can be considered as white. Hereto the covariance function is estimated as:

$$\hat{R}_e(i) = \frac{1}{N} \sum_{k=1}^{N} \varepsilon_{k+i}(\hat{\theta}) \varepsilon_k(\hat{\theta})$$

This function should be "close to zero" for time lags $i \neq 0$. Confidence intervals on being "close to zero" are in this case provided by the statistical F-distribution. If the residuals cannot be considered as white noise, they still contain information about the system that it is not picked up by the model.

If enough data is available, it can be split in two data sets: *estimation data* that is used to estimate the model and *validation data* that is not yet used. Evidently, assessing the quality of a model using validation data is more challenging than using estimation data.

6.3 USING THE MODEL FOR SIMULATIONS

Once a good model is obtained, it can be used for simulations[1]. New input measurements are fed to the model generating the outputs. If the simulated output values are "deviating too much" from the measured ones, the model is not valid anymore. If we were sure about the initial quality of the model, we can conclude that the system has changed. To make it more practical: new temperature measurements are fed to the environmental model of a bridge. If the simulated model frequencies are deviating too much from the measured system frequencies something happened to the bridge that cannot be explained by temperature effects. Especially, if the measured frequencies are lower, the bridge is probably damaged.

The statement "deviating too much" in last paragraph is a rather subjective criterion to judge of the state of a structure. More objective statistical criteria are needed. These will be developed in the following. Subsection 6.3.1 discusses the general case, whereas Subsection 6.3.2 specializes to the **ARX** case.

6.3.1 The simulation error and its statistical properties

A general parametrized linear input-output model structure is given by:

$$y_k = G(q,\theta)\,u_k + H(q,\theta)\,e_k \tag{6.14}$$

where G is the transfer function and H is the noise model. As before, q is the shift operator and θ is the parameter vector. Based on the input-output data, the model parameters can be estimated by so-called prediction error methods [LJUN99]. The estimate is denoted as $\hat{\theta}$. In case of an **ARX** model, the prediction error method corresponds to the linear least squares method (see Subsection 6.2.2).

[1]Notice that in system identification one speaks of *simulation* if only input information is used to estimate the outputs. If next to the inputs, also the outputs up to some previous time instant are used to estimate the current output, one speaks of *prediction*.

Assume that new inputs u_k^* are available[2]. The corresponding new outputs y_k^* from the true system are assumed to be generated by:

$$y_k^* = G(q,\theta_0)u_k^* + H(q,\theta_0)e_k^0 \tag{6.15}$$

where θ_0 is the true model parameter vector and e_k^0 are the actual disturbances with covariance λ_0. All these true model quantities are of course unknown. The noise-free simulated outputs from the estimated model can be computed as:

$$\hat{y}_k = G(q,\hat{\theta})u_k^* \tag{6.16}$$

It is interesting to examine the statistical properties of the simulation error $\hat{d}_k$, defined as the difference between the true (measured) outputs and the simulated ones:

$$\begin{aligned}\hat{d}_k &= y_k^* - \hat{y}_k \\ &= G(q,\theta_0)u_k^* + H(q,\theta_0)e_k^0 - G(q,\hat{\theta})u_k^* \\ &= (G(q,\theta_0)u_k^* - G(q,\hat{\theta})u_k^*) + H(q,\theta_0)e_k^0 \\ &\approx J(q,\theta_0)u_k^*\ (\theta_0 - \hat{\theta}) + H(q,\theta_0)e_k^0\end{aligned} \tag{6.17}$$

The last step is obtained as the first order approximation of an expanded Taylor series, where the transfer operator row vector $J(q,\theta_0)$ is defined as:

$$J(q,\theta_0) = \left.\frac{\partial G(q,\theta)}{\partial \theta}\right|_{\theta=\theta_0} \tag{6.18}$$

Since $\hat{\theta}$ is a consistent and unbiased estimate of θ_0 and e_k^0 is a zero-mean Gaussian distributed noise sequence, it follows from Equation (6.17) that $\hat{d}_k$ is asymptotically (i.e. for $N \to \infty$) Gaussian distributed with zero mean $\mathbf{E}[\hat{d}_k] = 0$ and asymptotic covariance $\mathbf{E}[\hat{d}_k^2] = P_{\hat{d}_k}$. This is denoted as:

$$\hat{d}_k \sim \mathbf{N}(0, P_{\hat{d}_k}) \tag{6.19}$$

An expression for $P_{\hat{d}_k}$ remains to be determined. For convenience of notation, we introduce:

---

[2]The asterix is used as a superindex to make the difference with the "old" quantities that were used to estimate the model.

$$J_0 = J(q,\theta_0)$$
$$H_0 = H(q,\theta_0)$$

Inserting Equation (6.17) into the definition of the covariance $P_{\hat{d}_k}$ yields:

$$P_{\hat{d}_k} = \mathbf{E}[\hat{d}_k^2] = \mathbf{E}[(J_0 u_k^* (\theta_0 - \hat{\theta}) + H_0 e_k^0)\ ((\theta_0 - \hat{\theta})^T (J_0 u_k^*)^T + H_0 e_k^0)]$$

Because the input u_k^* is a deterministic sequence and the expected value of the actual noise sequence is zero, this expression can be simplified as:

$$P_{\hat{d}_k} = J_0 u_k^*\ \mathbf{E}[(\theta_0 - \hat{\theta})(\theta_0 - \hat{\theta})^T]\ (J_0 u_k^*)^T + \mathbf{E}[(v_k^0)^2]$$

where the noise contribution is written in shorthand notation as:

$$v_k^0 = H_0 e_k^0$$

By defining the covariance function of the stochastic sequence v_k^0 as:

$$R_v^0(i) = \mathbf{E}[v_{k+i}^0 v_k^0] \tag{6.20}$$

and introducing the asymptotic covariance matrix of the model parameters $P_{\hat{\theta}}$, the asymptotic covariance of the simulation error equals:

$$P_{\hat{d}_k} = J_0 u_k^*\ P_{\hat{\theta}}\ (J_0 u_k^*)^T + R_v^0(0) \tag{6.21}$$

In next section we will see how this covariance can be estimated in the case of an **ARX** model.

The covariance matrix can be used to establish confidence intervals. Hereto Equation (6.19) is normalized:

$$\frac{y_k - \hat{y}_k}{\sqrt{P_{\hat{d}_k}}} \sim \mathbf{N}(0,1)$$

The true $P_{\hat{d}_k}$ is not known. If it is replaced by its estimate $\hat{P}_{\hat{d}_k}$, the Student's t-distribution should be used instead of the normal distribution. The $100(1-\alpha)\%$ confidence interval on the true value y_k is therefore given by:

$$\left[\hat{y}_k - t_{\frac{\alpha}{2},\nu} \sqrt{\hat{P}_{\hat{d}_k}} \;,\; \hat{y}_k + t_{\frac{\alpha}{2},\nu} \sqrt{\hat{P}_{\hat{d}_k}} \right] \tag{6.22}$$

where $t_{\alpha/2,\nu}$ is found from a statistical table of Student's t-distribution. The symbol ν is the number of degrees of freedom of the data after modelling, which equals in this case $\nu = N - d$, with $d = \dim(\theta)$. In order to compute the 95% confidence interval, for instance, we have $\alpha = 0.05$ and $t_{\alpha/2,\nu} = 1.96$ (for a large number of data points N). The significance of the 95% confidence interval is that 95% of these intervals will contain the true value y_k.

In the introduction of this section, it was stated that damage could be detected if the measured frequencies are lower than the simulated ones. The confidence interval (6.22) gives a statistical guidance in judging how much lower a measured frequency should be.

6.3.2 The ARX case

The asymptotic covariance of the simulation error (6.21) remains to be estimated. We will specialize to the **ARX** case to derive the estimate. Equation (6.21) constitutes of 3 quantities: $P_{\hat{\theta}}$, $J_0 u_k^*$ and $R_v^0(0)$. They are estimated in the following.

Asymptotic model parameter covariance matrix estimate $\hat{P}_{\hat{\theta}}$

As explained in Subsection 6.2.2, the asymptotic model parameter covariance matrix estimate $\hat{P}_{\hat{\theta}}$ follows from the statistical properties of the **LS** method that was used to find $\hat{\theta}$, see Equation (6.12).

Transfer operator estimate $J(q,\hat{\theta})$

The row vector $J_0 u_k^*$ was defined in Equation (6.18) as:

$$J_0 u_k^* = \left. \frac{\partial G(q,\theta)}{\partial \theta} \right|_{\theta=\theta_0} u_k^*$$

The parameter vector of an **ARX** model is given by Equation (6.3). The partial derivatives of the transfer function to these model parameters are:

$$\left. \frac{\partial G}{\partial \theta} \right|_{\theta=\theta_0} = \left[\frac{\partial G}{\partial a_i} \; (i=1,\ldots,n_a) \; \frac{\partial G}{\partial b_j} \; (j=1,\ldots,n_b) \right]_{\theta=\theta_0}$$

By comparing the **ARX** model (6.1) with the general model structure (6.14), the transfer function G can be written as:

$$G(q,\theta) = \frac{b(q)}{a(q)}$$

and by introducing the definitions of the operator polynomials $a(q)$ and $b(q)$, see Equation (6.4), the partial derivatives can finally be written as:

$$\left.\frac{\partial G}{\partial a_i}\right|_{\theta=\theta_0} = -\frac{b_0(q)}{a_0^2(q)}\, q^{-i} \qquad (i=1,\ldots,n_a)$$

$$\left.\frac{\partial G}{\partial b_j}\right|_{\theta=\theta_0} = \frac{1}{a_0(q)} q^{-j-n_k+1} \qquad (j=1,\ldots,n_b)$$

These expressions are time domain filtering operations on the input sequence u_k^*. An estimate of $J(q,\theta_0)u_k^*$ is obtained by replacing the true, but unknown, parameters θ_0 by their estimate to yield $J(q,\hat{\theta})u_k^*$.

Filtered white noise covariance estimate $\hat{R}_v^0(0)$

Finally, the covariance of the noise contribution has to be estimated, see Equation (6.20):

$$R_v^0(0) = \mathbf{E}[(v_k^0)^2]$$

By comparing the **ARX** model (6.1) with the general model structure (6.14), the noise model H can be written as:

$$H(q,\theta) = \frac{1}{a(q)}$$

By consequence, the noise sequence v_k^0 is the sequence that, when filtered through an auto-regressive filter, yields the white noise sequence e_k^0:

$$a_0(q)\; v_k^0 = e_k^0 \tag{6.23}$$

The computation of $R_v^0(0)$ goes as follows. With the definitions:

$$x_k = \begin{pmatrix} v_{k-1}^0 \\ v_{k-2}^0 \\ v_{k-3}^0 \\ \dots \\ v_{k-n_a}^0 \end{pmatrix}, \quad A = \begin{pmatrix} -a_1^0 & -a_2^0 & \dots & -a_{n_a-1}^0 & -a_{n_a}^0 \\ 1 & 0 & \dots & 0 & 0 \\ 0 & 1 & \dots & 0 & 0 \\ \dots & \dots & \dots & \dots & \dots \\ 0 & 0 & \dots & 1 & 0 \end{pmatrix}, \quad w_k = \begin{pmatrix} e_k^0 \\ 0 \\ 0 \\ \dots \\ 0 \end{pmatrix}$$

where $x_k \in \mathbb{R}^{n_a}$ is the state vector; $A \in \mathbb{R}^{n_a \times n_a}$ is the state transition matrix and $w_k \in \mathbb{R}^{n_a}$ is the process noise vector, Equation (6.23) can be written as:

$$x_{k+1} = Ax_k + w_k$$

The state covariance matrix is defined as $\Sigma = \mathbf{E}[x_k x_k^T]$ and the process noise covariance matrix as $Q = \mathbf{E}[w_k w_k^T]$. Assuming stationarity and because e_k^0 is independent of any of the previous outputs $v_{k-1}^0, \dots, v_{k-n_a}^0$, we have:

$$\begin{aligned} \mathbf{E}[x_{k+1} x_{k+1}^T] &= A\mathbf{E}[x_k x_k^T]A^T + \mathbf{E}[w_k w_k^T] \\ &\Updownarrow \\ \Sigma &= A\Sigma A^T + Q \end{aligned}$$

This is a Lyapunov equation that can be solved for Σ. Any of the diagonal elements of Σ equals $R_v^0(0)$. By consequence an estimate $\hat{R}_v^0(0)$ of $R_v^0(0)$ is obtained by replacing λ_0 by $\hat{\lambda}$ as the single non-zero element in Q and $a_0(q)$ by $\hat{a}(q)$ in A.

6.4 SYNTHESIS

This section synthesizes the method that was developed in previous sections to discriminate damage events from temperature effects. The method is split in two parts. Part A discusses the preliminary steps to undertake with data from the healthy structure. Part B is the monitoring part that indicates how data from a possibly damages structure should be used to detect damage. The overview is given in Figure 6.2.

A. The healthy structure

1. Normalize the input-output data:

$$u_k = \frac{u_k^{\mathrm{m}} - \bar{u}}{\hat{\sigma}_u}, \quad y_k = \frac{y_k^{\mathrm{m}} - \bar{y}}{\hat{\sigma}_y}$$

2. Use the **LS** method to estimate **ARX** models and their statistical properties:

$$\hat{\theta} = (Z^T Z)^{-1} Z^T Y$$

$$\hat{\lambda} = \frac{1}{N-d} |Y - Z\hat{\theta}|^2$$

$$\hat{P}_{\hat{\theta}} = \hat{\lambda}(Z^T Z)^{-1}$$

3. Select "the best" **ARX** model by comparing quality criteria:

V, **FPE**, **MDL**, $\hat{\sigma}_{\hat{\theta}_i}$, $\hat{R}_e(i)$

B. The (possibly) damaged structure

4. Normalize the new input-output data with <u>the same values</u> as in step 1 to yield:

$$u_k^*, \; y_k^*$$

5. Simulate the output from the model of step 3:

$$\hat{a}(q)\hat{y}_k = \hat{b}(q)u_k^*$$

6. Compute the simulation error and its statistics:

$$\hat{d}_k = y_k^* - \hat{y}_k$$

$$\hat{P}_{\hat{d}_k} = J(q,\hat{\theta})u_k^* \; \hat{P}_{\hat{\theta}} \; (J(q,\hat{\theta})u_k^*)^T + \hat{R}_v^0(0)$$

7. Establish confidence intervals and detect outliers:

$$\left[\hat{y}_k - t_{\frac{\alpha}{2},\nu} \sqrt{\hat{P}_{\hat{d}_k}}, \quad \hat{y}_k + t_{\frac{\alpha}{2},\nu} \sqrt{\hat{P}_{\hat{d}_k}} \right]$$

Figure 6.2: Environmental model of a vibrating structure: estimation and simulation.

6.5 CONCLUSIONS

In this chapter, a method was developed to detect damage in the presence of varying environmental parameters such as temperature. A literature survey and our own experience revealed the undeniable influence of temperature on the eigenfrequencies of a construction and provided the motivation to develop a method that distinguishes temperature effects from damage events. We relied upon a system identification approach to estimate an environmental model. This model can be used for simulation by feeding it with new temperature data. The idea is that, if the construction has changed, the simulated frequencies will significantly deviate from the measured frequencies. This chapter discussed the theoretical development of the method and provided a statistical framework. The practical use (and success) of the method will be demonstrated in next chapter.

7

THE Z24-BRIDGE

In this chapter, a final application is presented. The Z24-Bridge was extensively instrumented and tested with the aim of providing a “feasibility proof” for vibration-based health monitoring in civil engineering. We have chosen to discuss this final case at the end of this thesis since almost all theoretical developments of previous chapters can be applied to it. The chapter is organized as follows. An introduction to the bridge and the tests is given in Section 7.1. In Section 7.2 different excitation sources that have been applied to the bridge are compared. Section 7.3 discusses the evolution of the modal parameters with progressive artificial (but realistic) damage. The practical use of the environmental model of Chapter 6 for damage detection is demonstrated in Section 7.4. Section 7.5, finally, concludes the chapter.

7.1 INTRODUCTION

The data of this final application originate from the European Brite-EuRam project **SIMCES**[1]. The project was running from January 1997 to April 1999. Seven partners from 6 European countries were involved. The Structural Mechanics division of the K.U.Leuven coordinated the project. The work programme consisted of 4 tasks: (1) data collection, (2) adaptation, application and assessment of stochastic system identification methods, (3) **FE** modelling of reinforced concrete structures and (4) model-based damage identification methods. The main efforts were concentrated on 1 test object: the Z24-Bridge. The Swiss Federal Laboratories for Material Testing and Research EMPA were responsible for all bridge tests.

The Z24-Bridge overpassed the national highway A1 between Bern and Zürich, Switzerland. It was a classical post-tensioned concrete box girder bridge with a main span of 30 m and 2 side-spans of 14 m (Figure 7.1). Both abutments consisted of 3 concrete columns connected with concrete hinges to the girder. Both intermediate supports were concrete piers clamped into the girder. Although there were no known structural problems, the bridge dating from 1963 was demolished at the end of 1998. A new railway adjacent to the highway required a new bridge with one larger side-span.

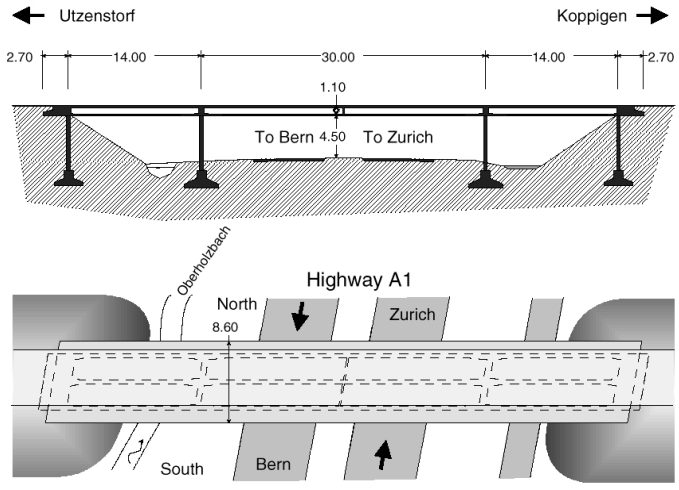

Figure 7.1: The Z24-Bridge: longitudinal section and top view [KRAE99b]. The bridge is slightly skew: the supports are not perpendicular to the longitudinal axis.

[1]The acronym **SIMCES** stands for **S**ystem **I**dentification to **M**onitor **C**ivil **E**ngineering **S**tructures [http://www.bwk.kuleuven.ac.be/bwm/SIMCES.htm]. It was a Brite-EuRam III project [http://www.cordis.lu].

Before complete demolition the bridge sacrificed its last months for the sake of science. It was subjected to three types of testing:

- A long-term *continuous monitoring* test. This test took place during the year before demolition. The aim was to quantify the environmental variability of the bridge dynamics. Results will be presented in Section 7.4 (see also [PEET00b, PEET00c, PEET00f, PEET00e]).

- Short-term *intermittent monitoring* tests. The aim was to compare the results from different excitation types and system identification methods. Results will be presented in Section 7.2 (see also [PEET98b, PEET99d, PEET00a, PEET00d]).

- *Progressive damage tests*. These tests took place in a one-month time period shortly before the demolition of the bridge and alternated with the intermittent monitoring tests. The aim was to prove that realistic damage has a measurable influence on the dynamics. Results will be presented in Section 7.3 (see also [PEET98d, DERO00]). Additionally the continuous monitoring system was still running during the progressive damage tests, see Section 7.4.

The bridge test and data acquisition procedures are described in [KRAE99c, KRAE99b, KRAE99a]. The tests were unique in that they combined long-term monitoring with the application of realistic damage scenarios. Other bridge-test examples are available in literature but either of the two aspects is missing. A well-known example is the I40-Bridge in Albuquerque, NM, USA [FARR98, FARR00]. The applied damage scenarios were torch cuts in the web and flange of the steel girder. No long-term monitoring was performed. In Section 6.1, a literature survey of long-term monitoring projects was given, but in these cases no damage could be applied to the bridges.

Similar to the beam data (Chapter 5, Page 118), the Z24-Bridge data were selected as "benchmark" data by working group 2 of COST 1 action F3 on Structural Dynamics. Furthermore, the Z24-Bridge is adopted as a case study by the Civil Engineering Group of IMAC, the International Modal Analysis Conference. Participating researchers will present their system identification results at the next conference, IMAC 19, to be held in February 2001 in Kissimmee, FL, USA.

7.2 EXCITATION SOURCES

7.2.1 Introduction

Since a few decades, people are performing vibration tests on large civil engineering structures. An important issue is how to excite such structures in order to obtain measurable acceleration levels. We will give a short overview of some typical excitation sources without claiming exhaustiveness. More references can be found in [GREE95, FARR99a].

The extrapolation to civil engineering of traditional input devices used in mechanical engineering leads to huge reaction mass shakers or impact testing based on a falling weight. In literature also other, sometimes creative solutions are proposed to excite large structures. Gentile *et al.* [GENT98] are describing vibration tests on a cable-stayed bridge that was excited in the vertical direction by a heavy truck that drove over a plank and in horizontal direction by sudden braking of the truck. Another way of vertically exciting a bridge is a sudden release of a heavy mass that was suspended from the bridge. This technique was applied to the Vasco Da Gama Bridge in Lisbon, Portugal as reported by Cunha *et al.* [CUNH99]. Delaunay *et al.* [DELA99] are describing tests where the Normandie Bridge, France, was horizontally excited by a sudden release of a tension cable that connected the bridge with a tug-boat. Finally, Deger *et al.* [DEGE94] used rocket engines to excite a composite steel/concrete bridge both horizontally and vertically. All these excitation methods are also referred to as free vibration testing. The input is not necessarily measured but it is impact-like and the responses are free vibrations.

The last ten years or so, more attention was paid to so-called ambient excitation. The structural response to freely available "natural" sources such as traffic, wind, waves and micro-earthquakes is measured. Obviously the exact forces from these sources that are transmitted into the bridge cannot be measured. The advantage of using ambient sources is that they are cheap (for free!). Ambient excitation that causes sometimes unacceptable noise during forced or free vibration testing, turned out to be beneficial in vibration testing of large structures.

7.2.2 Excitation sources applied to the Z24-Bridge

During the night after the application of a certain damage scenario (see next section for details about the damage scenarios), an ambient and a shaker test were performed by EMPA [KRAE99c]. After scenario 8, additionally a drop weight was used to excite the bridge. That is why this comparison study uses the data originating from the vibration

measurements after that scenario. Figure 7.2 illustrates the excitation sources that have been applied to the Z24-Bridge.

In order to capture the mode shapes in some detail, the accelerations of the bridge were measured in 9 setups of 28 roving and 5 reference sensors. A roving sensor changes position from one setup to another, whereas a reference sensor is common to all setups. The data were sampled at a rate of 100 Hz; the cut-off frequency of the anti-aliasing filter was 30 Hz.

The ambient sources acting on the bridge were highway traffic, wind and walking of the test crew in case of low traffic density. Typical bridge response data are shown in Figure 7.3. The measurement time was 10 min 55.36 s for each setup, corresponding to 65536 samples. Two shakers have been used in the shaker tests: one was located at a side-span, the other at the mid-span. The input signals were uncorrelated band-limited noise between 3−30 Hz. Typical output data are shown in Figure 7.4. Finally, also a drop weight, located at mid-span, served as excitation source. Four impacts were generated per setup as apparent from the response data (Figure 7.5). The measurement time was in this case 81.92 s, corresponding to 8192 samples. The maximum level of the drop weight response corresponds to the shaker response level. The ambient response level is 40 times lower. The response spectra of the three excitation types are compared in Figure 7.6.

Figure 7.2: Photographs illustrating the applied excitation sources. Left: traffic on the highway as ambient excitation. Middle: the installation of a reaction mass shaker of EMPA. Right: the drop weight system developed by the Structural Mechanics division of the K.U.Leuven.

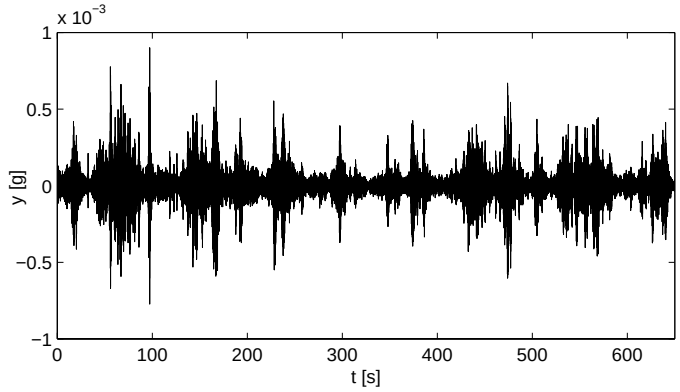

Figure 7.3: Ambient response data. Vertical acceleration at 1st reference location.

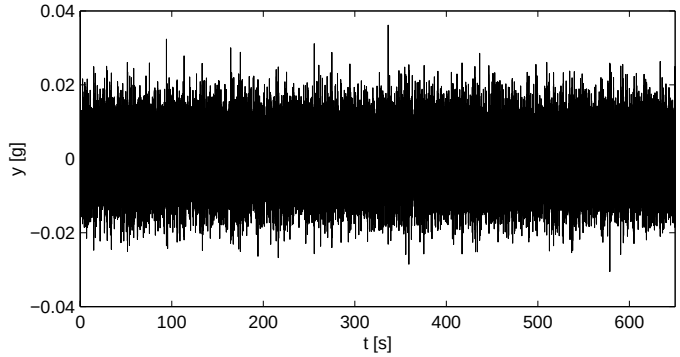

Figure 7.4: Shaker response data. Vertical acceleration at 1st reference location.

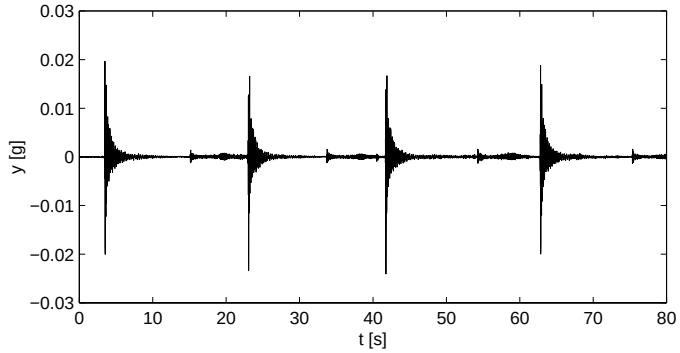

Figure 7.5: Drop weight response data. Vertical acceleration at 1st reference location.

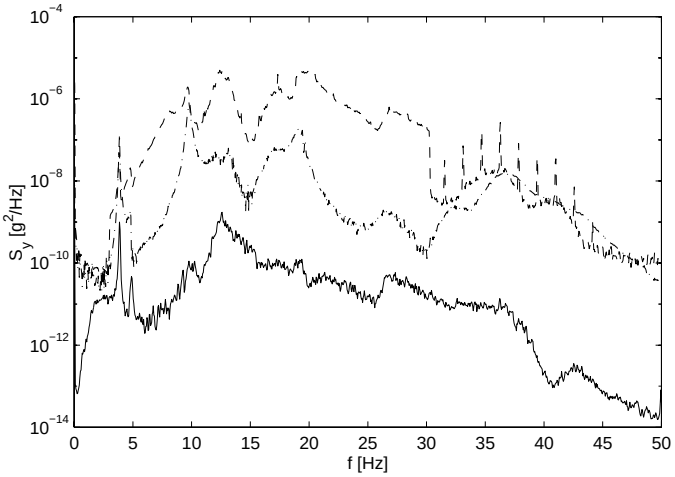

Figure 7.6: Comparison of response spectra: ambient response (full line), shaker response (dashed line), drop-weight response (dash-dotted line). The accelerations were all measured at the 1st reference location.

7.2.3 System identification results

From the numerical simulations of Chapter 3, we learnt that subspace identification is the most accurate stochastic system identification method. In [PEET98b], the peak-picking (**PP**), the instrumental-variable (**IV**) and the data-driven stochastic subspace identification (**SSI-DATA**) method were compared using data from a preliminary vibration test on the Z24-Bridge. It was confirmed that subspace identification is the preferred method.

The large amount of data (33 channels × 65536 samples) makes the direct use of **SSI-DATA** difficult, since it requires the *QR* factorization of a data Hankel matrix with 65536 columns, see Equation (3.44). This is not feasible in practice due to the memory and speed limitations of a standard computer anno 2000. A first solution is using recursive *QR* updating, i.e. recomputing the *R* factor as new data becomes available [GOLU89]. This relaxes the memory requirement but, unfortunately, increases the computation time. A more practical solution is simply using only a part of the data. The high number of samples was inspired by frequency resolution and spectrum averaging considerations of frequency domain methods. Time domain methods typically need less samples. It suffices that the data contain a "reasonable" number of cycles of the slowest mode. Additionally time domain methods have no averaging mechanism.

If for instance the (ambient) excitation does not excite all modes continuously, it can be advantageous to use all 65536 samples. In this case the covariance-driven stochastic

subspace identification method (**SSI-COV**) can be used. As discussed in Section 3.6, the **SSI-COV** method has the advantage that the data can efficiently be compressed to covariances by applying the **FFT**. In this section the **SSI-COV** method was applied to three data sets: ambient, shaker and drop weight data. The identification parameters were:

- the number of samples: $N = 65536$ (ambient and shaker), $N = 8192$ (drop weight);
- the number of channels: $l = 33$;
- the number of reference sensors: $r = 5$ (the reference sensors for the identification of one setup were chosen to coincide with the reference sensors for gluing the mode shape parts of the different setups together);
- the number of time lags: $i = 40$;
- the system orders for constructing the stabilisation diagrams: $n = 2,3,...,80$.

A typical stabilization diagram for the ambient data is shown in Figure 7.7. Seven modes could be identified from all three data sets. The eigenfrequencies and damping ratios are represented in Tables 7.1 and 7.2. The frequency differences between the excitation types are generally small. The variances of the modal parameters and the differences between the excitation types are partly explained by changing temperature. Measuring 9 setups for all 3 excitation types took almost one day and, as shown in Section 7.4, changing temperature has a significant influence on the frequencies of this bridge. The standard

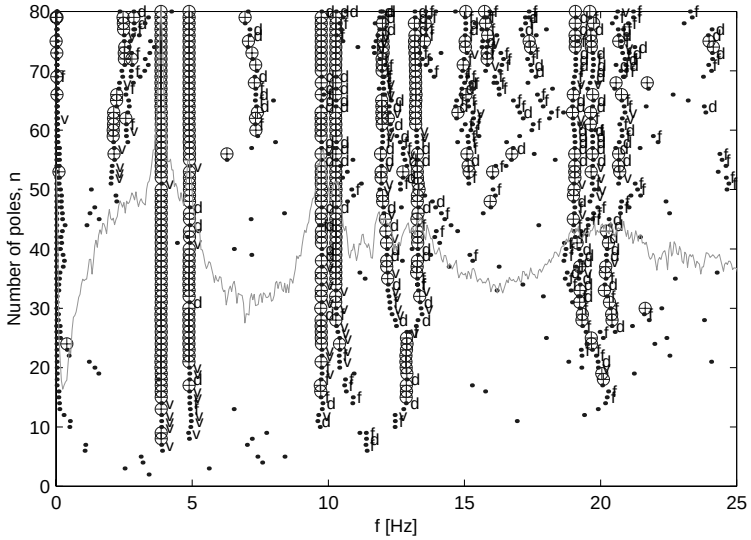

Figure 7.7: Stabilization diagram obtained by applying the **SSI-COV** method to ambient data from the Z24-Bridge. The criteria are 1% for frequencies, 5% for damping ratios and 2% for the mode shape correlations. The used symbols are: '⊕' for a stable pole; '**.**v' for a pole with stable frequency and vector; '**.**d' for a pole with stable frequency and damping; '**.**f' for a pole with stable frequency and '**.**' for a new pole (3.23).

deviations of the ambient results are somewhat larger. Taking into account their higher uncertainty, the damping ratios seem to be consistently identified from all three data sets.

The identified mode shapes are shown in Figure 7.8. The 1st mode is a vertical bending mode. The 2nd mode is a transverse bending mode, combined with torsion of the girder. The 3rd and 4th mode are combining vertical bending with torsion, which is typical for skew bridges. The 5th mode is a vertical symmetric bending mode. The 6th mode is a vertical anti-symmetric bending mode with an important vertical movement of the piers. Finally, the 7th mode is a torsion mode. The correlations between the corresponding modal vectors from different excitation types are represented in Table 7.3. Mode 5 was not well identified from the drop weight data, the shaker data yielded a 6th mode shape of lower quality and also the 7th ambient mode was not well identified.

Table 7.1: Comparison of eigenfrequencies identified from three data sets with respectively ambient, shaker and drop weight excitation. The mean values $\overline{f}$ and estimated standard deviations $\hat{\sigma}_f$ are based on 9 samples originating from the 9 independent setups.

Mode		1	2	3	4	5	6	7
Ambient	$\overline{f}$ [Hz]	3.859	4.903	9.75	10.29	12.43	13.37	18.99
	$\hat{\sigma}_f$ [Hz]	0	0.02	0.02	0.05	0.15	0.14	0.3
Shaker	$\overline{f}$ [Hz]	3.846	4.816	9.739	10.42	12.41	13.16	19.14
	$\hat{\sigma}_f$ [Hz]	0	0	0	0.03	0.05	0.05	0.05
Drop weight	$\overline{f}$ [Hz]	3.844	4.817	9.743	10.38	12.19	13.2	19.18
	$\hat{\sigma}_f$ [Hz]	0	0	0	0.04	0.11	0.05	0.02

Table 7.2: Comparison of damping ratios identified from three data sets with respectively ambient, shaker and drop weight excitation. The mean values $\overline{\xi}$ and estimated standard deviations $\hat{\sigma}_\xi$ are based on 9 samples originating from the 9 independent setups.

Mode		1	2	3	4	5	6	7
Ambient	$\overline{\xi}$ [%]	1.1	1.2	1.4	1.5	3.1	4.3	2.3
	$\hat{\sigma}_\xi$ [%]	0.3	0.1	0.2	0.4	0.4	1.2	0.3
Shaker	$\overline{\xi}$ [%]	1.1	1.7	1.7	2.6	3.5	3.3	2.4
	$\hat{\sigma}_\xi$ [%]	0.1	0.1	0.1	0.4	0.4	0.3	0.2
Drop weight	$\overline{\xi}$ [%]	0.83	1.6	1.7	1.9	4.1	4.3	2.5
	$\hat{\sigma}_\xi$ [%]	0.02	0.1	0.1	0.1	0.8	0.2	0.2

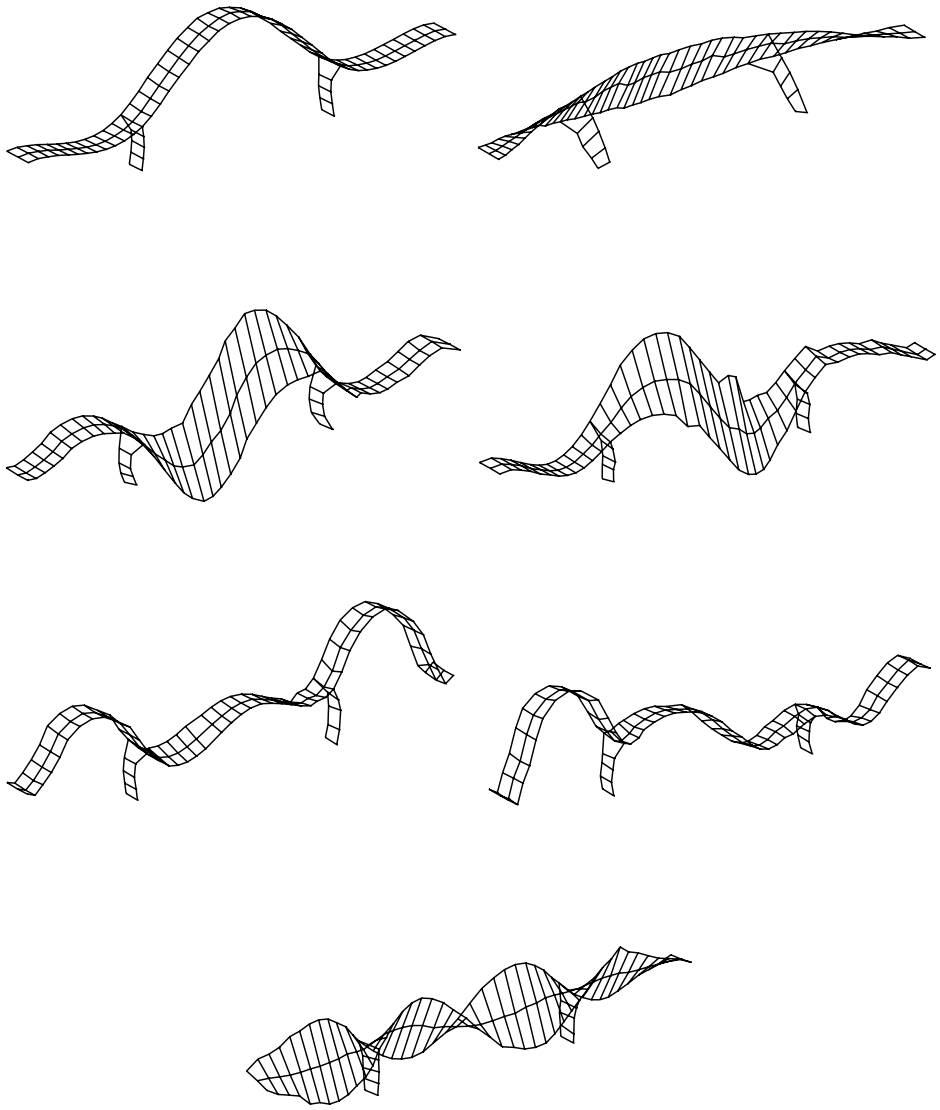

Figure 7.8: Seven mode shapes of the Z24-Bridge, ordered from left to right, from top to bottom. Except for the 7^{th} mode all represented shapes were identified from ambient data.

Table 7.3: MAC values (3.24) between the corresponding mode shapes from the three excitation types. The **MAC** is a value between 0 (i.e. no correlation) and 1 (i.e. perfect correlation).

Mode	1	2	3	4	5	6	7
Ambient *vs.* shaker	1	0.99	0.94	0.88	0.94	0.73	0.81
Ambient *vs.* drop weight	1	0.97	0.94	0.87	0.79	0.96	0.8
Shaker *vs.* drop weight	0.99	0.98	0.98	0.92	0.85	0.77	0.9

7.2.4 Conclusions

Except for the higher standard deviations of the ambient results, all three excitation types yielded comparable modal parameters. But next to the accuracy of the results, other criteria guide the choice of an excitation source:

- If mass-normalized mode shapes are required, one cannot use ambient excitation. To obtain the correct scaling of the mode shapes, the applied force has to be known.

- If the cost of testing is a major concern, the use of shakers can be excluded. The price of a shaker and the additional man power needed to install it on a structure, makes it not very cost-effective, see also [KRAE99c].

- If a structure has low-frequency (below 1 Hz) modes, it may be difficult to excite them with a shaker, whereas this is generally no problem for a drop weight or ambient sources. The high-frequency modes on the other hand, are not always well excited by ambient sources.

- By adjusting the settings of the damper on which the mass of the drop weight system falls, the frequency content of the excitation can be controlled in some sense. The level of excitation can be determined by the initial height of the mass. Above a certain frequency, the frequency content and the level of excitation of the shaker can also be controlled. This is evidently not the case for the ambient sources.

- The use of artificial excitation only makes sense when the generated response surpasses the ambient response which is always present. For very large structures, e.g. long span cable-stayed bridges, this becomes almost impossible.

- If the purpose of the tests is continuous monitoring, only ambient excitation can be used. For intermittent monitoring, also the use of a drop weight can be considered: it is cheap, fast and easy to install.

Previous discussion is synthesized in Table 7.4.

The accelerations of a structure as a result of ambient excitation are typically very small and can vary considerably during acquisition, for instance depending on whether a truck, a car or no traffic is passing (Figure 7.3). This causes challenges to the sensors, the acquisition system and the identification algorithms that, in the limit, need to extract weakly excited modes from noisy data. The developments of the last years both on the acquisition side as on the identification side (i.e. the development of subspace identification methods) greatly enhanced the use of ambient vibration testing to estimate the modal parameters of a structure.

Table 7.4: Strong points (+) and weak points (–) of the three excitation sources.

Criterion	Ambient	Shaker	Drop Weight
Mass-normalized mode shapes	–	+	+
Price	+	–	+
Low frequency excitation	+	–	+
High frequency excitation	–	+	+
Controlled amplitude	–	+	+
Continuous monitoring	+	–	–
Intermittent monitoring	+	+	+

7.3 PROGRESSIVE DAMAGE TESTS

7.3.1 The scenarios

The aim of the progressive damage tests was to study the influence of damage on the dynamics of a bridge. A detailed description of the design and implementation of the damage scenarios that have been applied to the Z24-Bridge can be found in [KRAE99b, KRAE99a]. The discussion in this thesis is limited to the elements that are essential for understanding the proposed damage detection method.

The choice and extent of the scenarios were guided by following criteria:

- In order to be convincing as a "feasibility proof", the scenarios should be realistic. Hereto, the Swiss database of bridge damage cases was consulted[2].

- The traffic on the most important highway of Switzerland must not be disturbed, nor the people endangered when applying the scenarios. Therefore special safety measures were taken (see [KRAE99b, KRAE99a] for details) and the scenarios were never pursued to the safety limits. A consequence was that the induced damages remained small.

- There was only a limited time period available for applying the damage scenarios. This period was situated between the opening of the new bridge adjacent to the Z24-Bridge and the complete demolition of the Z24-Bridge.

The retained damage scenarios are listed in Table 7.5. Some photographs of the damage scenarios are collected in Figure 7.9.

[2]Bundesministerium für Verkehr, Abteilung Strassenbau. *Schäden an Brücken und anderen Ingenieurbauwerken*, 1982 & 1994.

Table 7.5: Progressive damage test scenarios. The dates are referring to the start of the vibration measurements.

#	Date	Scenario	Comments
1	04.08.98	1st Reference measurement	"Healthy" structure
2	09.08.98	2nd Reference measurement	After installation of the settlement system
3	10.08.98	Settlement of pier: 2 cm	Natural causes: erosion, flooding, soil settling
4	12.08.98	Settlement of pier: 4 cm	
5	17.08.98	Settlement of pier: 8 cm	
6	18.08.98	Settlement of pier: 9.5 cm	
7	19.08.98	Tilt of foundation	
8	20.08.98	3rd Reference measurement	Cracks are closing after removal of settlement
9	25.08.98	Spalling of concrete: 12 m^2	Natural causes: vehicle impact, carbonisation, corrosion
10	26.08.98	Spalling of concrete: 24 m^2	
11	27.08.98	Landslide at abutment	Natural causes: erosion, flooding
12	31.08.98	Failure of a concrete hinge	Natural causes: corrosion, overload
13	02.09.98	Failure of anchor heads I	Natural causes: corrosion
14	03.09.98	Failure of anchor heads II	
15	07.09.98	Rupture of tendons I	Natural causes: bad injection of tendon tubes + corrosion
16	08.09.98	Rupture of tendons II	
17	09.09.98	Rupture of tendons III	

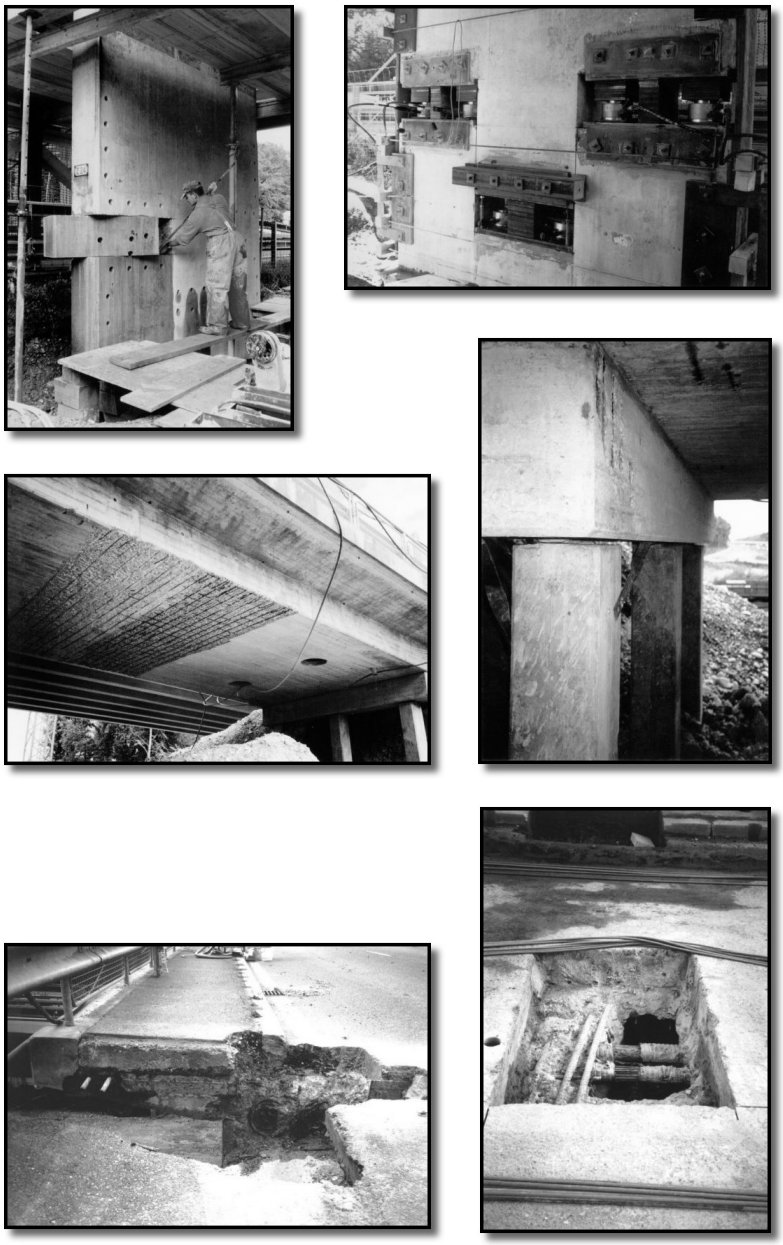

Figure 7.9: Photographs illustrating the applied damage scenarios. From left to right, from top to bottom: (1) cutting of a pier to install the settlement system, (2) settlement system, (3) spalling of concrete, (4) failure of a concrete hinge, (5) failure of anchor heads, (6) failure of tendon wires. The first two photographs are provided by EMPA.

7.3.2 Evolution of the modal parameters

The **SSI-DATA** method was applied to the ambient data acquired after each damage scenario. The acquisition strategy was already explained in Section 7.2. Here, the preprocessing consisted of the selection of a high-quality segment of 8192 data points and sending the data through a digital low-pass filter with a cut-off frequency of 20 Hz. Afterwards the data was resampled at a 2 times slower rate (i.e. 50 Hz) than the original one. The **SSI-DATA** identification parameters were:

- the number of samples: $N = 4096$;
- the number of channels: $l = 33$;
- the number of reference sensors: $r = 5$ (the reference sensors for the identification of one setup were chosen to coincide with the reference sensors for gluing the mode shape parts of the different setups together);
- the number of time lags: $i = 20$;
- the system orders for constructing the stabilisation diagrams: $n = 2,3,...,80$.

These parameters led to a reasonable computation time to digest 17 data sets, each consisting of 9 setups. The results after scenario 8 were discussed in detail in previous section.

The evolution of eigenfrequencies throughout the progressive damage tests is somewhat obscured by temperature effects. Therefore the frequency results will only be treated in next section, after correcting for temperature. In this section, we will concentrate on the evolution of the damping ratios and mode shapes.

The estimated damping ratios of the first 5 modes of all damage scenarios are represented in Appendix C.1. The main conclusions are:

- The damping ratios of the Z24-Bridge are in the range 1–3%, which is normal.
- The uncertainties on the damping ratio estimates is quite high.
- There is no clear trend in the evolution of the damping with damage.
- It will be difficult to incorporate damping ratios in a damage detection method.

It is more interesting to observe how the mode shapes are changing with damage. To compare mode shapes, the modal amplitudes are divided by the norm of the modal vector. The evolution of the first 5 mode shapes between some damage scenarios are represented in Figures 7.10–7.15. Mode shape changes between scenarios are clearly visible. They contain useful information for model updating and damage identification methods. The use of the first mode shape to locate damage on the Z24-Bridge is shown in [MAEC98b, MAEC00b].

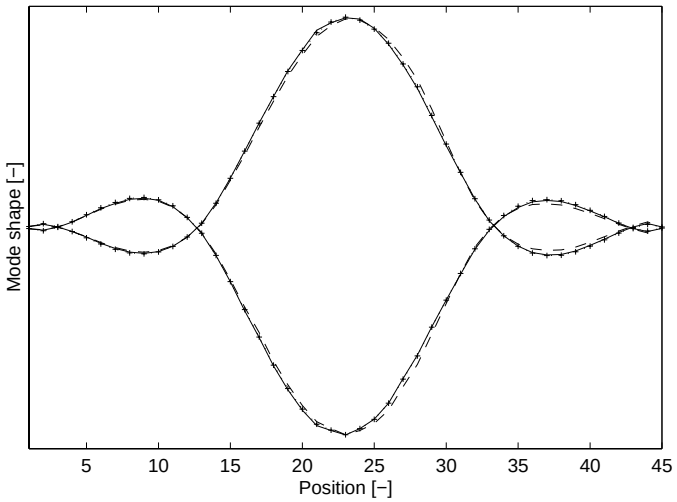

Figure 7.10: Vertical components of mode shape 1. The sign of the modal displacements at one side of the bridge is switched to allow visualization of both sides in one graph. The full line corresponds to scenario 2, the dashed line is from scenario 6 and the dotted line with crosses is from scenario 8. There is a (small) change of the mode shape at the side of the settled pier. After removal of the settlement, the mode shape coincides with the original one.

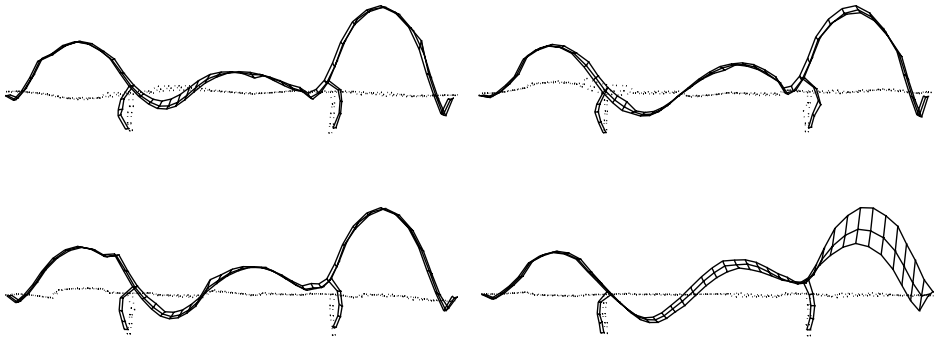

Figure 7.11: Evolution of mode shape 5. The full line is the real part; the dotted line is the imaginary part. Scenario 4, 6, 11 and 12 are represented. Settling the pier makes the mode shape losing its symmetry (top figures). Cutting a concrete hinge at the abutment on the right introduced a torsion component (bottom figures).

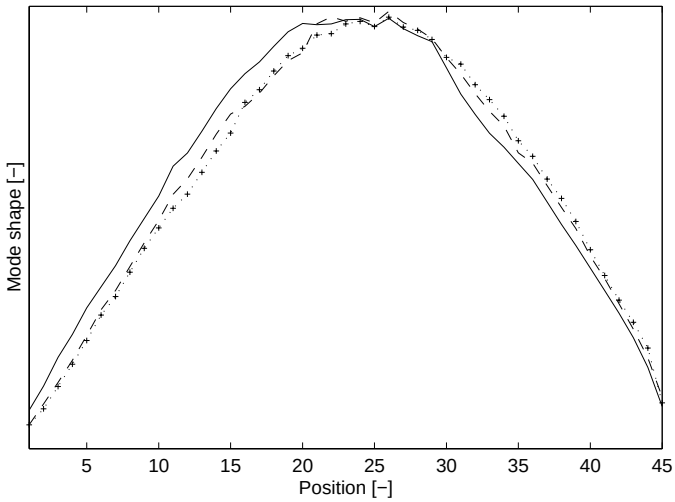

Figure 7.12: Transverse components of mode shape 2. The full line corresponds to scenario 1, the dashed line is from scenario 2 and the dotted line with crosses is from scenario 6. Only cutting the pier already affects this mode. Imposing the settlement further changed the mode.

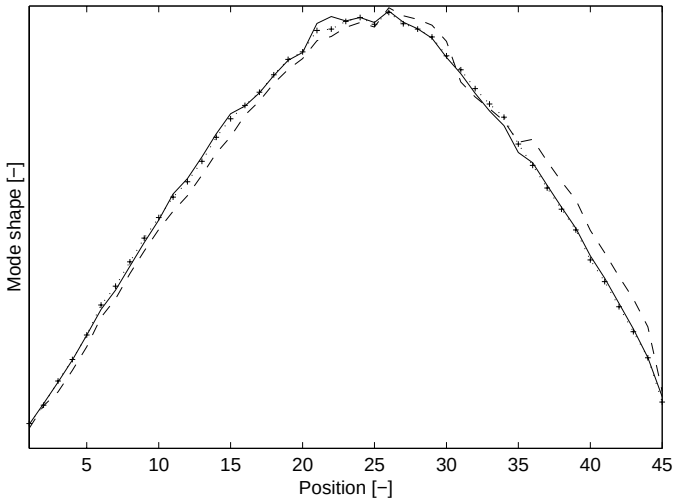

Figure 7.13: Transverse components of mode shape 2. The full line corresponds to scenario 2, the dashed line is from scenario 7 and the dotted line with crosses is from scenario 8. After removal of the settlement and tilt, the mode shape coincides with the mode from scenario 2 (after cutting the pier).

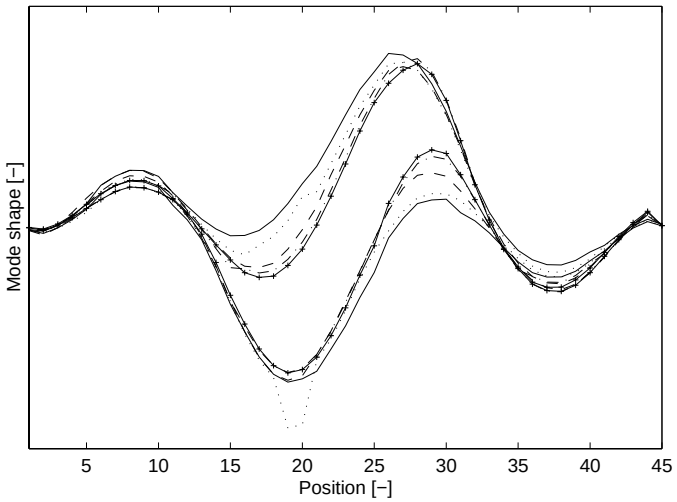

Figure 7.14: Vertical components of mode shape 3. Scenarios 2, 3, 4, 5 and 6 are respectively represented by a full line, a dotted line, a dashed line, a dash-dotted line and a full line with crosses. Gradually increasing the settlement uniformly changes this mode (disregarding some anomalies in scenario 3).

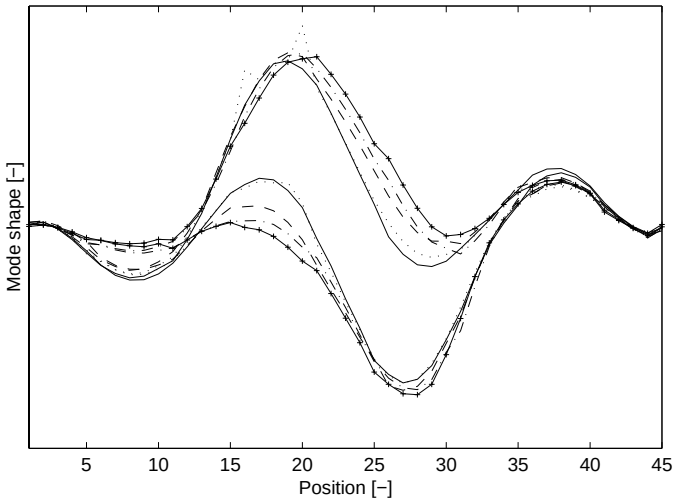

Figure 7.15: Vertical components of mode shape 4. Scenarios 2, 3, 4, 5 and 6 are respectively represented by a full line, a dotted line, a dashed line, a dash-dotted line and a full line with crosses. Gradually increasing the settlement uniformly changes this mode (disregarding some anomalies in scenario 3).

7.4 CONTINUOUS MONITORING AND DAMAGE DETECTION

In this section, the damage detection capabilities of the continuous monitoring system installed on the Z24-Bridge will be demonstrated. The method outlined in Chapter 6 and synthesized in Figure 6.2 will be applied. The input data are measured environmental parameters; the output data are eigenfrequencies, identified with the **SSI-DATA** method. In [RUSH99] an alternative approach was pursued, based on eigenfrequencies identified with the **PP** method and a "static" linear regression model.

7.4.1 The monitoring system

From 11 November 1997 till 11 September 1998, the bridge has continuously been monitored. The aim of the monitoring system was to provide both environmental and vibration data. A detailed description of the system is given in [KRAE99b, KRAE99a]. Every hour, 49 environmental parameters were measured: air temperature, wind characteristics, humidity, bridge expansion and several soil, concrete and asphalt temperatures. The locations of the thermocouples are shown in Figure 7.17. Figure 7.16 shows the air temperature and the soil temperature at one of the piers. Additionally, every hour during 11 minutes, 8 accelerometers are capturing the vibrations of the bridge. Notice that the number of accelerometers and measurement locations used in the continuous monitoring system is much less than the number of accelerometers used in the intermittent monitoring system (Section 7.2).

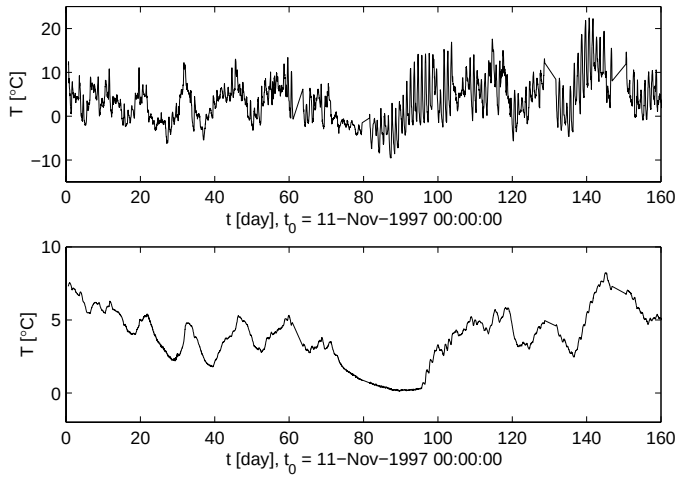

Figure 7.16: Typical environmental data. Top: air temperature. Bottom: soil temperature at one of the piers. The represented measurement period is from 11 November 1997 till 20 April 1998. The sampling time is 1 h. The soil temperature variations are much smoother.

As indices for the dynamic behaviour of the structure, it is natural to take the modal parameters. A problem is that they cannot be measured directly and have to be estimated from acceleration data. A key issue in our approach to continuous monitoring is therefore the automatic extraction of the modal parameters. The *automatic modal analysis* procedure, proposed in Section 4.2 was applied to the 5652 data sets from the continuous monitoring system. The results are summarized in Table 7.6. Due to the sometimes low excitation (especially at night when there is not much traffic) the automatic procedure could not identify all 4 modes at every time instant. However, especially for the first 3 modes, the automatic procedure performs very well. The two close modes around 10–11 Hz caused problems for the automated **PP** method described in [RUSH99]. Figure 7.18 provides a graphical representation of the results.

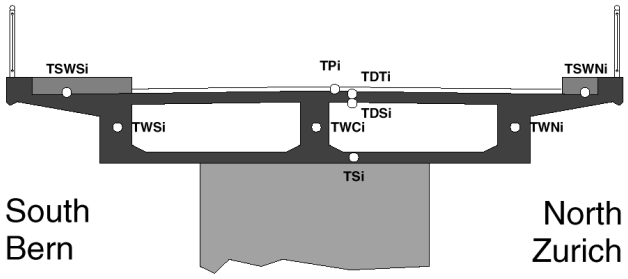

Figure 7.17: Cross-section of the Z24-Bridge and location of the thermocouples in any of the three spans [KRAE99b].

Table 7.6: Automatic modal analysis results for the first 4 modes of the healthy structure. The "success rate" expresses the percentage of successful identifications of a certain mode. The minimum (min.), average (avg.) and maximum (max.) frequencies are specified, together with the relative maximal differences (max. diff.). The frequency differences (14–18%) occurred before any known damage took place and have to be explained by normal environmental changes. See also Figure 7.18.

Mode	Success rate [%]	Eigenfrequency			
		Min. [Hz]	Avg. [Hz]	Max. [Hz]	Max.diff. [%]
1	98	3.81	4	4.38	14
2	93	4.98	5.21	5.89	18
3	96	9.6	10.16	11.2	16
4	77	10.24	10.84	12.09	17

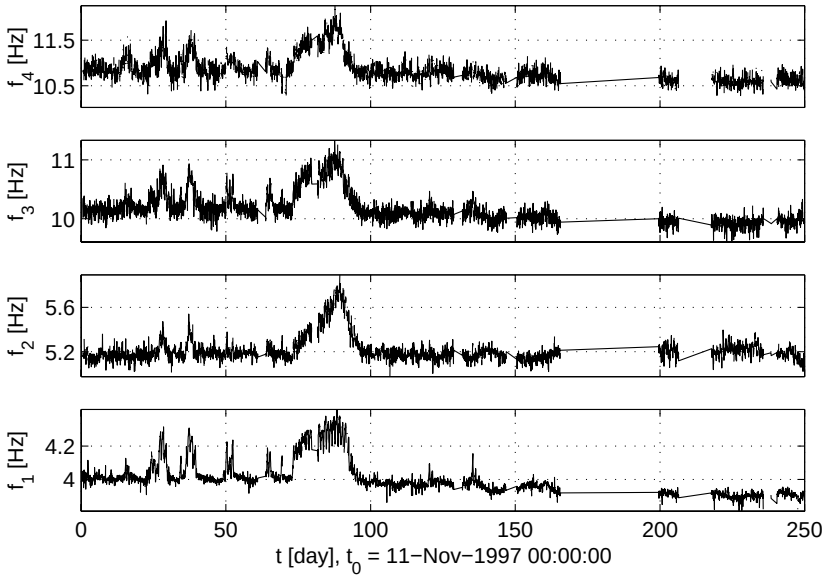

Figure 7.18: Automatic modal analysis results for the first 4 modes of the healthy structure. A clearly visible quite long cold period starts at day 75 (i.e. beginning of February 1998). Besides shorter periods, the monitoring system was not operating from day 166 till day 200. See also Table 7.6.

7.4.2 System identification

Plotting the data

The first step in system identification is plotting the data in various ways. This step reveals already quite useful information about the behaviour of the Z24-Bridge under a changing environment. In Figure 7.19, the 1st eigenfrequency is plotted *vs.* the temperature of the asphalt layer TP1. In Figure 7.20, the 2nd eigenfrequency is plotted *vs.* the temperature of the deck soffit TDS2. In both cases, the relation between temperature and frequency can roughly be described by two straight lines, with the knee situated around 0°C. This bilinear behaviour is observed for almost all combinations of frequency *vs.* temperature. With increasing temperature, the bridge stiffness normally decreases. Mode 2 is somewhat an exception in the sense that its frequency increases with increasing temperatures (for positive temperatures).

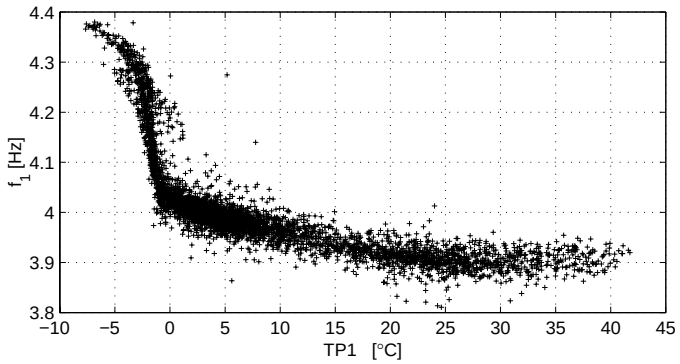

Figure 7.19: 1st Eigenfrequency *vs.* asphalt layer temperature TP1. The data comes from the healthy structure.

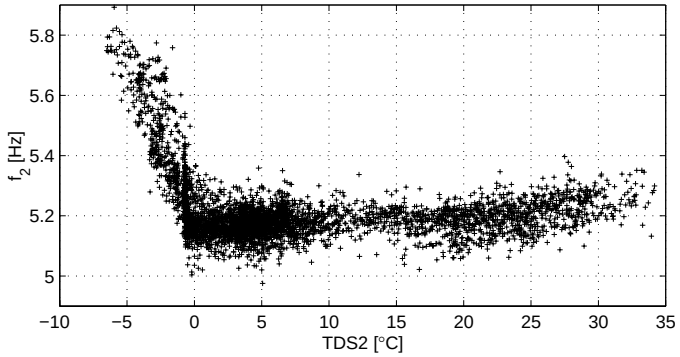

Figure 7.20: 2nd Eigenfrequency *vs.* deck soffit temperature TDS2. The data comes from the healthy structure.

Some effort was spent in trying to find out the cause of the bilinear behaviour. Whereas the temperature *vs.* time functions are very smooth; the frequency *vs.* time functions are rather irregular. This can be observed in Figure 7.21, where three different temperatures and the sign-reversed first eigenfrequency $-f$ are plotted as a function of time. All quantities have been normalized. At first sight there seems to be no relation between frequency and temperature, although on a larger time scale it would be clear that the frequency follows the main trends of the temperature data. However, by plotting the same quantities measured during a cold period (Figure 7.22), it appears that the normalized opposite frequency is almost perfectly in line with the normalized temperature of the asphalt layer TP1. The central web temperature TWC1 and the soffit temperature TS1 are lagging behind and can by consequence not be the driving forces of the eigenfrequency variation. Also freezing of the soil around the boundaries of the bridge cannot explain the variations. The soil

temperature has a much lower frequency content (Figure 7.16) than the eigenfrequencies[3]. We conclude that during warm periods the asphalt does not play any role, but during cold periods it contributes significantly to the stiffness of the structure. This explains the observed non-linearity in Figures 7.19 and 7.20.

This conclusion is confirmed by the results of a recent paper [WATS00] in which the seasonal variations of asphalt road pavements are experimentally studied with falling weight deflectometer tests. Figure 7.23 is an extract from that paper, representing the change of Young's modulus of asphalt with changing temperature. The role of the asphalt layer in the overall stiffness of the Z24-Bridge is also apparent from geo-radar measurements [KRAE99a]. It was found that the asphalt layer of the bridge deck had an average thickness of 16 cm instead of 8 cm as indicated on the construction drawings of the bridge.

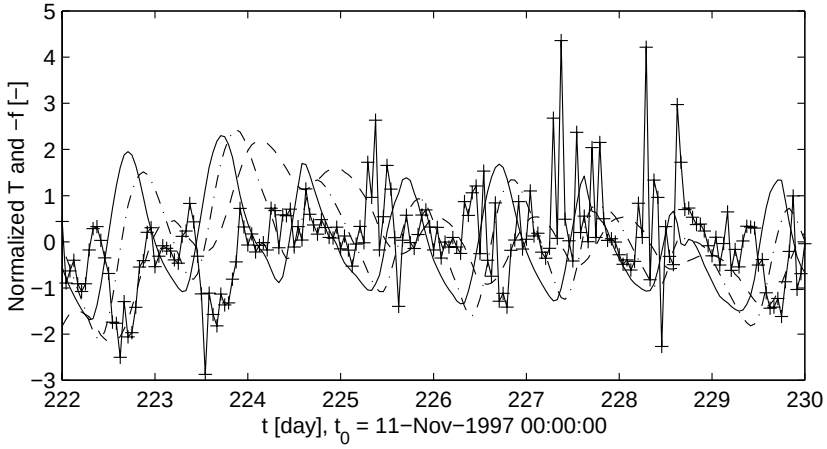

Figure 7.21: Normalized temperatures and sign-reversed 1st eigenfrequency during a warm period: TP1 (full line), TWC1 (dashed line), TS1 (dash-dotted line) and - f1 (full line with crosses).

[3]In this section, the eigenfrequencies are considered as a time series of measurement values, so it makes sense to speak about the frequency content of the eigenfrequencies.

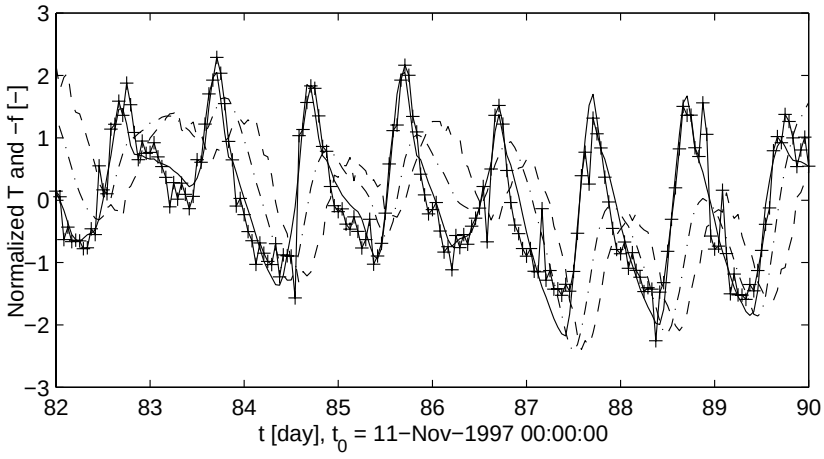

Figure 7.22: Normalized temperatures and sign-reversed 1st eigenfrequency during a cold period: TP1 (full line), TWC1 (dashed line), TS1 (dash-dotted line) and - f1 (full line with crosses).

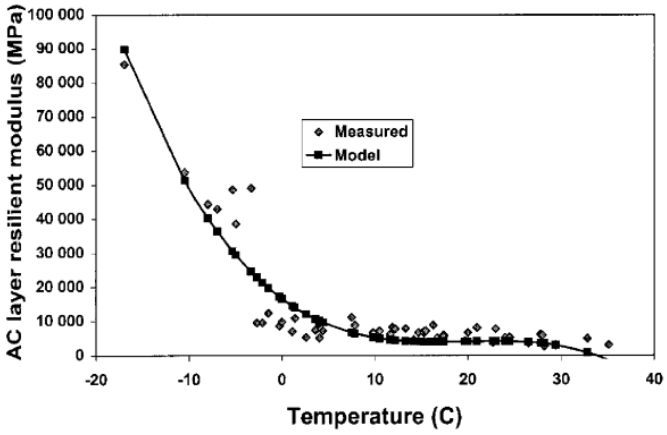

Figure 7.23: Young's modulus of asphalt as a function of temperature. Below 0 °C the stiffness of asphalt increases dramatically [WATS00].

Environmental model of the Z24-Bridge

For simplicity linear models are considered. Therefore only data from periods where the asphalt does not play any role is taken into account. If desired, a separate linear environmental model for the negative temperature range could be identified or more involved nonlinear models could be derived for the whole temperature range. In any case, in the following only positive temperature data are considered.

The high number of input candidates (= 49) makes it necessary to apply *variable selection procedures*. Many inputs offer redundant information and not all of them should be included in the model. The high number of measured quantities is fine in a research project, but an economic monitoring system should operate with only a few environmental parameters.

Next to several temperatures also the wind characteristics, rainfall and humidity have been monitored. Since no relation was found between these last three quantities and the eigenfrequencies, only temperature variables are retained as input candidates. Next reduction is forced by circumstances. Due to *collateral damage* from the construction of a new bridge adjacent to the Z24-Bridge all the soil temperature sensors failed at the end of the monitoring period. Also other sensors failed. The number of input candidates could already be reduced from 49 to 22: the air temperature and 21 concrete and asphalt temperatures are retained.

In a next step the correlations between all inputs and outputs are determined. The correlation $\hat{r}_{xy}$ between two variables x and y is defined as:

$$\hat{r}_{xy} = \frac{\hat{R}_{xy}}{\hat{\sigma}_x \, \hat{\sigma}_y} , \quad \hat{R}_{xy} = \frac{1}{N-1} \sum_{k=1}^{N} (x_k - \bar{x})(y_k - \bar{y})$$

with x_k a sample, $\bar{x}$ the mean value and $\hat{\sigma}_x$ the sample standard deviation of variable x; see Equation (6.7). $\hat{R}_{xy}$ is the sample covariance. An absolute value of the correlation close to 1, indicates a high linear association between the two variables. Input variables for which the (absolute) correlation exceeds 0.99 are grouped together, since they offer almost the same information. Six groups are obtained. The input variable that has the largest correlation with most of the 4 eigenfrequencies is selected as representative for the group. The retained variables are TWN2, TP2, TDT2, TS2, TSWN3 and the air temperature. Almost all representative variables are originating from the main span (span 2) of the bridge. An important remark is that a low correlation can also mean that there is just a time delay between two signals, so it is possible that the six retained variables still contain some redundancy.

Table 7.7: Comparison between **ARX** and static regression SISO models: TDT2 *vs.* eigenfrequency. The model parameters are given in Appendix C.2.

Mode	**ARX** model			Static regression model		
	$n_a\, n_b\, n_k$	V	**FPE**	$n_a\, n_b\, n_k$	V	**FPE**
1	2 1 4	0.145	0.145	0 1 0	0.212	0.213
2	3 2 0	0.533	0.536	0 1 0	0.896	0.897
3	2 1 0	0.507	0.509	0 1 0	0.548	0.549
4	2 2 0	0.569	0.572	0 1 0	0.612	0.613

Having reduced the number of possible input candidates to 6, input-output model are identified according to the theory of Section 6.2. Our strategy to find a good model is the following. For all 4 eigenfrequencies and remaining 6 input candidates, single-input single-output (SISO) **ARX** models are estimated. A good and simple (i.e. with only a few parameters) model is selected for each of the 24 input-output combinations, according to the quality criteria of Subsection 6.2.3. Next, the input is selected that yields "on the average" the best models for all 4 frequencies. The best models have the lowest values for the loss function V (6.13) and Akaike's **FPE**. It turned out that the model based on TDT2 performed best; but it must be added that not much quality loss was observed when using any of the temperatures TWN2, TP2 or TS2. The results are represented in Table 7.7. The input and output data were normalized (6.8) before the models were identified. The model for the first mode seems to be much better than the models for the other 3 modes. The static regression results are also represented. Especially for the first 2 modes, the improvements of an **ARX** model over a static model are evident. The estimated model parameters and their standard deviations are given in Appendix C.2.

Afterwards input variables were added to the SISO models. It was observed that the **ARX** models hardly improved. For instance, the quality measures of a multiple-input single-output (MISO) ARX214 model, that includes all 6 input variables and has the first eigenfrequency as output, are: $V = 0.142$, **FPE** $= 0.143$. These values have to be compared with the values on the first line of Table 7.7. The static models on the other hand could be improved. The quality criteria for a MISO ARX010 model that includes all input variables are: $V = 0.187$, FPE $= 0.188$. It is not only more expensive to measure many temperatures, but also redundant. Multiple static linear regression does not perform better that single-input **ARX** modelling (0.187 > 0.145).

Another indication that **ARX** models perform better than static models is provided by the whiteness test of the residuals; see Subsection 6.2.3. In Figure 7.24 the auto-correlation function $\hat{R}_e(i)/\hat{\lambda}$ of the SISO ARX214 and static models are plotted, together with the

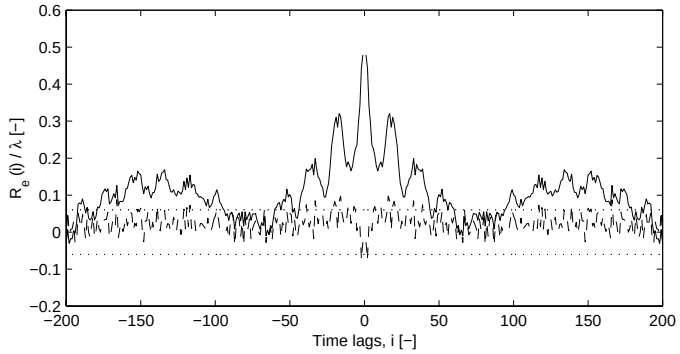

Figure 7.24: Auto-correlation function of the residuals of the TDT2 *vs.* f_1 models. The ARX214 residual auto-correlation function is represented by a dashed line; the static residual auto-correlation is represented by a full line. The 99% confidence intervals are shown as a dotted line. A white noise sequence would have its auto-correlation function in this interval for lags different from zero.

99% confidence intervals. The residual sequence of the static model is not white noise at all.

7.4.3 Damage detection

Once a good model is obtained, it can be used for simulation. New temperature measurements are fed to the models and they simulate the eigenfrequencies of the Z24-Bridge. In Section 6.3 an objective statistical criterion was established that determines whether a simulated frequency, determined by the temperature history and the environmental model, is deviating too much from the measured one. The data which were already used to identify the **ARX** models, and also new data, are fed to the models to yield the simulated frequencies and the 95% confidence intervals (6.22).

The simulation errors and the confidence intervals for mode 1 are plotted in Figure 7.25. An outlier is defined as a point that exceeds the confidence interval. A random outlier is probably due to a bad identification of the eigenfrequency whereas repeated outliers are indicating that something happened with the bridge. The vertical dash-dotted line is splitting the simulation errors in two parts: the left part is related to data that was already used to identify the model, the right part is related to new data. Figure 7.26 is a zoom of Figure 7.25 that concentrates on the period of the progressive damage tests. The comparison between the simulated and measured first eigenfrequency is made in Figure 7.27; see also Equations (6.9) and (6.10). This figure is basically giving the same information but in terms of the eigenfrequencies themselves, rather than the simulation errors of the normalized eigenfrequencies. The simulation errors and the confidence intervals for mode 2, 3 and 4 are plotted in Figures 7.28−7.30.

It is immediately clear that damage is detected at the end of the monitoring period for all frequencies. By taking a closer look at the figures, following observations can be made:

- Concerning mode 1, damage is detected from day 277 on (15 Augustus 1998). This corresponds to the period between the pier settlement of 4 cm and the settlement of 8 cm (see Table 7.5). The preceding scenarios seem to have no large influence on the first eigenfrequency.

- The reversible character of the settlement damage scenarios is evident around day 282 (20 Augustus 1998). It appears also that the bridge did not completely recovered after removal of the settlement as the simulation errors are still exceeding the confidence intervals; see Figures 7.25–7.27.

- As apparent from Figures 7.28–7.30, the environmental models for modes 2, 3 and 4 detect damage from day 269–270 on (7–8 Augustus 1998). Around these dates, the settlement system was installed. Although the bridge was not yet settled and there were no cracks in the bridge girders, the installation of the settlement system required that one of the piers needed to be cut; see also Figure 7.9 and Table 7.5. Damaging the pier clearly affects the frequencies of modes 2 to 4.

- The decrease of the second eigenfrequency with damage is very spectacular, see Figure 7.28.

- There are some anomalies in the simulation errors of the first and second eigenfrequency; see Figures 7.25 and 7.28. They are clearly exceeding the confidence limits at days 248–249 (17–18 July 1998). We are not sure what the cause of that frequency drop could be. Maybe it was a temporarily increase of the mass of the bridge due to some heavy trucks that were standing on the bridge for the installation of the two shakers, see Figure 7.2.

- From Figure 7.26, also a strange increase of the first eigenfrequency around day 270 (8 Augustus 1998) is observed. This date coincides with the installation of the settlement system. Maybe one of the safety measures caused this apparent stiffness increase.

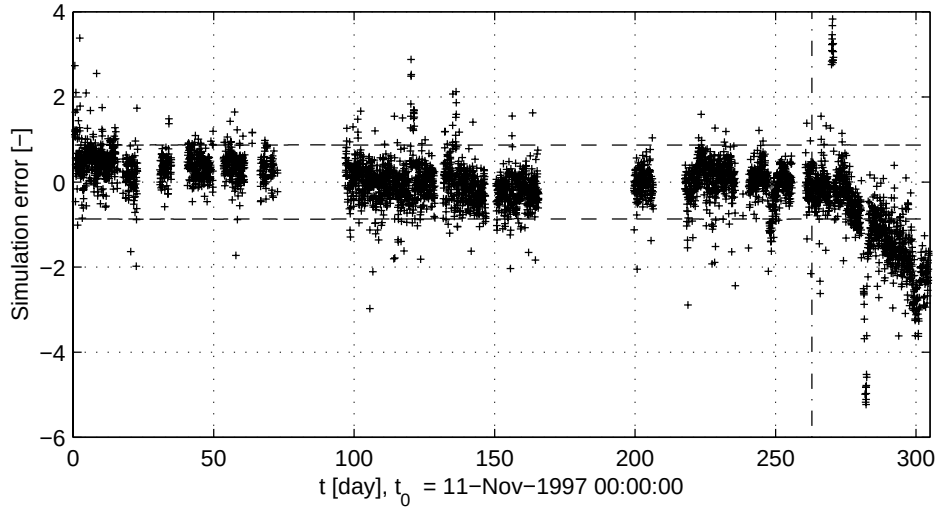

Figure 7.25: Mode 1 results. Simulation errors (crosses) and 95% confidence intervals (dashed lines) of the ARX214 model for TDT2 *vs.* f_1.

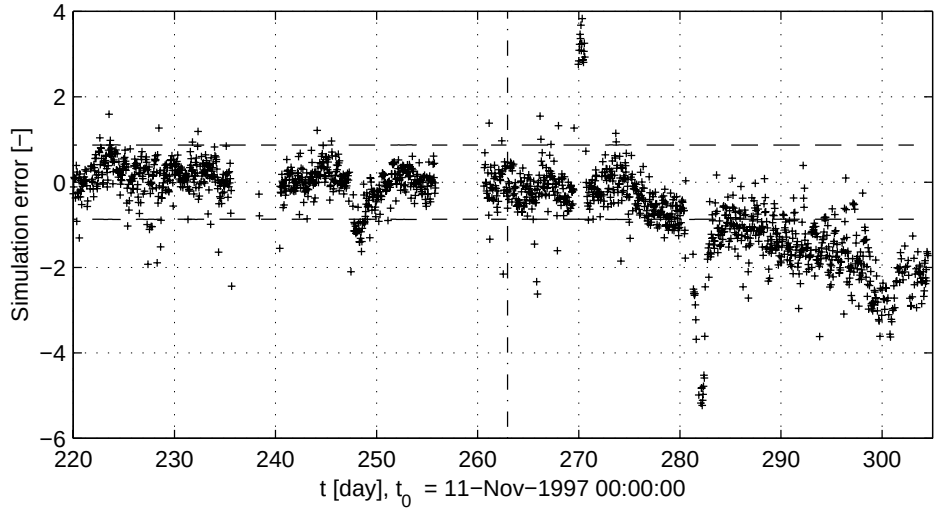

Figure 7.26: Zoom of Figure 7.25. Mainly the period of the progressive damage tests is represented.

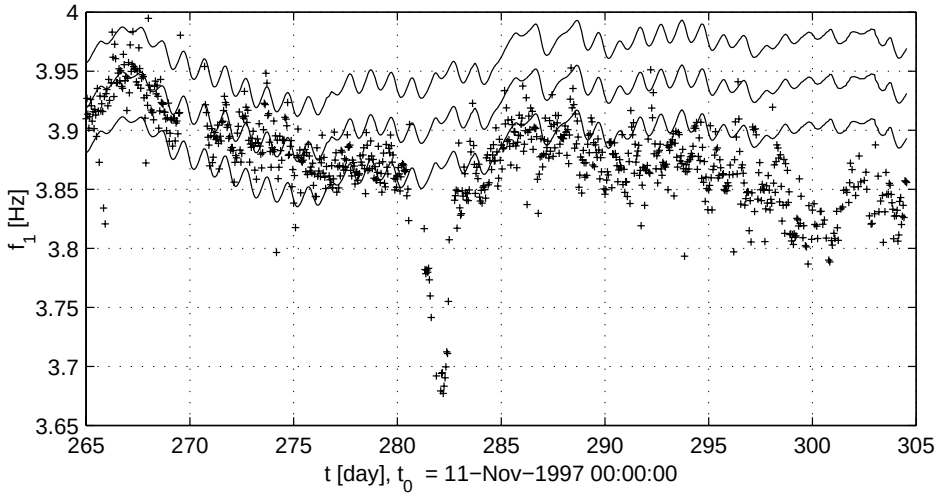

Figure 7.27: Mode 1 results. The measured eigenfrequencies are represented by crosses, the simulated frequencies and the 95% confidence intervals are represented by full lines.

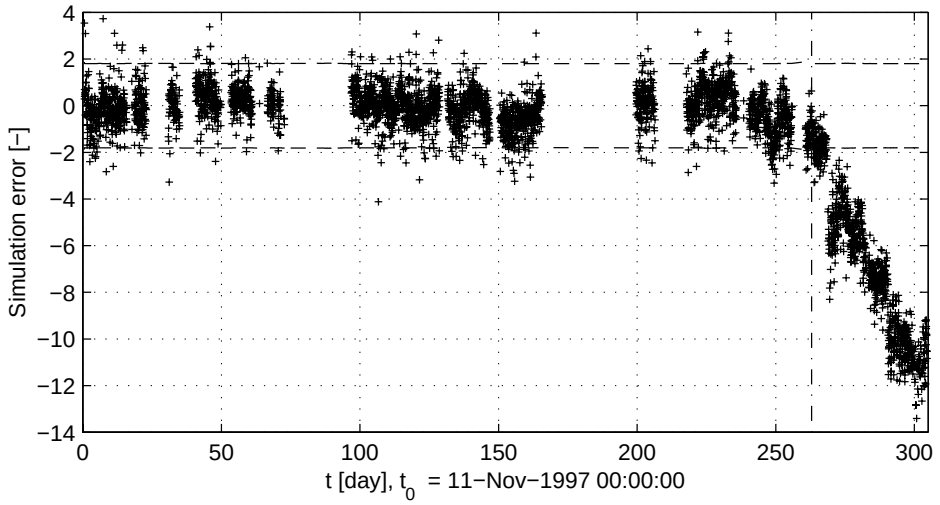

Figure 7.28: Mode 2 results. Simulation errors (crosses) and 95% confidence intervals (dashed lines) of the ARX320 model for TDT2 *vs.* f_2.

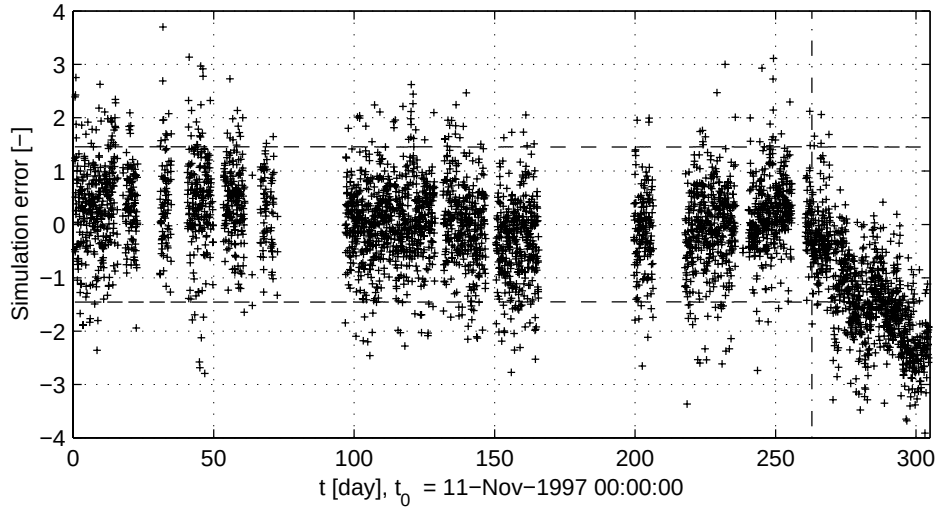

Figure 7.29: Mode 3 results. Simulation errors (crosses) and 95% confidence intervals (dashed lines) of the ARX210 model for TDT2 *vs.* f_3.

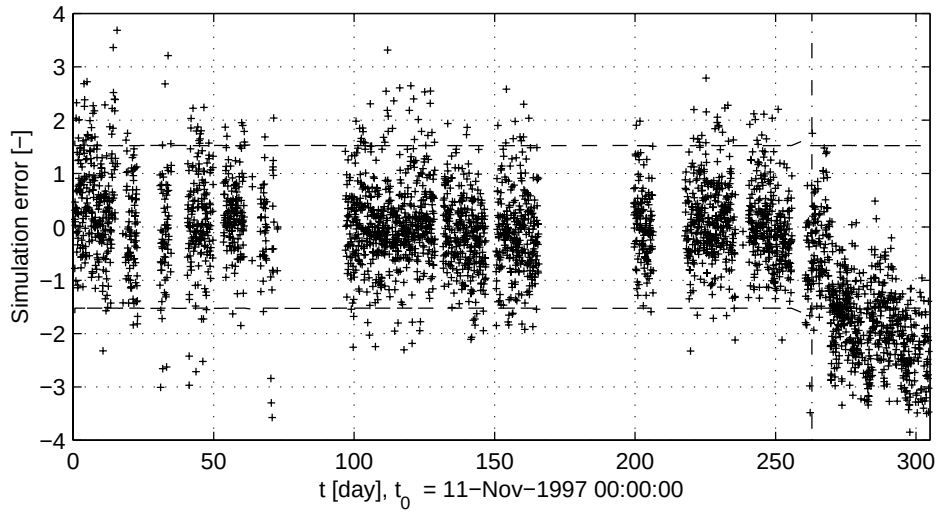

Figure 7.30: Mode 4 results. Simulation errors (crosses) and 95% confidence intervals (dashed lines) of the ARX220 model for TDT2 *vs.* f_4.

7.4.4 Conclusions and recommendations

In this section, the damage detection capabilities of the continuous monitoring system installed on the Z24-Bridge was demonstrated. The method outlined in Chapter 6 and synthesized in Figure 6.2 was applied. **ARX** models were fitted to data from the healthy structure. An **ARX** model that includes the thermal dynamics of the bridge is superior to a static regression model. Also, it turned out that a temperature measurement at one location was sufficient to find an accurate model. The **ARX** models are used for simulating the eigenfrequencies. If a new measured eigenfrequency lies outside the estimated confidence intervals, it is likely that the bridge is damaged. In case of the Z24-Bridge and the applied damage scenarios, we could successfully detect damage.

A first and important problem is the choice and the number of quantities that have to be included in the monitoring system. The vibration sensors (accelerometers) should not be put on nodal points of the mode shapes of interest. For the studied Z24-Bridge, a good place to put a temperature sensor was the top of the concrete deck, under the asphalt layer, in a central location of the main span of the bridge. It was also important to catch the temperature course of the asphalt. Below $0\,^{\circ}C$, the asphalt layer seemed to be responsible for the frequency variations.

Not only the temperatures at different locations have been monitored, but also the wind characteristics, rainfall and humidity. However no relation was found between these last three quantities and the eigenfrequencies. Therefore only temperature variables are retained as inputs.

The added dynamics of the traffic on the bridge has not been studied. We have no measurements of this input variable; so it has to be considered as a disturbance source in the identified **ARX** models.

Sometimes "moisture absorption" is mentioned as another source of environmental variability. However we do not believe that this significantly changes the mass of the bridge. It is well known that concrete hardly absorbs any water and furthermore every bridge has a draining system so that the actual amount of water on the bridge will always be limited.

Since the **ARX** models are "dynamic" models, they need some time to start up. If temperature information is fed into the models, it takes some time before the simulated frequencies converge to the steady state frequencies. It was observed that 24 h was a safe margin for all 4 modes to obtain reliable simulations.

The Young's modulus of fresh concrete increases significantly during the first months. Therefore it is better to wait until convergence before starting to identify environmental models for a new bridge.

In [FARR97, SOHN99] it is suggested that temperature differentials across the deck of the Alamosa Canyon Bridge are the driving forces for the frequency variations, whereas for the Z24-Bridge temperature measurements at a single location seem to be sufficient. The difference is that in [SOHN99] a static regression model was used[4], whereas we are using dynamic **ARX** models. Probably the use of temperature differentials is an attempt to overcome the lack of dynamics in the model. That is also what we observed: in contrast to the dynamic models, our static models could be improved by adding more input variables.

7.5 CONCLUSIONS

In this chapter, a final application was presented. The Z24-Bridge was extensively instrumented and tested with the aim of providing a "feasibility proof" for vibration-based health monitoring in civil engineering.

From the comparison of different excitation types it can be concluded that ambient vibration testing is a valuable approach to estimate the modal parameters of large structures, especially with the improvements of acquisition systems and identification algorithms of the last years.

The progressive damage tests prove that realistic damage scenarios have a measurable influence on the dynamics of the bridge.

The long-term *continuous monitoring* test made it possible to derive environmental models for the bridge. These models are essential to detect damage in the presence of varying temperatures.

[4]Due to the limited amount of data from the studied bridge it was not feasible to identify dynamic models. Identifying a static regression model was the best strategy in that case.

8

CONCLUSIONS AND FUTURE RESEARCH

8.1 CONCLUSIONS

This thesis discussed system identification and damage detection in civil engineering. The work did not only consist of the application of available theory to civil engineering structures, but also contained theoretical developments. The main conclusions of this thesis are the following.

- The relation between **FE** models of vibrating structures, stochastic state-space models and modal models justifies the use of stochastic system identification to estimate the modal parameters of a structure excited by white noise (see Chapter 2).

- Almost all state-of-the-art stochastic system identification methods — peak-picking, complex mode indication function, instrumental variables, covariance-driven and data-driven stochastic subspace identification — are theoretically and experimentally compared (see Chapter 3). From the comparison of the estimated modal parameters, it is concluded that the subspace methods are the preferred methods (see Section 3.9). The prediction error method applied to an **ARMA** model is only briefly discussed, because until present this nonlinear time-domain

method did not reach an acceptable level of robustness and speed for civil engineering modal analysis applications.

- The data-driven stochastic subspace identification method could be adapted and extended to make it suitable for modal analysis applications. The adaptation consists of reducing the dimensions of the matrices (and the computation time) by removing some of the redundancy that is typically present in a modal analysis experiment because usually many sensors are used. The extension consists of efficiently combining the stabilization diagram with subspace methods. Additionally, a technique was developed to split the total measured time response in modal responses.

- The theoretical development of subspace methods combined with developments on the acquisition side greatly enhanced the use of ambient vibration testing in which case weakly excited modes and noisy data are no exception (see Section 7.2)

- The development of a **GUI** for output-only modal analysis makes the subspace identification method accessible to non-experienced users (see Section 4.1). The development of an automatic modal analysis procedure is a key issue of a continuous monitoring system that relies upon the evolution of the modal parameters (see Section 4.2).

- Many simulated (Chapters 2 and 3), laboratory (Chapter 5) and real-life applications (Chapters 5 and 7) are presented in this thesis to illustrate the modelling concepts and the use of the system identification methods.

- A method was developed to distinguish normal environmental from damage influences on the eigenfrequencies of a structure (Chapter 6). This method combined with subspace identification was validated on real data and showed to be a successful real-life damage detection method.

8.2 FUTURE RESEARCH

We believe that this thesis contains useful contributions to the solution of the vibration-based structural health monitoring problem. Nevertheless future research is certainly needed to obtain a *robust, automatic, generally applicable* monitoring system.

- By the introduction of subspace methods in civil engineering, the output-only modal analysis problem seems to be largely solved and it is expected that not much can be improved on the quality of the estimated modal parameters. A related topic that can be improved, however, is the automatic modal analysis procedure. The (simple) approach that we proposed in Section 4.2 turned out to work quite well, but not in 100% of the cases (see Table 7.6). It is still possible to build some more intelligence in the method.

- Concerning the identification and use of the environmental model (see Chapter 6 and Section 7.4) some further improvements are possible. As visible on Figures 7.19 and 7.20, the frequency-temperature relation of the Z24-Bridge exhibits a nonlinear behaviour. It may be worthwhile to try to identify a nonlinear environmental model to include the data from temperatures below 0 °C. It would be interesting to validate the use of the environmental model to detect damage (Section 7.4) on other structures too. Of course, structures like the Z24-Bridge that were monitored during almost a year and artificially damaged afterwards, are not daily available. In this thesis the problem of structural damage detection was reduced to a problem of detecting outliers (see Figures 7.25, 7.28, 7.29 and 7.30). In this case methods from the statistical process control literature can be useful (see for instance [MONT96]).

- This thesis addressed level 1 damage detection (see Sections 1.1 and 1.2) based on eigenfrequencies of the structure. A predictive condition-based maintenance strategy can rely upon the continuous application of level 1 methods. It would however be interesting to extend the monitoring capabilities by using mode shape information and/or an analytical structural model in some automatic manner. This would allow for a localization and quantification of the damage.

- A last open problem has a more theoretical nature. In Chapter 2 the route was followed from a physical model of a vibrating structure to models that can be identified from data. It is an interesting exercise to explore this route in the other direction in order to find out which conditions need to apply to the identified first-order state-space model so that it can be converted to a physically realizable equivalent second-order system consisting of masses, dampers and springs (see for instance [ALVI93]). Notions as stability and positive realness are likely to play an important role in this matter.

A

FREQUENCY-DOMAIN MODAL MODELS

A.1 TRANSFER FUNCTIONS

In Section 2.7, following expression for the transfer function in the Laplace domain was found, see Equation (2.71):

$$H_c(s) = V_c(sI - \Lambda_c)^{-1} L_c^T + D_c$$

This expression can be rewritten by introducing the expressions of V_c, L_c^T, D_c in terms of the modal parameters of the original **FE** model. This will be developed in the following two subsections.

A.1.1 From forces to displacements

In case of displacement measurements, the matrix D_c equals zero; see Equation (2.24). After substituting the participation matrix L_c^T by Equation (2.31) and the observed mode shapes V_c by Equation (2.33), the transfer function from forces to displacements can be written as:

$$H_c(s) = C_d \left(\sum_{i=1}^{n_2} \frac{1}{a_i} \frac{\{\theta_i\} < \theta_i^T >}{s - \lambda_i} + \frac{1}{a_i^*} \frac{\{\theta_i^*\} < \theta_i^H >}{s - \lambda_i^*} \right) B_2 \qquad \text{(A.1)}$$

where $\{\theta_i\} \in \mathbb{C}^{n_2}$, the i^{th} column of Θ, is an eigenvector of the original **FE** model (2.1). The modal decomposition (A.1) explicitly shows that the modes occur in complex conjugated pairs. The expression between brackets is the full $n_2 \times n_2$ transfer function matrix that contains the transfer functions between all **DOF**s of the discretized system. Pre-multiplying by C_d and post-multiplying by B_2 selects the rows and columns of the transfer function matrix at the output and input locations respectively.

A.1.2 From forces to accelerations

As stated before, in most practical cases accelerations are measured. By consequence matrix D_c can be written in terms of the modal parameters $D_c = V_c \Lambda_c^{-1} L_c^T$, see Equation (2.36). The transfer function from forces to accelerations can now be written as:

$$H_c(s) = V_c \, s \Lambda_c^{-1} (sI - \Lambda_c)^{-1} L_c^T \qquad \text{(A.2)}$$

Accelerations are the second derivatives of displacements. This corresponds in the Laplace domain to a multiplication by s^2. However, at first sight this seems not to be the case: a multiplication by $s\Lambda_c^{-1}$ is observed by comparing Equation (A.2) with (2.71). In order to convert this expression to a different form, the orthogonality conditions for the *P* matrix (2.17) are rewritten as:

$$P^{-1} = \begin{pmatrix} 0 & M^{-1} \\ M^{-1} & -M^{-1} C_2 M^{-1} \end{pmatrix} = \Psi \begin{bmatrix} \ddots & & \\ & \frac{1}{a_i} & \\ & & \ddots \end{bmatrix} \Psi^T$$

The upper left block of this equation is isolated:

$$0 = (\Theta \quad \Theta^*) \begin{bmatrix} \ddots & & \\ & \frac{1}{a_i} & \\ & & \ddots \end{bmatrix} \begin{pmatrix} \Theta^T \\ \Theta^H \end{pmatrix}$$

Both sides are multiplied by *s*, pre-multiplied by C_a and post-multiplied by B_2; also two identity matrices are inserted into the right hand side to yield:

$$0 = C_a \begin{pmatrix} \Theta & \Theta^* \end{pmatrix} \Lambda_c^2 \Lambda_c^{-2} s (sI - \Lambda_c)(sI - \Lambda_c)^{-1} \begin{bmatrix} \ddots & \\ & \frac{1}{a_i} \\ & & \ddots \end{bmatrix} \begin{pmatrix} \Theta^T \\ \Theta^H \end{pmatrix} B_2$$

By adding this "zero" to (A.2), substituting the participation matrix L_c^T by Equation (2.31) and the observed mode shapes V_c by Equation (2.34), the transfer function from forces to accelerations can be written as:

$$H_c(s) = V_c \Lambda_c^{-2} s^2 (sI - \Lambda_c)^{-1} L_c^T \tag{A.3}$$

or:

$$H_c(s) = C_a \left(\sum_{i=1}^{n_2} \frac{1}{a_i} \frac{s^2}{s - \lambda_i} \{\theta_i\} \langle \theta_i^T \rangle + \frac{1}{a_i^*} \frac{s^2}{s - \lambda_i^*} \{\theta_i^*\} \langle \theta_i^H \rangle \right) B_2$$

By comparing this expression with the displacement transfer function (A.1), it is indeed observed that a multiplication by s^2 was needed to go from displacements to accelerations.

A.2 SPECTRA

In Section 2.7, following expression for the spectrum was found, see Equation (2.75):

$$S_y(s) = (V_c(sI - \Lambda_c)^{-1} L_c^T + D_c) R_u (D_c^T + L_c(s^* I - \Lambda_c)^{-1} V_c^T)$$

Some identification methods of Chapter 3 need an expression for the spectrum that is written as a sum of modal contributions instead of a product. This can be achieved by applying the partial fraction expansion.

A.2.1 The displacement spectrum

In case of displacement measurements, the matrix D_c equals zero; see Equation (2.24). The modal decomposition of the spectrum (2.75) reduces to:

$$S_y(s) = (V_c(sI - \Lambda_c)^{-1} L_c^T) R_u (L_c(s^* I - \Lambda_c)^{-1} V_c^T)$$

In the application of the partial fraction expansion, two residual matrices P_1, P_2 need to be found that satisfy:

$$(sI - \Lambda_c)^{-1} L_c^T \, R_u \, L_c (s^* I - \Lambda_c)^{-1} = (sI - \Lambda_c)^{-1} \, P_1 + P_2 \, (s^* I - \Lambda_c)^{-1}$$

Both sides are pre-multiplied by $(sI - \Lambda_c)$ and post-multiplied by $(s^* I - \Lambda_c)$ to yield:

$$L_c^T \, R_u \, L_c = s^* P_1 + sP_2 - P_1 \Lambda_c - \Lambda_c P_2$$

This expression should hold for all values of s. In practice, s is restricted to purely imaginary values $s = j\omega$ where ω [rad/s] is an arbitrary frequency. Since then $s^* = -s$, it is found that $P_1 = P_2$ by imposing that the term in s disappears. If P_1 and P_2 are replaced by $P_{c,m}$, as to stress its continuous-time character and its relation to the modal parameters, the residuals of the partial fraction expansion are found from:

$$P_{c,m} \Lambda_c + \Lambda_c P_{c,m} = -L_c^T \, R_u \, L_c \tag{A.4}$$

which is a so-called *continuous-time Lyapunov equation* that can be solved for $P_{c,m}$. From Equation (A.4) it is seen that $P_{c,m} \in \mathbb{C}^{n \times n}$ is a symmetric matrix that depends on the system poles, the participation factors and the input covariance. After introducing the partial fraction expansion, the displacement spectrum reads:

$$S_y(j\omega) = V_c (sI - \Lambda_c)^{-1} P_{c,m} V_c^T + V_c P_{c,m} (s^* I - \Lambda_c)^{-1} V_c^T \Big|_{s = j\omega}$$

Note that s is substituted by $j\omega$ as the argument of S_y. With the matrix $G_{c,m} \in \mathbb{C}^{n \times l}$ defined as:

$$G_{c,m} = P_{c,m} V_c^T = P_{c,m} \begin{pmatrix} \Theta^T \\ \Theta^H \end{pmatrix} C_d^T \tag{A.5}$$

and its i^{th} row denoted as: $< g_{c_i}^T >$, the modal decomposition of the displacement spectrum can be rewritten as:

$$S_y(j\omega) = \sum_{i=1}^{n_2} \frac{\{v_{c_i}\} < g_{c_i}^T >}{s - \lambda_i} + \frac{\{v_{c_i}^*\} < g_{c_i}^H >}{s - \lambda_i^*} + \frac{\{g_{c_i}\} < v_{c_i}^T >}{s^* - \lambda_i} + \frac{\{g_{c_i}^*\} < v_{c_i}^H >}{s^* - \lambda_i^*} \Bigg|_{s = j\omega} \tag{A.6}$$

The matrix $G_{c,m}$ is called *continuous-time stochastic modal participation matrix*. However there is an important difference with the classical participation matrix L_c^T. Every row of this last matrix only depends on 1 mode, whereas a row of $G_{c,m}$ theoretically depends on all modes. This fact becomes more clear if we would find a closed-form expression for such a row $< g_{c_i}^T >$. From the definition of $G_{c,m}$ (A.5), it is found:

$$<g_{c_i}^T> = <p_{c_i}> V_c^T$$

In general, it is not possible to find a closed-form expression for the solution of a Lyapunov equation (A.4). However, thanks to the diagonal structure of Λ_c, the i^{th} row of $P_{c,m}$ can be written as:

$$<p_{c_i}> \Lambda_c + \lambda_i <p_{c_i}> = - <l_{c_i}^T> R_u L_c$$
$$\Updownarrow$$
$$<p_{c_i}> = <l_{c_i}^T> R_u L_c (-\Lambda_c - \lambda_i I)^{-1}$$

Inserting this closed-form expression and Equations (2.31) and (2.33) into the definition of $G_{c,m}$ (A.5), yields:

$$<g_{c_i}^T> = <p_{c_i}> V_c^T = \frac{1}{a_i} <\theta_i^T> B_2 R_u B_2^T \left(\sum_{j=1}^{n_2} \frac{1}{a_j} \frac{\{\theta_j\}<\theta_j^T>}{-\lambda_i - \lambda_j} + \frac{1}{a_j^*} \frac{\{\theta_j^*\}<\theta_j^H>}{-\lambda_i - \lambda_j^*} \right) C_d^T$$

It turns out that a single output-only modal participation vector $<g_{c_i}^T>$ depends on all modal parameters of the system, on the input locations and on the input covariance matrix.

An alternative way of obtaining the modal decomposition of the spectrum first computes all the products in Equation (2.75) and then applies the partial fraction expansion to every cross-product of two modal contributions. This approach is for instance followed in [HERM97] and [BRIN00].

A.2.2 The acceleration spectrum

If accelerations are measured, the modal decomposition of the spectrum is found by inserting the modal decomposition of the transfer function (A.3) into Equation (2.74):

$$S_y(s) = V_c \Lambda_c^{-2} s^2 (sI - \Lambda_c)^{-1} L_c^T R_u L_c (s^* I - \Lambda_c)^{-1} (s^*)^2 \Lambda_c^{-2} V_c^T \qquad \text{(A.7)}$$

The same partial fraction expansion may be applied as before. With the matrix $G_{c,m}$ in case of accelerations, defined as:

$$G_{c,m} = P_{c,m} \Lambda_c^{-2} V_c^T = P_{c,m} \begin{pmatrix} \Theta^T \\ \Theta^H \end{pmatrix} C_a^T$$

which is similar to Equation (A.5), the modal decomposition of the acceleration spectrum can be written as:

$$S_y(j\omega) = \sum_{i=1}^{n_2} \frac{(ss^*)^2}{\lambda_i^2(s-\lambda_i)} \{v_{c_i}\}\langle g_{c_i}^T\rangle + \frac{(ss^*)^2}{(\lambda_i^*)^2(s-\lambda_i^*)} \{v_{c_i}^*\}\langle g_{c_i}^H\rangle + \cdots$$
$$\cdots \frac{(ss^*)^2}{\lambda_i^2(s^*-\lambda_i)} \{g_{c_i}\}\langle v_{c_i}^T\rangle + \frac{(ss^*)^2}{(\lambda_i^*)^2(s^*-\lambda_i^*)} \{g_{c_i}^*\}\langle v_{c_i}^H\rangle \Bigg|_{s=j\omega} \quad \text{(A.8)}$$

B

STATE-SPACE MODEL OF THE SIMULATION EXAMPLE

In this appendix the numerical values of the state-space model of the simulation example of Chapters 2 and 3 are presented. The purpose of this appendix is to allow for reproducibility of the identification results by interested researchers.

Example

The discrete-time state-space matrices, with a sample time $\Delta t = 0.04\,\mathrm{s}$, of the simulation example are:

$$D = \begin{pmatrix} 0.0756 & -0.0048 & 0.0553 & -0.0048 & 0.0655 & 0.0129 \\ -0.0048 & 0.0701 & 0.0070 & 0.0701 & 0.0011 & 0.0599 \\ 0.0553 & 0.0070 & 0.0850 & 0.0070 & 0.0701 & -0.0188 \\ -0.0200 & 0.0024 & -0.0105 & 0.0024 & -0.0153 & -0.0059 \\ 0.0024 & -0.0173 & -0.0031 & -0.0173 & -0.0004 & -0.0125 \\ -0.0106 & -0.0031 & -0.0231 & -0.0031 & -0.0168 & 0.0077 \end{pmatrix} \cdots$$

$$\cdots \begin{pmatrix} -0.0200 & 0.0024 & -0.0106 & 0.0024 & -0.0153 & -0.0058 \\ 0.0024 & -0.0173 & -0.0031 & -0.0173 & -0.0004 & -0.0126 \\ -0.0105 & -0.0031 & -0.0231 & -0.0031 & -0.0168 & 0.0078 \\ 0.1301 & -0.0100 & 0.0888 & -0.0100 & 0.1095 & 0.0257 \\ -0.0100 & 0.1185 & 0.0138 & 0.1185 & 0.0019 & 0.0979 \\ 0.0888 & 0.0138 & 0.1454 & 0.0138 & 0.1171 & -0.0352 \end{pmatrix}$$

$$A = \mathrm{diag}\left\{ \begin{pmatrix} 0.9963 & 0.0766 \\ -0.0766 & 0.9963 \end{pmatrix}, \begin{pmatrix} 0.9874 & 0.1485 \\ -0.1485 & 0.9874 \end{pmatrix}, \begin{pmatrix} 0.9871 & 0.1502 \\ -0.1502 & 0.9871 \end{pmatrix} \right.$$
$$\left. \begin{pmatrix} 0.9648 & 0.2531 \\ -0.2531 & 0.9648 \end{pmatrix}, \begin{pmatrix} 0.9026 & 0.4203 \\ -0.4203 & 0.9026 \end{pmatrix}, \begin{pmatrix} 0.9005 & 0.4247 \\ -0.4247 & 0.9005 \end{pmatrix} \right\}$$

$$B = 10^{-3} \times \begin{pmatrix} 0.3640 & -0.1943 & -0.3181 & -0.1943 & 0.0229 & 0.3964 \\ 0.3304 & -0.1763 & -0.2887 & -0.1763 & 0.0208 & 0.3598 \\ -0.8032 & -0.1299 & -0.8715 & -0.1299 & -0.8373 & -0.0708 \\ -0.6776 & -0.1096 & -0.7352 & -0.1096 & -0.7064 & -0.0597 \\ -0.0946 & 0.8263 & -0.1318 & 0.8263 & -0.1132 & 0.8585 \\ -0.0797 & 0.6959 & -0.1110 & 0.6959 & -0.0953 & 0.7230 \\ 0.5558 & -0.2914 & -0.4595 & -0.2914 & 0.0482 & 0.5879 \\ 0.4201 & -0.2202 & -0.3473 & -0.2202 & 0.0364 & 0.4443 \\ 1.1588 & 0.2230 & 1.2835 & 0.2230 & 1.2212 & 0.1151 \\ 0.7228 & 0.1391 & 0.8005 & 0.1391 & 0.7617 & 0.0718 \\ 0.1573 & -1.2013 & 0.2280 & -1.2013 & 0.1926 & -1.2625 \\ 0.0976 & -0.7451 & 0.1414 & -0.7451 & 0.1195 & -0.7831 \end{pmatrix} \cdots$$

$$\cdots \begin{pmatrix} 0.5165 & -0.2755 & -0.4512 & -0.2755 & 0.0327 & 0.5625 \\ 0.4688 & -0.2501 & -0.4095 & -0.2501 & 0.0297 & 0.5105 \\ -1.1713 & -0.1883 & -1.2680 & -0.1883 & -1.2196 & -0.1045 \\ -0.9882 & -0.1588 & -1.0697 & -0.1588 & -1.0290 & -0.0882 \\ -0.1376 & 1.2032 & -0.1925 & 1.2032 & -0.1650 & 1.2507 \\ -0.1159 & 1.0132 & -0.1621 & 1.0132 & -0.1390 & 1.0533 \\ -0.7626 & 0.4068 & 0.6476 & 0.4068 & -0.0575 & -0.8144 \\ -0.5763 & 0.3075 & 0.4894 & 0.3075 & -0.0434 & -0.6155 \\ -1.3754 & -0.2693 & -1.5327 & -0.2693 & -1.4541 & -0.1331 \\ -0.8579 & -0.1680 & -0.9560 & -0.1680 & -0.9069 & -0.0830 \\ -0.1855 & 1.4308 & -0.2713 & 1.4308 & -0.2284 & 1.5051 \\ -0.1151 & 0.8875 & -0.1683 & 0.8875 & -0.1417 & 0.9336 \end{pmatrix}$$

$$C = \begin{pmatrix} -0.5304 & 0.5199 & 2.2337 & -2.1894 & 0.2661 & -0.2608 \\ 0.2831 & -0.2775 & 0.3613 & -0.3541 & -2.3239 & 2.2778 \\ 0.4636 & -0.4544 & 2.4236 & -2.3756 & 0.3707 & -0.3633 \\ -0.7527 & 0.7378 & 3.2574 & -3.1929 & 0.3869 & -0.3792 \\ 0.4015 & -0.3936 & 0.5235 & -0.5132 & -3.3837 & 3.3167 \\ 0.6575 & -0.6444 & 3.5262 & -3.4564 & 0.5412 & -0.5305 \end{pmatrix} \cdots$$

$$\cdots \begin{pmatrix} -2.5591 & 2.5084 & -8.5827 & 8.4127 & -1.1765 & 1.1532 \\ 1.3415 & -1.3149 & -1.6519 & 1.6192 & 8.9861 & -8.8082 \\ 2.1154 & -2.0735 & -9.5059 & 9.3176 & -1.7055 & 1.6718 \\ 3.5109 & -3.4414 & 10.1867 & -9.9850 & 1.3876 & -1.3601 \\ -1.8731 & 1.8360 & 1.9945 & -1.9550 & -10.7027 & 10.4908 \\ -2.9816 & 2.9225 & 11.3517 & -11.1269 & 2.0297 & -1.9895 \end{pmatrix}$$

C

DEFERRED Z24-BRIDGE RESULTS

C.1 EVOLUTION OF THE DAMPING RATIOS

The estimated damping ratios of the first 5 modes of all damage scenarios are represented in Table C.1. This table is teaching us that the relatively high uncertainties on the damping ratios makes it difficult to use them to detect damage.

C.2 ENVIRONMENTAL MODEL OF THE Z24-BRIDGE

The properties of the input-output data are given in Table C.2. These are required to convert the **ARX** models that are identified from normalized data back to engineering units, see Equations (6.8)–(6.10). The parameters of the identified **ARX** models are given in Table C.3, whereas the parameters of the static regression models can be found in Table C.4.

Table C.1: Evolution of the damping ratios with damage. The mean values $\bar{\xi}$ and estimated standard deviations $\hat{\sigma}_{\xi}$ are based on 9 samples originating from the 9 independent setups. The results were obtained by applying **SSI-DATA** to the ambient vibration data.

Scenario	mode 1		mode 2		mode 3		mode 4		mode 5	
	$\bar{\xi}$ [%]	$\hat{\sigma}_{\xi}$ [%]	$\bar{\xi}$ [%]	$\hat{\sigma}_{\xi}$ [%]	$\bar{\xi}$ [%]	$\hat{\sigma}_{\xi}$ [%]	$\bar{\xi}$ [%]	$\hat{\sigma}_{\xi}$ [%]	$\bar{\xi}$ [%]	$\hat{\sigma}_{\xi}$ [%]
1	0.9	0.2	1.4	0.3	1.4	0.3	2	0.5	2.4	0.7
2	1	0.8	1.4	0.4	1.4	0.4	1.6	0.6	2.6	0.4
3	0.9	0.4	1.1	0.2	1.1	0.3	1.5	0.4	2.8	1.1
4	1.1	0.3	1.3	0.2	1.4	0.4	1.6	0.3	2.5	0.7
5	1	0.7	1.4	0.5	1.5	0.5	2	1.2	3.3	1.2
6	1.3	0.5	1.8	0.9	1.4	0.5	1.3	0.3	2.5	0.7
7	1	0.5	1.3	0.4	1.5	0.3	1.4	0.4	2.3	0.6
8	1.1	0.4	1.3	0.4	1.4	0.6	1.4	0.3	2.7	1
9	1.3	0.6	1.5	0.5	1.3	0.5	1.5	0.3	2.6	0.7
10	1.2	0.7	1.1	0.4	1.4	0.3	1.8	0.7	2.6	0.7
11	1	0.4	1.6	0.5	1.1	0.4	2.1	0.8	2.5	0.7
12	1.2	1.1	1.6	0.6	1.3	0.4	1.8	0.4	2.5	1
13	1	0.2	1.8	0.4	1.3	0.4	1.8	1.8	2.2	0.5
14	1.2	0.5	1.7	0.5	2.3	1.8	1.8	0.6	2.4	0.4
15	1.4	0.6	1.9	0.5	1.7	0.3	1.9	0.4	2.7	0.6
16	1.1	0.3	1.9	0.6	1.4	0.4	1.6	0.4	2.3	0.9
17	1	0.7	1.6	0.5	1.6	0.2	1.6	0.4	2.3	0.5

Table C.2: Mean values and sample standard deviations of the input-output data, based on samples from the positive temperatures only. Therefore the mean values of the frequency outputs $\bar{y}$ are different from the values of Table 7.6 that considered all samples.

Mode	Input		Output	
	$\bar{u}$ [°C]	$\hat{\sigma}_u$ [°C]	$\bar{y}$ [Hz]	$\hat{\sigma}_y$ [Hz]
1	15.299	9.009	3.943	0.039
2	"	"	5.189	0.049
3	"	"	10.016	0.109
4	"	"	10.686	0.145

Table C.3: ARX model parameters. The estimated values $\hat{\theta}_i$ and their standard deviations $\hat{\sigma}_{\hat{\theta}_i}$ are specified.

Mode	Model		$\hat{a}_0$	$\hat{a}_1$	$\hat{a}_2$	$\hat{a}_3$	$\hat{b}_1$	$\hat{b}_2$
1	2 1 4	$\hat{\theta}_i$	10	-0.320	-0.282	–	-0.357	–
		$\hat{\sigma}_{\hat{\theta}_i}$		0.022	0.022	–	0.022	–
2	3 2 0	$\hat{\theta}_i$	10	-0.292	-0.266	-0.176	3.074	-2.996
		$\hat{\sigma}_{\hat{\theta}_i}$		0.023	0.023	0.023	0.242	0.243
3	2 1 0	$\hat{\theta}_i$	10	-0.204	-0.144	–	-0.435	–
		$\hat{\sigma}_{\hat{\theta}_i}$		0.023	0.023	–	0.026	–
4	2 2 0	$\hat{\theta}_i$	10	-0.166	-0.143	–	-1.476	1.052
		$\hat{\sigma}_{\hat{\theta}_i}$		0.023	0.023	–	0.251	0.248

Table C.4: Static regression model parameters. The estimated values $\hat{\theta}_i$ and their standard deviations $\hat{\sigma}_{\hat{\theta}_i}$ are specified.

Mode	Model		$\hat{b}_1$
1	0 1 0	$\hat{\theta}_i$	-0.887
		$\hat{\sigma}_{\hat{\theta}_i}$	0.011
2	0 1 0	$\hat{\theta}_i$	0.321
		$\hat{\sigma}_{\hat{\theta}_i}$	0.022
3	0 1 0	$\hat{\theta}_i$	-0.672
		$\hat{\sigma}_{\hat{\theta}_i}$	0.017
4	0 1 0	$\hat{\theta}_i$	-0.623
		$\hat{\sigma}_{\hat{\theta}_i}$	0.018

REFERENCES

[AKAI74a] Akaike H. Markovian representation of stochastic processes and its application to the analysis of autoregressive moving average processes. *Annals of the Institute of Statistical Mathematics*, **26**, 363-387, 1974.

[AKAI74b] Akaike H. Stochastic theory of minimal realization. *IEEE Transactions on Automatic Control*, **19**, 667-674, 1974.

[ALAM98] Alampalli S. Influence of in-service environment on modal parameters. In *Proceedings of IMAC 16*, pp. 111-116, Santa Barbara, CA, USA, February 1998.

[ALLE94] Allemang R.J., Brown D.L., and Fladung W.A. Modal parameter estimation: a unified matrix polynomial approach. In *Proceedings of IMAC 12, the International Modal Analysis Conference*, pp. 501-514, Honolulu, HI, USA, 1994.

[ALLE99] Allemang R.J. *Vibrations: Experimental Modal Analysis, Course Notes*. Seventh edition, Structural Dynamics Research Laboratory, University of Cincinnati, OH, USA, [http://www.sdrl.uc.edu/course_info.html], 1999.

[ALVI93] Alvin K.F. *Second-Order Structural Identification via State Space-Based System Realizations*. PhD thesis, Department of Aerospace Engineering Sciences, University of Colorado, Boulder, CO, USA, [http://www.nmia.com/~alvin/], April 1993.

[ANDE97] Andersen P. *Identification of Civil Engineering Structures Using Vector ARMA Models*. PhD thesis, Department of Building Technoloy and Structural Engineering, Aalborg University, Denmark, May 1997.

[AOKI87] Aoki M. *State Space Modelling of Time Series*. Springer-Verlag, Berlin, Germany, 1987.

[ARUN90] Arun K.S. and Kung S.Y. Balanced approximation of stochastic systems. *SIAM Journal on Matrix Analysis and Applications*, **11**, 42-68, 1990.

[ASKE88] Askegaard V. and Mossing P. Long term observation of RC-bridge using changes in natural frequency. *Nordic Concrete Research*, **7**, 20-27, 1988.

[ASMU97] Asmussen J.C. *Modal Analysis Based on the Random Decrement Technique - Application to Civil Engineering Structures* . PhD thesis, Department of Building Technology and Structural Enginering, Aalborg University, Denmark, 1997.

[BALE93] Balendra T. *Vibration of Buildings to Wind and Earthquake Loads*. Springer-Verlag, London, UK, 1993.

[BALM97] Balmès E. *Structural Dynamics Toolbox for Use With Matlab, User's Guide, Version 3*. Scientific Software Group, Sèvres, France, [http://www.sdtools.com], 1997.

[BASS93a] Basseville M., Benveniste A., Gach-Devauchelle B., Goursat M., Bonnecase D., Dorey P., Prevosto M., and Olagnon M. In situ damage monitoring in vibration mechanics: diagnostics and predictive maintenance. *Mechanical Systems and Signal Processing*, **7**(5), 401-423, 1993.

[BASS93b] Basseville M. and Nikiforov I.V. *Detection of Abrupt Changes: Theory and Applications*. Prentice-Hall, Englewood Cliffs, NJ, USA, [http://www.irisa.fr/sigma2/kniga/], 1993.

[BEND93] Bendat J.S. and Piersol A.G. *Engineering Applications of Correlation and Spectral Analysis*. Second edition, John Wiley & Sons, New York, USA, 1993.

[BENV85] Benveniste A. and Fuchs J.-J. Single sample modal identification of a nonstationary stochastic process. *IEEE Transactions on Automatic Control*, **AC-30**(1), 66-74, 1985.

[BRIN95] Brincker R., Andersen P., Kirkegaard P.H., and Ulfkjær J.P. Damage detection in laboratory concrete beams. In *Proceedings of IMAC 13*, Aalborg, pp. 668-674, Nashville, TN, USA, February 1995.

[BRIN00] Brincker R., Zhang L., and Andersen P. Modal identification from ambient responses using frequency domain decomposition. In *Proceedings of IMAC 18, the International Modal Analysis Conference*, pp. 625-630, San Antonio, TX, USA, February 2000.

[CADA98] *CADA-X, Modal Analysis Manual, Revision 3.5*. LMS International, Leuven, Belgium, [http://www.lmsintl.com], 1998.

[CHAS97] Chase S.B. and Washer G. Nondestructive evaluation for bridge management in the next century. *Public Roads*, **61**(1), [http://www.tfhrc.gov], 1997.

[COLE68] Cole H.A. On-the-line analysis of random vibrations. *AIAA Paper No. 68-288*, 1968.

[CONT97] *Control System Toolbox for Use With Matlab, User's Guide, Version 4*. The MathWorks, Natick, MA, USA, [http://www.mathworks.com], January 1997.

[COOL65] Cooley J.W. and Tukey J.W. An algorithm for the machine calculation of complex Fourier series. *Mathematics of Computation*, **19**(90), 297-301, 1965.

[CUNH99] Cunha A., Caetano E., Calçada R., and Delgado R. Modal identification and correlation with finite element parameters of Vasco da Gama Bridge. In *Proceedings of IMAC 17*, pp. 705-711, Kissimmee, FL, USA, February 1999.

[DAHL98] Dahlén A., Lindquist A., and Mari J. Experimental evidence showing that stochastic subspace identification methods may fail. *Systems and Control Letters*, **34**, 303-312, 1998.

[DEGE94] Deger Y., Cantieni R., and Pietrzko S. Modal analysis of a steel/concrete composite bridge: linking finite element analysis and experimental data. In *Proceedings of ISMA 19, the International Seminar on Modal Analysis*, EMPA, pp. 777-787, Leuven, Belgium, September 1994.

[DELA99] Delaunay D., Grillaud G., Biétry J., and Sacré C. Wind reponse of long-span bridges: in-situ measurements and modal analysis. In *Proceedings of IMAC 17*, pp. 719-725, Kissimmee, FL, USA, February 1999.

[DERO95] De Roeck G., Claesen W., and Van den Broeck P. DDS-methodology applied to parameter identification of civil engineering structures. In *Vibration and Noise '95*, pp. 341-353, Venice, Italy, April 1995.

[DERO00b] De Roeck G., Peeters B., and Maeck J. Dynamic monitoring of civil engineering structures. In *Proceedings of IASS-IACM 2000, Computational Methods for Shell and Spatial Structures*, Chania, Greece, June 2000.

[DEVI99] De Visscher J., De Wilde W.P., Ndambi J.-M., Vantomme J., Peeters B., Abdel Wahab M.M., and De Roeck G. An experimental study of damping in reinforced concrete. In *Proceedings of the International Congress on Creating With Concrete*, Dundee, UK, September 1999.

[DIET80] Dieterle R. and Bachmann H. Einfluss der Rissbildung auf die Dynamischen Eigenschaften von Leichtbeton- und Betonbalken. *Schweizer Ingenieur Und Architekt*, **32**, 1980.

[DOEB96] Doebling S. W., Farrar C. R., Prime M. B., and Shevitz D. W. *Damage Identification and Health Monitoring of Structural and Mechanical Systems From Changes in Their Vibration Characteristics: a Literature Review*. Research report LA-13070-MS, ESA-EA Los Alamos National Laboratory, Los Alamos, NM, USA, [http://www.lanl.gov/projects/ncsd/], 1996.

[EWIN84] Ewins D.J. *Modal Testing: Theory and Practice*. Research Studies Press Ltd., Letchworth, Hertfordshire, UK, 1984.

[FARR97] Farrar C.R., Doebling S.W., Cornwell P.J., and Straser E.G. Variability of modal parameters measured on the Alamosa Canyon Bridge. In *Proceedings of IMAC 15*, pp. 257-263, Orlando, FL, USA, February 1997.

[FARR98] Farrar C.R. and Jauregui D.A. Comparative study of damage identification algorithms applied to a bridge: I. Experiment. *Smart Materials and Structures*, **7**(5), 704-719, 1998.

[FARR99a] Farrar C.R., Duffy T.A., Cornwell P.J., and Doebling S.W. Excitation methods for bridge structures. In *Proceedings of IMAC 17*, pp. 1063-1068, Kissimmee, FL, USA, 1999.

[FARR99b] Farrar C.R., Doebling S.W., and Duffey T.A. Vibration-based damage detection. In *Proceedings of SD2000, the Structural Dynamics Forum*, Los Alamos, NM, USA, [http://www.lanl.gov/projects/ncsd/], April 1999.

[FARR00] Farrar C. R., Cornwell P. J., Doebling S. W., and Prime M. B. *Structural Health Monitoring Studies of the Alamosa Canyon and I-40 Bridges*. Report LA-13635-MS, Los Alamos National Laboratory, Los Alamos, NM, USA, [http://www.lanl.gov/projects/ncsd], July 2000.

[FELB93] Felber A.J. *Development of a Hybrid Bridge Evaluation System*. PhD thesis, University of British Columbia, Vancouver, Canada, 1993.

[FELB96] Felber A. J. and Cantieni R. *Introduction of a New Ambient Vibration Testing System - Description of the System and Seven Bridge Tests*. Internal Report 156'521, EMPA, Dübendorf, Switzerland, 1996.

[FRAN97] Franklin G.F., Powell J.D., and Workman M.L. *Digital Control of Dynamic Systems*. Third edition, Addison-Wesley, 1997.

[FRIS95] Friswell M.I. and Mottershead J.E. *Finite Element Model Updating in Structural Dynamics*. Kluwer Academic Publishers, Dordrecht, The Netherlands, 1995.

[GENT98] Gentile C., Martinez y Cabrera F., and Saisi A. Dynamic testing and seismic response of a cable-stayed bridge. In *Proceedings of the 11th European Conference on Earthquake Engineering*: A.A. Balkema, Rotterdam, 1998.

[GOLU89] Golub G.H. and Van Loan C.F. *Matrix Computations*. Third edition, The Johns Hopkins University Press, Baltimore, MD, USA, 1996.

[GREE95] Green M.F. Modal test methods for bridges: a review. In *Proceedings of IMAC 13*, pp. 552-558, Nashville, TN, USA, February 1995.

[GUI97] *Building GUIs With Matlab, Version 5*. The MathWorks, Natick, MA, USA, [http://www.mathworks.com], June 1997.

[GUIL98] Guillaume P., Verboven P., and Vanlanduit S. Frequency-domain maximum likelihood identification of modal parameters with confidence intervals. In *Proceedings of ISMA 23, Noise and Vibration Engineering*, K.U.Leuven, Belgium, 1998.

[GUIL99] Guillaume P., Hermans L., and Van der Auweraer H. Maximum likelihood identification of modal parameters from operational data. In *Proceedings of IMAC 17*, pp. 1887-1893, Kissimmee, FL, USA, February 1999.

[HERM97] Hermans L. and Van der Auweraer H. On the use of auto- and cross-correlation functions to extract modal parameters from output-only data. In *Proceedings of the 6th International Conference on Recent Advances in Structural Dynamics*, Work in progress paper, University of Southampton, UK, 1997.

[HERM98] Hermans L., Guillaume P., and Van der Auweraer H. A frequency-domain maximum likelihood approach for the extraction of modal parameters from output-only data. In *Proceedings of ISMA 23, Noise and Vibration Engineering*, K.U.Leuven, Belgium, 1998.

[HERM99] Hermans L. and Van der Auweraer H. Modal testing and analysis of structures under operational conditions: industrial applications. *Mechanical Systems and Signal Processing*, **13**(2), 193-216, 1999.

[HEYL95] Heylen W., Lammens S., and Sas P. *Modal Analysis Theory and Testing*. Department of Mechanical Engineering, Katholieke Universiteit Leuven, Leuven, Belgium, 1995.

[HOKA66] Ho B.L. and Kalman R.E. Effective construction of linear state-variable models from input/output data. *Regelungstechnik*, **14**, 545-548, 1966.

[HOUS97] Housner G.W., Bergman L.A., Caughey T.K., Chassiakos A.G., Claus R.O., Masri S.F., Skelton R.E., Soong T.T., Spencer B.F., and Yao J.T.P. Special issue. Structural control: past, present, and future. *Journal of Engineering Mechanics*, **123**(9), 897-971, 1997.

[IBRA77] Ibrahim S.R. Random decrement technique for modal identification of structures. *Journal of Spacecraft and Rockets*, **14**(11), 696-700, 1977.

[IBRA98] Ibrahim S.R., Asmussen J.C., and Brincker R. Vector Triggering Random Decrement for High Identification Accuracy. *Journal of Vibration and Acoustics*, **120**(4), 970-975, 1998.

[JAME95] James G.H., Carne T.G., and Lauffer J.P. The natural excitation technique (NExT) for modal parameter extraction from operating structures. *Modal Analysis: the International Journal of Analytical and Experimental Modal Analysis*, **10**(4), 260-277, 1995.

[JUAN85] Juang J.-N. and Pappa R.S. An eigensystem realization algorithm for modal parameter identification and model reduction. *Journal of Guidance, Control, and Dynamics*, 1985.

[JUAN94] Juang J.-N. *Applied System Identification*. Prentice Hall, Englewood Cliffs, NJ, USA, 1994.

[KOLL95] Kollár I. *Frequency Domain System Identification Toolbox for Use With Matlab, User's Guide, Version 2*. The MathWorks, Natick, MA, USA, [http://www.mathworks.com], 1995.

[KRAE99a] Krämer C. *Brite-EuRam Project SIMCES, Task A1 and A2: Long Term Monitoring and Bridge Tests*. Technical report 168'349/21, EMPA, Dübendorf, Switzerland, January 1999.

[KRAE99b] Krämer C., de Smet C.A.M., and De Roeck G. Z24 Bridge damage detection tests. In *Proceedings of IMAC 17, the International Modal Analysis Conference*, pp. 1023-1029, Kissimmee, FL, USA, February 1999.

[KRAE99c] Krämer C., de Smet C.A.M., and Peeters B. Comparison of ambient and forced vibration testing of civil engineering structures. In *Proceedings of IMAC 17, the International Modal Analysis Conference*, pp. 1030-1034, Kissimmee, FL, USA, February 1999.

[KUNG78] Kung S.Y. A new identification and model reduction algorithm via singular value decomposition. In *Proceedings of the 12th Asilomar Conference on Circuits, Systems and Computers*, pp. 705-714, Asilomar, CA, USA, November 1978.

[LAQU98] Laquière A. and Van den Branden B. *Multivariabele Stochastische Systeem Identificatie. MACEC, Modal Analysis on Civil Engineering Constructions.* MSc thesis, Department of Civil Engineering, Katholieke Universiteit Leuven, Belgium, 1998.

[LEUR84] Leuridan J. *Some Direct Parameter Model Identification Methods Applicable for Multiple Input Modal Analysis*. PhD thesis, University of Cincinnati, OH, USA, 1984.

[LJUN95] Ljung L. *System Identification Toolbox for Use With Matlab, User's Guide, Version 4*. The MathWorks, Natick, MA, USA, [http://www.mathworks.com], 1995.

[LJUN99] Ljung L. *System Identification: Theory for the User*. Second edition, Prentice Hall, Upper Saddle River, NJ, USA, 1999.

[MAEC98a] Maeck J., Abdel Wahab M.M., and De Roeck G. Damage detection in reinforced concrete structures by dynamic system identification. In *Proceedings ISMA 23, Noise and Vibration Engineering*, pp. 939-946, Leuven, Belgium, September 1998.

[MAEC98b] Maeck J. and De Roeck G. *Brite-EuRam Project SIMCES, Task D: Damage Identification by Direct Stiffness Derivation From Modal Curvatures*. Internal report Department of Civil Engineering, K.U.Leuven, December 1998.

[MAEC99] Maeck J. and De Roeck G. Dynamic bending and torsion stiffness derivation from modal curvatures and torsion rates. *Journal of Sound and Vibration*, **225**(1), 153-170, 1999.

[MAEC00a] Maeck J., Abdel Wahab M.M., Peeters B., De Roeck G., De Visscher J., De Wilde W.P., Ndambi J.-M., and Vantomme J. Damage identification in reinforced concrete structures by dynamic stiffness determination. *Engineering Structures*, **22**(10), 1339-1349, 2000.

[MAEC00b] Maeck J., Peeters B., and De Roeck G. Damage identification on the Z24-Bridge using vibration monitoring. In *Proceedings of the European COST F3 Conference on System Identification and Structural Health Monitoring*, pp. 233-242, Madrid, Spain, June 2000.

[MAIA97] Maia N.M.M., Silva J.M.M., He J., Lieven N.A.J., Lin R.M., Skingle G.W., To W.-M., and Urgueira A.P.V. *Theoretical and Experimental Modal Analysis*. Edited by Maia N.M.M. and Silva J.M.M. Research Studies Press, Taunton, Somerset, UK, 1997.

[MARC96] Marchand P. *Graphics and GUIs With Matlab*. CRC Press, Boca Raton, FL, USA, 1996.

[MARI00] Mari J., Stoica P., and McKelvey T. Vector ARMA estimation: a reliable subspace approach. *IEEE Transactions on Signal Processing*, **48**(7), 2092-2104, 2000.

[MARP87] Marple S.L. *Digital Spectral Analysis With Applications*. Prentice-Hall, Englewood Cliffs, NJ, USA, 1987.

[MATL96] *Using Matlab Version 5*. The MathWorks, Natick, MA, USA, [http://www.mathworks.com], December 1996.

[McKE95] McKelvey T. *Identification of State-Space Models From Time and Frequency Data*. PhD thesis, Department of Electrical Engineering, Linköping University, Sweden, [ftp://ftp.control.isy.liu.se/pub/Reports/Ph.D.Thesis/PhD380.ps.Z], 1995.

[MEVE00] Mevel L., Benveniste A., Basseville M., and Goursat M. In operation structural damage detection and diagnosis. In *Proceedings of the European COST F3 Conference on System Identification and Structural Health Monitoring*, INRIA, pp. 641-650, Madrid, Spain, June 2000.

[MITC86] Mitchell L.D. Signal processing and the Fast-Fourier-Transform (FFT) analyzer - a survey. *Modal Analysis: the International Journal of Analytical and Experimental Modal Analysis*, **1**(1), 24-36, 1986.

[MONT91] Montgomery D.C. and Peck E.A. *Introduction to Linear Regression Analysis*. Second edition, John Wiley & Sons, New York, USA, 1991.

[MONT96] Montgomery D.C. *Introduction to Statistical Quality Control*. Second edition, John Wiley & Sons, New York, USA, 1996.

[MOUS86a] Moustakides G. *The Problem of Diagnosis With Respect to Physical Parameters for Changes in Structures*. Research report 295, INRIA, Rennes, France, 1986.

[MOUS86b] Moustakides G. and Benveniste A. Detecting changes in the AR parameters of a nonstationary ARMA process. *Stochastics*, **16**, 137-155, 1986.

[MOUS88] Moustakides G., Basseville M., Benveniste A., and Le Vey G. *Diagnosing Mechanical Changes in Vibrating Systems*. Research report 942, INRIA, Rennes, France, 1988.

[PAND91a] Pandit S.M. *Modal and Spectrum Analysis: Data Dependent Systems in State Space*. John Wiley & Sons, New York, USA, 1991.

[PAND91b] Pandey A.K., Biswas M., and Samman M.M. Damage detection from changes in curvature mode shapes. *Journal of Sound and Vibration*, **145**(2), 321-332, 1991.

[PASC99a] Pascual R. *Model Based Structural Damage Assessment Using Vibration Measurements*. PhD thesis, LTAS, Université de Liège, Belgium, 1999.

[PASC99b] Pascual R., Trendafilova I., Golinval J.C., and Heylen W. Damage detection using model updating and identification techniques. In *Proceedings of the 2nd International Conference on Identification in Engineering Systems*, pp. 588-597, Swansea, UK, March 1999.

[PEET95] Peeters B., De Roeck G., Pollet T., and Schueremans L. Stochastic subspace techniques applied to parameter identification of civil engineering structures. In *Proceedings of the International Conference MV2 on New Advances in Modal Synthesis of Large Structures, Non-Linear, Damped and Non-Deterministic Cases*, pp. 151-162, Lyon, France, October 1995.

[PEET96] Peeters B., Abdel Wahab M.M., De Roeck G., De Visscher J., De Wilde W.P., Ndambi J.-M., and Vantomme J. Evaluation of structural damage by dynamic system identification. In *Proceedings ISMA 21, Noise and Vibration Engineering*, pp. 1349-1361, Leuven, Belgium, September 1996.

[PEET97] Peeters B. and De Roeck G. The performance of time domain system identification methods applied to operational data. In *Proceedings DAMAS '97, Structural Damage Assessment Using Advanced Signal Processing Procedures*, pp. 377-386, Sheffield, UK, June-July 1997.

[PEET98a] Peeters B. and De Roeck G. Stochastic subspace system identification of a steel transmitter mast. In *Proceedings of IMAC 16, the International Modal Analysis Conference*, pp. 130-136, Santa Barbara, CA, USA, February 1998.

[PEET98b] Peeters B., De Roeck G., Hermans L., and Wauters T. Comparison of system identification methods using operational data of a bridge test. In *Proceedings ISMA 23, Noise and Vibration Engineering*, pp. 923-930, Leuven, Belgium, September 1998.

[PEET98d] Peeters B. and De Roeck G. *Brite-EuRam Project SIMCES, Task B1: Stochastic Subspace Identification Applied to Progressive Damage Test Vibration Data From the Z24-Bridge*. Internal report BWM-1998-07, Department of Civil Engineering, K.U.Leuven, November 1998.

[PEET99a] Peeters B., De Roeck G., and Andersen P. Stochastic system identification: uncertainty of the estimated modal parameters. In *Proceedings of IMAC 17, the International Modal Analysis Conference*, pp. 231-237, Kissimmee, FL, USA, February 1999.

[PEET99b] Peeters B., Van den Branden B., Laquière A., and De Roeck G. Output-only modal analysis: development of a GUI for Matlab. In *Proceedings of IMAC 17, the International Modal Analysis Conference*, pp. 1049-1055, Kissimmee, FL, USA, February 1999.

[PEET99c] Peeters B., Van den Branden B., and De Roeck G. Output-only modal analysis: a GUI for Matlab. In *Proceedings of the 2nd Benelux Matlab Usersconference*, Brussels, Belgium, March 1999.

[PEET99d] Peeters B. and De Roeck G. Reference based stochastic subspace identification in civil engineering. In *Proceedings of the 2nd International Conference on Identification in Engineering Systems*, pp. 639-648, Swansea, UK, March 1999.

[PEET99e] Peeters B. and De Roeck G. Experimental dynamic analysis of a steel mast excited by wind load. In *Proceedings of the 4th European Conference on Structural Dynamics: Eurodyn '99*: A.A. Balkema, Rotterdam, pp. 1075-1080, Prague, Czech Republic, June 7-10 1999.

[PEET99f] Peeters B. and De Roeck G. Reference-based stochastic subspace identification for output-only modal analysis. *Mechanical Systems and Signal Processing*, **13**(6), 855-878, 1999.

[PEET00a] Peeters B. and De Roeck G. Reference based stochastic subspace identification in civil engineering. *Inverse Problems in Engineering*, **8**(1), 47-74, 2000.

[PEET00b] Peeters B. and De Roeck G. One-year monitoring of the Z24-Bridge: environmental influences versus damage events. In *Proceedings of IMAC 18, the International Modal Analysis Conference*, pp. 1570-1576, San Antonio, TX, USA, February 2000.

[PEET00c] Peeters B., Maeck J., and De Roeck G. Dynamic monitoring of the Z24-Bridge: separating temperature effects from damage. In *Proceedings of the European COST F3 Conference on System Identification and Structural Health Monitoring*, pp. 377-386, Madrid, Spain, June 2000.

[PEET00d] Peeters B., Maeck J., and De Roeck G. Excitation sources and dynamic system identification in civil engineering. In *Proceedings of the European COST F3 Conference on System Identification and Structural Health Monitoring*, pp. 341-350, Madrid, Spain, June 2000.

[PEET00e] Peeters B. and De Roeck G. One-year monitoring of the Z24-Bridge: environmental effects versus damage events. *Earthquake Engineering and Structural Dynamics*, Accepted for publication, 2000.

[PEET00f] Peeters B., Maeck J., and De Roeck G. Vibration-based damage detection in civil engineering: excitation sources and temperature effects. *Smart Materials and Structures*, Submitted for publication, 2000.

[PINT94] Pintelon R., Guillaume P., Rolain Y., Schoukens J., and Van Hamme H. Parametric identification of transfer functions in the frequency domain - a survey. *IEEE Transactions on Automatic Control*, **AC-39**(11), 2245-2260, 1994.

[PIOM93] Piombo B., Ciorcelli E., Garibaldi L., and Fasana A. Structures identification using ARMAV models. In *Proceedings of IMAC 11, the International Modal Analysis Conference*, pp. 588-592, Orlando, FL, USA, 1993.

[PREV82] Prevosto M. *Algorithmes d'Identification des Caractéristiques Vibratoires de Structures Mécaniques Complexes* . PhD thesis, Université de Rennes I, France, March 1982.

[ROBE98] Roberts G.P. and Pearson A.J. Health monitoring of structures - towards a stethoscope for bridges. In *Proceedings of ISMA 23, the International Conference on Noise and Vibration Engineering*, Leuven, Belgium, September 1998.

[ROHR00] Rohrmann R.G., Baessler M., Said S., Schmid W., and Rücker W.F. Structural causes of temperature affected modal data of civil engineering structures obtained by long time monitoring. In *Proceedings of IMAC 18*, pp. 1-7, San Antonio, TX, USA, February 2000.

[ROHR91] Rohrmann R. G., Rücker W., Möller G., and Nitschke K. *Dynamische Untersuchungen an Einem Stahlbeton-Zweifeld-Träger Unter Zunehmender Schädigung Und Rißverfolgung Mit Piezofolien*. Forschungsbericht BAM-MAN, Berlin, Germany, 1991.

[RUSH99] Rushton A., Pearson A. J., and Roberts G. P. *Brite-EuRam Project SIMCES, Task A1: Environmental Monitoring of Z24 Bridge*. Report AM3548/ R004, WS Atkins Science & Technology, Bristol, UK, February 1999.

[RUCK95] Rücker W.F., Said S., Rohrmann R.G., and Schmid W. Load and condition monitoring of a highway bridge in a continous manner. In *Proceedings of the IABSE Symposium on Extending the Lifespan of Structures*, San Francisco, CA, USA, 1995.

[RYTT93] Rytter A. *Vibration Based Inspection of Civil Engineering Structures*. PhD thesis, Department of Building Technology and Structural Engineering, Aalborg University, Denmark, 1993.

[SCHO91] Schoukens J. and Pintelon R. *Identification of Linear Systems: a Practical Guideline to Accurate Modelling*. Pergamon Press, London, UK, 1991.

[SHIH88] Shih C.Y., Tsuei Y.G., Allemang R.J., and Brown D.L. Complex mode indication function and its application to spatial domain parameter estimation. *Mechanical Systems and Signal Processing*, **2**(4), 367-377, 1988.

[SIGN97] *Signal Processing Toolbox for Use With Matlab, User's Guide, Version 4*. The MathWorks, Natick, MA, USA, [http://www.mathworks.com], January 1997.

[SOHN99] Sohn H., Dzonczyk M., Straser E.G., Kiremidjian A.S., Law K.H., and Meng T. An experimental study of temperature effect on modal parameters of the Alamosa Canyon Bridge. *Earthquake Engineering and Structural Dynamics*, **28**(8), 879-897, 1999.

[STOI00] Stoica P., McKelvey T., and Mari J. MA estimation in polynomial time. *IEEE Transactions on Signal Processing*, **48**(7), 1999-2012, 2000.

[STOI97] Stoica P. and Moses R.L. *Introduction to Spectral Analysis*. Prentice-Hall, Englewood Cliffs, NJ, USA, 1997.

[VAND99] Van den Branden B., Peeters B., and De Roeck G. *Introduction to MACEC V2.0, Modal Analysis on Civil Engineering Constructions*. Department of Civil Engineering, Katholieke Universiteit Leuven, Belgium, [http://www.bwk.kuleuven.ac.be/bwk/mechanics/macec], March 1999.

[VANO91] Van Overschee P. and De Moor B. Subspace algorithm for the stochastic identification problem. In *Proceedings of the 30th IEEE Conference on Decision and Control*, pp. 1321-1326, Brighton, UK, 1991.

[VANO93] Van Overschee P. and De Moor B. Subspace algorithm for the stochastic identification problem. *Automatica*, **29**(3), 649-660, 1993.

[VANO96] Van Overschee P. and De Moor B. *Subspace Identification for Linear Systems: Theory - Implementation - Applications*. Kluwer Academic Publishers, Dordrecht, The Netherlands, 1996.

[VANO97] Van Overschee P., De Moor B., Dehandschutter W., and Swevers J. A subspace algorithm for the identification of discrete time frequency domain power spectra. *Automatica*, **33**(12), 2147-2157, 1997.

[WATS00] Watson D.K. and Rajapakse R.K.N.D. Seasonal variation in material properties of a flexible pavement. *Canadian Journal of Civil Engineering*, **27**(1), 44-54, 2000.

[ZEIG74] Zeiger H.P. and McEwen A.J. Approximate linear realization of given dimension via Ho's algorithm. *IEEE Transactions on Automatic Control*, **AC-19**(2), 153, 1974.

SYSTEEMIDENTIFICATIE EN SCHADEDETECTIE IN DE BOUWKUNDE

Situering van het onderwerp

Gezondheidscontrole van structuren is een bloeiend onderzoeksdomein gedreven door de noodzaak om subjectieve visuele inspectiemethodes aan te vullen met objectieve niet-destructieve methodes die gebaseerd zijn op metingen van fysische grootheden en computeranalyses. Men onderscheidt *globale* en *lokale* methodes. Lokale methodes gaan de toestand na van een beperkt deel van de structuur en maken gebruik van: akoestiek, wervelstromen, hardheidstesten, magnetische velden, radiografie, ... Een van de weinige globale controlemethodes maakt gebruikt van trillingsmetingen. Het globale schadedetectie mechanisme van de methode bestaat hierin dat een lokale stijfheidsverandering de globale dynamische eigenschappen van de structuur verandert. In de "0 Hz variante" van de methode worden de verplaatsingen van de structuur gemeten onder een statische belasting.

Het grote voordeel van een globale methode is dat de metingen op slechts één plaats volstaan om een beeld te krijgen van de toestand van de hele structuur. Methodes gebaseerd op trillingsmetingen kunnen met regelmatige tussenpozen toegepast worden — wat dan en tijdelijke meetopstelling zou vergen — ofwel permanent — wat verondersteld dat de sensoren permanent geïnstalleerd blijven op de structuur. Dankzij de permanente opstelling is een verschuiving mogelijk van een *preventieve tijdsgebonden* naar een *voorspellende toestandsgebonden* onderhoudstrategie. Zo'n verschuiving vermindert zowel het risico op een ernstig falen van de structuur als de totale onderhoudskost door het vermijden van overbodige inspecties.

Het veelbelovende perspectief dat gezondheidscontrole met behulp van trillingsmetingen biedt, heeft vele onderzoekers wereldwijd geïnspireerd. Doebling *et al.* maakten een overzicht en een klasseverdeling van de literatuur [DOEB96]. Er is enige consensus om vier niveaus van schade-identificatie te onderkennen (zie bijvoorbeeld [RYTT93]):

- niveau 1 – *ontdekking*: Is de structuur al dan niet beschadigd?
- niveau 2 – *plaatsbepaling*: Waar bevindt zich de schade?
- niveau 3 – *begroting*: Hoe ernstig is de schade?

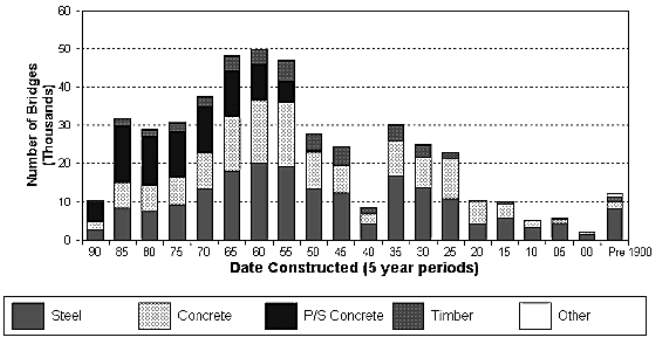

Figuur N.1: Leeftijdsverdeling van bruggen in de VS [CHAS97]. The tijdsas loopt van rechts naar links.

- niveau 4 – *voorspelling*: Hoe lang gaat de structuur nog standhouden en wat is de overgebleven dienstbelasting?

De ontdekking van schade (niveau 1) komt neer op het vaststellen van veranderingen van de dynamische eigenschappen zoals eigenfrequenties. Twee benaderingen zijn denkbaar om trillingsonderzoek boven niveau 1 uit te tillen. In een eerste benadering wordt een groot aantal sensoren ingezet om lokale veranderingen van modevormen vast te stellen. De plaatsbepaling van de schade is dan typisch nauwkeurig tot op de afstand tussen twee sensoren na. Een tweede benadering heeft niet zoveel sensoren nodig, maar wel een analytisch model van de structuur. Model parameters die met de schade verband houden worden zodanig bijgesteld dat de dynamische eigenschappen van het model overeenkomen met die op de structuur gemeten zijn. *Eindige-elementenmodel updating* (bijstelling) methodes zijn hier een voorbeeld van [FRIS95].

Alhoewel trillingsonderzoek toepasbaar is op allerlei structuren worden bruggen beschouwd als belangrijke kandidaten. Zoals blijkt uit Figuur N.1 beleefde het bouwen van bruggen in de VS een hoogconjunctuur in de jaren 60 toen het autowegennet dat de deelstaten verbindt vorm kreeg. De Europese situatie is vergelijkbaar waar de aanleg van de meeste autowegen in de zelfde periode geschiedde. Veel van de toen gebouwde bruggen bereiken hun kritische leeftijd en aan de hand van voorspellingen kan men aantonen dat de onderhoudsvraag tegen 2010 een ongekende hoogte zal bereiken. Trillingsonderzoek is een nuttige methode om de toestand van deze bruggen in te schatten en onderhoudsprogramma's op te stellen.

Recente tuikabel en hangbruggen met een grote overspanning worden standaard uitgerust met een ingebouwd controlesysteem dat bestaat uit allerlei soorten sensoren: versnellingsopnemers, windmeters, verplaatsingsopnemers, hellingmeters, rekstrookjes, thermometers, ... Over de hele wereld vindt men dergelijke goed uitgeruste bruggen, maar een van de best uitgeruste is de Tsing Ma Brug in Hong-Kong (zie Figuur N.2). Gebouwd in 1997 en met een hoofdoverspanning van 1377 m, wordt deze brug gecontroleerd met

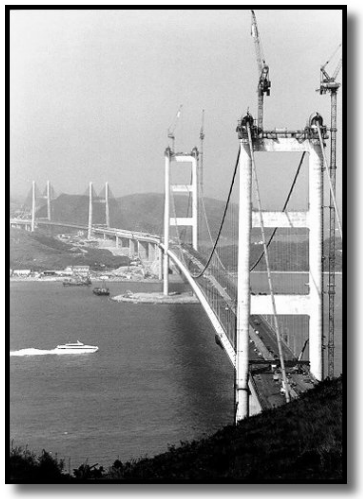

Figuur N.2: De Tsing Ma Brug in Hong-Kong is uitgerust met ongeveer 600 sensoren.

behulp van ongeveer 600 sensoren.

Controlesystemen worden voor meer gebruikt dan enkel voor schadedetectie. Beschreven toepassingen en doelstellingen van werkzame systemen zijn: kwaliteitscontrole tijdens de constructie van de brug; het controleren van ontwerpparameters van een pas voltooide brug; bij uitzonderlijke windsnelheden dienst doen als waarschuwingssysteem om de brug voor alle verkeer te sluiten; in de loop van zijn bestaan de gebruiksgrens en uiterste grenstoestand van de brug opvolgen. Er bestaat echter enige vaagheid omtrent de concrete vertaling van meetgegevens naar de gezondheidstoestand van een brug toe. Hierbij speelt een "ingenieursbeoordeling" blijkbaar een niet te onderschatten rol.

Bij het gebruik van trillingen voor gezondheidscontrole worden nogal wat meetgegevens gegenereerd. Daarom is het nodig om de essentie van deze hoeveelheid gegevens te vatten in een *experimenteel model* van de structuur. Dit proces wordt *systeemidentificatie* genoemd. Algemene systeemidentificatie is een onderzoeksdomein uit de elektronica. Een gezaghebbende referentie is het boek van Ljung [LJUN99]. Actuele ontwikkelingen situeren zich op het domein van *deelruimte* methodes [VANO96] en *maximale waarschijnlijkheid* frequentie-domein methodes[1] [SCHO91].

Het toepassen van systeemidentificatie op trillende structuren leverde een nieuw onderzoeksdomein op in de mechanica: de *experimentele modale analyse*. Het

[1]Het enkel meegeven van de Nederlandse term zou tot verwarring kunnen leiden. *Deelruimte* is beter bekend als *subspace*, en *maximum likelihood* klinkt wellicht wat bekender dan *maximale waarschijnlijkheid*.

geïdentificeerde model is in dit geval een *modaal model*[2], bestaande uit eigenfrequenties, dempingsverhoudingen, modevormen en modale participatiefactoren. Het eerste modale analyse boek was geschreven door Ewins [EWIN84]. Een meer recente stand-van-zaken vindt men in [HEYL95, MAIA97, ALLE99].

Gewoonlijk is schade-identificatie gebaseerd op het volgen van veranderingen in het modale model. Een alternatief bestaat erin om slechts een model van de gezonde structuur te identificeren. Nadien worden statistische hypothese tests aangewend om te beoordelen of nieuwe meetgegevens nog steeds kunnen verklaard worden door het oorspronkelijke "gezonde" model. Deze methodes werden ontwikkeld in INRIA, Frankrijk [MOUS86a, MOUS86b, MOUS88, BASS93a, BASS93b, MEVE00]. Het voordeel van dergelijke methodes is dat geen nieuw experimenteel model hoeft geïdentificeerd te worden wanneer nieuwe gegevens beschikbaar komen. Dit is immers een procedure die soms moeilijk te automatiseren is.

Focus van de thesis

Uit vorige afdeling blijkt dat er reeds heel wat gebeurd is op het vlak van gezondheidscontrole van structuren met behulp van trillingsmetingen. Desalniettemin zijn vele van de voorgestelde methodes blijven steken in het stadium van de numerieke simulaties of de traditionele "zaagsneden" aangebracht in stalen profielen in het laboratorium.

Deze thesis behandelt twee onmisbare elementen van een reëel controlesysteem. Het eerste element is de bepaling van een experimenteel model van een trillende structuur louter op basis van uitgangsmetingen (versnellingen). De kosten verbonden aan trillingstesten kunnen in belangrijke mate gedrukt worden door het gebruik van vrij beschikbare — maar onmeetbare — trillingsbronnen uit de omgeving. Hierdoor hoeft men geen dure kunstmatige — maar meetbare — bronnen zoals shakers te gebruiken, wat trouwens ondenkbaar zou zijn in een permanent controlesysteem. Reeds enkele decennia bestaan er basismethodes om de modale parameters louter op basis van uitgangsmetingen te bepalen. De basisoplossing bestaat uit het selecteren van pieken in de spectra van de uitgangssignalen. Zoals aangetoond in Hoofdstuk 3 bestaan er meer gevorderde technieken die de kwaliteit van het experimentele model in belangrijke mate verhogen.

Het tweede element dat behandeld wordt in deze thesis is de detectie van schade onder veranderende omgevingsparameters. Het probleem is dat zowel schade als temperatuur de eigenfrequenties van een structuur beïnvloeden. Er wordt een oplossing aangedragen die het mogelijk maakt om beide invloeden te scheiden. Voor de goede orde vermelden we nog dat enkel niveau 1 schade-identificatie behandeld wordt. De voorgestelde methode ontdekt schade zonder er evenwel de plaats van te bepalen of ze te begroten. Echter, de

[2] *Modaal* heeft hier (uiteraard) niet de betekenis van *middelmatig*, maar wel van *bestaande uit modes*.

ontwikkeling van een permanente en automatische detectiemethode wordt beschouwd als een zeer belangrijke stap. Het betekent immers dat een snel waarschuwingssysteem beschikbaar komt dat slechts een handvol sensoren nodig heeft en geen analytisch model van de structuur behoeft.

De meer gedetailleerde originele bijdragen van dit werk zijn de volgende.

- Eindige-elementenmodellen van trillende structuren geëxciteerd door witte ruis worden in wiskundig verband gebracht met stochastische toestandsruimte en modale modellen. De analyse van de modellen en hun onderlinge verbanden maken duidelijk hoe ze geïdentificeerd kunnen worden uitgaande van uitgangsmetingen en vervolgens gebruikt in modale en spectrum analyse. Modale parameters worden beschouwd als belangrijke kenmerken om structurele schade te bepalen.

- Bijna alle beschikbare stochastische systeemidentificatie methodes worden kritisch ontleed. Ze worden geklasseerd naar de vorm waarin de meetgegevens gegoten moeten worden: spectra, covarianties of de oorspronkelijke tijdreeksen. De methodes worden niet alleen theoretisch vergeleken maar ook aan de hand van een Monte-Carlo simulatiestudie. De theoretische vergelijking maakt onder andere duidelijk dat ─ omwille van historische redenen ─ essentieel dezelfde methodes verschillende namen hebben gekregen in de literatuur. Bijvoorbeeld de bekende *poly-referentie tijdsdomein* methode toegepast op covarianties (in de plaats van impulsresponsies) kan beschouwd worden als een *instrumentaal variabele* methode. Evenzo is het *eigensysteem realisatie algoritme* toegepast op covarianties gelijkwaardig aan de *covariantie-gedreven deelruimte* methode[3]. De vergelijkende simulatiestudie licht het praktisch gebruik van de methodes toe en maakt het mogelijk om de kwaliteit van de identificatieresultaten relatief te beoordelen.

- De *tijdreeks-gedreven stochastische deelruimte*[4] methode wordt aangepast en uitgebreid om ze meer geschikt te maken als modale-analysemethode. De aanpassing bestaat uit het beperken van de dimensies van de matrices (en de rekentijd) door een deel van de overtolligheid weg te werken die typisch aanwezig is bij modale-analyse-experimenten waar gewoonlijk vele sensoren gebruikt worden. De uitbreiding bestaat uit een efficiënte combinatie van het (klassieke) stabilisatiediagram met deelruimte methodes. Het stabilisatiediagram

---

[3]Het enkel meegeven van de Nederlandse term zou tot verwarring kunnen leiden. *Poly-referentie tijdsdomein* is beter bekend als *polyreference time domain*, *instrumentaal variabele* staat voor *instrumental variable*, en *eigensysteem realisatie algoritme* klinkt als *eigensystem realization algorithm* in het Engels. *Covariantie-gedreven deelruimte* staat voor *covariance-driven subspace*.

[4]*Tijdreeks-gedreven stochastische deelruimte* wordt vertaald als *data-driven stochastic subspace*.

wordt gebruikt om de modale parameters te bepalen uit de geïdentificeerde deelruimtemodellen. Een andere originele bijdrage is het splitsen van het totale uitgangssignaal in modale responsies. De eerste toepassingen van de tijdreeks-gedreven stochastische deelruimte methode op louter op uitgangssignalen gebaseerde modale analyse dateert van 1995 [PEET95].

- Er wordt een methode ontwikkeld om normale omgevingseffecten te scheiden van schade. Beide beïnvloeden de gemeten eigenfrequenties van de structuur. In het kort bestaat de methode uit het identificeren van een dynamisch omgevingsmodel van de "gezonde" structuur, uitgaande van temperatuur-eigenfrequentie tijdreeksen. Een statistische test maakt het vervolgens mogelijk om te beslissen of nieuwe metingen overeenkomen met het oorspronkelijke omgevingsmodel. De originaliteit van de methode ligt hierin dat deelruimte-identificatie op een automatische wijze aangewend wordt om de eigenfrequenties van de structuur te bepalen uitgaande van een immense hoeveelheid versnellingsmetingen en dat dynamische **ARX** omgevingsmodellen geïdentificeerd worden in plaats van de gebruikelijke statische lineaire regressiemodellen.

- Wat de software-implementatie van de methodes betreft, werd de ontwikkeling van een grafische gebruikersinterface in goede banen geleid. Daarenboven werd een *automatische modale-analyseprocedure* ontwikkeld, gebaseerd op de automatische interpretatie van stabilisatiediagrammen. Het is wellicht overbodig te vermelden dat dergelijke procedure beslissend is voor het succes van een permanent controlesysteem dat de evolutie van de modale parameters volgt

- Wat de praktische toepassingen betreft, werd nogal wat experimenteel werk verzet. Vier gewapend betonnen balken werden onderworpen aan een toenemende statische belasting en ondergingen voortschrijdende schade. Bij elke belastingsstap vond een trillingsexperiment plaats. De bedoeling van de balktests was niet enkel het opstellen van een gegevensbestand waaruit geput kan worden om systeem identificatie methodes te valideren, maar ook om na te gaan of het fundamenteel mogelijk is om veranderingen van dynamische eigenschappen onder invloed van schade te meten. Buiten het laboratorium werden ook trillingsmetingen uitgevoerd: op een stalen zendmast en op enkele Belgische bruggen over de E19-autoweg. Deze metingen laten toe om gevoel te krijgen voor realistische testomstandigheden en dito meetgegevens.

- Tenslotte werd een diepgaande analyse van de meetgegevens van de Zwitserse Z24-Brug uitgevoerd. De meetgegevens zijn uniek door de combinatie van langeduur controlemetingen en de toepassing van realistische schadescenario's. Er wordt aangetoond dat de schade inderdaad ontdekt kan worden, ondanks de veranderende omgevingsparameters.

Organisatie van de tekst

In onze bijdrage tot gezondheidscontrole met behulp van trillingsmetingen komen twee systeemidentificatie benaderingen naar voren. Het eerste (en grootste) deel handelt over systeemidentificatie die louter gebaseerd is op uitgangssignalen. Er wordt beschreven hoe belangrijke kenmerken van de structuur — de modale parameters — bepaald kunnen worden uit trillingsmetingen. Hierbij hoeft men niet te beschikken over een exacte kennis van de excitatie (de ingangen) die de oorzaak is van de trillingen van de structuur (de uitgangen). De modale parameters bevatten nuttige informatie over de gezondheidstoestand van de structuur.

Het tweede deel handelt over een toepassing van ingang-uitgang systeemidentificatie. Een blijvend probleem na het eerste deel is dat de modale parameters niet enkel veranderen onder invloed van schade, maar ook door variërende omgevingsparameters. Een omgevingsmodel van de gezonde structuur maakt het mogelijk om beide invloeden te scheiden. Het omgevingsmodel wordt geïdentificeerd op basis van gemeten omgevingsparameters zoals temperaturen (de ingangen) en de in het eerste deel bepaalde kenmerken, de eigenfrequenties (de uitgangen).

Een meer gedetailleerd hoofdstuk-per-hoofdstuk overzicht wordt nu gegeven (zie ook Figuur N.3).

Hoofdstuk 1
: is de algemene inleiding. Het onderwerp wordt gesitueerd, de eigen bijdragen worden duidelijk gemaakt en de organisatie van de tekst wordt besproken

Hoofdstuk 2
: behandelt modellen van trillende structuren. Stapsgewijs worden modellen die dicht staan bij de fysische realiteit omgevormd tot algemene dynamische modellen die nuttiger zijn voor systeemidentificatie. Dit hoofdstuk verbindt Eindige-elementenmodellen van bouwkundige constructies, toestandsruimtemodellen afkomstig uit de elektronica, en modale modellen oorspronkelijk ontwikkeld in de mechanica. Een simulatiestudie verduidelijkt de modelleringsconcepten.

Hoofdstuk 3
: gaat over stochastische systeemidentificatie methodes. Louter op basis van uitgangsmetingen identificeren deze methodes de modellen van Hoofdstuk 2. Spectrum-gedreven, covariantie-gedreven en tijdreeks-gedreven methodes worden achtereenvolgens besproken. Om de theorie te verduidelijken en het praktisch gebruik toe te lichten, worden de besproken methodes toegepast op een gesimuleerd voorbeeld.

Hoofdstuk 4

beschrijft de implementatie van een grafische gebruikersinterface naar stochastische systeemidentificatie methodes. Naast identificatie algoritmes werden ook voorbehandelings- en visualisatiefuncties in het programma opgenomen. Daarenboven werd een automatische modale-analyseprocedure ontwikkeld die het mogelijk maakt om een groot aantal gegevensbestanden te doorworstelen zonder tussenkomst van de gebruiker.

Hoofdstuk 5

behandelt twee voorbeelden. Trillingstests op betonnen balken die onderworpen zijn aan voortschrijdende schade halen de schadedetectie mogelijkheden van de modale parameters naar boven. De tests werden uitgevoerd in optimale laboratoriumomstandigheden. In het tweede voorbeeld worden de modale parameters van een door de wind geëxciteerde stalen mast bepaald. Dit is een test in reële omstandigheden waarin de mogelijkheden van stochastische systeemidentificatie kunnen verkend worden.

Hoofdstuk 6

is opnieuw een theoretisch hoofdstuk. Het gebruik van ingang-uitgang systeemidentificatie ter bepaling van een omgevingsmodel dat het verband beschrijft tussen temperaturen en eigenfrequenties wordt aangetoond. Er wordt ook aangegeven hoe het model kan gebruikt worden om temperatuurseffecten uit de trillingsmeetgegevens te filteren.

Hoofdstuk 7

stelt systeemidentificatie en schadedetectie resultaten voor die bekomen zijn uit de meetgegevens van de Z24-Brug. Het interessante van dit voorbeeld is dat alle ontwikkelingen van deze thesis erop kunnen toegepast worden. Verschillende kunstmatige en natuurlijke trillingsbronnen worden vergeleken; de evolutie van de modale parameters van de brug onder toenemende schade wordt beschreven en een omgevingsmodel voor de Z24-Brug wordt geïdentificeerd dat met succes aangewend kan worden om schade te ontdekken.

Hoofdstuk 8

bevat de gevolgtrekkingen van dit werk. Ook worden de onopgeloste problemen overlopen en suggesties aan de hand gedaan voor verder onderzoek in het domein van de gezondheidscontrole van structuren met behulp van trillingsmetingen.

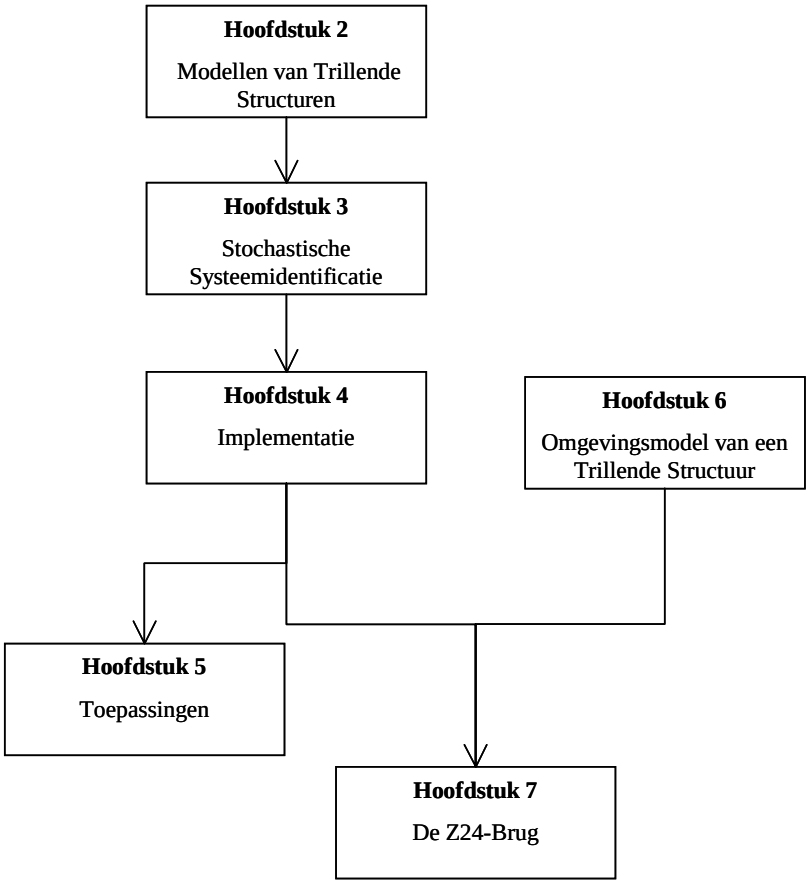

Figuur N.3: Organisatie van de tekst. De linkerkant van de grafiek gaat over de identificatie van een model van een trillende structuur. De rechterkant geeft aan hoe omgevingsparameters dit model beïnvloeden. Alle theoretische ontwikkelingen komen samen in de Z24-Brug toepassing van hoofdstuk 7.

CURRICULUM VITAE

Bart Peeters was born in Herentals, Belgium, on April 2, 1971. He is married to Hilde De Beuckeleer and has one son, Karel (° January 2, 2000).

Education

1994 – 2000
PhD student at the Department of Civil Engineering, K.U.Leuven.

1989 – 1994
Degree of Civil Engineering, K.U.Leuven

1983 – 1989
Secondary Education, Mathematics – Latin, Sint-Pieters College, Leuven.

Work

September 2000 – Today
Manager RTD projects and training, LMS International, Leuven

October 1994 – August 2000
Research and teaching assistant, Department of Civil Engineering, K.U.Leuven.

Summer holidays 1991 – 1994
Steward on night trains, Wagons-Lits, Brussels.

Publications

Theses

[PEET00g] Peeters B. *System Identification and Damage Detection in Civil Engineering*. PhD thesis, Department of Civil Engineering, K.U.Leuven, Belgium, December 2000.

[PEET94] Peeters B., and Schaerlaekens S. *Nonlinear Multi-material 2D Beam Element with Initial Curvature: Development – Implementation – Verification*. MSc thesis,

Department of Civil Engineering, K.U.Leuven, Belgium and EPFL, Lausanne, Switzerland, July 1994.

International journal papers

[PEET00f] Peeters B., Maeck J., and De Roeck G. Vibration-based damage detection in civil engineering: excitation sources and temperature effects. *Smart Materials and Structures*, Submitted for publication, 2000.

[PEET00e] Peeters B. and De Roeck G. One-year monitoring of the Z24-Bridge: environmental effects versus damage events. *Earthquake Engineering and Structural Dynamics*, Accepted for publication, 2000.

[PEET00a] Peeters B. and De Roeck G. Reference based stochastic subspace identification in civil engineering. *Inverse Problems in Engineering*, **8**(1), 47-74, 2000.

[PEET99f] Peeters B. and De Roeck G. Reference-based stochastic subspace identification for output-only modal analysis. *Mechanical Systems and Signal Processing*, **13**(6), 855-878, 1999.

Conference proceedings

[DERO00b] De Roeck G., Peeters B., and Maeck J. Dynamic monitoring of civil engineering structures. In *Proceedings of IASS-IACM 2000, Computational Methods for Shell and Spatial Structures*, Chania, Greece, June 2000.

[DERO00a] De Roeck G., Peeters B., and Ren W.-X. Benchmark study on system identification through ambient vibration measurements. In *Proceedings of IMAC 18, the International Modal Analysis Conference*, pp. 1106-1112, San Antonio, TX, USA, February 2000.

[PEET00d] Peeters B., Maeck J., and De Roeck G. Excitation sources and dynamic system identification in civil engineering. In *Proceedings of the European COST F3 Conference on System Identification and Structural Health Monitoring*, pp. 341-350, Madrid, Spain, June 2000.

[PEET00c] Peeters B., Maeck J., and De Roeck G. Dynamic monitoring of the Z24-Bridge: separating temperature effects from damage. In *Proceedings of the European COST F3 Conference on System Identification and Structural Health Monitoring*, pp. 377-386, Madrid, Spain, June 2000.

[PEET00b] Peeters B. and De Roeck G. One-year monitoring of the Z24-Bridge: environmental influences versus damage events. In *Proceedings of IMAC 18, the International Modal Analysis Conference*, pp. 1570-1576, San Antonio, TX, USA, February 2000.

[PEET99e] Peeters B. and De Roeck G. Experimental dynamic analysis of a steel mast excited by wind load. In *Proceedings of the 4th European Conference on Structural Dynamics: Eurodyn '99*: A.A. Balkema, Rotterdam, pp. 1075-1080, Prague, Czech Republic, June 7-10 1999.

[PEET99d] Peeters B. and De Roeck G. Reference based stochastic subspace identification in civil engineering. In *Proceedings of the 2nd International Conference on Identification in Engineering Systems*, pp. 639-648, Swansea, UK, March 1999.

[PEET99c] Peeters B., Van den Branden B., and De Roeck G. Output-only modal analysis: a GUI for Matlab. In *Proceedings of the 2nd Benelux Matlab Usersconference*, Brussels, Belgium, March 1999.

[PEET99b] Peeters B., Van den Branden B., Laquière A., and De Roeck G. Output-only modal analysis: development of a GUI for Matlab. In *Proceedings of IMAC 17, the International Modal Analysis Conference*, pp. 1049-1055, Kissimmee, FL, USA, February 1999.

[PEET99a] Peeters B., De Roeck G., and Andersen P. Stochastic system identification: uncertainty of the estimated modal parameters. In *Proceedings of IMAC 17, the International Modal Analysis Conference*, pp. 231-237, Kissimmee, FL, USA, February 1999.

[PEET98b] Peeters B., De Roeck G., Hermans L., and Wauters T. Comparison of system identification methods using operational data of a bridge test. In *Proceedings ISMA 23, Noise and Vibration Engineering*, pp. 923-930, Leuven, Belgium, September 1998.

[PEET98a] Peeters B. and De Roeck G. Stochastic subspace system identification of a steel transmitter mast. In *Proceedings of IMAC 16, the International Modal Analysis Conference*, pp. 130-136, Santa Barbara, CA, USA, February 1998.

[PEET97] Peeters B. and De Roeck G. The performance of time domain system identification methods applied to operational data. In *Proceedings DAMAS '97, Structural Damage Assessment Using Advanced Signal Processing Procedures*, pp. 377-386, Sheffield, UK, June-July 1997.

[PEET96] Peeters B., Abdel Wahab M.M., De Roeck G., De Visscher J., De Wilde W.P., Ndambi J.-M., and Vantomme J. Evaluation of structural damage by dynamic system identification. In *Proceedings ISMA 21, Noise and Vibration Engineering*, pp. 1349-1361, Leuven, Belgium, September 1996.

[PEET95] Peeters B., De Roeck G., Pollet T., and Schueremans L. Stochastic subspace techniques applied to parameter identification of civil engineering structures. In *Proceedings of the International Conference MV2 on New Advances in Modal Synthesis of Large Structures, Non-Linear, Damped and Non-Deterministic Cases*, pp. 151-162, Lyon, France, October 1995.

Internal reports

[PEET98d] Peeters B. and De Roeck G. *Brite-EuRam Project SIMCES, Task B1: Stochastic Subspace Identification Applied to Progressive Damage Test Vibration Data From the Z24-Bridge*. Internal report BWM-1998-07, Department of Civil Engineering, K.U.Leuven, November 1998.

[PEET98c] Peeters B. and De Roeck G. *Brite-EuRam Project SIMCES, Task B1: Stochastic Subspace Identification: Context, Theory, Application*. Internal report BWM-1998-04, Department of Civil Engineering, K.U.Leuven, May 1998.